**Department of Chemistry**

# Crystallisation of Calcium Oxalate Solids in the Presence of Tetrazoles

**Calum John McMulkin**

**This thesis is presented for the Degree of**
**Doctor of Philosophy**
**of**
**Curtin University**

**October 2017**

# Declaration

To the best of my knowledge and belief this thesis contains no material previously published by any other person except where due acknowledgement has been made.

This thesis contains no material which has been accepted for the award of any other degree or diploma in any university.

I warrant that I have obtained, where necessary, permission from the copyright owners to use any third-party copyright material reproduced in this thesis, or to use any of my own published work (e.g. journal articles) in which the copyright is held by another party (e.g. publisher, co-author).

I warrant that all research data for this thesis will be stored in a safe location (i.e. Curtin R-drive) for at least 5 years after the thesis is published, in line with data storage guidelines at Curtin University.

Signature:

Date: 30/10/2017

# Abstract

This study has investigated the nucleation, crystal growth and associated mechanisms of calcium oxalate monohydrate (COM) crystals in the presence of a series of 26 tetrazole-containing molecules in aqueous solutions. Through the use of microscopy, spectroscopy and light scattering techniques, changes to the thermodynamically stable COM grown in the presence of the series of tetrazole molecules can be compared to the pure system. Trends based on the visual and numerical data obtained allow for the identification of structure-activity relationships between COM crystal morphologies and the tetrazole molecular structures. The aforementioned experimentation includes the first measurements and research on the effects of tetrazole-containing molecules on calcium oxalate crystallisation. Optical microscopy, SEM and quantitative data analysis of the crystals' shape and particle numbers provided a large amount of valuable data on morphological changes. The tetrazole molecules containing multiple tetrazole functional groups were discovered to be the most potent, often altering the habit of COM from the typical 6-sided elongated hexagonal shape to a shortened 4-sided diamond shape. The underlying mechanism responsible for the observed change in habit of the crystals being due to the strength of the tetrazole moiety to bind selectively to specific crystallographic faces of COM. The most commonly affected surfaces were found to be the apical tips or (12-1), (1-2-1), (021) and (0-21) faces of COM, resulting in shortened crystals in the [001] direction. To investigate the underlying reasons for the inhibition seen with microscopy, nucleation rates of COM in the presence of the additive series utilising dynamic light scattering (DLS) were studied. The results indicated that the vast majority of tetrazole molecules in the series inhibited the nucleation rate detected to varying degrees. Several inhibited the nucleation rate relative to the control with a reduction of particle numbers (or nuclei) by more than 70%. Among these, typically the di-tetrazole-containing species impacted with greater potency than mono-tetrazole-containing molecules. Differences in nucleation rate inhibition between molecules of similar structures were also observed, indicating that structure can strongly impact the strength of inhibition; moreover this is typically thought to be *via* the charge of the inhibiting species, which at pH ~7 relies on the charge of the tetrazole ring in solution. The complexation of the additive series with $Ca^{2+}$ in solution was studied to determine the amount of impact the tetrazole molecules

would have on the supersaturation state and consequently, whether nucleation rate inhibition was actually a reduction in the supersaturation state. Removal of free calcium from solution *via* complexation at equilibrium subsequently lowers the supersaturation (due to the decrease in available calcium ions), thus, complexation can have a pronounced overall effect on calcium oxalate nucleation rate. The dissolved calcium was measured using ICP-AES. The results indicated the strength of the di-tetrazole-containing molecules to inhibit calcium oxalate nucleation. Additionally, the di-tetrazole molecules also complexed calcium much more strongly than many mono-tetrazole molecules in the series, up to 5 times more relative to the control. Thus, complexation of the tetrazole molecules to $Ca^{2+}$ can significantly impact on the supersaturation and contributes to the nucleation inhibition of COM. Interestingly, a unique interaction of the tetrazole species occurred with COM as determined by investigations with confocal Raman microscopy (CRM) and photophysics. Incorporation of additives into the crystal lattice during growth occurs routinely, however in the case of the tetrazole molecules studied; the overlap of $\pi$ orbitals once incorporated within the crystal lattice enabled an aggregated emission to be observed using the excitation and emission properties of the tetrazole molecules, meaning that the tetrazole molecules incorporate as aggregates of molecules and not individually. Additionally, the additives location and intensity embedded within the crystals could be ascertained with CRM. Lastly, an investigation into the crystal growth impacts of several of the tetrazole molecules in the series with atomic force microscopy (AFM) was conducted. Spiral crystal growth was achieved first in the absence of additives to measure the control growth rate, before exposing the crystals to the tetrazole-containing molecules and determining their impact. Most tetrazoles reduced the crystal growth rates of the [001] and [100] steps on the (010) COM face. The underlying mechanism of the reduced growth rates was observed to be *via* step pinning, where molecules adsorbed to the surface interfere with the step growth. This is typically indicated by the roughening of the COM crystal step edges. Steps were found to be of multi elementary step sizes, corresponding to a triple step (macro step). The work conducted indicates that the tetrazole functionality can be used in crystal growth modification to inhibit calcium oxalate monohydrate crystallisation and may provide a new promising moiety for the control of crystal growth and morphology of biominerals and crystals.

# Acknowledgements

First and foremost, I would like to thank my PhD supervisors Dr. Franca Jones and Dr. Massimiliano Massi for their guidance, suggestions, patience and generous support. You allowed me to pursue my work autonomously, whilst keeping me on track and grounded. I am sure that this thesis would not be possible without their guidance and I am extremely grateful for the opportunity to have worked on this project which has kept me intrigued for many years. Many thanks Franca, for the many hours of SEM, and many unforgettable experiences and opportunities at the summer workshop and conference in Japan in 2016. Thanks to Max and his Empire, for allowing me to be the light entertainment in group meetings, and for always being interested in what I was doing.

The AFM, Raman and optical measurements presented in this work could not have been achieved without the knowledge and patience of Dr. Thomas Becker and constant assistance from Emily Barker, when software and hardware issues were making long days even longer. I now have an invaluable respect for what is more of an art than a science.

I am thankful to Jamie Woodward and the Murdoch University Marine and Freshwater Research Laboratory for their help with all ICP-AES measurements.

To all my friends and staff at Curtin who made postgraduate life challenging and enjoyable, I am grateful to each and every one of you. Special thanks to my nanotechnology cohort, for without the solid base of our undergraduate together, my study would not have continued.

There are a number of people without whom this thesis would not have been possible. My close friends and family outside of academic life, without your encouragement, help and love throughout all of my study would have made finishing this work an impossible task. Thank you.

# Table of Contents

**Declaration** ---------- ii

**Abstract** ---------- iii

**Acknowledgements** ---------- v

**Table of Contents** ---------- vi

**Abbreviations** ---------- ix

**Compound Numbering and Codes** ---------- xi

**1 Introduction** ---------- 1

*1.1 Overview* ---------- *1*

*1.2 Biomineralisation* ---------- *1*

*1.3 Calcium oxalate structures* ---------- *5*

*1.4 Nucleation theories of crystallisation* ---------- *10*

1.4.1 Introduction ---------- 10

1.4.2 Classical nucleation theory ---------- 10

*1.5 Crystal growth pathways* ---------- *15*

1.5.1 Introduction ---------- 15

1.5.2 Crystal growth theories ---------- 15

1.5.3 Crystal growth in biominerals ---------- 19

*1.6 Calcium oxalate crystal growth modifiers* ---------- *22*

1.6.1 Introduction ---------- 22

1.6.1 Inhibitors of calcium oxalate-containing kidney stones ---------- 23

1.6.2 Tetrazoles as calcium oxalate crystal growth modifiers ---------- 26

**2 Methodology** ---------- **28**

*2.1 Materials* ---------- *28*

2.1.1 Chemicals ---------- 28

*2.2 Methods* ---------- *29*

2.2.1 Calcium oxalate crystallisations – control ---------- 29

2.2.2 Calcium oxalate crystallisations – in the presence of additives ---------- 30

2.2.3 Calcium oxalate crystallisation - timed experiments ---------- 30

2.2.4 Calcium oxalate crystallisation - artificial urine ---------- 31

2.2.5 Dissolution studies ---------- 32
2.2.6 Scanning electron microscopy (SEM) ---------- 32
2.2.7 Confocal Raman spectroscopy (CRS) and optical microscopy ---------- 33
2.2.8 Dynamic light scattering (DLS) ---------- 34
2.2.9 Atomic force microscopy (AFM) ---------- 35

**3 Synthesis and Characterisation of Tetrazoles ---------- 38**

*3.1 Introduction ---------- 38*

*3.2 Synthesis and characterisation of 5-Aryl-1H-tetrazole series ---------- 40*

*3.3 Raman spectroscopy characterisation ---------- 43*
3.3.1 Introduction ---------- 43
3.3.2 Characterisation ---------- 43

*3.4 Photophysical investigation ---------- 45*
3.4.1 Introduction ---------- 45
3.4.2 Characterisation and investigation ---------- 46

*3.5 Conclusion ---------- 51*

*3.6 Experimental ---------- 52*
3.6.1 General procedures ---------- 52
3.6.2 Photophysical measurements ---------- 53
3.6.3 Synthesis ---------- 53
3.6.3.1 General methodology for the synthesis of tetrazole molecules ---------- 53

**4 Structure Activity Relationships of Tetrazoles and Calcium Oxalate Crystals ---------- 67**

*4.1 Introduction ---------- 67*

*4.2 Control calcium oxalate crystallisation ---------- 68*

*4.3 Calcium oxalate crystal growth modification ---------- 70*

*4.4 Artificial urine study ---------- 84*

*4.5 Conclusion ---------- 88*

**5 Nucleation and complexation behaviour ---------- 90**

*5.1 Introduction ---------- 90*

*5.2 Dynamic light scattering (DLS) ---------- 91*
5.2.1 DLS methodology ---------- 91
5.2.2 DLS results and discussion ---------- 92
5.2.3 Conclusion ---------- 99

*5.3 Complexation behaviour* ---------- *100*

5.3.1 Introduction ---------- 100

*5.4 Conclusion* ---------- *104*

**6 Aggregation mechanism investigation of tetrazoles within calcium oxalate crystals ----- 106**

*6.1 Introduction* ---------- *106*

*6.2 Dissolution of COM in the presence of 1H-5-phenyltetrazole* ---------- *106*

*6.3 Confocal Raman microscopy (CRM) of COM* ---------- *110*

*6.4 Photophysical investigation of tetrazoles within COM* ---------- *115*

*6.5 Conclusion* ---------- *119*

**7 Growth studies of calcium oxalate utilising atomic force microscopy (AFM) ---------- 120**

*7.1 Introduction* ---------- *120*

*7.2 Results and Discussion* ---------- *121*

7.2.1 *In situ* AFM imaging of control COM ---------- 121

7.2.2 *In situ* AFM imaging in the presence of tetrazoles ---------- 123

*7.3 Conclusion* ---------- *138*

**8 Conclusions and Future directions ---------- 139**

**9 References ---------- 143**

**Appendix ---------- 157**

*A1 Raman Spectroscopy of Tetrazole Series* ---------- *157*

*A1b Tetrazole Spectra not synthesised by Author* ---------- *171*

*A2 Absorption of Tetrazole Series* ---------- *174*

*A3 Emission and Excitation of Tetrazole Series* ---------- *177*

*A4 SEM Micrographs for Quantitative Analysis* ---------- *203*

*A5 Aggregation Mechanism Investigation* ---------- *221*

*A6 AFM snapshots and Video Link* ---------- *223*

*A7 Copyright Permissions* ---------- *229*

# Abbreviations

| | |
|---|---|
| COD | calcium oxalate dihydrate |
| COM | calcium oxalate monohydrate |
| COT | calcium oxalate trihydrate |
| EDG | electron donating groups |
| EWG | electron withdrawing groups |
| FT-IR | Fourier transform infrared |
| ICP-AES | inductively coupled plasma- atomic emission spectroscopy |
| CRM | confocal Raman microscopy |
| NMR | nuclear magnetic resonance |
| S | supersaturation |
| SEM | scanning electron microscopy |
| DMF | dimethylformamide |
| AFM | atomic force microscopy |
| SAR | structure-activity relationships |
| CNT | classical nucleation theory |
| ACC | amorphous calcium carbonate |
| HA | hydroxyapatite |
| CA | citrate |
| HCA | hydroxycitrate |
| OPN | osteopontin |
| GAG | glycosaminoglycans |
| COA | anhydrous calcium oxalate |
| ACO | amorphous calcium oxalate |
| ACP | amorphous calcium phosphate |
| CPA | crystallisation by particle attachment |
| OA | oriented attachment |
| PAA | polyacrylate |
| EDS | energy dispersive x-ray spectroscopy |
| AU | artificial urine |
| kcps | a thousand counts per second |
| ATR | attenuated total reflectance |
| ppm | parts per million |

# Compound Numbering and Codes

methyl 4-(1H-tetrazol-5-yl) benzoate (**Tzmeb**H)

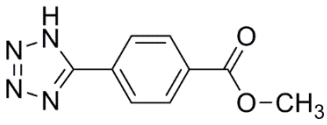

1

4-(1H-tetrazol-5-yl) acetylbenzene (**Tzacb**H)

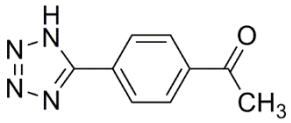

2

1H-5-phenyltetrazole (**TzPh**H)

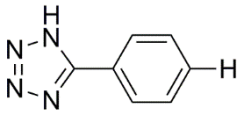

3

4-(1H-tetrazol-5-yl) benzaldehyde (**TzPha**H)

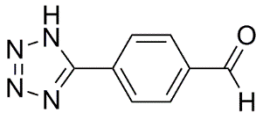

4

4-(1H-tetrazol-5-yl) benzonitrile (**TzPhCN**H)

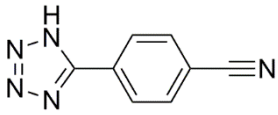

5

4-(1H-tetrazol-5-yl) benzoic acid (**TzBa**$H_2$)

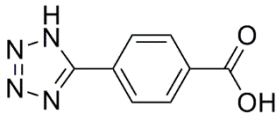

6

5-(2-acetyloxyphenyl) tetrazole (**TzAcoPh**H)

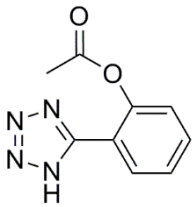

7

1,2-bis(1H-tetrazol-5-yl) benzene (*o***TzTz**$H_2$)

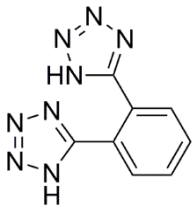

8

1,3-bis(1H-tetrazol-5-yl) benzene (*m***TzTz**$H_2$)

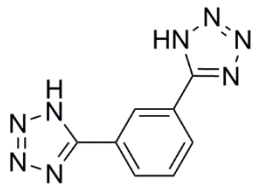

9

1,4-bis(1H-tetrazol-5-yl) benzene (*p***TzTz**$H_2$)

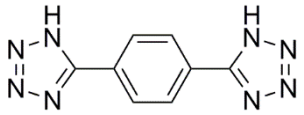

10

2,6-bis(1H-tetrazol-5-yl) pyridine (**TzTzPyr**$H_2$)

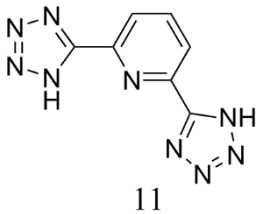

11

1H-5-(2-pyridyl) tetrazole (*o***TzPyr**H)

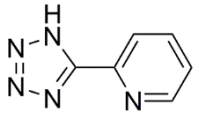

12

1H-5-(3-pyridyl) tetrazole (*m***TzPyr**H)

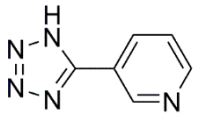

13

1H-5-(4-pyridyl) tetrazole (*p***TzPyr**H)

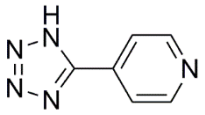

14

1H-5-(2-pyrazine) tetrazole (**TzPyz**H)

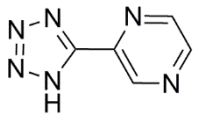

15

1H-5-(4-bromophenyl) tetrazole (**TzBrPh**H)

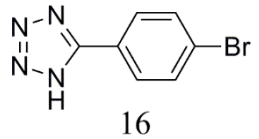

16

1H-5-(4-methoxyphenyl) tetrazole (**TzmeoxPh**H)

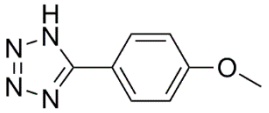

17

4-(1H-tetrazol-5-yl) benzamide (**TzPham**H)

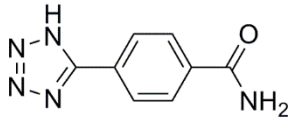

18

4-(1H-tetrazol-5-yl) phenol (**TzPhOH**H)

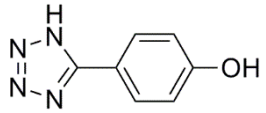

19

1H-5-(4-bromo-2-pyridyl)-tetrazole (**TzBrPyr**H)

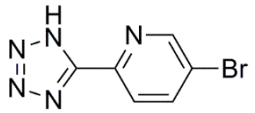

20

1H-5-(allylphenyl)-tetrazole (**TzAlPh**H)

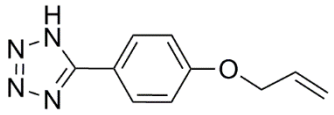

21

2-(1H-tetrazol-5-yl) quinoline (**TzQn**H)

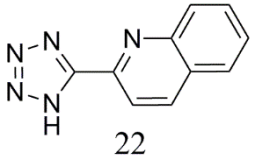

22

1-(1H-tetrazol-5-yl) isoquinoline (**TzIsoQn**H)

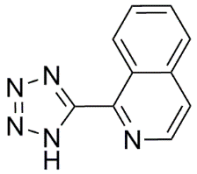

23

1H-5-(naphthyl)-tetrazole (**TzNaph**H)

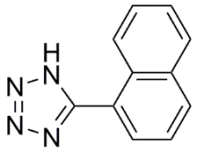

24

2-(1H-tetrazol-5-yl) pyrimidine +(**TzPyrm**H)

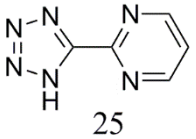

25

2-(1H-tetrazol-5-yl) phenol (*o***TzPhOH**H)

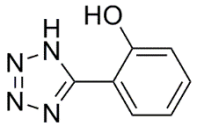

26

# 1 Introduction

## 1.1 Overview

In this chapter, firstly an introduction to biomineralisation will be discussed. A brief literature overview of human kidney stones with emphasis on calcium oxalate containing stones will follow. Subsequently, the calcium oxalate structure (***Section 1.3)***, the theories of nucleation (***Section 1.4***) and crystal growth (***Section 1.5***) mechanisms will be discussed. Finally a summary of the calcium oxalate crystal growth modifier literature (***Section 1.6***) will be presented under the context of kidney stone inhibition.

## 1.2 Biomineralisation

Biomineralisation refers to the processes by which inorganic minerals are formed by organisms. These biological mineralisation events occur widely in nature,[1–7] with organisms of each kingdom (plants, animals, fungi, etc.) capable of producing a vast variety of minerals. The study of these naturally occurring, fascinating biominerals can provide researchers with strategies in preparing new materials with far superior properties.[8–10] These biominerals can be categorised into two groups: biologically induced mineralisation whereby the biominerals are essentially by-products that the organism has little control over, and biologically controlled mineralisation, which involves the regulation or direct control of the crystallisation by the organism.[7] Examples of biologically controlled minerals can be seen in nature and our everyday lives, such as bone[6,11], egg shells[12,13], mollusc shells[2,14–18] and coccoliths,[19–21] echinoderm exoskeletons,[22,23] silica in diatoms,[24] and tooth enamel.[6,25–27] Many of these biologically controlled mineralisation examples showcase the organism's control over many aspects of the biominerals including, the size, shape, nucleation and composition which can result in unique morphologies,

organisation of the materials and complex mechanisms of formation.[2–4,14,15,28–35] It has become increasingly evident that inorganic ions and organic molecules take part in controlling the nucleation and growth of these biominerals, increasing the difficulty in describing the mechanisms involved in their formation.[3,27–29,36]

Despite the vast literature, a complete mechanism for the formation of biologically controlled minerals has yet to be described. Recently, research has shown that classical nucleation theory (CNT) cannot easily explain all mechanisms within biomineralisation; research on the assembly of nanoparticles, molecular clusters and other solution species more complex than simple ions are being recognised as a common mechanism for crystal growth in a variety of materials.[37,38] Of particular note, the discovery of stable prenucleation clusters,[39–41] and dense liquid phases,[42–44] have advanced the understanding of the very early stages of biomineralisation. Moreover, this indicates that non-classical nucleation pathways may occur for many of the cases of biologically controlled mineralisation stated above resulting in the formation of "mesocrystals". These biomineral mesocrystals form mainly in the presence of dissolved macromolecules, which have been reported to drastically alter the pathways and rates of formation, particularly using acidic proteins and peptides to alter crystal shape, polymorph, control nucleation and crystal growth.[16,17,28,32,38,45–47].

Systematic investigations of the interactions of organic species with inorganic minerals are essential for understanding the development of order in simple to complex material systems, with potential for the discovery and isolation of new states of matter. In the field of biomineralisation calcium-containing minerals account for a large portion of known biominerals, thus understanding and controlling the formation of minerals such as calcium carbonate, calcium phosphate and calcium oxalate can have global implications. Calcium carbonate for instance, is a common component in industrial scale (incrustation),[48] and the most abundant biogenic mineral in the world.[49–51] Calcium carbonates exist as several mineral phases, calcite (the thermodynamically stable polymorph), aragonite, vaterite, calcium carbonate hexahydrate (ikaite), calcium carbonate monohydrate and amorphous calcium carbonate (ACC). The ability to control the various polymorphs of calcium carbonate and determine their pathways of formation continues to be researched experimentally and computationally. Other minerals of importance on a global scale include calcium

phosphates and calcium oxalate minerals, these have both attracted substantial attention due to their medical significance.[27,52,53] Calcium phosphates can be found in bone, teeth and tendons in the form of carbonated hydroxyapatite (HA) giving the organs stability, hardness and function. The presence of calcium phosphate in these hard tissues is considered vital, however, if calcium phosphate minerals crystallise in irregular ways or in undesired regions they can cause considerable damage, this phenomena is called pathological crystallisation.[10,27]

Pathological crystallisation occurs through the process of uncontrolled mineralisation, or as previously mentioned, biologically induced mineralisation.[3,7] These processes occur mainly due to the imbalance of ion levels which result in insoluble precipitates forming in undesirable locations such as soft tissues. In the case of calcium phosphate this can result in atherosclerosis,[54] stone formation,[55] and dental calculus.[56] Urolithiasis, the formation of stones in the urinary tract, including bladder and kidneys, affects more than 10% of the human population in their lifetime.[57–59] Without medical treatment, recurrence rates can exceed 50% within 5-10 years increasing to 75% within 20 years with the relapse rate increasing with progressively shorter intervals between recurrences. The factors that are directly associated with urolithiasis include: age, sex, diet, geographic location, medical conditions, genetic disposition and urinary composition.[58] Human urinary composition essentially relies on three factors, the quantity of inhibitors, the quantity of promoters and the quantity of stone forming components. As mentioned above, stone formation within humans is considered a pathological mineralisation event, the most prevalent being the formation of renal calculi better known as kidney stones. Kidney stones are predominantly made of calcium oxalates at ~70%,[57–62] with lower percentages of calcium phosphate (apatite), uric acid, magnesium ammonium phosphate (struvite) and cystine constituting the remaining fraction (***Figure 1.1***).[57]

Calcium oxalate stones are principally composed of the insoluble salt and an organic matrix which is interlaced throughout the entire structure.[47,63–65] The organic matrix present throughout is suggested to play a role in inducing the formation of kidney stones.[55,66–68] The organic matrix, which is composed of organic macromolecules, has been proposed to attach to the formed calcium oxalate crystals that subsequently attach to epithelial cells of human kidneys and results in the aggregation of the crystals resulting in the formation of kidney stones (***Figure 1.2***).[69]

The organic matrix constitutes around 2% of kidney stone weight and is approximately 60% proteins such as osteopontin (OPN), serum albumin and prothrombrin fragment 1.[47,64,70] Other components of the matrix include glycosaminoglycans (GAGs) at (20%),[71] red blood cells and lipids.[72,73] The study of organic macromolecule crystal growth modifiers of calcium oxalate will be discussed in greater detail in ***Section 1.6***.

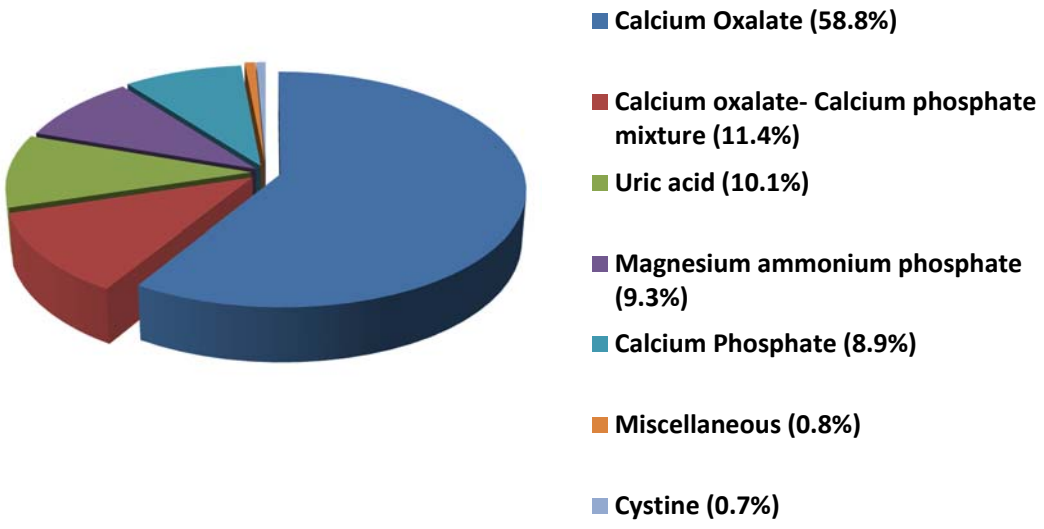


***Figure 1.1***: Calcium oxalate and calcium oxalate-calcium phosphates represent the major fraction of human kidney stones.[57–62]

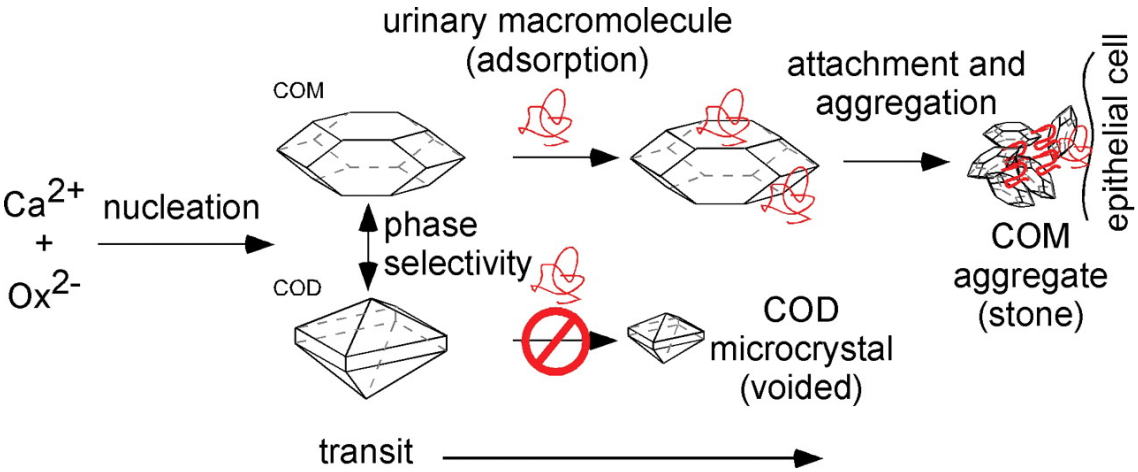


***Figure 1.2***: A possible pathway for the formation of calcium oxalate containing kidney stones and attachment to epithelial cells, reproduced with permission from the work of Wesson *et al.*.[69] Copyright © (2007) Mineralogical Society of America.

## 1.3 Calcium oxalate structures

In nature, calcium oxalate can crystallise as three hydrates, calcium oxalate monohydrate (COM, $CaC_2O_4 \cdot H_2O$, also known as whewellite), is thermodynamically the most stable phase at room temperature and is monoclinic.[74] The tetragonal calcium oxalate dihydrate (COD, $CaC_2O_4 \cdot (2 + x)H_2O$; ($x \leq 0.5$, weddellite) is the metastable form of calcium oxalate[75] and lastly the triclinic calcium oxalate trihydrate (COT, $CaC_2O_4 \cdot (3 - x)H_2O$; $x < 0.5$, caoxite) can also form.[76] The first two hydrates, COM and COD are found in human kidney stones, while COT is rarely seen due to its instability in the normal urinary environment.[77] Aside from kidney stones,[74–79] the calcium oxalate hydrate forms can also be found in many species of plant, can crystallise in bone marrow and blood vessels,[80] and can also exist as amorphous and anhydrous phases.[81–83]

The accepted crystal structure of COM as presented by Tazzoli and Domeneghetti (1980) has recently been re-investigated by Echigo *et al.*[78] at low-temperature (LT) to further interpret the role of water in the crystal structure. The symmetry space group was found to be $P2_1/c$ with unit cell parameters $a$ = 6.250(1) Å, $b$ = 14.471(2) Å, $c$ = 10.114(2) Å, $\beta$ = 109.978(5)°, $Z$ = 8, $V$ = 859.73(3) Å$^3$.[78] The above LT structure is one of three polymorphs of COM. The second, the high-temperature (HT) structure is similar to the LT crystal structure, however, it belongs instead to the space group $I2/m$, with unit cell parameters $a$ = 9.978(1) Å, $b$ = 7.295(1) Å, $c$ = 6.291(1) Å, $\beta$ = 107.03(3)° , $Z$ = 4.[79] The two forms are often referred to as the basic structure (HT) and the derivative structure (LT). The transition between polymorphs takes place upon ordering below 45° C, with the HT crystal form possessing a unit cell with $b$ equal to half of that of the LT crystal form, as stated. The third, relatively unknown polymorph of COM can only be produced by the dehydration of COD (weddellite) and has an orthorhombic structure unlike the two monoclinic phases mentioned previously with unit cell parameters of $a$ = 12.088(9) Å, $b$ = 10.112(7) Å, $c$ = 14.634(12) Å, and $\alpha = \beta = \gamma = 90°$.[84] The unit cell, calcium coordination polyhedron and stacking of multiple unit cells of COM are presented in ***Figure 1.3***. As illustrated by ***Figure 1.3(A)*** the COM or whewellite exhibits a sheet framework.

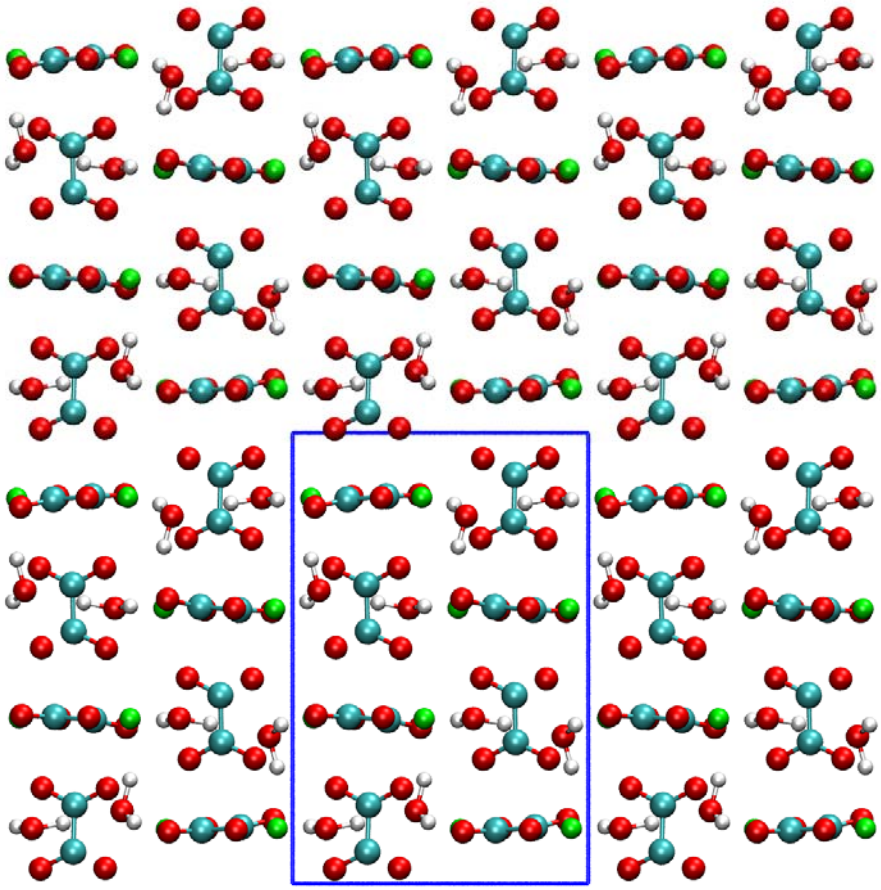

***Figure 1.3***: Crystal structure of COM (whewellite) viewed along a-axis (assumes that a-axis is normal to the page). Green spheres represent $Ca^{2+}$, blue and red spheres represent carbon and oxygen in oxalate groups, respectively. White spheres represent hydrogens attached to red oxygen atoms of crystalline water molecules, while the blue square represents the unit cell of COM.

Both natural and synthetic COM do not commonly present as single crystals, but rather are found as twins.[85–87] As illustrated in ***Figure 1.4***, single crystals, contact twins and penetration twins are possible natural forms of COM. The penetration type twinning of COM crystals is the most frequent among the derivative crystals (LT) polymorph as a result of an off-plane distortion of oxalate (Ox1) ions at low temperatures. Penetrations twins are also determined by observing the interpenetration between different parts of the crystals. In the case of single crystals the polyhedral habit is bound by (100), (010), (021), (0-21), (12-1) and (1-2-1) faces (***Figure 1.4(C)***) using Tazzoli's notation.[74] For contact and penetrations twins, the twin planes are (100) or (-101) using Deganello's notation.[79,87]

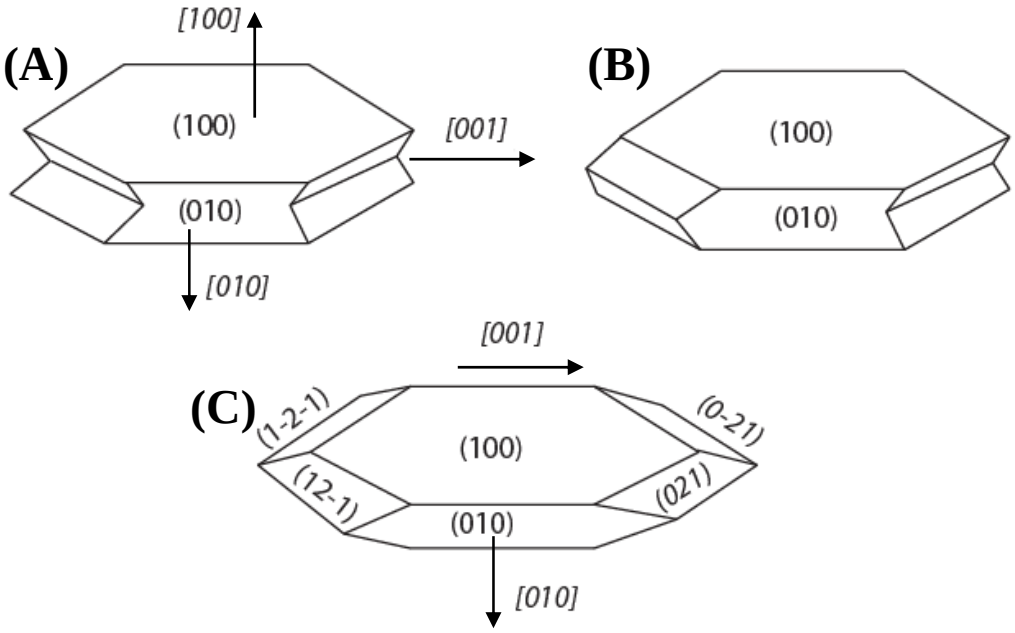


***Figure 1.4***: COM crystal habit and twinning, penetration twin (A), contact twin (B) and single crystal (C) bound by labelled crystallographic faces and directions using Tazzoli's notation.[74]

The dihydrate form of calcium oxalate, known as weddellite (COD) belongs to the tetragonal crystal system with space group *I4/m* and unit cell parameters $a = b = 12.371$ Å, $c = 7.357$ Å, $\alpha = \beta = \gamma = 90°$, $Z = 8$, $V = 1125.9$ Å$^3$. In weddellite the calcium coordination polyhedron is a distorted square antiprism and forms a channelled structure rather than the sheet structure of COM, illustrated by the presence of the "zeolitic" water ((***Figure 1.5(A)*** denoted by z) in the channel which accounts for the chemical composition of COD, $CaC_2O_4 \cdot (2 + x)H_2O$; ($x \leq 0.5$) when $x = 0.5$, the maximum water content is equal to 2.5 $H_2O$ as confirmed by Tazzoli and Domeneghetti.[74] COD typically precipitates tetragonal bipyramidal crystals grown from aqueous solutions with the (101) faces dominant, and in the case of tetragonal prisms, the (100) and (101) pyramidal faces can be seen (***Figure 1.5(B)***). Though COD is a metastable form, it is still found throughout nature in sea sediments,[88] plants,[89,90], and can be found in human kidney stones, though to a lesser extent than COM.[91]

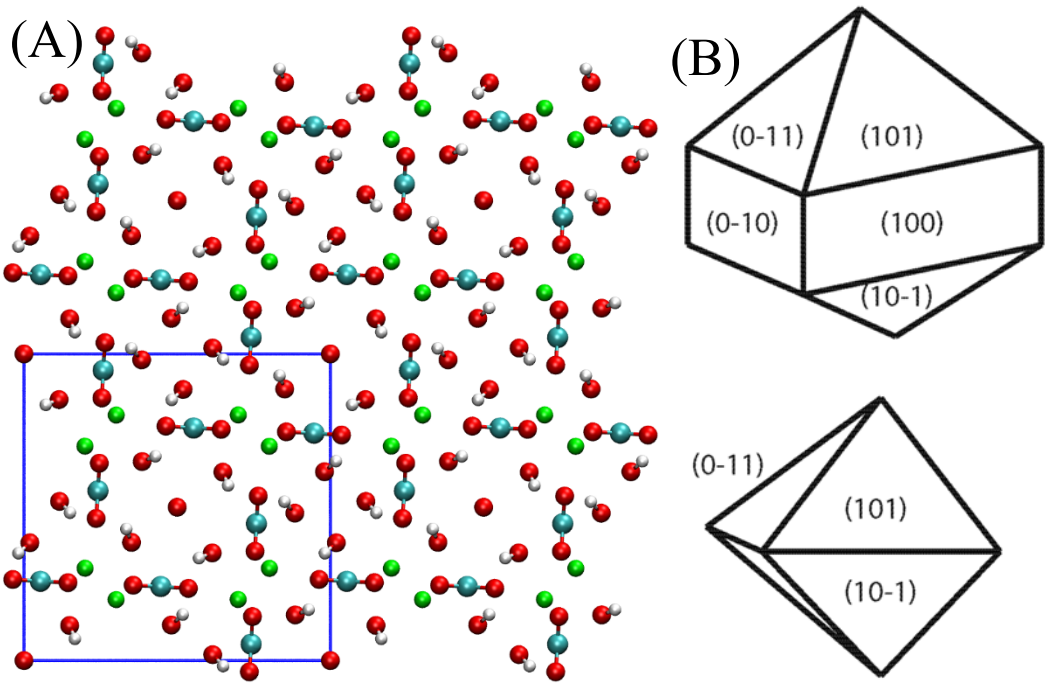


***Figure 1.5***: (A) The crystal structure of COD (weddellite) with zeolitic-like water viewed along c-axis (assumes that c-axis is normal to the page). Colours are defined as in ***Figure 1.3*** for calcium, oxalate, and crystalline water molecules. Oxygen atoms in additional zeolitic-like water molecules in the channel are also in red at the centre of the unit cell (blue square) and at each corner of the unit cell. (B) The crystal habits of COD, tetragonal prism and tetragonal bipyramidal with their crystallographic phases labelled.

The last hydrate phase, COT also known as caoxite crystallises in the triclinic crystal system with $P\bar{1}$ space group with the following lattice parameters, $a$ = 6.11 Å, $b$ = 7.167 Å, $c$ = 8.457 Å, α = 76.5°, $\beta$ = 70.35°, γ = 70.62°, $Z$ = 2 and $V$ = 325.9 Å$^3$.[76,78] Similarly to COM, COT has recently been re-investigated and refined by Echigo *et al.*[78] and also exhibits a sheet structure consisting of $Ca^{2+}$ ions and oxalate ions with zig-zag chains linked by oxalate ions (***Figure 1.6***) and intercalated water molecules *via* hydrogen bonding. The structure of COT connects the calcium-oxalate chains with interlayered water molecules, while COMs sheet structure is connected by intralayer water. As a result, and directly related to the phases' stabilities, where whewellite (COM) > weddellite (COD) > caoxite (COT), caoxite is the least stable and unsurprisingly rarely found in nature. Its scarcity to precipitate in nature is due to the aforementioned interlayered hydrogen bonds of the water molecules connecting

the sheet structure. If COT becomes exposed to high temperatures for instance, the hydrogen bonding can break resulting in the dehydration of the crystal structure. Thus COT is proposed to act as the precursor phase to the formation of both COM and COD *via* dehydration of the crystal structure in kidney stone formation.[92] Another possible mechanism of formation suggests that COM is formed directly from COT by dehydration due to the similarity in structures, and due to COD having a significantly different structure to the other two hydrates.[92]

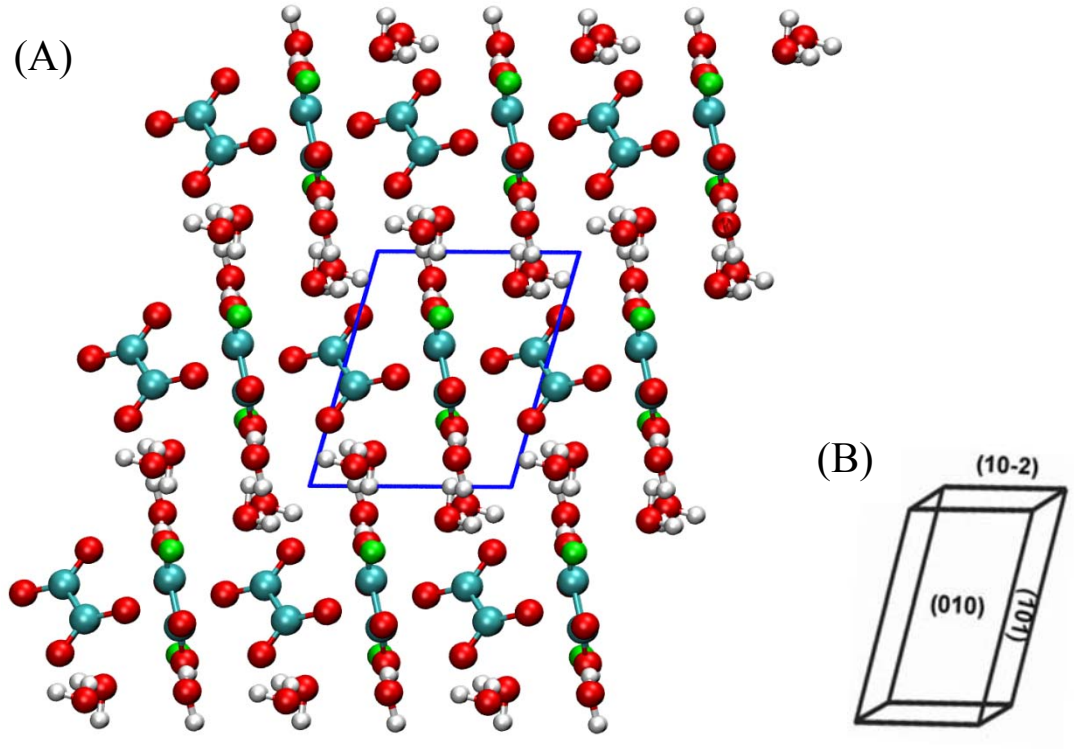


***Figure 1.6***: (A) The crystal structure of COT (caoxite) viewed along c-axis. Colours are defined as in ***Figure 1.3*** for calcium, oxalate, and crystalline water molecules. (B) Schematic of a triclinic prismatic habit COT crystal with labelled faces.

In addition to the three hydrate phases, an anhydrous calcium oxalate (COA) form does not exist in nature as it readily absorbs water molecules from the atmosphere. Structurally, very little is known about the phases of COA. Studies suggest that dehydration of COM or COD result in three temperature-dependant COA polymorphs, α, *β* and γ-COA with the only structure reported being of *β*-COA.[83] Anhydrous calcium oxalate has recently been formed from aqueous and ethanolic solutions,[81,82] and investigated computationally.[93]

## 1.4 Nucleation theories of crystallisation

### 1.4.1 Introduction

Nucleation mechanisms of biominerals are difficult to determine and in many cases unsolved. In this section, classical nucleation theory will be briefly discussed before turning to specific cases of interest in the field. Application of the theory to current materials through advanced techniques in both experimental and computational fields can yield new ideas of how many biominerals form.

### 1.4.2 Classical nucleation theory

Crystallisation begins with nucleation, the first essential step in crystal formation, explained by Gibbs in the 1870s in terms of thermodynamic principles for the formation of raindrops.[94] Gibbs described the condensation of water into droplets from humid air and this has since been applied to crystal formation, and what has come to be known as classical nucleation theory (CNT).[95] CNT can be applied equally to vapour, melts and, for the purpose of this thesis, the nucleation of species from solution to form solids.

Nucleation can be classified into two types: primary and secondary (induced by solute crystals), with primary nucleation divided further into either homogenous (spontaneous) or heterogeneous (induced by foreign particles or surfaces).[96] To achieve a change from solution to solid from bulk solution (homogeneous nucleation) a driving force has to be created, as nucleation is not a spontaneous process. The driving force causing the transformation, namely the free energy of the initial solution phase must be greater than the sum of the free energies of the crystalline phase plus the final solution phase for nucleation.[94] The free-energy change ($\Delta G$) is thus equal to contributions from the bulk solution phase ($G_b$), which acts to promote crystal formation, and the contribution from the interfacial terms ($G_i$), which act to destabilise the nucleus forming, namely:

$$\Delta G = G_b + G_i = -\frac{4\pi}{3} r^3 \left(\frac{\Delta\mu}{\Omega}\right) + 4\pi r^2 \alpha \qquad (1.1)$$

where Ω is the volume per molecule, and α is the interfacial free energy and Δμ is the measure of the free energy response to molecules transferring from one phase to another, the larger Δμ becomes, the greater the driving force for crystallisation.[96] For the case of particles in a supersaturated solution the free energy difference for nucleation, ΔG, for undersaturated solutions, those at equilibrium, and supersaturated solutions are ΔG < 0, ΔG = 0 and ΔG > 0, respectively. At equilibrium, the free energy of solution per molecule and the change in chemical potential can be expressed as:

$$\Delta G_{sol} = -k_B T \ln K_{sp} \qquad (1.2)$$

$$\Delta\mu = k_B T \ln AP - \Delta G_{sol} = k_B T \ln\left(\frac{IAP}{K_{sp}}\right) \qquad (1.3)$$

where $k_B$ is the Boltzmann constant, T is the temperature, IAP is the ion activity product of the reactants, and $K_{sp}$ is the solubility product. However, rather than use Δμ, crystal growth analyses refer to the supersaturation, σ, which is related to Δμ by:

$$\Delta\mu = k_B T \ln\sigma\,, \qquad \sigma \equiv \ln\left\{\frac{AP}{K_{sp}}\right\} \qquad (1.4)$$

However, the supersaturation is often defined as $(AP/K_{sp}) - 1$ or more commonly $(C/C_e) - 1$, where C and $C_e$ are the equilibrium reactant concentrations. The use of concentration over activity is only valid for low concentrations and when insignificant complexation occurs, for higher concentrations, the expression should be based on activity rather than concentration. Thus concentration can be expressed in terms of the activity coefficients: $a = C\gamma$ and $a_e = C_e\gamma_e$, where a, is the solute activity and γ the activity coefficient, the subscript "e" refers to the activity at equilibrium. The excess free energy, $\Delta G_{ex}$, regarded as the basis of the thermodynamic barrier for nucleation, corresponds to the critical nucleus of size, $r_c$. For a spherical cluster, $r_c$ is obtained by maximising ***Equation 1.1*** by setting $d\Delta G/dr = 0$:

$$r_c = \frac{2\Omega\alpha}{\Delta\mu} = \frac{2\Omega\alpha}{k_B T\sigma} \qquad (1.5)$$

Consequently, clusters smaller than the critical size will dissolve and clusters greater in size than the critical size will grow in a supersaturated solution. ***Figure 1.7*** illustrates the contributions of both energy terms (described in ***Equation 1.1***) and the critical radius for the formation of a stable nucleus. The nucleation barrier is only significant when nucleation occurs at low supersaturations, when the supersaturation is high, the nucleation barrier vanishes and nucleation is instead affected by factors such as density and rates of transport of energy or mass.[97,98] Another case when the nucleation barrier can be lowered is for heterogeneous nucleation, nucleation on a foreign surface (***Figure 1.7 (C)***).

The rate of nucleation, *J*, the number of nuclei formed per unit time per unit volume, can be expressed as:

$$J = Aexp^{\left(\frac{-\Delta G_{ex}}{k_B T}\right)}, \quad \Delta G_{ex} = B\frac{\alpha^3}{\sigma^2} \qquad (1.6)$$

where *A* is a material-dependant constant, *B* is a constant that depends on the shape and density of the nucleating solid as well as the temperature, α is the interfacial free energy (surface energy) and σ is the supersaturation, as previously defined.[96,99,100] The main variables from ***Equation 1.6*** that govern the rate for nucleation for CNT are: supersaturation and the interfacial free energy, the supersaturation can be controlled in the laboratory, and the interfacial free energy is determined by the properties of the two phases.

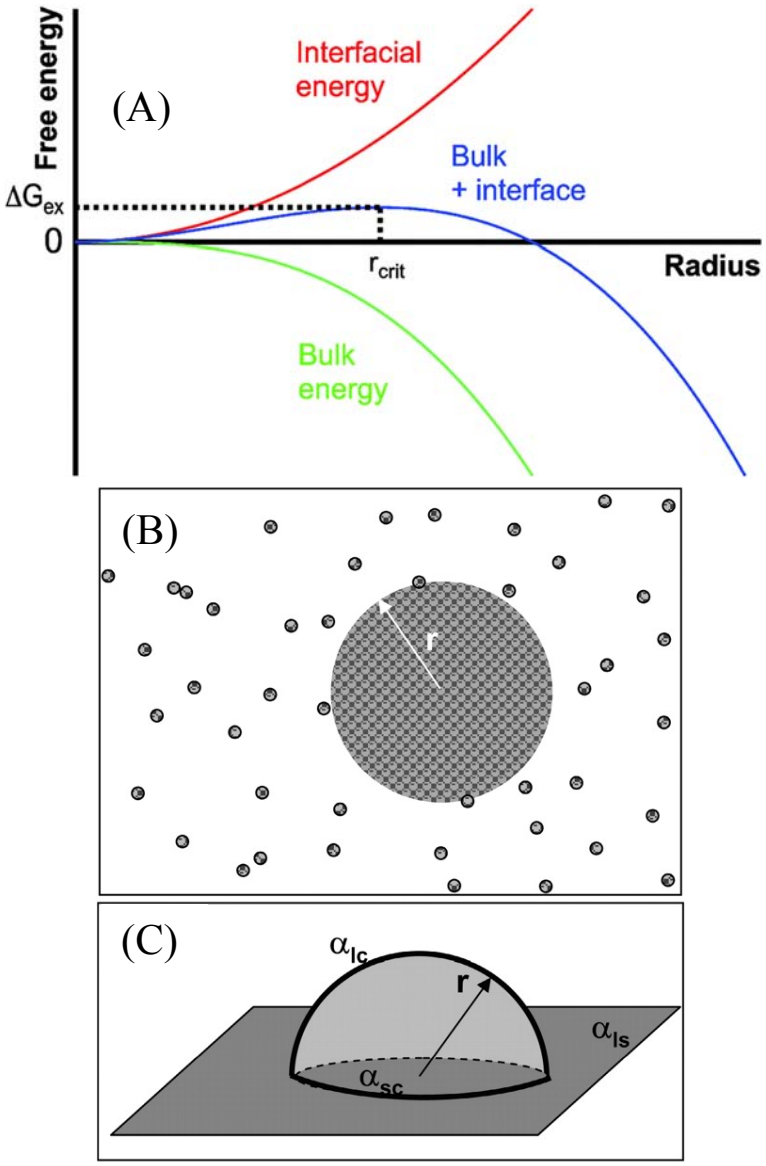


***Figure 1.7***: (A) Relationship of Free energy to the radius, $r_{crit,}$ the critical nucleus size, and $\Delta G_{ex}$ is the maximum free energy barrier within the framework of CNT. (B), Formation of a spherical nucleus of radius *r* from a solution leads to the free energy changes shown in (C) Heterogeneous formation of a hemispherical nucleus at a foreign substrate. Figure 1.7(A) was reproduced with permission from the work of Gebauer *et al*..[39] Copyright © (2014) Royal Society of Chemistry. Figure 1.7 (B, C) were reproduced with permission from the work of De Yoreo and Vekilov.[100] Copyright © (2007) Mineralogical Society of America.

For heterogeneous nucleation the free energy change (ΔG) has two additional interfacial energies to consider, the crystal-surface and crystal-substrate energies. The new expression becomes:

$$\Delta G = -\frac{2\pi}{3} r^3 \left(\frac{\Delta\mu}{\Omega}\right) + \pi r^2 (2\alpha_{lc} + \alpha_{sc} - \alpha_{ls}) \quad (1.7)$$

where the new terms for the interfacial energies are given by subscripts "*lc*", "*sc*", and "*ls*" refer to liquid-crystal, substrate-crystal and liquid-substrate, respectively.[100] The presence of this substrate can act as a preferential nucleation site, potentially resulting in a lowered nucleation barrier and therefore nucleation can occur at much lower supersaturations for heterogeneous nucleation compared to homogeneous.

In general, classical nucleation theory can describe the pathways of nucleation of crystals. In many cases of biomineralisation, however, the systems are often more complex with CNT failing to describe their nucleation and crystal growth. Research on dense liquid phases,[42–44,101] pre-nucleation clusters,[39–41] and more recently, observations of multi-stage nucleation pathways, as examples, are more aptly described by non-classical nucleation mechanisms.[102,103] Calcium carbonate ($CaCO_3$) has become the model material for the study of nucleation theory in the field of crystal growth.[3,33,38,104–106] The main focus of the studies involves the determination and description of classical vs non-classical nucleation pathways utilising various experimental techniques; such as *in situ* and cryogenic transmission electron microscopy (Cryo-TEM),[107,108] and computational simulations for the formation of pre-nucleation clusters and dynamically ordered liquid-like oxyanion polymer (DOLLOP) clusters.[39,40,109] The improvements made in the field to spatial and temporal resolution for studying biomimetic mineralisation systems combined with computational studies are revealing that calcium carbonate nucleates *via* both direct and indirect pathways simultaneously.[103] The three polymorphs of calcium carbonate, vaterite, aragonite and the most stable phase calcite, as well as amorphous calcium carbonate have been formed directly in laboratory conditions. While these forms can nucleate directly from solution, they can also form indirectly through transformation from amorphous and crystalline precursors.[103]

Despite the recent surge of non-classical nucleation theory to describe model materials such as $CaCO_3$ in complex systems (detailed above), classical nucleation

theories developed over a century ago continue to explain complex biomineralisation mechansisms.[99,110] Nevertheless, the study of these model systems in biomineralisation and crystallisation are crucial to progress towards a framework for the description of nucleation pathways. Armed with this framework predicting the formation of crystals in complex systems and new materials, as well as providing useful information for the control of minerals can be achieved. Thus, progressing from nucleation theory in ***Section 1.5*** our focus turns to the literature of crystal growth by classical and non-classical mechanisms and their application to biomineralisation.

## 1.5 Crystal growth pathways

### 1.5.1 Introduction

In this section various proposed theories to describe crystal growth will be discussed with a focus on the formation of biominerals. Lastly, the literature for calcium oxalate crystal growth and the formation of kidney stones will be presented.

### 1.5.2 Crystal growth theories

Once stable nuclei have formed, i.e. particles larger in size than the critical size ($r_c$), in a supersaturated or supercooled system, they begin to grow into crystals of detectable dimensions. Many proposed mechanisms of crystal growth exist, the most important of which include: surface energy theories,[111] diffusion theory, adsorption layer theory,[112,113] and screw dislocation theory.[114] Gibbs was the first to propose a theory of crystal growth, describing the growth of crystals to be analogous to the growth of a water droplet from vapour.[94] Later Kossel, Volmer and others explained the role of step and kink sites on crystal surfaces to promote the growth process.[113,115] The figures in this section visualise some of these classical theories of crystal growth.

In the adsorption layer theory proposed by Volmer,[113] atoms, ions or molecules will link into lattice positions where the attractive forces are greatest, and under ideal conditions this step-wise build-up will continue until the face is completed. When units of the crystallizing substance arrive at the crystal face, however, they do not immediately integrate into the lattice but instead are free to migrate over the crystal face by surface diffusion (***Figure 1.8***). These loosely adsorbed units result in a layer called the adsorption layer and this layer plays an important role in crystal growth and secondary nucleation.

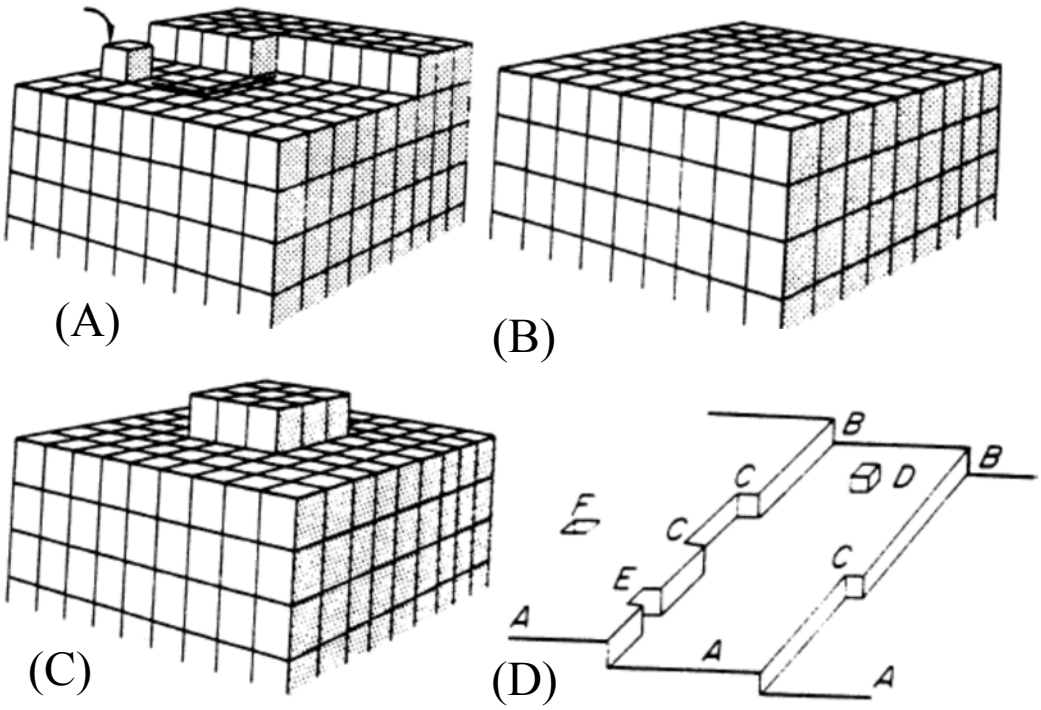


***Figure 1.8***: A mode of crystal growth without dislocations: (A) migration towards desired location; (B) completed layer; (C) surface nucleation. (D) Kossel's model of a growing crystal surface with terraces represented by the label A, steps B, kinks C, surface-adsorbed growth units D, edge vacancies E, and surface vacancies F. Reproduced with permission from Mullin, J.W. Crystallization 4th Ed. Copyright © (2011) American Chemical Society.

Following the model described by Kossel,[115] a growing crystal face is depicted (***Figure 1.8 (D)***) whereby a flat crystal surface is made up of moving layers (steps) of monatomic height which contain one or more kinks sites and terraces. Additionally, loosely adsorbed growth units (which can be atoms, molecules or ions)

are present on the crystal surface as well as vacancies in the steps and surfaces. The order of attachment is described to be at a maximum when incorporated into a kink site in a ledge and any point on the ledge is greater than that of an atom attached to a terrace, following ***Figure 1.8 (D)*** the growth unit prefers positions F>E>C>B>D. Frank postulated that few crystals grow in the ideal layer-by-layer fashion, as most crystals contain dislocations which cause steps to be formed on the faces and promote growth.[114] Screw dislocations, for instance can act as a continuous source of steps which can propagate across the surface of the crystal and promote crystal growth (***Figure 1.9 (A-C)***). This theory was not limited by the need for surface nucleation like Kossel and Volmers theories and so could explain growth at low supersaturations.

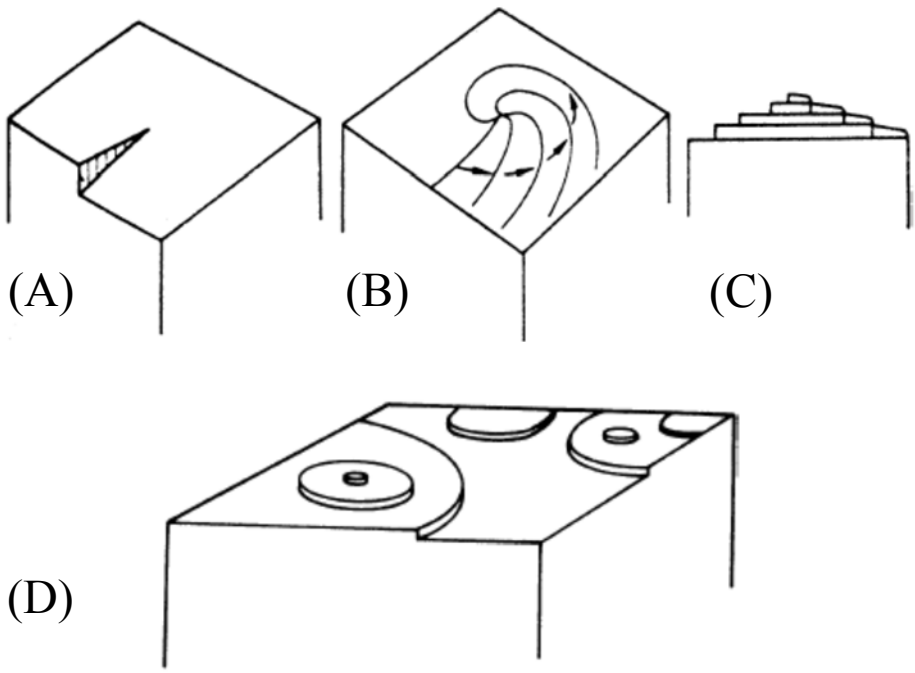


***Figure 1.9***: Development of a growth spiral starting from a screw dislocation (A-C) proposed by Frank and the development of polynuclear growth by the birth and spread (B + S) mechanism (D). Reproduced with permission from Mullin, J.W. Crystallization 4th Ed.[96] Copyright © (2011) American Chemical Society.

The birth and spread model (B + S) is based on two-dimensional nucleation followed by the spread of monolayers as illustrated in ***Figure 1.9(D)***.[116,117] As depicted, growth develops from surface nucleation that can occur at the edges, corners and on the faces of a crystal. The aforementioned models are mostly based on the monomer-by-monomer addition of simple chemical species, and despite the success of these theories, recently, a number of phenomena associated with crystal formation cannot be satisfactorily explained by these classical theories. For example, the habits and microstructures of biominerals found in organisms,[3] the nucleation of amorphous phases of calcium phosphate at concentrations lower than those predicted by classical models.[118] Additionally, irregular and branched crystal morphologies observed in synthetic nanocrystals cannot be readily interpreted within the framework of classical mineral formation processes.[119]

Many proposed mechanisms for the formation of kidney stones exists, particularly those containing high amounts of COM. Typically these stones are found as complex aggregates of crystals and organic components, as mentioned earlier. Of great interest is the role that the kidney's surfaces play including, the papillary tip and epithelial cells, in the nucleation of COM crystals and the eventual formation of kidney stones. A study by Nancollas *et al*. discovered that calcium phosphate can play a critical role in the nucleation and formation of calcium oxalate stones.[120] The results of their study showed that amorphous calcium phosphate (ACP) precursor clusters promote the aggregation of amorphous calcium oxalate (ACO) at low phosphate concentrations. This mechanism is a result of the amorphous coaggregation of ACO surrounding an ACP sphere and may provide a possible mechanism for the formation of renal stones (***Figure 1.12***).

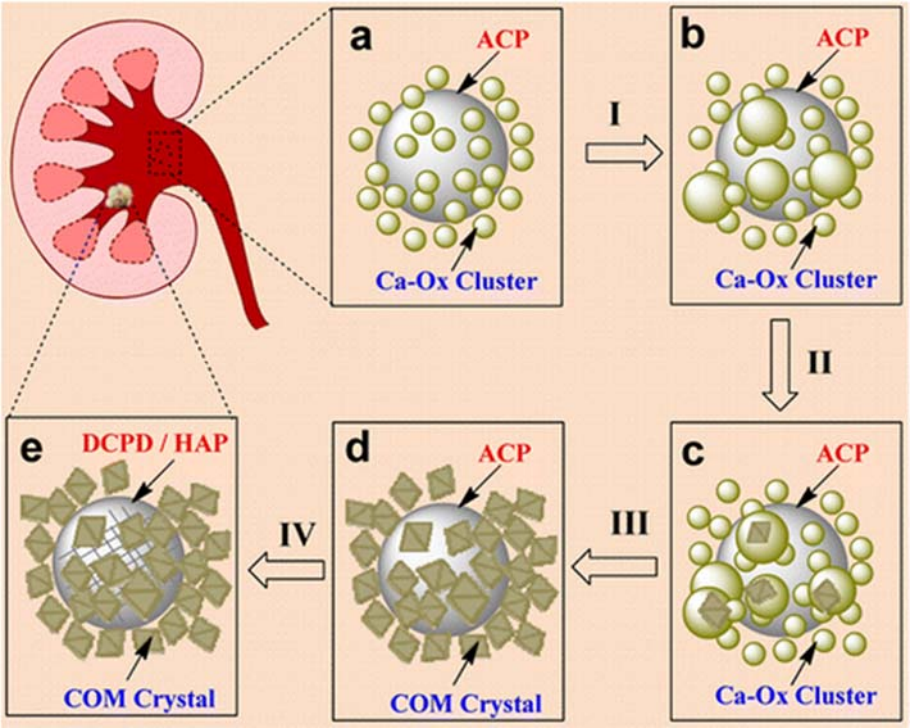


***Figure 1.12***: Illustration of the nucleation and growth mechanism for COM in the presence of phosphate in biological conditions. The formation of ACP-ACO coaggregates as small amorphous calcium-oxalate clusters around a larger ACP sphere in the early stages (***Figure 1.12 (a)***). The presence of the ACP promotes the aggregation of ACO and the eventual formation of COM crystals to the ACP spheres (***Figure 1.12 (b-e)***, eventually forming the COM and calcium-phosphate containing kidney stones. Reproduced with permission from the work of Nancollas *et al*.[120] Copyright © (2014) American Chemical Society.

### 1.5.3 Crystal growth in biominerals

Research in the past decade on biominerals has revealed that crystallisation can occur by attachment of a wide range of species more complex than simple ions, such as oligomers, nanoparticles and multi-ion complexes (***Figure 1.10***).[109,118,119,121] These examples have been demonstrated to occur *via* non-classical crystal growth processes which are distinctly different from the classical models.[102] One such model, crystallisation by particle attachment (CPA), is a relatively new non-classical crystal growth pathway that falls under the umbrella of oriented attachment (OA), which describes the aggregation of nanoparticles and leads to structures that can fuse to form a single crystal, if stable. These crystal formations can include pre-nucleation

clusters, and are thermodynamically stable for many biominerals cases such as calcium carbonate (calcite),[122,123] and calcium phosphate.[39]

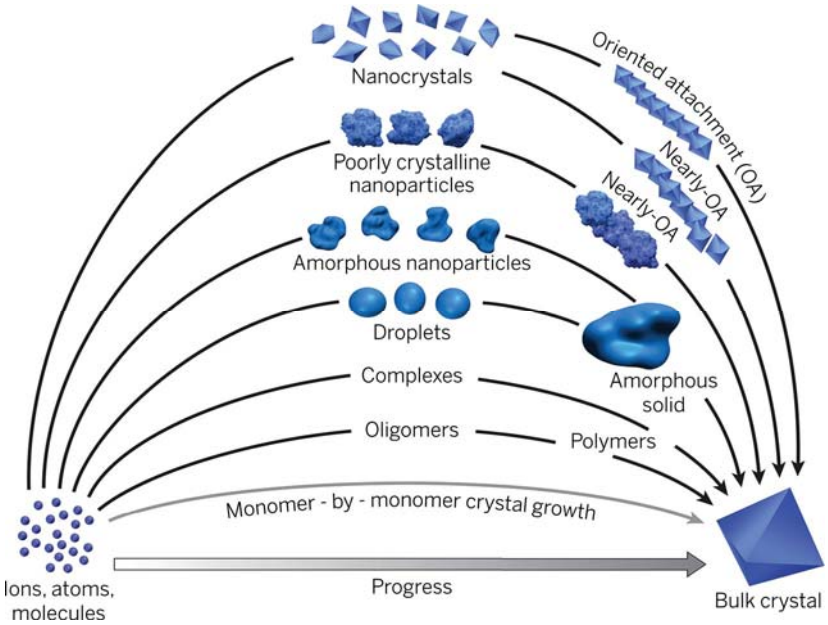


***Figure 1.10***: Pathways to crystallisation by particle attachment (CPA). Monomer-by monomer addition as described in classical models of crystal growth (gray curve), CPA occurs by the addition of higher-ordered species ranging from multi-ion complexes to fully formed nanocrystals. Reproduced with permission from the work of From De Yoreo *et al.*.[38] Copyright © (2015). Crystallization by particle attachment in synthetic, biogenic, and geologic environments. *Science (2015).* **349** (6247) aaa6760. Reprinted with permission from AAAS.

In many cases in biomineral crystallisation a thermodynamic equilibrium treatment does not predict crystal morphologies, often presented by minerals with different polymorphs. These polymorphs and their individual morphologies are controlled through energy barriers of nucleation, growth and their phase transitions.[2] These pathways to form the biomineral illustrate what is commonly referred to as Ostwald's rule. The thermodynamically unstable phases often form first, typically these phases are less dense and eventually transform to the denser material or most thermodynamically stable phase. Both the kinetic and thermodynamic pathways for Ostwald's rule of stages are illustrated in ***Figure 1.11***.

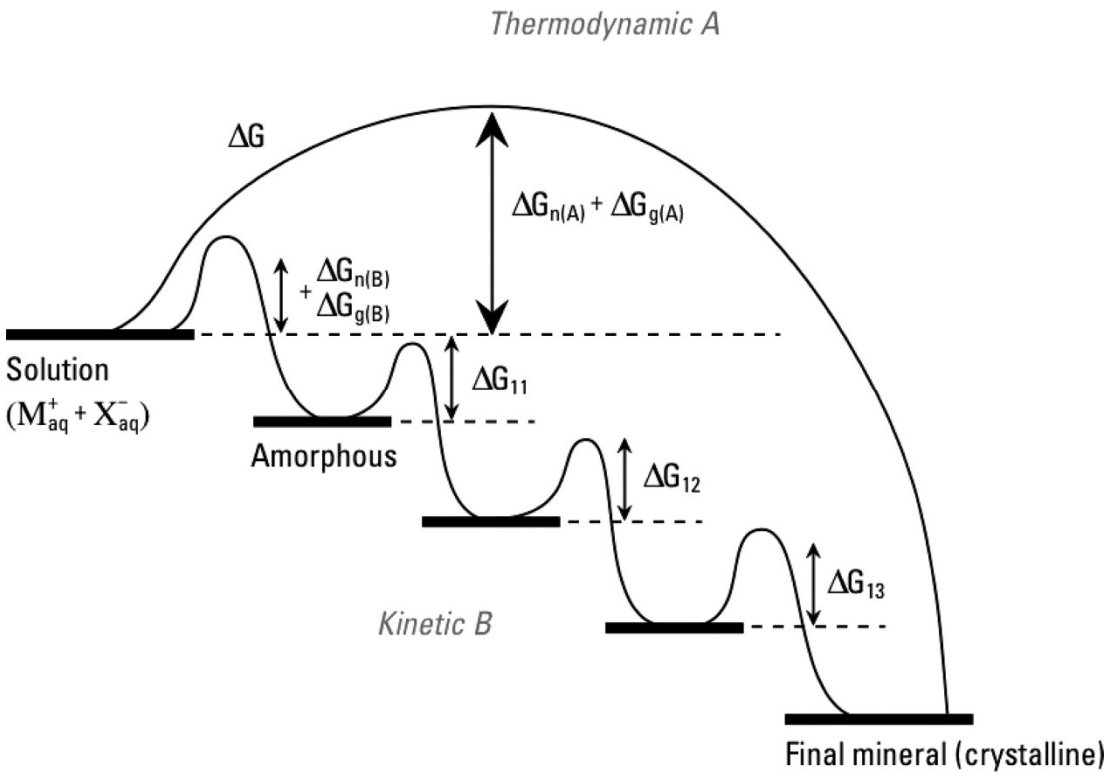


***Figure 1.11***: A simplified view of the pathways of crystallisation under thermodynamic and kinetic control. The pathways A and B, thermodynamic and kinetic, respectively, depend on the free energy of activation associated with nucleation (n) and growth (g) from solution. Reproduced with permission from the work of Coelfen and Mann.[124] Copyright © (2003) American Chemical Society.

In the case of calcium oxalate, the molecular mechanisms for its formation, particularly the nucleation and growth, phase transformations and polymorphism are not well understood. Under thermal analysis laboratory conditions, Echigo *et al.* determined that calcium oxalate trihydrate (COT) crystals can directly transform to the calcium oxalate monohydrate (COM) phase *via* dehydration.[78] The dihydrate species, COD, was not formed as an intermediate species during this dehydration transformation due to the disparity in the structures of COD and COT. Anhydrous calcium oxalate (COA) phases have also been detected during *in situ* synchrotron XRD and *ab initio* computational methods by Zhao *et al.*.[93]

In general, the growth rate of a crystal face is directly related to its surface energy, i.e. faces that have higher surface energies will grow quickly, have smaller surface areas, or vanish completely upon crystal growth completion. Conversely,

faces with lower surface energies will grow more slowly and dominate the final shape of the crystal. Wullf's rule assumes that the equilibrium morphology of a crystal can be calculated by the sum of the surface energy multiplied by the surface area of all exposed faces and defined by its minimum surface free energy (***Equation 1.8***).[125]

$$\sum_i \gamma_i A_i = F_s \qquad (1.8)$$

With $\gamma_i$ = surface energy of the surface $i$, $A_i$ = area of surface $i$, and $F_s$ = total surface free energy.

Thus, Wulff's rule can help predict additive-based crystal morphologies. This is particularly useful in explaining crystal morphology when additives have selective adsorption on one family of crystal faces. Thus the final section details the literature describing the changes to calcium oxalate crystal growth and morphology in the presence of additives.

## 1.6 Calcium oxalate crystal growth modifiers

### 1.6.1 Introduction

Although the literature of calcium oxalate and kidney stone inhibitors is vast, to-date problems are still being encountered in implementing effective medical methods for a permanent cure of these pathological mineralisation events. No single theory of pathogenesis can account for human kidney stones as they are too various and their formation too complex. This section discusses some of the known pathways of kidney stone formation in conjunction with examples of inhibitors, natural or synthetic, organic or inorganic, researched over the years.

### 1.6.1 Inhibitors of calcium oxalate-containing kidney stones

Many pathways have been identified in the formation of kidney stones including: their formation on interstitial apatite plague, crystal deposits in renal tubules and their crystallisation from free solution.[55,58,61,62,69,126,127] Unfortunately, kidney stone formation arises from multifactorial causes, as stone formation is complicated by a combination of biological causes including physico-chemical, genetic, environmental and dietary factors.[128–131] The study of urinary inhibitors of calcium oxalate crystallisation in particular has received a large amount of attention. The list of compounds both natural and synthetic, which can retard calcium oxalate crystallisation, is enormous. It includes metal ions such as $Mg^{2+}$, $Na^{+}$, $K^{+}$, $Fe^{3+}$, $Al^{3+}$, etc.,[132–134] simple compounds such as tartaric, aspartic, hippuric and citric acid,[64,70,135–144] to more complex macromolecules such as proteins and peptides.[47,71,135,145–149]

To illustrate examples from each of the aforementioned types of inhibitors and how they change the morphology, growth and nucleation, the following ***Figures 1.13-1.15***, are presented. First, ***Figure 1.13*** regards the work by Farmanesh *et al*. and the influence alkali metals have on COM crystallisation. Relative growth rates of COM in the presence of $Cs^{+}$, $K^{+}$, $Na^{+}$ and $Li^{+}$, in addition to changes in the morphology of the crystals were determined. They concluded that alkali metals can function as crystal growth inhibitors. In addition, they also observed distinct morphological changes to COM crystal shapes, sizes and habit.

The work of Rimer *et al*. investigated the use of citrate (CA) and hydroxycitrate (HCA) as crystal growth modifiers of COM. Citrate has been extensively studied over the years,[68,140,142,150] however compared to macromolecules, citrate has been shown to have only a moderate inhibition impact on kidney stones (***Figure 1.14***). Compared to the morphology of the control COM, the addition of CA and HCAs final crystal morphologies indicate changes to the crystal habit. This change of habit is due to the adsorption of the two species on different crystallographic faces. CA alters the growth in the c direction (***Figure 1.14 (a)***) while HCA, though different by only a single alcohol group, prefers to bind to the apical

tips or (121) and (021) faces. The effect results in diamond-shaped crystals for HCA compared to control COM.

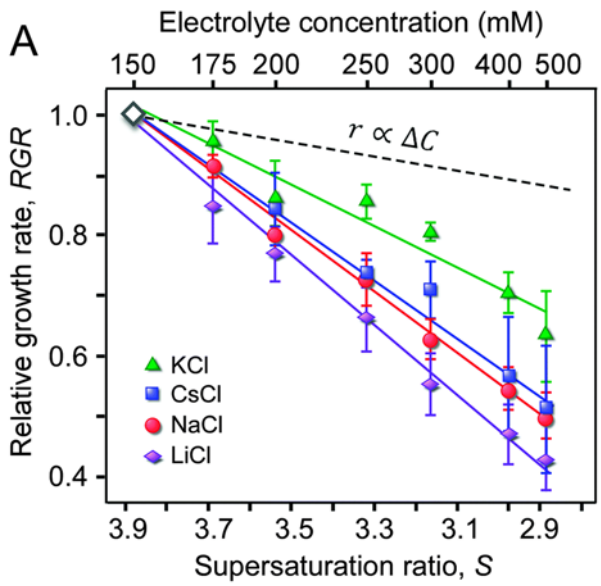


***Figure 1.13***: (A) Alkali metals impact on the relative growth rates (RGR) of COM at various concentrations. Reproduced with permission from the work of Farmanesh *et al.*[133] Copyright © (2015) The Royal Society of Chemistry.

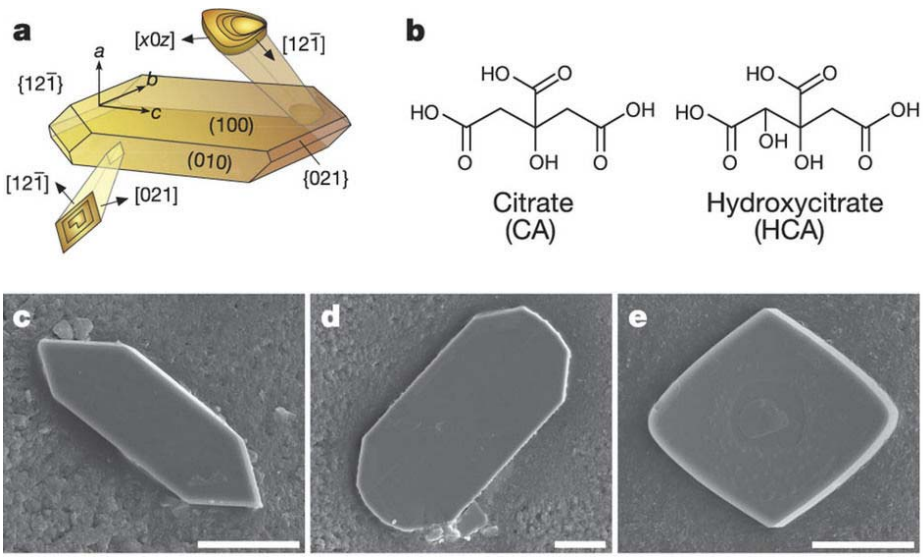


***Figure 1.14***: Effects of inhibitors on COM crystallisation, (a) COM crystal habit with indexed face, (b) molecular structures of CA and HCA, (c-e) SEM images of COM crystals in the absence of inhibitor (c), and in the presence of 20 µg $ml^{-1}$ CA (d) and in the presence of 20 µg $ml^{-1}$ HCA (e). Reproduced with permission from the work of Rimer *et al.*[150] Copyright © 2016 Nature Publishing Group.

Macromolecules found to inhibit kidney stone formation include, osteopontin (OPN), urinary prothrombin fragment 1, nephrocalcin, Tamm-Horsfall glycoprotein, and glycosaminoglycans are generally considered to impact kidney stone formation to a greater extent than smaller organic molecules.[65] The ability to inhibit the aggregation of crystals is considered to be one of the critical steps in stone formation. These acid-rich urinary proteins prevent the formation of precipitates in human urine supersaturated with respect to calcium oxalate.[3,151] However, urinary proteins with substantial anionic functions can act as adhesives that promote COM aggregation and attachment to epithelial cells instead of inhibiting COM crystallisation.[152,153] Like most biomineralisation processes, the role of acid-rich urinary proteins is not completely understood, exhibiting ambiguous effects on COM growth, nucleation and aggregation pathways. Nonetheless, macromolecule additives such as poly-L-aspartate, poly-L-glutamate and polyacrylate (PAA) have been found to control crystallisation, specifically the hydration states of calcium oxalate (COM or COD).[154] Another study by Thomas *et al*. further investigated the effects PAA had on calcium oxalate morphology (***Figure 1.15***). The macromolecules stabilised the dihydrate polymorph of calcium oxalate, COD. Additionally, the morphology of the COD crystals was altered with increasing PAA from the standard COD morphology, tetragonal bipyramidal to dumbbells and rodlike tetragonal bipyramidal prisms.

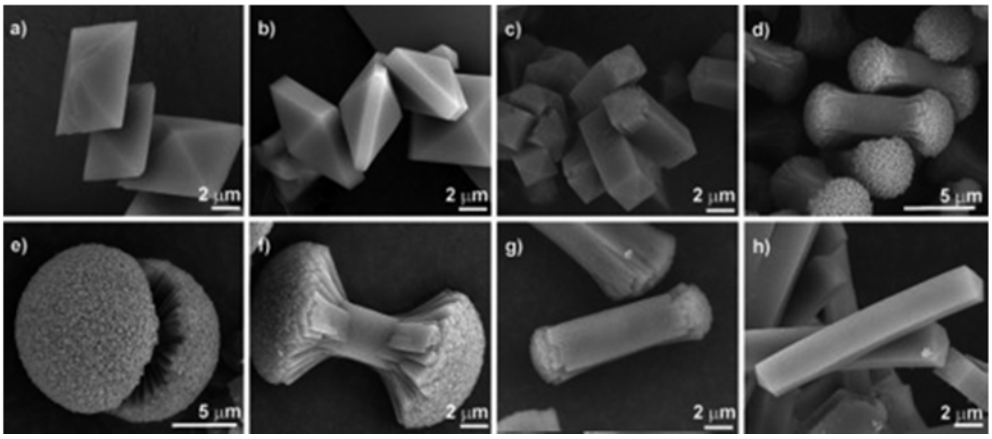


***Figure 1.15***: SEM images of individual COD crystals morphologies grown from 0.8 mM calcium-oxalate solutions in the presence of increasing PAA concentrations (a) 3, (b) 6, (c), 12, (d) 16, (e) 96, (f) 148, (g) 188, and (h) 225 µg/mL. Reproduced with permission from the work of Thomas *et al.*[155] Copyright © (2012) WILEY-VCH Verlag GmbH & Co. KGaA, Weinheim.

As mentioned above, acid-rich molecules, small and large, continue to be investigated due to their presence in urinary proteins, and in the organic matrices of calcium oxalate-containing kidney stones, and also due to their abilities to promote or inhibit pathways to calcium oxalate crystallisation and kidney stone aggregation. The following section describes the steps towards the possibility of a new calcium oxalate inhibitory species, the tetrazole.

### 1.6.2 Tetrazoles as calcium oxalate crystal growth modifiers

Tetrazoles were first discovered in 1885 by Bladin[156]. Tetrazoles are a class of organic compound often used as carboxylic acid analogues.[157–165] Several emerging applications for the use of the tetrazole group include their use in medicinal applications,[157,161,164] as light emitting devices,[166–169] and more recently as crystal growth modifiers.[170–172] A study by Jones *et al.*[170] utilised the fact that tetrazole molecules have similar $pK_a$ values to carboxylic acids,[165] and are in fact a more metabolically stable (more biocompatible) surrogate of a carboxylic acid group to inhibit various crystallites. Barium sulfate and calcium carbonate crystals were grown in the presence of several tetrazole molecules, with both found to be impacted on by the tetrazole molecules to varying degrees. The stabilisation of vaterite instead of the typical calcite phase in the presence of the tetrazole derivative 4-(1H-tetrazole-5-yl)benzaldehyde was one interesting find from the study. More importantly, however, the tetrazole molecules studied appeared to be more potent inhibitors than simple carboxylate-containing amino acids. Additionally, the chemical functionality of the additives influences the nature of the impact on both barium sulfate and calcium carbonate (***Figure 1.16***).

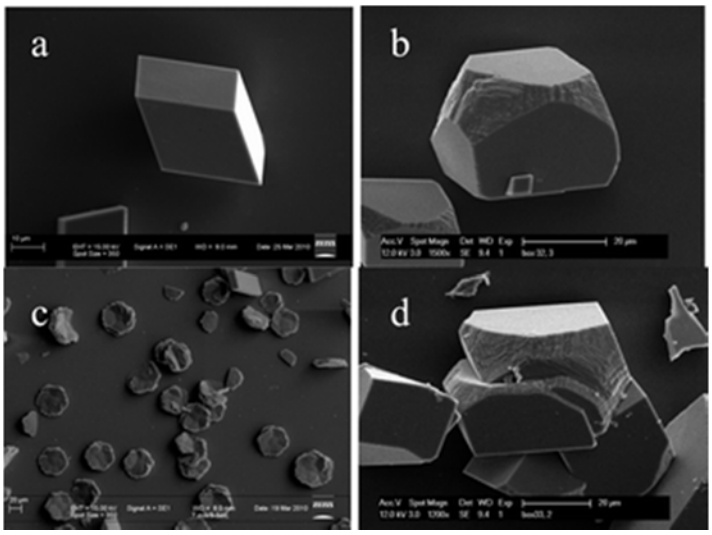


***Figure 1.16***: Calcium carbonate crystallised in the presence of (a) 0 mM tetrazoles, (b) 1.71 mM **phtet**$^{-}$, (c) 1.44 mM **bztet**$^{-}$ and (d) 1.24 mM **phtet**$_2^{2-}$. Reproduced with permission from the work of Jones *et al.*[170] Copyright © (2010) Royal Society of Chemistry.

In summary, as the literature review above shows, the use of acidic molecules for the inhibition of calcium oxalate with the aim of preventing kidney stone formation is of great interest. The continued study of all compounds, synthetic or natural that inhibits or controls nucleation, crystal growth and aggregation of COM, in particular, will continue to expand the understanding of this complex system in the context of biomineralisation. The study of tetrazole molecules as calcium oxalate crystal growth modifiers may provide a new direction and approach to tackling pathological mineralisation. This thesis contains the first experiments utilising tetrazole-containing molecules to investigate their impact on COM crystallisation. Hence, in the next chapter, the methodology for the experimentation for calcium oxalate crystallisation will be presented. The specific aims of this work include the synthesis and characterisation of a series of tetrazole molecules for the sole purpose of determining whether the inhibition of calcium oxalate solids is possible in their presence. If modification is possible, to what extent does each species interact with the crystals during nucleation, growth and how are their crystal morphologies affected? By studying these processes and their inherent mechanisms, it is hoped that structure activity relationships may be developed for the future use of tetrazoles as crystal growth modifiers to control the crystallisation of COM and other biologically relevant minerals.

# 2 Methodology

Some of the work presented in this chapter and chapters 3, 4, 5 and 6 have been published in peer reviewed journals which are cited below:

C. J. McMulkin, M. Massi, F. Jones, *CrystEngComm*. **2015**, *17(13)*, 2675-2681. doi: 10.1039/C4CE01717J

C. J. McMulkin, M. Massi, F. Jones, *J. Cryst. Growth*. **2017**, 468, 295-298. doi: 10.1016/j.jcrysgro.2016.10.038

The experimental procedures reported herein, were performed by the author, unless stated otherwise.

## 2.1 Materials

### 2.1.1 Chemicals

$CaCl_2 \cdot 2H_2O$ (Merck, 99.5%)

$CaC_2O_4 \cdot H_2O$ (Alfa Aesar, 99%)

KCl (APS Finechem, 99.8%)

HCl (Ajax Finechem, 32%)

$NaC_2O_4$ (APS Finechem, 99.6%)

$Na_3C_6H_5O_7$. $2H_2O$ (Ajax Finechem, 99.0%)

$NH_4Cl$ (Ajax Finechem, 99.5%)

$NaH_2PO_4$ (Merck, 99.0%)

NaOH (Merck, 99%)

$MgSO_4$ (Merck, 99%)

Ultra-pure (18 MΩ $cm^{-1}$) water was used in all experiments.

All chemicals were used as purchased without further purification.

## 2.2 Methods

### 2.2.1 Calcium oxalate crystallisations – control

Calcium chloride dihydrate (0.588 g, 0.004 mol) was added to ultrapure water (200 mL) to prepare stock calcium chloride solution (0.02 mol $L^{-1}$). Sodium oxalate (0.536 g, 0.004 mol) was added to ultrapure water (200 mL) in a separate 250 mL flask to prepare the stock sodium oxalate solution (0.02 mol $L^{-1}$), with the use of a sonicator, where necessary. All crystallisation reactions took place in separate 20 mL glass vials. Inside the vials, cleaned glass discs of radius 0.5 cm were placed before addition of solutions, to provide a removable crystal growth site. Once the glass discs have been added, the two stock solutions are preheated in a water bath at 30°C for half an hour before the addition to the vials. Once the solutions have reached 30°C, the stock solutions (300 µL) are added in 1:1 ratio with the required amount of modifier (if any) added to the vials followed by the addition of ultrapure water, up to a final volume of 20 mL. Through all experimentation calcium chloride solution (0.02 mol $L^{-1}$) was added before the sodium oxalate solution (0.02 mol $L^{-1}$), which once added begins the reaction. The reaction mixtures' initial pH was measured at an average of 6.56 ± 0.15, while samples after a period of 3 days were measured with an average pH of 7.64 ± 0.19. The vials were left in a water bath at 30°C for 3 days before the glass discs were removed, washed several times with ultrapure water before drying using a combination of air and adsorbing the excess fluid using tissue paper. All discs were placed into labelled, dry sample wells for future analysis. A final calcium oxalate concentration of 0.3 mM was chosen as it formed the most consistent calcium oxalate crystals. These crystals served as controls and were

analysed by optical microscopy, scanning electron microscopy (SEM) and Raman spectroscopy and atomic force microscopy (AFM).

### 2.2.2 Calcium oxalate crystallisations – in the presence of additives

All crystals were prepared identically to the control crystals. However, addition of a predetermined amount of modifier was added to the flask followed by the addition of ultrapure water, almost up to the final volume (20 mL). Stock solutions of the modifying species (tetrazole or carboxylic acid) were made up to 10 g $L^{-1}$ concentrations using distilled deionized water and adjusted to pH 7 (adjusted by 0.1 - 1.0 M sodium hydroxide and/or hydrochloric acid solutions). The additive concentrations were 0.1, 1.0 or 5.0 g/L for all additive species. The calcium chloride solution with any additive concentration required was equilibrated in a water bath to the reaction temperature for half an hour before the addition of the sodium oxalate solution to begin the reaction. The vials were left in the 30°C water bath for 3 days before the glass disc from each sample vial was removed, washed with ultrapure water, the excess fluid adsorbed using tissue paper and air dried. The glass discs were then placed in dry labelled sample wells for analysis by optical microscopy, SEM, photophysics and Raman spectroscopy.

### 2.2.3 Calcium oxalate crystallisation - timed experiments

All crystals were prepared identically to the additive grown crystals, except, crystals were removed at longer time periods. Crystals were grown up to a time of 1 month, with removal of samples at 3 days, 6 days, 9 days, etc. up to 30 days. After each set was removed, they were washed and dried as per the method stated in 2.2.1, ready for analysis by optical microscopy, SEM, photophysical investigation and Raman spectroscopy. Additive 3, 1H-5-phenyltetrazole, was investigated *via* this method to further explore the dissolution mechanism occurring in the presence of the phenyl-tetrazole species. As a comparison, control crystals and crystals grown in the

presence of the carboxylate equivalent species, benzoic acid, were also grown using the same method.

### 2.2.4 Calcium oxalate crystallisation - artificial urine

Crystals were grown in an artificial urinary (AU) growth solution. There are many AU solutions proposed thus, comparisons of many AU combinations were studied by Thongboonkerd et al.[173] Following the literature search, an artificial urine solution, as described by Brown et al.[75] was selected. The AU composition and properties of this solution are shown in ***Table 2.1***. Vials were prepared identically to ***Section 2.2.1***, additive solutions were added to AU solution up to 20 mL, kept at 30°C for 3 days and reported concentrations in ***Table 2.1*** are final concentrations taking into account dilution by addition of the tetrazole solutions. The crystals were extracted on the glass slide and cleaned as per ***Section 2.1.1*** ready for analysis by optical microscopy, SEM and Raman spectroscopy. ***Table 2.2*** reports the concentrations of the tetrazoles used in the AU experiments.

***Table 2.1***: Properties and composition of Artificial Urine (AU) used in this study

| Property and composition | AU (Brown et al.[75]) | AU (this study) |
|---|---|---|
| pH | 6.50 | 6.50 |
| $Na_3C_6H_5O_7$ (mM) | 3.21 | 2.89 |
| NaCl (mM) | 105.50 | 94.95 |
| KCl (mM) | 63.70 | 57.33 |
| $NH_4Cl$ (mM) | 27.60 | 24.84 |
| $CaCl_2$ (mM) | 5.75 | 5.17 |
| $MgSO_4$ (mM) | 3.95 | 3.55 |
| $Na_2C_2O_4$ (mM) | 0.032 | 0.029 |
| $NaH_2PO_4$ (mM) | 3.23 | 2.91 |

***Table 2.2***: Concentrations of tetrazoles used in AU experiments

| Tetrazole | Concentration (mM) |
|---|---|
| **4** | 5.74 |
| **5** | 5.84 |
| **10** | 4.67 |
| **12** | 6.80 |
| **13** | 6.80 |
| **14** | 6.80 |

### 2.2.5 Dissolution studies

To 20 mL vials, excess COM solids (0.10 g, 0.68 mmol) were added with additives at several concentrations (0.1, 1.0 and 5.0 g/L). Ultrapure water was added up to the final volume (20 mL). The samples were adjusted to pH ~7 before being left for one week at 30°C, afterwards the filtrate was collected by vacuum filtration through 0.2 µm filter membranes for analysis. ICP-AES analysis was performed externally on a Varian Vista Axial CCD ICP-AES at Murdoch University's Centre for Marine and Freshwater Research Laboratory.

### 2.2.6 Scanning electron microscopy (SEM)

Designated samples were prepared for SEM analysis at the Curtin University Electron Microscope Facility using a Zeiss Evo 40XVP SEM using either secondary electron or back-scatter detectors. Energy dispersive X-ray spectroscopy (EDX) was also employed in determining the qualitative elemental composition of our samples. Each sample analysed was sputter coated with either platinum or gold with a typical

thicknesses of 2 - 20 nm. Each SEM image was also analysed using the software ImageJ, to determine the number of particles, their size and standard deviation of particles from the mean. The measuring tool and scale bar calibration was used to measure the length (*c-axis* length) and width of each particle in the SEM image to obtain their aspect ratio. Additionally, images obtained are compared across all additive grown crystals and control crystals to determine any changes to crystal morphology.

The free software ImageJ and Fiji were employed to measure the crystals dimensions observed in the SEM images collected. The files were opened directly with the software and the measuring tool utilised to determine the length of the scale bar (in micrometres), and thus accurately determine the crystals lengths and widths. From this data, the aspect ratio's (AR), mean particle lengths and standard deviations were calculated for all crystals grown in the presence of the series of tetrazole molecules and observed by SEM.

### 2.2.7 Confocal Raman spectroscopy (CRS) and optical microscopy

After crystallisation, the dry glass discs with each sample were analysed by Raman spectroscopy using silicon as a reference material for all spectra obtained. Optical images and confocal Raman spectra were collected using the WITec alpha 300SAR, utilising a frequency-doubled NdYAG laser of wavelength 532 nm and of 50 mW power. Each Raman spectrum collected consists of 10 accumulations at an integration time of 0.08371 seconds. Analysis was performed using the WITec Project FOUR® software. In addition to single spectrum acquisitions where the focus of the laser is on the surface of the crystal, line spectra (confocal Raman measurements) were acquired that collect multiple images at different depths (penetrating the crystals). Confocal Raman is possible by first focussing the laser onto the surface of the crystal as per single spectrum acquisitions, before utilising the z-control to set the start and finish positions of the laser to 4 µm and -8 µm, above the surface and below the surface of the crystal, respectively. The positions of the start and end points were determined by finding the average crystal thickness from control crystals imaged by SEM. Once the positions are set, the instrument

accumulates 10 spectra per step with a total of 50 steps across the 12 μm depth. Optical images were obtained at magnifications of 20x and 100x for all crystals.

### 2.2.8 Dynamic light scattering (DLS)

Nucleation rates were determined by DLS, using a Malvern Instruments Zetasizer Nano-ZS. Solutions of calcium chloride dihydrate (0.8 mM, 22.5 mL) and sodium oxalate (0.8 mM, 22.5 mL) were mixed at a ratio of 1:1 with constant stirring. Experiments in the presence of additives had sodium oxalate solution added last to begin nucleation. Additive concentrations were 1.0 g/L across all experiments, except the control experiments. All conditions were run in triplicate, with each run recorded over 30 minutes. In order to ensure result consistency across each additive, the Zetasizer integration time was fixed at ten seconds averaging, ten readings and three minutes apart. This allowed for direct comparison of each time step through the recorded kilocounts per second. The kilocounts per second (kcps) are also referred to as the mean count rate. If the detector in the Zetasizer collects 1,000,000 photons over the duration of 100 seconds, then the mean count rate during that measurement was 1,000,000 photons/ 100 sec which is equal to 10,000 photons/ sec or 10 kcps.

As described above in ***Section 2.2.1***, stock solutions are made fresh for both calcium chloride, sodium oxalate and any tetrazole species required. The set up for DLS included the abovementioned Zetasizer Nano-ZS, a small magnetic stirrer plate on which the teflon beaker containing a small magnetic stirrer bar was placed. The solutions, similar to ***Section 2.2.2,*** are added in the following order. First, calcium chloride solution, tetrazole species (all of which had a final concentration of 1.0 g/L) and lastly the sodium oxalate solution to begin the reaction. Once all three solutions were added, an initial aliquot of mixed solution was pipetted into a cuvette for analysis (time = 0 minutes). Once the Zetasizer completed its first data point, the solution was returned from the cuvette to the teflon beaker and immediately a new aliquot taken for the next data point. This process was repeated until the 45 minute mark in triplicate for each tetrazole species and several more times for the control experiment.

### 2.2.9 Atomic force microscopy (AFM)

To further elucidate the mechanism of inhibition, including the rate of inhibition of growth of faces by the additives, AFM was performed on calcium oxalate crystals with and without the presence of inhibitors. Tetrazoles selected for AFM analysis were determined by the impact of the various tetrazoles on COM, as well as trends amongst tetrazole functional groups. Control crystals were always used as the starting material in *in situ* measuring, with the additives chosen spiked into the growth solution to alter growth behaviours. The solutions used for the growth of the calcium oxalate (pre-grown according to ***Section 2.2.1***) were calcium chloride dihydrate (0.8 mM) and sodium oxalate (0.8 mM). The solutions were diluted from 0.02 M stock solutions and filtered through PALL® Life Sciences 0.2 µm Acrodisc syringe filters. The solutions were then mixed at a ratio of 1:1 with using a KDS 200 Legacy Syringe Pump. Solutions were pumped at rates between 0.25 mL/min and 1 mL/min.

The complete set up is shown in ***Figure 2.1*** and ***Figure 2.2***. The Bruker Dimension FastScan® is housed on the ground floor of the department purposefully built on a separate concrete slab to the rest of the building to reduce vibrations. The instrument is housed, as shown in ***Figure 2.2***, in an acoustic and vibration isolation enclosure within which the entire stage is suspended to further reduce external vibrations. Attached to the stage, the *in situ* sample stage is positioned and kept in position with the stage vacuum or multiple strips of strong double-sided tape. The only danger when using the stage vacuum can be that water may enter the stage vacuum and ruin the controller and thus the experiment. Thus, the latter option was used preferentially. The two growth solution tube ends can be seen in ***Figure 2.1*** on the left hand side, positioned carefully so as to not disturb the scan head. On the right hand side of ***Figure 2.1***, a separate tube pumping solution out is visible. This is run on a separate system utilising a Masterflex® L/S economy variable-speed drive peristaltic pump, set to match the inflow of solution.

The AFM instrument used for all images was a Bruker Dimension FastScan® utilising two imaging modes (ScanAsyst® and PeakForce Tapping®). ScanAsyst® mode images were typically collected using scan rates between 2 and 4 Hz, with gain set to between 2 and 5, and a typical set point force between 5 - 15 nN. PeakForce

Tapping® images were collected using scan rates of 2 - 3 Hz, with a gain between 2 and 4, the peak force set point was typically between 2 - 15 nN and the tapping amplitude set to 250 mV. All experiments were performed at room temperature with the average relative humidity recorded at 59%.

Probes throughout imaging were either Bruker Sharp Nitride Lever (SNL) - 10 or Bruker ScanAsyst®-fluid probes. SNL-10 probes are made from silicon nitride, having a tip radius of 2 nm (nom.) for tips A and B which were used exclusively throughout imaging and these tips have spring constants of 0.35 (nom.) and 0.12 (nom.), respectively. All other measurements were made using ScanAsyst®-fluid probes also made from silicon nitride with a tip radius of 20 nm (nom.) and a spring constant of 0.7 (nom.).

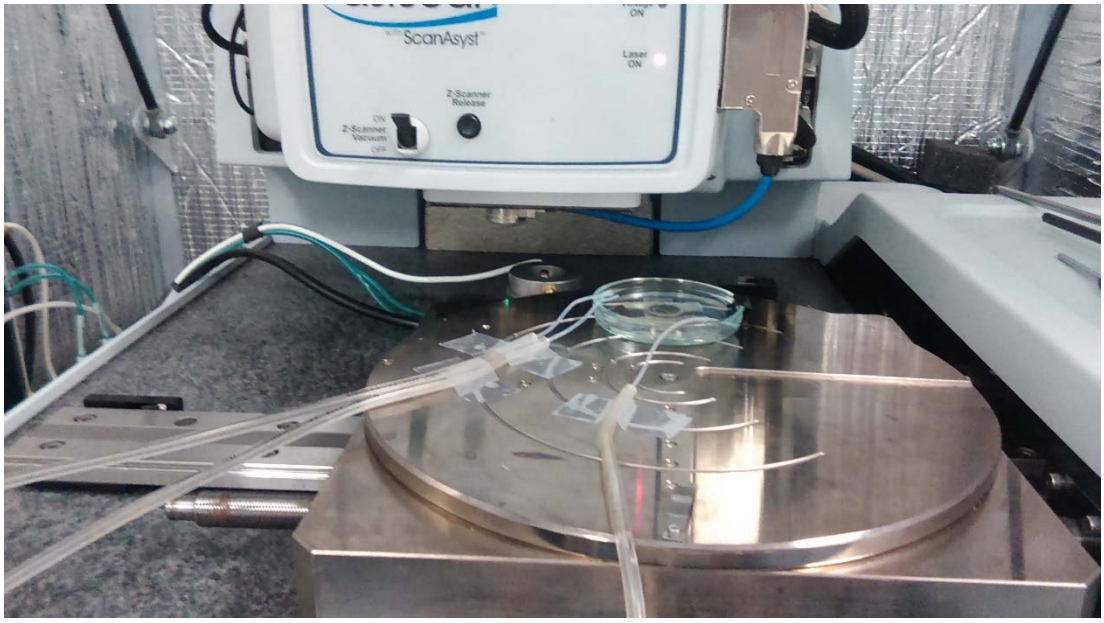


***Figure 2.1***: *In situ* AFM petri dish set up with inflow tubes on left hand side and outflow tube on right hand side. Sample is glued to bottom of petri dish on metal spacers. Ultrapure water shown fills the petri dish ready for focussing of tip in fluid for *in situ* measurements.

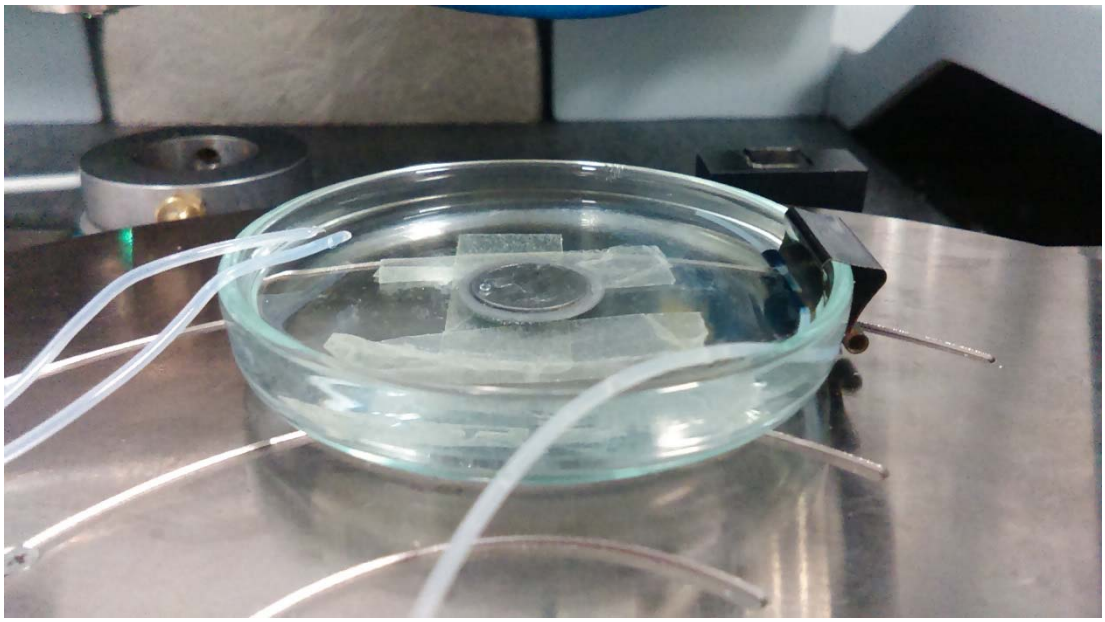

***Figure 2.2***: *In situ* AFM setup shown on stage ready for alignment before measurements on the Bruker Dimension FastScan®.

# 3 Synthesis and Characterisation of Tetrazoles

## 3.1 Introduction

The synthesis of tetrazole molecules has been thoroughly researched with numerous methods appearing in the literature during the past two decades that are relatively safe, high yielding, and involve simple procedures.[174,175] Most differ only in terms of the solvent,[141,176] and catalyst,[177–182] while some methods have begun utilising microwaves to assist in the synthesis of their desired tetrazoles.[183,184] The work detailed in this chapter will cover the design, synthesis and characterisation of a series of tetrazole molecules for their use as crystal growth modifiers. In addition to the standard characterisation methods employed, NMR, IR, melting point, Raman spectroscopy, fluorescence and absorption measurements were made for the entire tetrazole series and are vital for the characterisation of each tetrazole molecule within calcium oxalate crystals discussed in later chapters. While the tetrazole molecules in the series are predominantly *para* substituted 5-aryltetrazoles with a phenyl backbone, *ortho* and *meta* substituted 5-aryltetrazoles with pyridine and isoquinoline and naphthalene backbones were also studied. The tetrazole molecules in the series are as follows in ***Table 3.1***. All tetrazole-containing molecules were synthesised in-house by the author except for **8**, **15**, **16**, **19**, **21** and **22**, which were synthesised by colleagues at Curtin University. For more details see ***Section 3.6.3***. The tetrazoles in this study were selected for a multitude of reasons, including; functional group similarity, chelating properties, structural properties and as they were readily available in our group.

***Table 3.1***: Tetrazole series, names and codes for referencing

| Tetrazole nomenclature | Tetrazole codes |
|---|---|
| methyl 4-(1H-tetrazol-5-yl) benzoate | **1** |
| 4-(1H-tetrazol-5-yl) acetylbenzene | **2** |
| 1H-5-phenyltetrazole | **3** |
| 4-(1H-tetrazol-5-yl) benzaldehyde | **4** |
| 4-(1H-tetrazol-5-yl) benzonitrile | **5** |
| 4-(1H-tetrazol-5-yl) benzoic acid | **6** |
| 5-(2-acetyloxyphenyl) tetrazole | **7** |
| 1,2-bis(1H-tetrazol-5-yl) benzene | **8** |
| 1,3-bis(1H-tetrazol-5-yl) benzene | **9** |
| 1,4-bis(1H-tetrazol-5-yl) benzene | **10** |
| 2,6-bis(1H-tetrazol-5-yl) pyridine | **11** |
| 1H-5-(2-pyridyl) tetrazole | **12** |
| 1H-5-(3-pyridyl) tetrazole | **13** |
| 1H-5-(4-pyridyl) tetrazole | **14** |
| 1H-5-(2-pyrazine) tetrazole | **15** |
| 1H-5-(4-bromophenyl) tetrazole | **16** |
| 1H-5-(4-methoxyphenyl) tetrazole | **17** |
| 4-(1H-tetrazol-5-yl) benzamide | **18** |
| 4-(1H-tetrazol-5-yl) phenol | **19** |
| 1H-5-(4-bromo-2-pyridyl)-tetrazole | **20** |
| 1H-4-allylphenyl-tetrazole | **21** |
| 2-(1H-tetrazol-5-yl) quinoline | **22** |
| 1-(1H-tetrazol-5-yl) isoquinoline | **23** |
| 1-(1H-tetrazol-5-yl) naphthalene | **24** |
| 2-(1H-tetrazol-5-yl) pyrimidine | **25** |
| 2-(1H-tetrazol-5-yl) phenol | **26** |

## 3.2 Synthesis and characterisation of 5-Aryl-1H-tetrazole series

The formation of the tetrazole ring in all target compounds was carried out using the straightforward and well known procedure developed by Koguro *et al*.[174] as outlined by ***Scheme 3.1***.

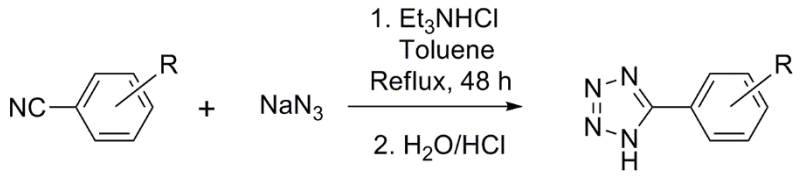


***Scheme 3.1***: Synthesis of the 1H-5-aryltetrazoles.

First the formation of the triethylammoniumchloride salt is required, the salt is made *in situ* but soon reacts with addition of the inorganic azide to form the intermediate $Et_3N{\bullet}HN_3$, required for progression of the reaction. Toluene is an excellent solvent for the reaction as it does not dissolve the product, thus shifting the equilibrium of the reaction towards the product, which is in the form of a triethylamine intermediate. The reaction between the newly formed intermediate $Et_3N{\bullet}HN_3$ is first polarised as $Et_3NH^{\delta+}$ and $N_3^{\delta-}$, each subsequently reacting with the triple bond of the nitrile group and *via* the concerted 1,3-dipolar cycloaddition, the triethylammonium salt final product is formed.[176] See ***Scheme 3.2*** for a proposed mechanism for the formation of the tetrazole.

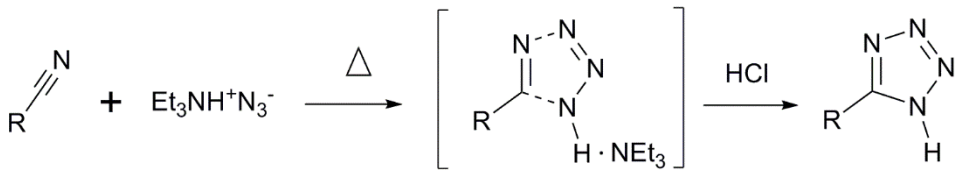


***Scheme 3.2***: Concerted 1,3-dipolar cycloaddition mechanism proposed by Himo *et al.*[176]

The tetrazolate salt is brought to the water layer before dropwise addition of aqueous hydrochloric acid and precipitates the desired neutral tetrazole product as a colourless solid. Melting points were collected for each tetrazole synthesised, however, most decomposed when attempted due to the high percentage of nitrogen atoms. In this study the decomposition points of the tetrazole molecules varied, up to 30 °C from the literature decomposition values, in a few cases. Difficulties in obtaining consistent tetrazole data has been previously reported.[175] One tetrazole in this study, 1-(1H-tetrazol-5-yl) naphthalene (**24**), in particular has literature melting points that vary from 168 °C,[185] 216-218 °C,[186] and 264-268 °C.[177] Nonetheless, all melting points were collected with most tetrazole molecules synthesised in this study matching closely to literature data. The yields of the tetrazole molecules synthesised in this work are reported in ***Table 3.2***.

A variety of yields were obtained, as studies have shown,[187,188] these can be attributed to the functional group present (whether the –R group is electron withdrawing or electron donating in character), and whether it is located at the *para*, *ortho* or *meta* position on the aromatic ring, relative to the tetrazole functional group. Reactivity of the nitrile increases if the -R group is electron withdrawing as electron density is removed from the $\pi$ system resulting in polarisation of the nitrile making the carbon atom more likely to undergo nucleophilic addition. Moreover, low yields result from the opposite effect. Electron donating groups add electron density to the $\pi$ system making it more nucleophilic and decrease the reactivity of the nitrile. Additionally, the solubility of both the starting nitrile species and product in toluene greatly impacts the formation and yield of the product as reflected by ***Table 3.2***, for –R groups with higher solubility in toluene such as **23** and **24**, the yields are subsequently much lower. Species shown in ***Table 3.2*** were characterised by IR, NMR, Raman spectroscopy and photophysically investigated. The main IR bands that are indicative of tetrazole formation include, the presence of aromatic N-H stretches at approximately 3400 $cm^{-1}$ and the aromatic C=N stretch at 1600 $cm^{-1}$. The absence of the characteristically sharp nitrile band (C≡N) at 2260-2240 $cm^{-1}$ indicates the depletion of the starting nitrile.

***Table 3.2***: Yields obtained for each prepared tetrazole.

| Tetrazole | Yield (%) |
|---|---|
| methyl 4-(1H-tetrazol-5-yl) benzoate (**Tzmeb**H, **1**) | 92 |
| 4-(1H-tetrazol-5-yl) acetylbenzene (**Tzacb**H, **2**) | 73 |
| 1H-5-phenyltetrazole (**TzPh**H, **3**) | 53 |
| 4-(1H-tetrazol-5-yl) benzaldehyde (**TzPha**H, **4**) | 60 |
| 4-(1H-tetrazol-5-yl) benzonitrile (**TzPhCN**H, **5**) | 62 |
| 4-(1H-tetrazol-5-yl) benzoic acid (**TzBa**H, **6**) | 95 |
| 5-(2-acetyloxyphenyl) tetrazole (**TzAcoPh**H, **7**) | 46 |
| 1,3-bis(1H-tetrazol-5-yl) benzene (***m*TzTz**$H_2$, **9**) | 64 |
| 1,4-bis(1H-tetrazol-5-yl) benzene (***p*TzTz**$H_2$, **10**) | 90 |
| 2,6-bis(1H-tetrazol-5-yl) pyridine (**TzTzPyr**$H_2$, **11**) | 63 |
| 1H-5-(2-pyridyl) tetrazole (***o*TzPyr**H, **12**) | 44 |
| 1H-5-(3-pyridyl) tetrazole (***m*TzPyr**H, **13**) | 94 |
| 1H-5-(4-pyridyl) tetrazole (***p*TzPyr**H, **14**) | 18 |
| 1H-5-(4-methoxyphenyl) tetrazole (**TzmeoxPh**H, **17**) | 55 |
| 4-(1H-tetrazol-5-yl) benzamide (**TzPham**H, **18**) | 56 |
| 1H-5-(4-bromo-2-pyridyl)-tetrazole (**TzBrPyr**H, **20**) | 44 |
| 1-(1H-tetrazol-5-yl) isoquinoline (**TzIsoQn**H, **23**) | 20 |
| 1-(1H-tetrazol-5-yl) naphthalene (**TzNaph**H, **24**) | 16 |
| 2-(1H-tetrazol-5-yl) pyrimidine (**TzPyrm**H, **25**) | 24 |
| 2-(1H-tetrazol-5-yl) phenol (***o*TzPhOHH**, **26**) | 76 |

## 3.3 Raman spectroscopy characterisation

### 3.3.1 Introduction

Tetrazole-containing molecules are commonly characterised by infrared (IR) spectroscopy to determine the presence or absence of functional groups. Raman is often used in combination with IR due to the differences in IR active and Raman active groups. Both techniques provide useful functional group detection and fingerprint regions which permit identification of specific compounds.[189] Daimay *et al*. have published a comprehensive study of Raman functional group frequencies.[190] However, very few Raman spectra have been recorded for tetrazole-containing organic molecules, with Keresztury *et al*. being one of the only studies of the tetrazole functional group alone.[191] Most studies only include the Raman spectra complementary to the IR data for the characterisation of their tetrazole-containing molecules. In this thesis, the characterisation of each tetrazole-containing compound with Raman is also used to identify the bonding environments when the tetrazole molecules are employed as additives during the growth of calcium oxalate crystals.

### 3.3.2 Characterisation

All tetrazole molecules were analysed with Raman spectroscopy to complement the IR characterisation, but also to act as a baseline as tetrazole additives were present during calcium oxalate crystal growth. Subsequently, Raman spectroscopy was used for analysis of COM crystals in the presence of tetrazole molecules (see ***Chapter 6*** for Raman spectroscopy results of and ***Section 2.2.7*** for instrumental parameters). Confocal spectroscopy was not required for analysis of the tetrazole molecules, thus single Raman spectra only were recorded at low laser intensities (due to the fluorescence of the tetrazole upon excitation with the 532 nm wavelength laser). Setting laser intensity to a minimum, characteristic peaks were observed, compared to nominal laser intensity whereby a large fluorescent band appears which dominates the spectra as seen in ***Figure 3.1*** and ***Figure 3.2***, respectively.

As anticipated, similar to IR, each tetrazole molecule in the series had a unique Raman spectrum. Common peaks are identifiable throughout the series studied, the most prevalent vibrational modes include the phenyl aromatic ring at ~1000 (C-C aromatic), ~1580 (C=C aromatic), ~1600 (C=C) and ~3000 $cm^{-1}$ (C-H aromatic).[192] In addition to the aromatic backbone signals, tetrazole ring vibrational modes are identifiable[166,193] at ~1610 (N=N stretching), 1560 (N=N bending), 1320 (N-N stretching), 1210 (N-H bending), 1120 (N-N bending), 1060 (N-N stretching) and 623 $cm^{-1}$ (C-N out-of-plane bending). The Raman signals for all synthesised tetrazole-containing compounds, together with their complementary infrared signals, are reported in ***Section 3.6.3***. In addition, their individual Raman spectra can be found in ***Appendix 1***.

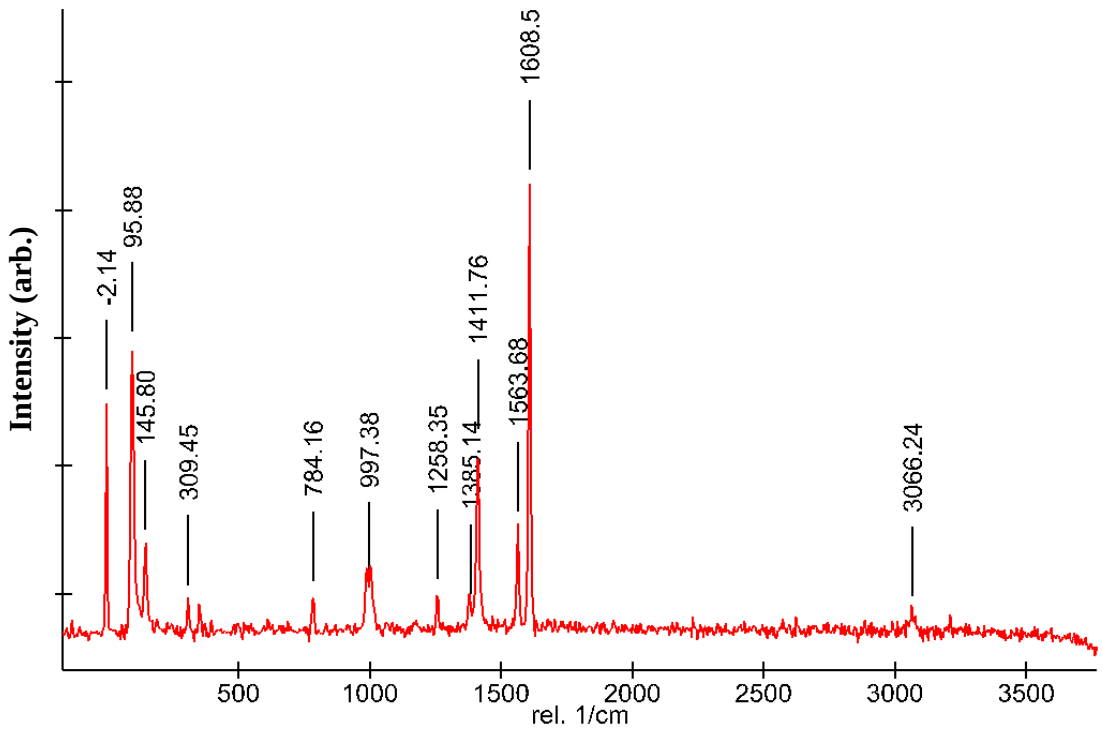


***Figure 3.1***: Raman spectrum of Tetrazole **3**, 1H-5-phenyltetrazole, at minimal laser intensity (10%) with individual peak resolution.

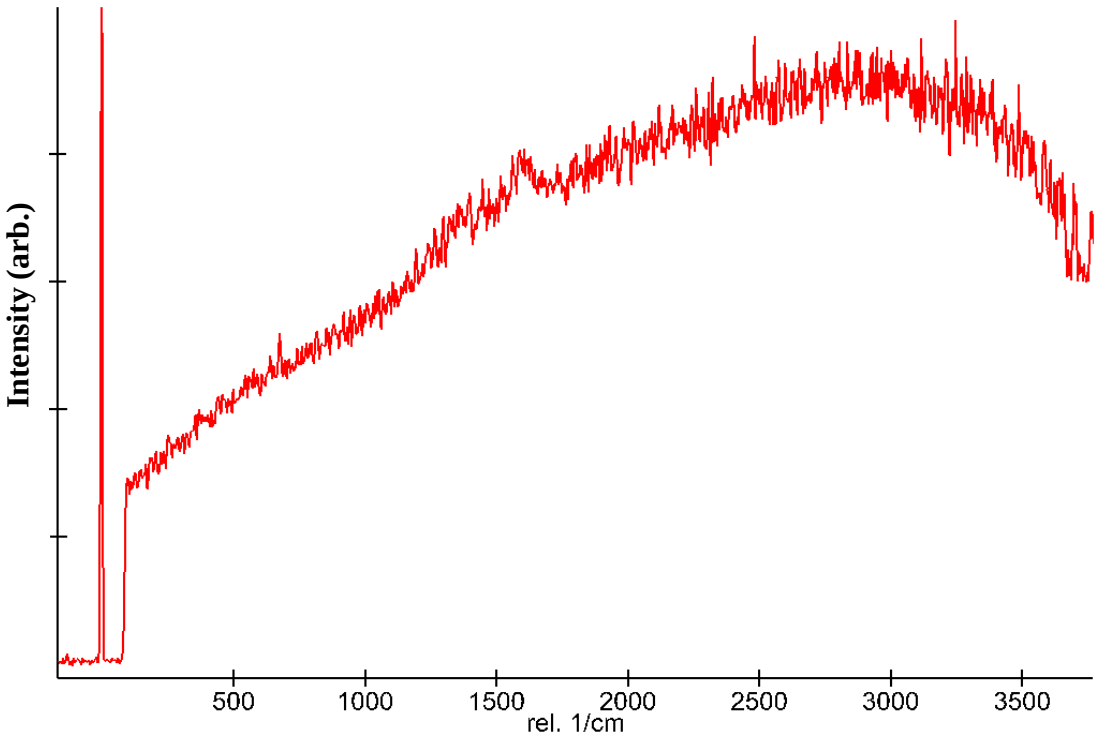


***Figure 3.2***: Raman spectrum of Tetrazole **3** at nominal laser intensity (100%). Fluorescent band observed overpowering individual peaks seen in ***Figure 3.1*** at lower intensity.

## 3.4 Photophysical investigation

### 3.4.1 Introduction

Tetrazole molecules as mentioned in ***Chapter 1*** are often used in medicinal chemistry and in light emitting devices. For instance, the work by Massi *et al*. have utilised the properties of tetrazole molecules as ligands in lanthanide-containing complexes as biomarkers with anti-cancer and anti-microbial properties.[194–197] These complexes are often very fluorescent, enabling researchers to visualise these complexes in cells once irradiated to ascertain cellular dynamics under various physiological conditions.[196] The characterisation of the complexes' photophysical properties can be crucial in determining if changes have occurred to the complexes' structures.[195] Thus the following sections investigate the series of tetrazole molecules' excitation and emission properties for characterisation.

### 3.4.2 Characterisation and investigation

The absorption spectra for each tetrazole molecule were required to determine the excitation wavelengths for the successful collection of their subsequent emission profiles. Each tetrazole molecule was measured in water at approximately $10^{-6}$ M. Where necessary, aqueous sodium hydroxide was added to dissolve the tetrazole solids, nonetheless as shown in ***Figure 3.3***, comparing ultra-pure water and aqueous sodium hydroxide, the absorption maxima remain very similar. The absorption maxima for the entire series of tetrazole compounds are presented in ***Table 3.3***.

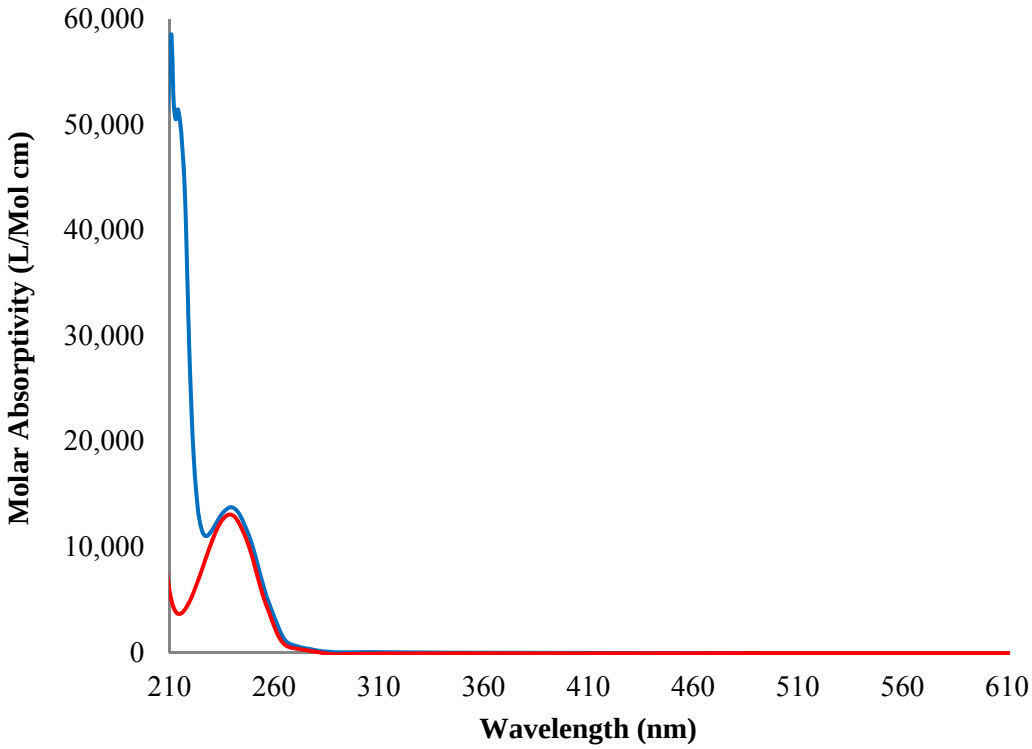


***Figure 3.3***: Absorption of 1H-5-phenyltetrazole (**3**) in water (red trace) and aqueous sodium hydroxide (blue trace) both at $10^{-6}$ M.

***Table 3.3***: Absorption data for each tetrazole compound at $10^{-6}$ M in $H_2O$.

| Tetrazole Series | Absorption $\lambda_{max}$/nm ($\varepsilon$ /$10^4$ $M^{-1}cm^{-1}$) |
|---|---|
| methyl 4-(1H-tetrazol-5-yl) benzoate (**1**) | 260 (3.00) |
| 4-(1H-tetrazol-5-yl) acetylbenzene (**2**) | 276 (1.73) |
| 1H-5-phenyltetrazole (**3**) | 239 (1.31) |
| 4-(1H-tetrazol-5-yl) benzaldehyde (**4**) | 282 (1.73) |
| 4-(1H-tetrazol-5-yl) benzonitrile (**5**) | 262 (1.97 |
| 4-(1H-tetrazol-5-yl) benzoic acid (**6**) | 259 (1.67) |
| 5-(2-acetyloxyphenyl) tetrazole (**7**) | 243 (0.94), 298 (0.37) |
| 1,2-bis(1H-tetrazol-5-yl) benzene (**8**) | 223 (2.87) |
| 1,3-bis(1H-tetrazol-5-yl) benzene (**9**) | 209 (2.55) |
| 1,4-bis(1H-tetrazol-5-yl) benzene (**10**) | 269 (1.83) |
| 2,6-bis(1H-tetrazol-5-yl) pyridine (**11**) | 223 (2.35), 290 (1.04) |
| 1H-5-(2-pyridyl) tetrazole (**12**) | 230 (1.05), 273 (0.64) |
| 1H-5-(3-pyridyl) tetrazole (**13**) | 239 (0.99) |
| 1H-5-(4-pyridyl) tetrazole (**14**) | 244 (1.50) |
| 1H-5-(2-pyrazine) tetrazole (**15**) | 235 (0.70), 284 (0.86) |
| 1H-5-(4-bromophenyl) tetrazole (**16**) | 250 (2.12) |
| 1H-5-(4-methoxyphenyl) tetrazole (**17**) | 252 (1.79) |
| 4-(1H-tetrazol-5-yl) benzamide (**18**) | 262 (2.11) |
| 4-(1H-tetrazol-5-yl) phenol (**19**) | 275 (1.79) |
| 1H-5-(4-bromo-2-pyridyl)-tetrazole (**20**) | 238 (1.24) |
| 1H-4-allylphenyl-tetrazole (**21**) | 252 (1.93) |
| 2-(1H-tetrazol-5-yl) quinolone (**22**) | 210 (3.46), 248 (3.92), 332 (0.71) |
| 1-(1H-tetrazol-5-yl) isoquinoline (**23**) | 221 (3.58), 327 (0.40) |
| 1-(1H-tetrazol-5-yl) naphthalene (**24**) | 224 (3.84), 290 (0.60) |
| 2-(1H-tetrazol-5-yl) pyrimidine (**25**) | 247 (2.53), 285 (1.41) |
| 2-(1H-tetrazol-5-yl) phenol (**26**) | 207 (3.58), 241 (1.49), 292 (0.68) |

Each tetrazole molecule's absorption spectrum exhibited moderately intense transitions in the UV region between 210 and 350 nm, these transitions are assigned to $\pi - \pi^*$ transitions.[198] Each absorption spectrum can be found in ***Appendix 2***. Absorption maxima were employed for excitation of the molecule to collect emission spectra and subsequently, the emission maxima were used to obtain the excitation spectra. Absorption wavelengths, collected in ***Table 3.3***, were employed to excite each tetrazole to yield emission and excitation profiles of the entire series in both the tetrazole's solid and solution form. The excitation-emission profiles of **3**, dissolved in water and sodium hydroxide solution are compared in ***Figure 3.4***, while excitation-emission profiles of **3** in the solid state are shown in ***Figure 3.5***. As found for the adsorption spectra (***Figure 3.3***), the excitation-emission profiles of **3** in both water and aqueous sodium hydroxide (presented in ***Figure 3.4***) show no difference. The same solution was used for both adsorption and excitation-emission analysis.

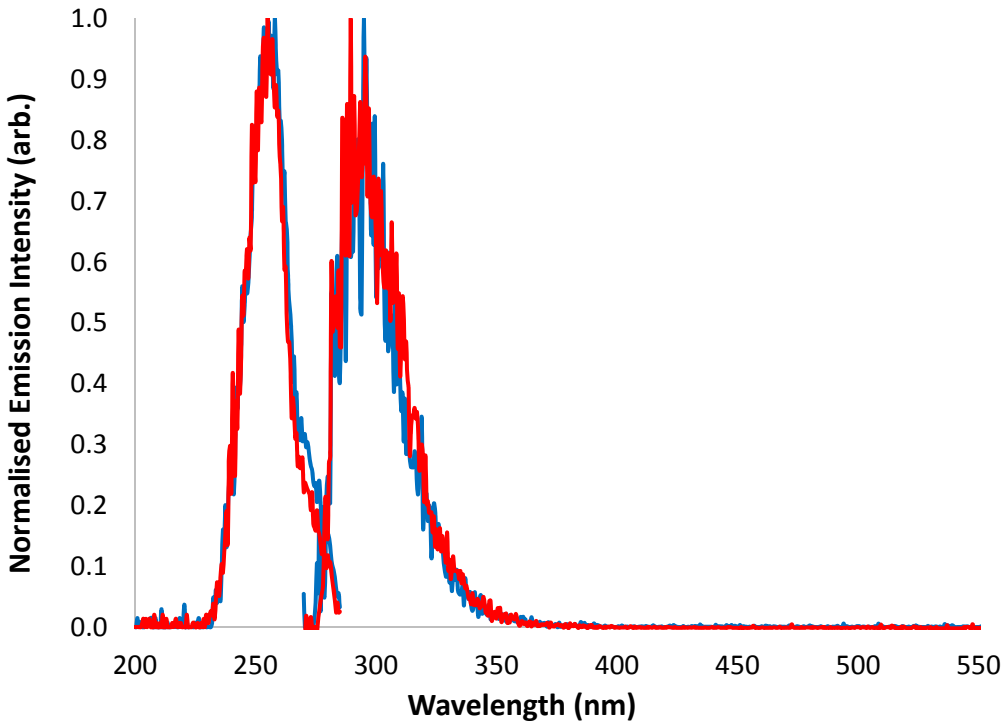


***Figure 3.4***: Solution excitation-emission profiles of 1H-5-phenyltetrazole (**3**) in water (red) and in aqueous sodium hydroxide (blue).

Comparing ***Figure 3.4*** and ***Figure 3.5***, an additional emission band is clearly visible from ~350-550 nm. This band is not observed in ***Figure 3.4***, thus adding further support that this observed additional emission band is not a result of either the tetrazole species being in the protonated or deprotonated form. As is common for aromatic molecules, the extra emission observed is due to the stacking of tetrazole molecules on top of one another. This stacking allows for the mixing of molecular orbitals and subsequent intramolecular π-π* transitions resulting in the emission observed as a broad unstructured band. The distance all tetrazole molecules are positioned between one another in the solid state determines the broadness of the emissive band. The recorded emission maxima wavelengths for all tetrazoles in the series in both solution and solid state can be found in ***Table 3.4***.

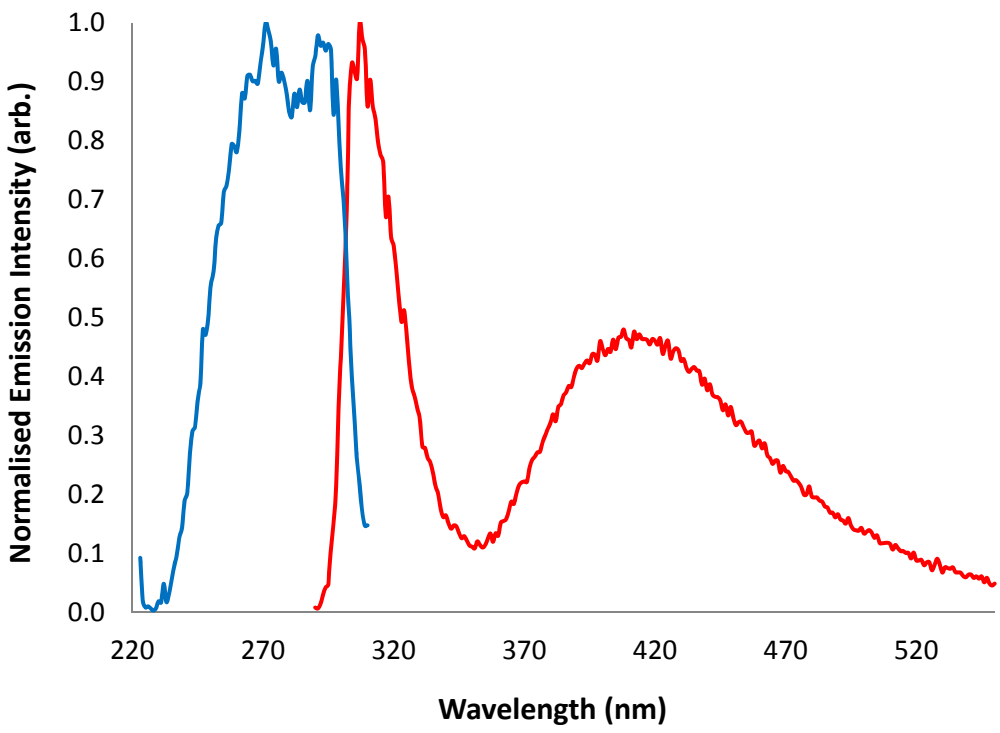


***Figure 3.5***: Solid state excitation (blue trace)-emission (red trace) profile of 5-phenyl-1H-tetrazole (**3**). Two emissive bands are visible (red trace), the original emission (~320 nm) and a new emissive band (~420 nm).

***Table 3.4***: Emission maxima data for each tetrazole compound in solution (at $10^{-6}$ M in $H_2O$) and in the solid state at 298 K.

| Tetrazole Series | Emission ($10^{-6}$ M) $\lambda_{max}$ (nm) | Emission (Solid state) $\lambda_{max}$ (nm) |
|---|---|---|
| methyl 4-(1H-tetrazol-5-yl) benzoate (**1**) | 380 | 350 |
| 4-(1H-tetrazol-5-yl) acetylbenzene (**2**) | 420 | 490 |
| 1H-5-phenyltetrazole (**3**) | 300 | 310 |
| 4-(1H-tetrazol-5-yl) benzaldehyde (**4**) | 425 | 490 |
| 4-(1H-tetrazol-5-yl) benzonitrile (**5**) | 350 | 360 |
| 4-(1H-tetrazol-5-yl) benzoic acid (**6**) | 315 | 370 |
| 5-(2-acetyloxyphenyl) tetrazole (**7**) | 380 | 310 |
| 1,2-bis(1H-tetrazol-5-yl) benzene (**8**) | 360 | 360 |
| 1,3-bis(1H-tetrazol-5-yl) benzene (**9**) | 330 | 330 |
| 1,4-bis(1H-tetrazol-5-yl) benzene (**10**) | 320 | 380 |
| 2,6-bis(1H-tetrazol-5-yl) pyridine (**11**) | 340 | 330 |
| 1H-5-(2-pyridyl) tetrazole (**12**) | 360 | 360 |
| 1H-5-(3-pyridyl) tetrazole (**13**) | 445 | 355 |
| 1H-5-(4-pyridyl) tetrazole (**14**) | 330 | 350 |
| 1H-5-(2-pyrazine) tetrazole (**15**) | 365 | 370 |
| 1H-5-(4-bromophenyl) tetrazole (**16**) | 315 | 550 |
| 1H-5-(4-methoxyphenyl) tetrazole (**17**) | 320 | 500 |
| 4-(1H-tetrazol-5-yl) benzamide (**18**) | 380 | 330 |
| 4-(1H-tetrazol-5-yl) phenol (**19**) | 320 | 400 |
| 1H-5-(4-bromo-2-pyridyl)-tetrazole (**20**) | 350 | 400 |
| 1H-4-allylphenyl-tetrazole (**21**) | 325 | 430 |
| 2-(1H-tetrazol-5-yl) quinolone (**22**) | 335 | 360 |
| 1-(1H-tetrazol-5-yl) isoquinoline (**23**) | 390 | 455 |
| 1-(1H-tetrazol-5-yl) naphthalene (**24**) | 335 | 380 |
| 2-(1H-tetrazol-5-yl) pyrimidine (**25**) | 360 | 370 |
| 2-(1H-tetrazol-5-yl) phenol (**26**) | 335 | 350 |

This stacking only takes place when aggregation of the tetrazole molecules occurs and planar conformations align. In solution at $10^{-6}$ M, the molecules are completely separated by solvent and thus the aggregated emission is not observed. In each the tetrazole molecule is surrounded by solvent molecules, thus not allowing for aggregation or stacking of the pi systems, which would result in the extra emission band. Whereas, in the solid form, the tetrazole and phenyl rings are now locked into place, thus allowing for stacking of the tetrazole and phenyl rings' pi systems and subsequent emission when excited. The interaction responsible for the emission can be attributed to the pi stacking. All remaining emission-excitation profiles of the tetrazole-containing molecules can be found in ***Appendix 3***, the relevance for characterising each tetrazole *via* photophysical investigation, is discussed in ***Chapter 6***.

## 3.5 Conclusion

A series of tetrazole compounds have been synthesised and characterised structurally and photophysically. All characterisation and analyses provide confidence in confirming the presence of each identifiable tetrazole (in the series) in the presence of COM crystals. Raman spectroscopy studies have provided insight into the likely signals present when a tetrazole is irradiated, as well as the photophysical investigations shedding light on the emission, excitation and absorption profiles of each tetrazole. Each technique is crucial for the discussion of results in ***Chapters 4*** through ***7***, which examine structure activity relationships, nucleation, dissolution, crystal growth and mechanisms of interaction between the tetrazole series synthesised and COM crystals.

## 3.6 Experimental

### 3.6.1 General procedures

All reagents were purchased from chemical suppliers and used as received without further purification. Nuclear Magnetic Resonance (NMR) spectra were recorded using a Bruker Avance 400 spectrometer (400.1 MHz for $^{1}H$; 100 MHz for $^{13}C$) at room temperature. The data were acquired and processed by the Bruker TopSpin 3.1 software. $^{1}H$ and $^{13}C$ chemical shifts were referenced to residual solvent signals. The assignment of peaks for the tetrazole compounds are outlined in ***Scheme 3.3***.

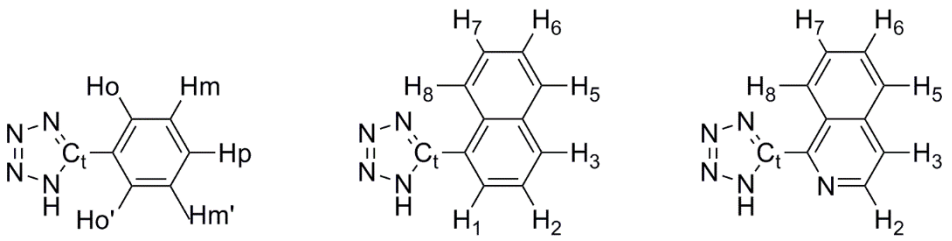


***Scheme 3.3***: NMR referencing layout

$^{1}H$ NMR characterisation was carried out on all tetrazole compounds synthesised and the spectra matched their target structures. For the majority of the compounds synthesised, a phenyl is present, however, two compounds (**23, 24**) had naphthalene and isoquinoline –R groups, respectively. See referencing in ***Scheme 3.3***. In addition to these, many compounds have nitrogen atoms replacing carbon in the phenyl group (making pyridine, pyrimidine and pyrazine backbones), however, the referencing scheme in such cases remains the same for proton NMR. Infrared spectra (IR) were recorded on solid-state samples using an attenuated total reflectance (ATR) Perkin Elmer Spectrum 100 FT-IR with a diamond stage. IR spectra were recorded from 4000 to 650 $cm^{-1}$, the intensities of the IR bands were reported as strong (s), medium (m) or weak (w), with broad (br) bands also specified. Melting points were determined using a BI Barnsted Electrothermal 9100 apparatus and are uncorrected.

### 3.6.2 Photophysical measurements

Absorption spectra were recorded at room temperature using a Perkin Elmer Lambda 35 UV/Vis spectrometer. Uncorrected steady state emission and excitation spectra were collected using an Edinburgh FLSP980-S2S2-stm spectrometer equipped with a 450 W Xenon arc lamp and Peltier cooled Hamamatsu R928P photomultiplier tube (spectral range 200 - 870 nm). Emission and excitation spectra were corrected for source intensity (lamp and grating) and emission spectroscopic response (detector and grating) by a calibration curve supplied with the instrument. For solution measurements, each species was made to ~$10^{-6}$ M.

### 3.6.3 Synthesis

#### 3.6.3.1 General methodology for the synthesis of tetrazole molecules

The synthesis of 1H-5-aryltetrazoles was adapted from a previously reported procedure by Koguro *et al.*[174] Unless otherwise stated, the following conditions were used. Triethylamine (1.2 eq) was added to toluene (~50 mL) and the solution was cooled to 0°C. 32% Hydrochloric acid (1.2 eq) was added to the reaction and the flask immediately stoppered. After ~10 minutes, the corresponding nitrile (1.0 eq) and sodium azide (1.2 eq) were added to the mixture and heated at reflux for 48 hours. The mixture was allowed to cool to room temperature. Water (~20 mL) was added and the reaction mixture stirred vigorously. The aqueous phase was separated and acidified with 32% hydrochloric acid (*ca.* 2 mL). Acidification of the aqueous layer produced a colourless solid, which was filtered, washed with water and air dried to yield the corresponding tetrazole.

**Methyl 4-(1H-tetrazol-5-yl) benzoate** (**Tzmeb**H)

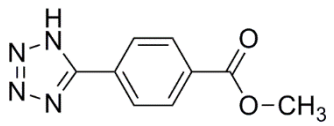


1

Yield of **1**: 1.368 g, 92%. M.p. 217-219 °C (dec.) (literature value 225.7°C).[199] ATR-IR : ν = 3502 (s), 3317 (s), 3229 (m), 3020 (w), 2912 (w), 2835 (w), 2763 (w), 2714 (w), 2632 (s), 2499 (m), 1710 (s), 1579 (m), 1569 (m), 1503 (w), 1470 (w), 1441 (m), 1427 (s), 1353 (w), 1310 (m), 1281 (s), 1250 (w), 1191 (w), 1180 (w), 1151 (w), 1111 (s), 1068 (w), 1036 (w), 1009 (w), 998 (w), 954 (w), 886 (w), 860 (w), 832 (w), 778 (w), 732 (m), 708 (w), 689 $cm^{-1}$ (w). Raman: ν = 3098 (6), 1704 (40), 1617 (100), 1444 (20), 1412 (19), 1314 (8), 1252 (10), 1178 (9), 999 (15), 833 (18), 636 (6), 128 (10), 97 $cm^{-1}$ (21). $^1$H NMR (δ, ppm, DMSO-$d_6$): 8.21 (2H, d, J = 8.7 Hz, $CN_4$-$C_6H_4$-$COOCH_3$ $H_{ortho}$), 8.16 (2H, d, J = 8.7 Hz, $CN_4$-$C_6H_4$-$COOCH_3$ $H_{meta}$), 3.90 (3H, s, $CN_4$-$C_6H_4$-$COOCH_3$). $^{13}$C NMR (δ, ppm, DMSO-$d_6$): 165.3 (ester C=O), 131.4, 129.9, 127.1, 52.2. The $C_t$ carbon was not visible.

**4-(1H-tetrazol-5-yl) acetylbenzene** (**Tzacb**H)

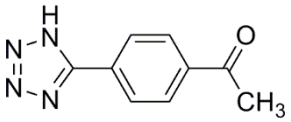


2

Yield of **2**: 1.878 g, 73%. M.p. 189-191°C (dec.) (literature value 173-175°C).[182] ATR-IR: ν = 3402 (s), 3326 (s), 3232 (s), 3098 (w), 3025 (w), 2926 (w), 2836 (w), 2697 (w), 2622 (w), 2562 (w), 2497 (w), 1851 (w), 1676 (s), 1618 (w), 1580 (m), 1440 (w), 1421 (w), 1364 (m), 1311 (w), 1268 (s), 1242 (w), 1193 (w), 1155 (w), 1120 (w), 1097 (w), 1063 (w), 1010 (w), 992 (w), 961 (w), 841 (m),761 (w), 752 (w), 722 (w), 704 $cm^{-1}$ (w). Raman: ν = 3090 (3), 1677 (22), 1622 (100), 1446 (9), 1424 (5), 1250 (3), 1192 (5), 1079 (3), 996 (5), 765 (5), 101 $cm^{-1}$ (30). $^1$H NMR (δ, ppm, DMSO-$d_6$): 8.19 (2H, d, J = 8.6 Hz, $H_{ortho}$), 8.15 (2H, d, J = 8.7 Hz, $CN_4$-$C_6H_4$-$COCH_3$ $H_{meta}$), 2.64 (3H, s, $CN_4$-$C_6H_4$- $COCH_3$). $^{13}$C NMR (δ, ppm, DMSO-$d_6$): 197.2 (Ketone C=O), 138.2, 128.9, 127.9, 126.9, 26.7. The $C_t$ carbon was not visible.

**1H-5-phenyltetrazole** (**TzPh**H)

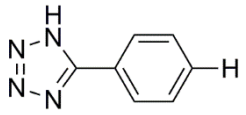

3

Yield of **3**: 1.504 g, 53%. M.p. 213-216°C (dec.) (literature value 214-215 °C).[200] ATR-IR: ν = 3600 (w), 3130 (w), 3055 (w), 2981 (w), 2916 (w), 2833 (w), 2687 (w), 2605 (m), 2480 (w), 1859 (w), 1609 (s), 1563 (s), 1485 (s), 1465 (s), 1410 (s), 1288 (w), 1256 (w), 1163 (s), 1084 (w), 1055 (w), 1034 (w), 1015 (w), 990 (w), 958 (w), 925 (w), 790 (w), 725 (s), 703 (s), 686 $cm^{-1}$ (s). Raman: ν = 3066 (2), 1608 (100), 1563 (14), 1411 (26), 1385 (2), 1258 (3), 997 (8), 784 (3), 309 (2), 145 (11), 95 $cm^{-1}$ (50). $^{1}H$ NMR (δ, ppm, DMSO-$d_6$): 8.25 (1H, s, $CN_4$-$C_6H_5$ $H_{para}$), 8.21 (2H, d, J = 8.0 Hz, $CN_4$-$C_6H_5$ $H_{meta}$), 8.05 (2H, d, J = 7.6 Hz, $CN_4$-$C_6H_5$ $H_{ortho}$). $^{13}C$ NMR (δ, ppm, DMSO-$d_6$): 155.5 (**$C_t$**), 133.5, 128.9, 127.9, 126.8.

**4-(1H-tetrazol-5-yl) benzaldehyde** (**TzPha**H)

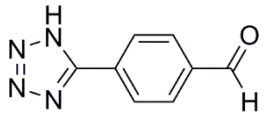

4

Yield of **4**: 0.404 g, 60%. M.p. 179-180 °C (dec.) (literature value 183-185 °C).[201]. ATR-IR: ν = 3402 (s), 3272 (s), 3080 (w), 3018 (w), 2926 (w), 2865 (w), 2815 (w), 2751 (w), 2675 (w), 2611 (w), 2563 (w), 2506 (w), 2051 (w), 1940 (w), 1858 (w), 1743.93 (w), 1687 (m), 1667 (s), 1617 (w), 1580 (s), 1571 (m), 1504 (w), 1445 (w), 1420 (w), 1404 (w), 1374 (w), 1357 (w), 1305 (w), 1289 (w), 1238 (w), 1213 (s), 1167 (w), 1147 (w), 1123 (w), 1088 (w), 1015 (w), 992 (w), 966 (w), 933 (w), 841 (s), 833 (s), 743 (w), 699 (w), 720 $cm^{-1}$ (w). Raman: ν = 3085 (5), 1673 (6), 1620 (100), 1576 (3), 1448 (8), 1424 (5), 1409 (4), 1242 (5), 1171 (20), 1019 (3), 999 (7), 847 (3), 636 (3), 135 (5), 98 $cm^{-1}$ (27). $^{1}H$ NMR (δ, ppm, DMSO-$d_6$): 10.09 (1H, s, $CN_4$-$C_6H_4$-C*H*O), 8.25 (2H, d, J = 8.4 Hz, $CN_4$-$C_6H_4$-CHO $H_{meta}$), 8.11 (2H, d, J = 8.4 Hz, $CN_4$-$C_6H_4$-CHO $H_{ortho}$). $^{13}C$ NMR (δ, ppm, DMSO-$d_6$): 192.7 (C=O), 155.5 (**$C_t$**), 137.6, 130.4, 128.6, 127.6.

**4-(1H-tetrazol-5-yl) benzonitrile** (**TzPhCN**H)

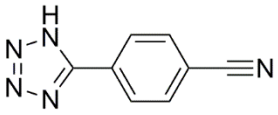

5

The pure form of **5** was not formed, a small percentage of 5% of the bis-tetrazole species (Tetrazole **10** in this study) was also present, see

Yield of **5**: 1.687 g, 62%. M.p. 200-202 °C (dec.) (literature value 258-260 °C).[201] ATR-IR: ν = 3360 (s), 3094 (s), 3010 (m), 2925 (w), 2855 (m), 2557 (w), 2240(s), 2231 (s), 1937 (w), 1643 (m), 1619 (w), 1576 (s), 1563 (s), 1498 (s), 1436 (s), 1370 (m), 1309 (w), 1280 (m), 1254 (w), 1244 (w), 1204 (w), 1151 (w), 1114 (m), 1058 (m), 1017 (w), 990 (s), 846 (s), 750 (s), 733 (w), 702 $cm^{-1}$ (w). Raman: ν = 3086 (3), 2242 (39), 1621 (100), 1440 (3), 1418 (4), 1259 (3), 1188 (24), 1000 (5), 788 (2), 306 (2), 100 $cm^{-1}$ (52). $^{1}H$ NMR (δ, ppm, DMSO-$d_6$): 8.30 (4H, s, $CN_4$-$C_6H_4$-$CN_4$ *H)* (bis-tetrazole impurity)*,* 8.22 (2H, d, J = 8.8 Hz, $CN_4$-$C_6H_4$-CN $H_{meta}$), 8.08 (2H, d, J = 8.4 Hz, $CN_4$-$C_6H_4$-CN $H_{ortho}$). $^{13}C$ NMR (δ, ppm, DMSO-$d_6$): 155.3 (**$C_t$**), 133.3 (bis-tetrazole impurity), 128.6, 127.9, 127.6, 126.6, 118.2 (C≡N), 113.4.

**4-(1H-tetrazol-5-yl) benzoic acid** (**TzBa**$H_2$)

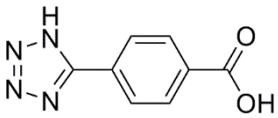

6

**1** (0.735 g, 3.6 mmol) was added to sodium hydroxide solution (0.40 g, 0.01 mol) and magnetically stirred overnight at room temperature. The methanol formed was rotary evaporated off to leave a colourless solid. This solid was acidified with concentrated hydrochloric acid (*ca.* 3 mL) to afford a colourless precipitate. The solid formed was filtered, washed with water and air dried to afford **6**.

Yield of **6**: 0.652 g, 95%. M.p 250 °C (dec.) (literature value 248-250 °C).[202] ATR-IR: ν = 3480 (s), 3355 (m), 2557 (s), 1815 (w), 1690 (s), 1584 (s), 1570 (s), 1437 (s), 1426 (s), 1300 (s), 1319 (s), 1285 (s), 1240 (m), 1091 (m), 993 (m), 929

(m), 862 (s), 732 $cm^{-1}$ (s). Raman: ν = 3081 (11), 1619 (100), 1436 (14), 1421 (10), 1241 (4), 1181 (6), 1135 (4), 1091 (6), 1016 (4), 994 (11), 809 (10), 633 (18), 144 (7), 94 $cm^{-1}$ (63). $^{1}H$ NMR (δ, ppm, DMSO-$d_6$): 8.17 (2H, d, J = 8.4 Hz, $CN_4$-$C_6H_4$-COOH $H_{meta}$), 8.12 (2H, d, J = 8.4 Hz, $CN_4$-$C_6H_4$-COOH $H_{ortho}$). $^{13}C$ NMR (δ, ppm, DMSO-$d_6$): 166.7 (C=O), 155.8 (**$C_t$**), 132.6, 130.2, 128.9, 127.1.

**5-(2-acetyloxyphenyl) tetrazole** (**TzAcoPh**H)

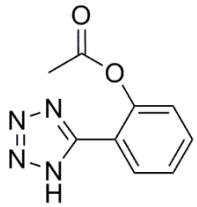

7

Two reactions were required to form 5-(2-acetlyoxyphenyl) tetrazole. First the formation of 2-(1H-terazol-5-yl) phenol from 2-cyanophenol *via* 1,3-dipolar cycloaddition.[174,181,203] Once obtained, **26** (0.5024 g, 3.09 mmol) was added with pyridine (0.752 mL, 9.30 mM) to acetic anhydride (*ca.* 5 mL) with constant stirring at 80 °C for 1 hour. The mixture was allowed to cool before addition of ethanol added to decompose the excess anhydride. Rotary evaporation followed by recrystallisation from ethanol yielded **7**.

Yield of **7**: 0.273 g, 46%. M.p 138-139 °C (literature value 137-138 °C (dec.)).[204] ATR-IR: ν = 2985-2719 (broad), 1757 (s), 1619 (m), 1486 (m), 1370 (m), 1190 (s), 911 $cm^{-1}$ (m). Raman: ν = 2945 (13), 1618 (100), 1550 (35), 1338 (11), 1015 (18), 556 (36), 399 (11), 325 (10), 129 $cm^{-1}$ (90). $^{1}H$ NMR (δ, ppm, DMSO-$d_6$): 7.99 (1H, d, J = 7.80 Hz, $CN_4$-$C_6H_4$-$OCOCH_3$ $H_{ortho}$), 7.65 (1H, t, J = 7.8 Hz, $CN_4$-$C_6H_4$-$OCOCH_3$ $H_{para}$), 7.50 (1H, t, J = 7.6 Hz, $CN_4$-$C_6H_4$-$OCOCH_3$ $H_{meta}$), 7.38 (1H, t, J = 8.2 Hz, $CN_4$-$C_6H_4$-$OCOCH_3$ $H_{meta'}$), 2.30 (3H, s, $CN_4$-$C_6H_4$-$OCOCH_3$) . $^{13}C$ NMR (δ, ppm, DMSO-$d_6$): 167.6 (acetyl C=O), 148.5 (Phenyl C-O), 132.7, 130.1, 127.1, 124.6, 118.6, 21.4 (Acetyl $CH_3$). The $C_t$ carbon was not visible.

**1,2-bis (1H-tetrazol-5-yl) benzene** (***o*TzTz**$H_2$)

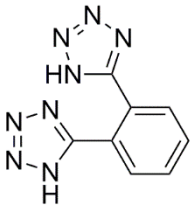

8

Tetrazole **8** was received in-house from Chiara Caporale and used without further purification.

**1,3-bis (1H-tetrazol-5-yl) benzene** (***m*TzTz**$H_2$)

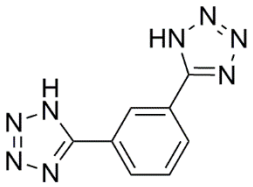

9

The synthesis of **9** employed 2.4 equivalents of sodium azide, triethyl amine and hydrochloric acid per equivalent of isophthalonitrile. The pure form of **9** was not isolated, after attempts to purify, the mono-tetrazole compound, 3-(1H-tetrazol-5-yl) benzonitrile (<18%) was present in the NMR (singlet at 8.42, doublet at 8.34, doublet at 8.06 and a triplet at 7.84 ppm) but the compound was used in crystal growth experiments regardless.

Yield of **9**: 2.15 g, 64%. M.p. 240-243 °C (dec.) (literature value 268-270 °C (dec.)).[205] ATR-IR: ν = 3505-3360 (br), 2780-2500 (br), 2250 (w), 1621 (w), 1567 (s), 1463 (m), 1247 (m), 1093 (s), 1030 (s), 914 (s), 802 (s), 731 (s), 679 $cm^{-1}$ (s). Raman: ν = 3080 (18), 2236 (60), 1616 (100), 1431 (20), 1257 (22), 1003 (199), 679 (18), 121 $cm^{-1}$ (88). $^1$H NMR (δ, ppm, DMSO-$d_6$): 8.78 (1H, s, $CN_4$-$C_6H_4$-$CN_4$ $H_{ortho}$), 8.23 (2H, dd, J = 7.6, 1.6 Hz, $CN_4$-$C_6H_4$-$CN_4$ $H_{para,\ ortho'}$), 7.82 (1H, t, 7.6 Hz, $CN_4$-$C_6H_4$-$CN_4$ $H_{meta'}$). $^{13}$C NMR (δ, ppm, DMSO-$d_6$): 157.0 (**$C_t$**), 130.4, 128.5, 127.8, 125.2.

**1,4-bis (1H-tetrazol-5-yl) benzene (*p*TzTz**$H_2$)

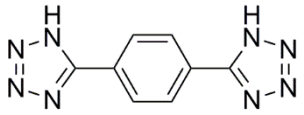

10

The synthesis of **10** employed 2.4 equivalents of sodium azide, triethyl amine and hydrochloric acid per equivalent of terephthalonitrile. Additionally, purification of the tetrazole required dilution of the 32% hydrochloric acid and addition in two fractions. First, slow acidification precipitated **10**, subsequent acidification resulted in precipitation of **5**.

Yield of **10**: 2.966 g, 90%. M.p. 295-297 °C (dec.) (literature value 296-297 °C (dec.)).[200] ATR-IR: ν = 3445-2599 (brs), 1657 (m), 1590 (s), 1507 (s), 1453 (s), 1414 (w), 1086 (s), 993 (s), 899 (s), 845 (s), 733 (s), 209 $cm^{-1}$ (s). Raman: ν = 1623 (100), 1530 (15), 1455 (29), 1410 (4), 1192 (10), 1082 (7), 1020 (8), 953 (33), 102 $cm^{-1}$ (11). $^1$H NMR (δ, ppm, DMSO-$d_6$): 8.14 (4H, s, $CN_4$-$C_6H_4$-$CN_4$ *H*). $^{13}$C NMR (δ, ppm, DMSO-$d_6$): 157.6 (**$C_t$**), 128.7, 126.9, 30.7.

**2,6-bis (1H-tetrazol-5-yl) pyridine** (**TzTzPyr**$H_2$)

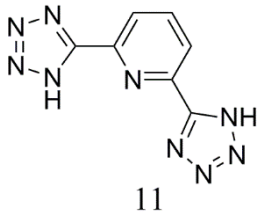

11

2.4 equivalents of triethylamine, 32% hydrochloric acid and sodium azide were used with 1 eq of 2, 6-pyridinecarbonitrile.

Yield of **11**: 1.358 g, 63%. M.p 290-292 °C (dec.) (literature value <260 °C (dec.)).[181] ATR-IR: ν = 3118-2764 (brs), 1606 (w), 1557 (s), 1453 (s), 1182 (s) 1093 (s), 1067 (s), 1015 (s), 1003 (s), 875 (s), 836 (s), 746 $cm^{-1}$ (s). Raman: ν = 3059 (3), 1606 (100), 1575 (36), 1559 (26), 1395 (23), 1359 (13), 1270 (4), 1224 (10), 1071 (3), 1019 (14), 993 (84), 766 (4), 652 (13), 425 (10), 328 (3), 281 (13), 157 (5), 143

(13), 111 $cm^{-1}$ (33). $^1$H NMR (δ, ppm, DMSO-$d_6$): 8.34 (3H, m, $CN_4$-$C_5H_3N$-$CN_4$ $H_{ortho,\ meta,\ para}$).

**1H-5-(2-pyridyl) tetrazole** (***o*TzPyr**H)

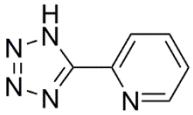

12

Yield of **12**: 0.876 g, 44%. M.p 210-212 °C (dec.) (literature value 210-211°C)).[175,201] ATR-IR: ν = 3092-2534 (brs), 1843 (w), 1602 (s), 1556 (s), 1483 (s), 1449 (s), 1284 (m), 1158 (s), 1067 (s), 1017 (s), 794 (s), 742 $cm^{-1}$ (s). Raman: ν = 1607 (40), 1576 (24), 1006 (24), 401 $cm^{-1}$ (100). $^1$H NMR (δ, ppm, DMSO-$d_6$): 8.79 (1H, dd, J = 4.8 Hz, $C_5H_4N$-$CN_4$ $H_{meta'}$), 8.22 (1H, d, splitting = 7.8 Hz, $C_5H_4N$-$CN_4$ $H_{para}$), 8.07 (1H, app. t, splitting = 7.8 Hz, $C_5H_4N$-$CN_4$ $H_{meta}$), 7.63 (1H, dd, splitting = 7.6 Hz, $C_5H_4N$-$CN_4$ $H_{ortho}$).

**1H-5-(3-pyridyl) tetrazole** (***m*TzPyr**H)

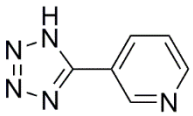

13

Yield of **13**: 1.985 g, 94%. M.p 225-228 °C (literature value 226-228°C).[201] ATR-IR: ν = 3061-2606 (brs), 1608 (s), 1525 (s), 1471(s), 1333 (m), 1072 (s), 1000 (s), 823 (s), 677 $cm^{-1}$ (s). Raman: ν = 3084 (19), 2882 (22), 1639 (90), 1582 (92), 1500 (47), 1463 (22), 1407 (27), 1144 (24), 1043 (70), 1019 (53), 713 (19), 468 (43), 135 (78), 103 $cm^{-1}$ (100). $^1$H NMR (δ, ppm, DMSO-$d_6$): 9.48 (1H, s, $CN_4$-$C_5H_4N$ $H_{ortho}$, 8.94 (2H, m, $CN_4$-$C_5H_4N$ $H_{ortho,\ meta'}$), 7.99 (1H, m, $CN_4$-$C_5H_4N$ $H_{para}$).

**1H-5-(4-pyridyl) tetrazole** (***p*TzPyr**H)

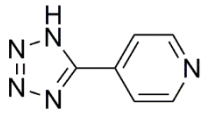

14

Yield of **14**: 0.482 g, 18%. M.p 268-270 °C (dec.) (literature value 255-258°C (dec.)).[201] ATR-IR: ν = 3074-2497 (brm), 1639 (m), 1619 (m), 1475 (s), 1397 (s), 1172 (s), 1072 (s), 1036 (s), 851 (m), 832 (m), 807 (m), 698 $cm^{-1}$ (m). Raman: ν = 1635 (82), 1535 (59), 1445 (100), 1204 (7), 1050 (57), 1023 (54), 131 $cm^{-1}$ (6). $^1H$ NMR (δ, ppm, DMSO-$d_6$): 8.82 (2H, m, $CN_4$-$C_5H_4N$ $H_{ortho,\ ortho'}$), 8.02 (2H, m, $CN_4$-$C_5H_4N$ $H_{meta,\ meta'}$).

**1H-5-(2-pyrazine) tetrazole** (**TzPyz**H)

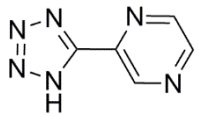

15

Tetrazole **15** was received in-house from Chiara Caporale and used without further purification.

**1H-5-(4-bromophenyl) tetrazole** (**TzBrPh**H)

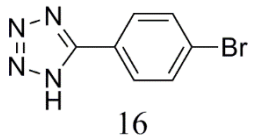

16

Tetrazole **16** was received in-house from Phillip Wright and used without further purification.

**1H-5-(4-methoxyphenyl) tetrazole** (**TzmeoxPh**H)

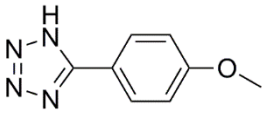

17

First, 4-hydroxybenzonitrile was converted to the 4-methoxybenzonitrile by the addition of methyl iodide (2.10 g, 0.0148 mol), 4-hydroxybenzonitrile (0.88 g, 7.30 mmol) with potassium carbonate (2.8 g, 0.02 mol) in acetone (30 mL) stirring at room temperature for 24 hours a colourless precipitate formed. Extraction of product with ethyl acetate (3x 20mL) and subsequent rotary evaporation yielded 4-methoxybenzonitrile. The product was used without further purification in the reaction with 1.2 eq of hydrochloric acid, triethylamine and sodium azide in toluene to form **17**.

Yield of **17**: 0.828 g, 55%. M.p 229-231 °C (dec.) (literature value 231-232°C (dec.)).[175] ATR-IR: ν = 3076-2650 (brs), 1615 (s), 1586 (m), 1506 (s), 1499 (s), 1406 (s), 1263 (s), 1183 (s), 1035 (s), 843 (s), 749 (s), 695 $cm^{-1}$ (s). Raman: ν = 1615 (100), 1574 (21), 1415 (89), 1191 (20), 1000 (12), 104 $cm^{-1}$ (14). $^{1}H$ NMR (δ, ppm, DMSO-$d_6$): 7.78 (2H, m, $CN_4$-$C_6H_4$-$OCH_3$ $H_{ortho,\ ortho'}$), 7.10 (2H, m, $CN_4$-$C_6H_4$-$OCH_3$ $H_{meta,\ meta'}$), 3.83 (3H, s, $CN_4$-$C_6H_4$-$OCH_3$). $^{13}C$ NMR (δ, ppm, DMSO-$d_6$): 161.9, 155.2 (**$C_t$**), 129.1, 116.7, 115.3, 55.9 ($CH_3$).

**4-(1H-tetrazol-5-yl) benzamide** (**TzPham**H)

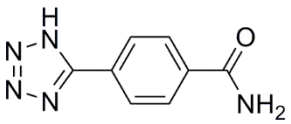

18

After attempts to purify the pure form of the product was not achieved with a small amount (<10%) of the starting material, 4-cyanobenzamide, was present in the NMR but the compound was used as a crystal growth modifiers without further purification.

Yield of **18**: 1.344 g, 56%. M.p 266-269 °C (dec.) (literature value 267-269 °C).[178,206] ATR-IR: ν = 3685 (S), 3554 (s), 3357 (s), 3159 (s), 2988-2901 (brs), 1656 (s), 1625 (s), 1578 (m), 1403 (s), 1057 (s), 791 $cm^{-1}$ (w). Raman: ν = 3081 (6), 1622 (100), 1441 (12), 1414 (11), 1157 (6), 1002 (9), 792 (9), 138 (9), 115 $cm^{-1}$ (42). $^{1}H$ NMR (δ, ppm, DMSO-$d_6$): 8.16-8.09 (2H, m, $CN_4$-$C_6H_4$-$CONH_2$ $H_{meta}$), 8.09-8.04 (2H, m, $CN_4$-$C_6H_4$-$CONH_2$ $H_{ortho}$), 7.53 (1H, s, $CN_4$-$C_6H_4$-$CONH_2$ $H_{amide}$). $^{13}C$ NMR (δ, ppm, DMSO-$d_6$): 167.5, 155.65 (**$C_t$**), 136.9, 132.8, 128.9, 127.3.

**4-(1H-tetrazol-5-yl) phenol** (**TzPhOH**H)

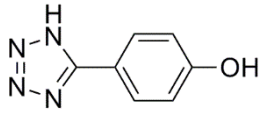


19

Tetrazole **19** was received in-house from Melissa Werrett and used without further purification.

**1H-5-(4-bromo-2-pyridyl)-tetrazole** (**TzBrPyr**H)

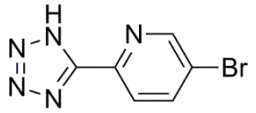


20

Yield of **20**: 0.274 g, 44 %. M.p 268-271 °C (dec.). ATR-IR: ν = 3061 (s), 2804-2457 (brs), 1929 (m), 1595 (w), 1555 (m), 1461 (s), 1421 (s), 1352 (s), 1173 (m), 1006 (s). 834 $cm^{-1}$ (s). Raman: ν = 1593 (100), 1558 (21), 1428 (3), 1390 (9), 1245 (3), 1004 (3), 753 (5), 356 (3), 236 (4), 92 $cm^{-1}$ (41). $^{1}H$ NMR (δ, ppm, DMSO-$d_6$): 8.95 (1H, dd, splitting = 2.3 Hz, $CN_4$-$C_5H_3N$-Br $H_{meta}$), 8.34 (1H, dd, splitting = 8.4 Hz, $CN_4$-$C_5H_3N$-Br $H_{meta'}$), 8.17 (1H, dd, splitting = 8.4 Hz, $CN_4$-$C_5H_3N$-Br $H_{ortho'}$). $^{13}C$ NMR (δ, ppm, DMSO-$d_6$): 151.4, 143.1, 141.3, 124.6, 122.9. The $C_t$ carbon was not visible.

**1H-4-allylphenyl-tetrazole** (**TzAlPh**H)

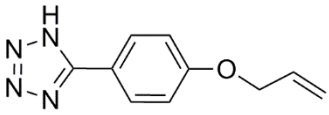

21

Tetrazole **21** was received in-house from Karen MaGee and used without further purification.

**2-(1H-tetrazol-5-yl) quinolone** (**TzQn**H)

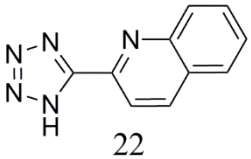

22

Tetrazole **22** was received in-house from Karen MaGee and used without further purification.

**1-(1H-tetrazol-5-yl) isoquinoline** (**TzIsoQn**H)

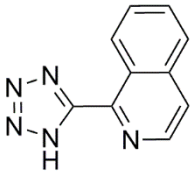

23

Yield of **23**: 0.169 g, 20 %. M.p 249-251 °C (dec.) (literature value 237-239 °C).[207] ATR-IR: ν = 3066-2500 (brs), 2037 (w), 1638 (s), 1373 (s), 1275 (s), 820 (s), 670 $cm^{-1}$ (w). Raman: ν = 3705 (46), 3380 (49), 3342 (52), 3312 (48), 2889 (36), 1918 (38), 1466 (48), 1376 (80), 1028 (95), 842 (41), 547 (51), 382 (37), 114 $cm^{-1}$ (100), $^{1}$H NMR (δ, ppm, DMSO-$d_6$): 9.36 (1H, d, splitting = 8.0 Hz, $CN_4$-$C_9N$*$H_6$* ***$H_2$***), 8.73 (1H, d, splitting = 4.0 Hz, $CN_4$-$C_9N$*$H_6$* ***$H_3$***), 8.18-8.09 (2H, m, $CN_4$-$C_9N$*$H_6$* ***$H_{5,8}$***), 7.93-7.84 (2H, m, $CN_4$-$C_9N$*$H_6$* ***$H_{6,7}$***). $^{13}$C NMR (δ, ppm, DMSO-$d_6$): 142.3, 137.1, 131.7, 129.7, 126.8, 126.2, 124.0. The $C_t$ carbon was not visible.

**5-(1H-napthyl) tetrazole** (**TzNaph**H)

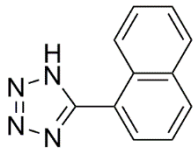

24

Yield of **24**: 0.247 g, 16 %. M.p 198-200 °C (dec.) (literature value 216-218 °C (dec.)).[177,185,186] ATR-IR: ν = 3048 (s), 3200-2400 (brs), 1567 (m), 1261 (m), 1052 (s), 805 (s), 772 $cm^{-1}$ (s). Raman: ν = 2441 (100), 1776 (25), 1533 (22), 1468 (19), 588 (15), 366 (36), 100 $cm^{-1}$ (17). $^{1}H$ NMR (δ, ppm, DMSO-$d_6$): 8.55 (1H, m, $CN_4$-$C_{10}H_7$ $H_{\mathbf{1}}$), 8.19 (1H, dt, splitting= 8.0 Hz, $CN_4$-$C_{10}H_7$ $H_{\mathbf{2}}$), 8.09 (1H, m, $CN_4$-$C_{10}H_7$ $H_{\mathbf{8}}$), 7.99 (1H, dd, splitting = 8.0 Hz, $CN_4$-$C_{10}H_7$ $H_{\mathbf{3}}$), 7.80-7.52 (3H, m, $CN_4$-$C_{10}H_7$ $H_{\mathbf{5,6,7}}$). $^{13}C$ NMR (δ, ppm, DMSO-$d_6$): 133.8, 131.8, 130.4, 129.1, 128.8, 128.1, 127.2, 125.8, 125.6. The $C_t$ carbon was not visible.

**2-(1H-tetrazol-5-yl) pyrimidine** (**TzPyrm**H)

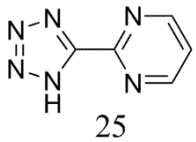

25

Yield of **25**: 0.515 g, 24 %. M.p 245-247 °C (dec.) (literature value 229-230 °C (dec.)).[163] ATR-IR: ν = 3550-3200 (brs), 3087 (m), 2987 (brs), 1644 (s), 1575 (s), 1394 (s), 1165 (s), 1044 (s), 826 (s), 737 $cm^{-1}$ (s). Raman: ν = 3087 (3), 1580 (86), 1522 (100), 1164 (4), 1072 (40), 1003 (47), 286 (3), 163 (4), 96 $cm^{-1}$ (28). $^{1}H$ NMR (δ, ppm, DMSO-$d_6$): 8.81 (2H, d, splitting = 4.0 Hz, $CN_4$-$C_4N_2H_3$ $H_{meta,\ meta'}$), 7.40 (1H, t, splitting = 4.0 Hz, $CN_4$-$C_4N_2H_3$ $H_{para}$). $^{13}C$ NMR (δ, ppm, DMSO-$d_6$): 161.2, 159.5, 157.5, 119.5. The $C_t$ carbon was not visible.

**2-(1H-tetrazol-5-yl) phenol** (**TzPhOH**H)

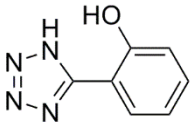

26

Yield of **26**: g, 76 %. M.p 228-230 °C (dec.) (literature value 220-222 °C (dec.)) [174,181,203]. ATR-IR: ν = 3400-2500 (brs), 1615 (s), 1464 (s), 1354 (s), 1299 (s), 746 $cm^{-1}$ (s). Raman: ν = 3078 (13), 1617 (100), 1547 (47), 1358 (16), 1271 (9), 1167 (7), 1004 (26), 837 (26), 673 (18), 130 $cm^{-1}$ (62). $^{1}H$ NMR (δ, ppm, DMSO-$d_6$): 7.99 (1H, dd, splitting = 7.80, 1.70 Hz, $CN_4$-$C_6H_4$-OH $H_{meta}$), 7.40 (1H, ddd, splitting = 8.4, 7.3, 1.7 Hz, $CN_4$-$C_6H_4$-OH $H_{para}$), 7.07 (1H, dd, splitting = 8.3, 1.1 Hz, $CN_4$-$C_6H_4$-OH $H_{ortho'}$), 7.00 (1H, td, splitting = 7.6, 1.1 Hz, $CN_4$-$C_6H_4$-OH $H_{meta'}$).

# 4 Structure Activity Relationships of Tetrazoles and Calcium Oxalate Crystals

## 4.1 Introduction

Tetrazole molecules have previously been used as crystal growth modifiers in barium sulfate and calcium carbonate systems,[170] and only recently as calcium oxalate crystal growth modifiers.[171,172] However, current research on COM inhibition is focussed around carboxylate containing macromolecules[152,153] and small organic compounds, including citric acid,[140,142,143,208–210] hydroxycitrate,[150,211] and amino acids such as glutamic and aspartic acids.[70,135,136,147,212,213] The carboxylate-containing compounds continue to be studied although tetrazole functionalities continue to be employed as carboxylic acid analogues in pharmaceutical chemistry formulations with improved potency for a broad range of purposes including, antifungal, antibacterial, anti-inflammatory and anticancer activities.[164]

The focus of this chapter is to determine the impact on calcium oxalate crystals morphology due to the presence of the tetrazole-containing additive series synthesised, discussed and characterised in ***Chapter 3***. In addition, it is hoped to discover trends across the molecules' functional groups and determine stereochemistry factors that can influence modification, vital for understanding mechanistic interactions. To begin identifying the impacts to morphology and habit of calcium oxalate crystals grown in the presence of the complete series, SEM micrographs were analysed and from the images, morphological changes and quantitative data on the effects of each tetrazole species can be obtained. In general, the morphology of a growing crystal is determined by the relative growth rates of its faces, the faster the growth rate in the direction perpendicular to a particular face, the smaller that face generally appears. Comparatively, the affected face will appear larger than in control crystals and, as a result, the crystals morphology will change. Thus, the faces which grow slowest due to an inhibitory molecules adsorption to a specific face, will determine the final growth morphology and provide evidence

towards developing the structure-activity relationships between the respective tetrazole molecules and their impact on COM crystals.

## 4.2 Control calcium oxalate crystallisation

Calcium oxalate monohydrate (COM) was crystallised by direct mixing (using the method described in ***Section 2.2.1***) to yield a supersaturated solution of calcium oxalate with a concentration of 0.30 mM (giving an approximate supersaturation of 7). The supersaturation, $S$, in low ionic strength solutions can be approximated as $S = C/C_e$, where $C$ is the initial concentration of calcium oxalate in solution and $C_e$ is the equilibrium solubility concentration at 25 °C. The equilibrium solubility concentration for $CaC_2O_4 \cdot H_2O$ at 25 °C was taken as $1.66 \times 10^{-9}$ M.[77]

In the absence of additives, COM precipitated as a mixture of single crystals but predominantly contact and penetration twins (***Figure 4.1***) with the typical elongated hexagonal shape; the common faces observed throughout are the prominent (100) and (010) faces and the smaller (12-1), (021), (1-2-1) and (0-21) faces. In addition to the three aforementioned COM forms in the pure system, aggregated particles were also occasionally present in the supersaturated conditions. While COM is the thermodynamically stable form of calcium oxalate, calcium oxalate dihydrate (COD) and calcium oxalate trihydrate (COT) are meta-stable hydrates and thus are possible to crystallise under different conditions, such as, with the addition of crystal growth modifiers,[214] or changes in pH.[215] However, the hydrate phase COT was never observed in any control experiments, while COD crystals were observed and measured when grown in an artificial urinary medium, discussed later (***Section 4.4***).

Unfortunately as mentioned in **Chapter 2**, Tetrazole **9** consists of 18% of the mono-tetrazole as an impurity, additionally; tetrazole **18** also contains ~10% of the starting material, which was unable to be removed during purification. Therefore any effects observed through this chapter must be observed with care, due to the unknown impact the impurities mentioned above may have on the results of the morphological impact and other analysis to come in ***Chapter 5***.

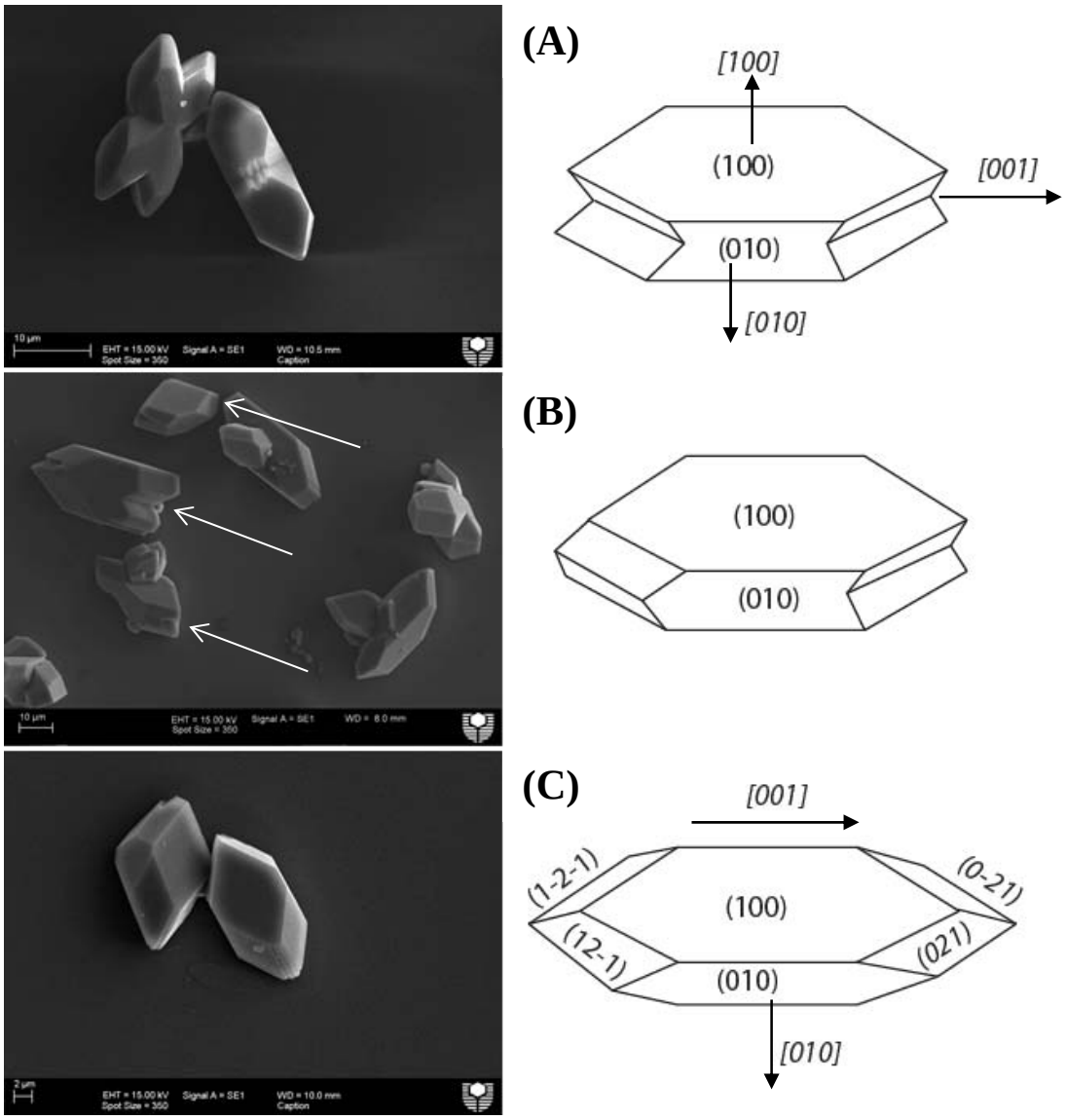


***Figure 4.1***: Schematics of several commonly seen COM crystal types compared to crystals observed by SEM in this study: (A) penetration twins, (B) contact twins (indicated by arrows), (C) single crystals of COM, their respective faces developed and major crystallographic directions are indicated using Tazzoli's notation[74,86].

Several SEM images of control COM crystals were used to gather quantitative data of their average length and width to find the aspect ratios, which will help determine the impact of each tetrazole molecule upon addition into the crystallisation process. The morphologies of the crystals in the presence of the different additives are subsequently compared to the morphology of the averaged control crystals. ***Figure 4.2*** illustrates the nominal size and crystal numbers of

control COM crystals utilising both optical microscopy and SEM. The average size of the control particles was found to be 9.40 ± 1.10 µm.

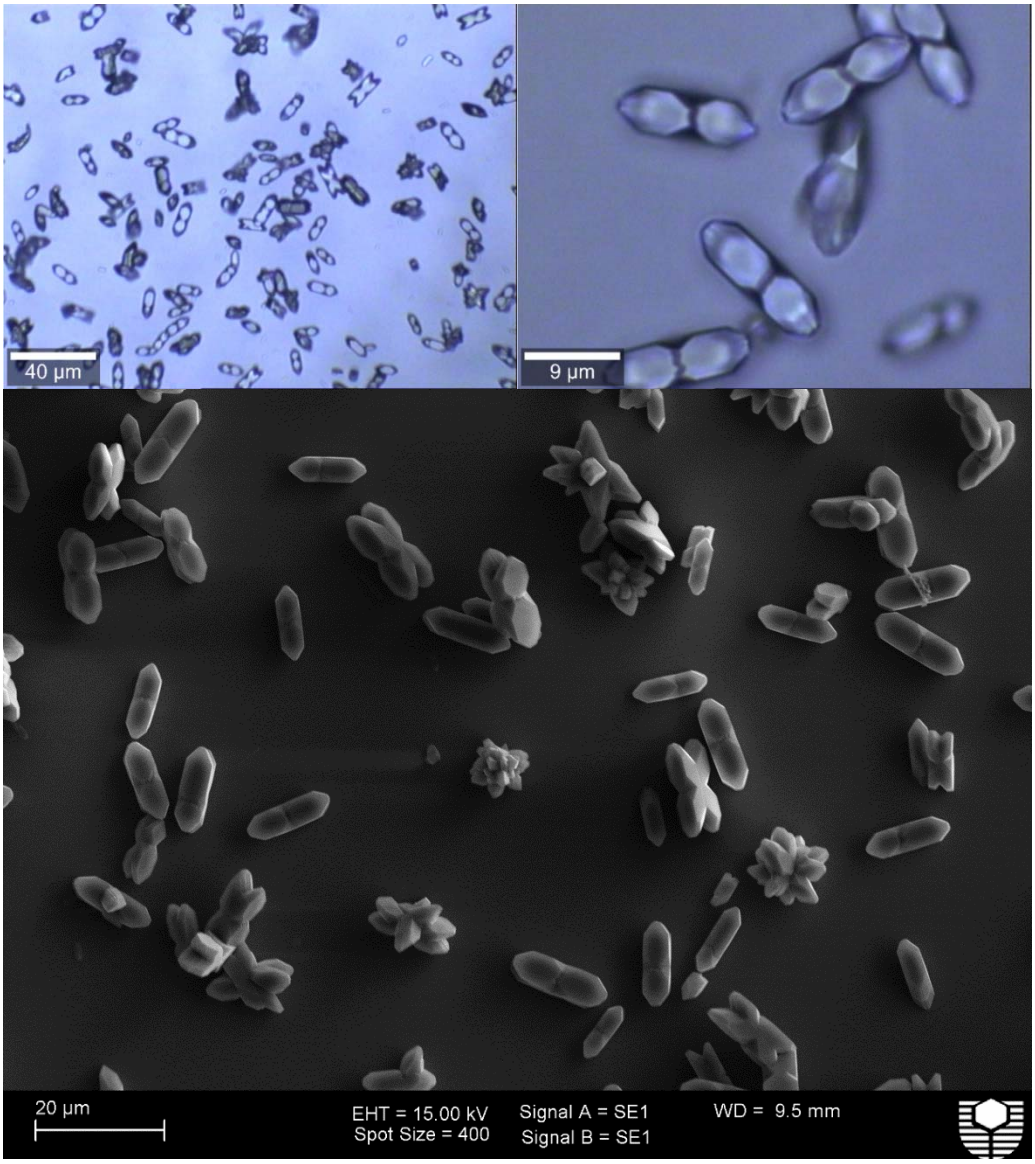


***Figure 4.2***: Optical microscopy at various magnifications (top left at 20x) (top right at 100x) and SEM (bottom) image of COM (0.30 mM) crystals grown without additives.

## 4.3 Calcium oxalate crystal growth modification

The impact of tetrazole additives on calcium oxalate crystallisation can be evaluated by comparing microscopy images for morphological modification. Quantitative data was extracted from the SEM micrographs to determine the

additives' impact on COM crystallisation. The initial structure activity relationships (SAR) are based upon changes in: crystal numbers, aspect ratio and morphological changes compared to the control crystals. ***Chapters 5*** and ***7*** discuss the nucleation, complexation, and crystal growth mechanism of COM in the presence of the difference tetrazole-containing molecules to complete the trends initially observed in this chapter. The quantitative data of the control and all tetrazole modified crystals at 1.0 g/L can be found in ***Table 4.1***, while all concentrations can be found in ***Table A1*** in the ***Appendix***. ***Table 4.1*** will be referenced throughout this chapter. Each Figure in this chapter compares the impact of a group of tetrazole molecules at two distinct concentration levels, 1.0 g/L (found on the left hand side of all Figures) and 0.1 g/L (right side of Figures) on COM crystallisation, the data of which is in turn compared to the control crystallisation of COM in ***Section 4.2***. All concentrations of the additives have been presented in mM for clarity and comparison. In the presence of the tetrazole series, calcium oxalate particles displayed a variety of morphological changes from the control (see ***Figure 4.3*** through ***Figure 4.8***). The following discussions will attempt to analyse the morphological changes experienced by the crystals in the presence of each tetrazole molecule.

Based on morphology (***Figure 4.3a***) the impacts of **1** on COM crystals yielded little changes to the crystals with only a rounding of the apical tips which is immediately lost when the lower concentration of the additive (***Figure 4.3b***) was present during crystallisation. From the quantitative data obtained, the average particle sizes of crystals in the presence of **1** were 7.46 μm and 10.52 μm with aspect ratios of 2.84 and 2.74, respectively, at the two concentrations. Utilising ***Table 4.1*** and comparing the values to the averaged control COM crystals size of 9.40 μm with an aspect ratio of 2.72 it becomes clear that **1** had weak interactions with the crystal surfaces of COM, resulting in the limited impact on the morphology and crystallisation indicated by the relative similarity in crystal size and shape to the control. In contrast, COM crystallised in the presence of the remaining additives in ***Figure 4.3*** (**2**, **4**, and **5**) all had altered morphologies relative to the control. Distinct changes in the habit from the typical 6-sided hexagonal shape (control COM) towards a 4-sided diamond shape increased from additive **2** to **4**, with **5** (4-(1H-tetrazol-5-yl) benzonitrile) having the strongest effect (***Figure 4.3c***, ***Figure 4.3e*** and ***Figure 4.3g***, respectively). The impact of tetrazole molecules **2**, **4** and **5** based upon

***Table 4.1***: Quantitative data determined from SEM images in ***Appendix 4*** - lower magnification micrographs of images presented in ***Chapter 4***: ***Figures 4.3-4.8***.

| Additive | Additive Concentration in mM | Mean Particle Size (μm)[2] | Standard Deviation | Aspect Ratio[1] | Particles Counted |
|---|---|---|---|---|---|
| Avg. Control | - | 9.40 | 1.15 | 2.72 | 150 |
| 1 | 4.90 | 7.46 | 1.83 | 2.84 | 50 |
| 2 | 5.31 | 9.08 | 1.57 | 1.80 | 50 |
| 4 | 5.74 | 20.52 | 4.96 | 1.73 | 40 |
| 5 | 5.84 | 31.73 | 7.94 | 1.70 | 12* |
| 10 | 4.67 | 12.85 | 2.93 | 2.93 | 34 |
| 9 | 4.67 | 21.62 | 1.85 | 3.11 | 50 |
| 8 | 4.67 | 38.53 | 7.78 | 2.66 | 50 |
| 6 | 5.26 | 49.06 | 15.63 | 2.32 | 21 |
| 18 | 5.29 | 18.49 | 3.15 | 3.08 | 50 |
| 16 | 4.44 | 20.80 | 9.94 | 1.89 | 5* |
| 11 | 0.46 | 48.63 | 8.57 | 2.51 | 20 |
| 20 | 4.42 | 66.96 | 16.22 | 2.53 | 23 |
| 7 | 4.90 | 18.29 | 3.72 | 2.04 | 4* |
| 26 | 6.17 | 12.59 | 2.00 | 2.91 | 50 |
| 19 | 6.17 | 22.42 | 4.56 | 2.65 | 50 |
| 21 | 5.31 | 25.38 | 3.44 | 1.35 | 50 |
| 17 | 5.68 | 25.96 | 6.52 | 2.77 | 36 |
| 3 | 6.84 | 21.35 | 2.92 | 2.11 | 50 |
| 23 | 5.10 | 21.47 | 6.49 | 2.01 | 20 |
| 22 | 5.07 | 38.06 | 7.40 | 2.51 | 36 |
| 24 | 5.10 | 43.14 | 9.78 | 2.88 | 29 |
| 12 | 6.80 | 19.03 | 9.63 | 1.74 | 7* |
| 14 | 6.80 | 22.67 | 4.76 | 2.33 | 50 |
| 13 | 6.80 | 27.87 | 9.40 | 2.20 | 37 |
| 15 | 6.75 | 30.90 | 7.29 | 2.41 | 50 |
| 25 | 6.75 | 50.80 | 8.25 | 3.05 | 22 |

1 Aspect ratio = Length (along [001]) / Width (along [010])

2 Particle size was measured along the [001] direction of each particle.

* Conditions that resulted in very few particles being observed, multiple micrographs were utilised to afford more representative particle sizes and aspect ratios.

Tetrazoles are grouped as per their Figures from lowest Mean particle size to largest within each subgroup to aid reader.

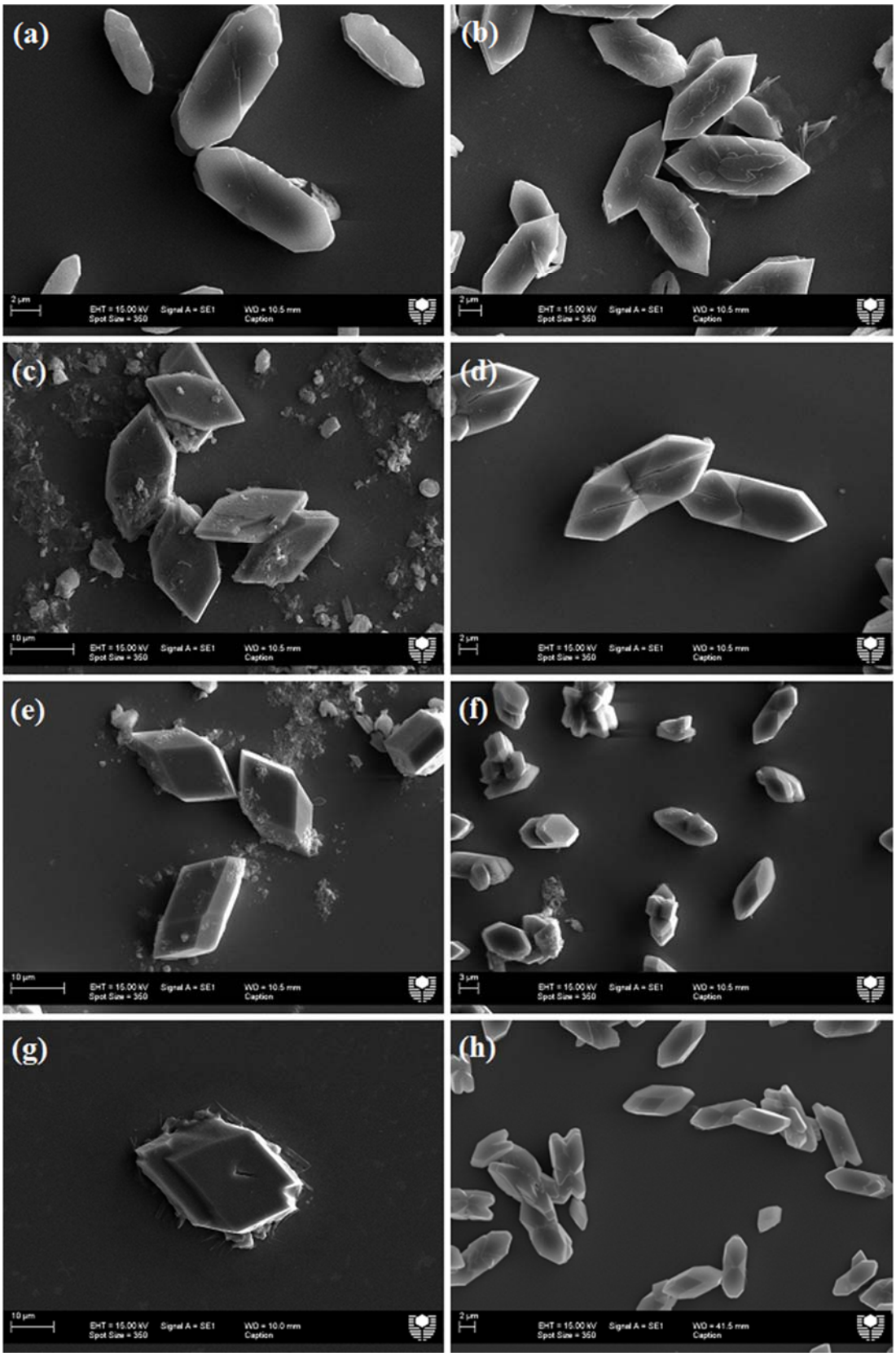


***Figure 4.3***: SEM micrographs of calcium oxalate (0.30 mM) crystal morphology in the presence of additives: (a) **1** at 4.90 mM, (b) **1** at 0.49 mM, (c) **2** at 5.31 mM, (d) **2** at 0.53 mM, (e) **4** at 5.74 mM, (f) **4** at 0.57 mM, (g) **5** at 5.84 mM, (h) **5** at 0.58 mM.

the habit changes indicates that adsorption on the apical tips or (12-1), (1-2-1), (021) and (0-21) faces resulted in the shortening of the crystals in the [001] direction and impedance of the growth of the (010) face as the slowest growing faces control the morphology of the crystals.

Comparing the crystal sizes and aspect ratios (***Table 4.1***) for **4** and **5**, it is apparent that the additives had not only an effect on the morphology, but also they were highly potent in the inhibition of COM crystallisation. Crystal numbers were noticeably reduced in the presence of **4** and **5**, with the average crystal size being increased to 2 and 3 times the control, respectively, thus indicating an impact on the nucleation of COM. Nucleation results in the presence of all tetrazole molecules will be discussed further in ***Chapter 5***. Aspect ratios (A.R.) can also indicate a change in habit of the crystals, with additives **2**, **4** and **5** all presenting A.R. of ~1.7 which are considerably reduced compared to the control average A.R. of 2.7, signifying that a change of habit has taken place in the presence of the aforementioned additives. At the lower concentration (0.1 g/L) the particles' morphologies in the presence of additives **1**, **2**, **4** and **5** all returned to control-like particles, except for **2** which had increased particle length at twice the control but still had a comparable A.R. and **5** which still seemed to affect the number of particles nucleated.

COM grown in the presence of **6**, **8**, **9** and **10** will be discussed from ***Figure 4.4***. Additive **6** (***Figure 4.4a***) showed similar interactions as **5**, indicating that it is a potent COM crystallisation modifier resulting in fewer, larger particles with a mean particle size of ~49 µm, 5 times the control average. The A.R., however, was only slightly reduced indicating the particles still exhibited similar habit as the control particles, but at a much larger size. Nucleation information gathered in ***Chapter 5*** will help further elucidate the impact of **6** on COM. Adsorption of **6** on the (12-1), (1-2-1), (021) and (0-21) faces similarly resulted in many 4 sided particles and particles with reduced prominence of the (010) face. In contrast, additives **8** and **9** had little effect on the habit of the COM crystals (***Figure 4.4c***, ***Figure 4.4 e***), which were very similar to the control crystals - aside from the enlarged crystal size, which was consistently observed across addition of most of the tetrazole series.

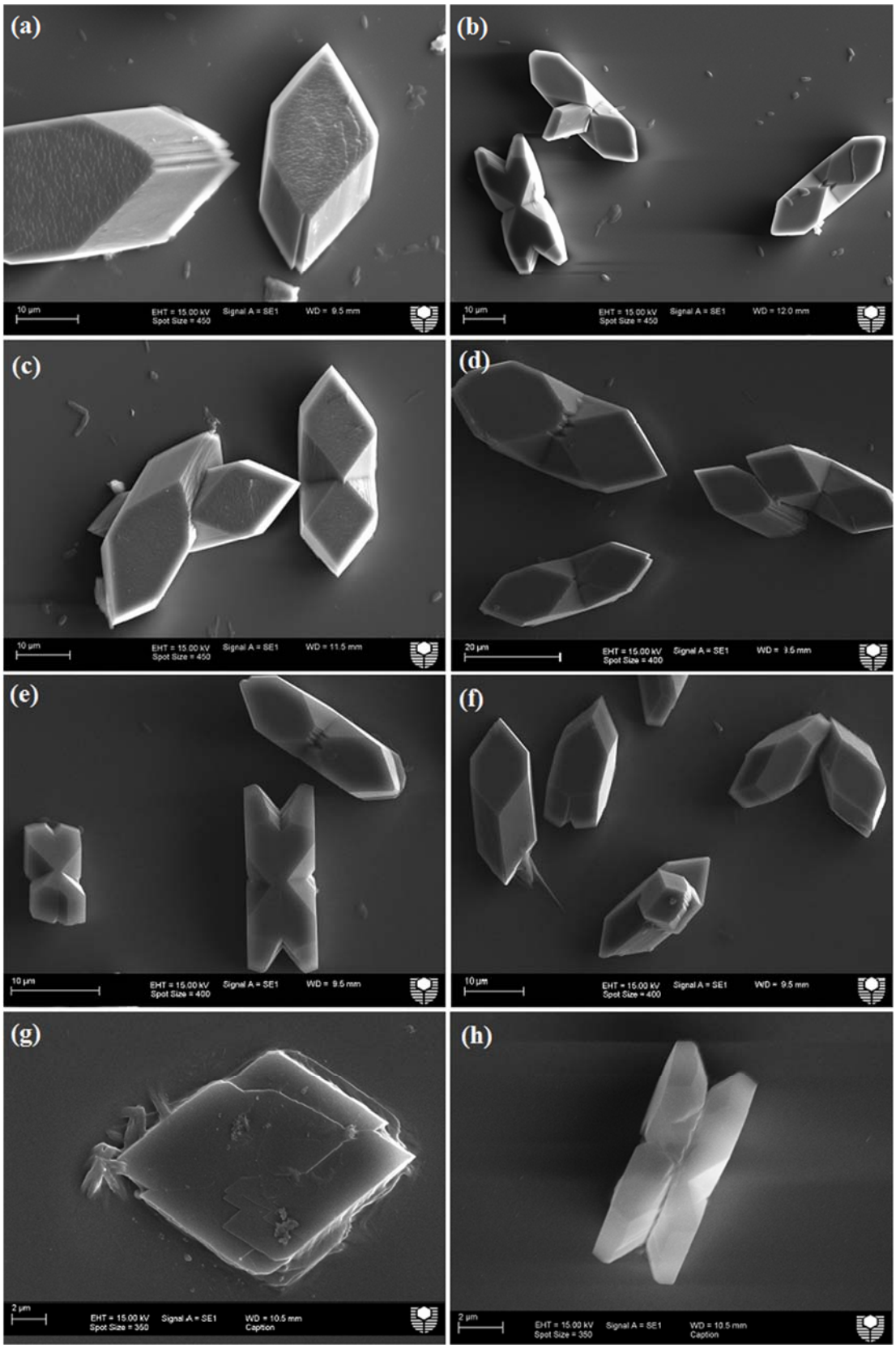


***Figure 4.4***: SEM micrographs of calcium oxalate (0.30 mM) crystal morphology in the presence of additives: (a) **6** at 5.26 mM, (b) **6** at 0.52 mM, (c) **8** at 4.67 mM, (d) **8** at 0.46 mM, (e) **9** at 4.67 mM, (f) **9** at 0.46 mM, (g) **10** at 4.67 mM, (h) **10** at 0.46 mM.

The structure of the bis-tetrazole species was an interesting study as it revealed that the *para* substituted species **10** (1,4-bis (1H-tetrazol-5-yl) benzene) had much greater impact on the crystallisation of COM than the *ortho* (**8**) or *meta* (**9**) species as reflected by ***Figure 4.4g*** and the quantitative data obtained. The morphology of COM grown in the presence of **10** resulted in 4-sided diamond shaped particles as seen previously; however in this case, the thickness of the crystals was also greatly affected. The growth in the [100] direction was significantly underdeveloped, indicating that in addition to the common adsorption of the (12-1), (1-2-1), (021) and (0-21) faces (refer again to ***Figure 4.1***), adsorption of **10** on the (100) face is surmised from the morphology of the crystals. Particles size and A.R. of **10** (***Table 4.1***) despite the change in crystal habit were similar to the control particles, however, fewer crystals were present indicating **10** impacts COM crystallisation strongly.

Unlike all other additives investigated, additive **11** (2,6-bis (1H-tetrazol-5-yl) pyridine) completely inhibited COM crystallisation at 1.0 g/L (4.65 mM), and unfortunately no particles can be shown at that concentration. Addition of **11** at 0.1 g/L (***Figure 4.5a***, ***Figure 4.5b***) demonstrated that even at the lower concentration, the size of the crystals were significantly increased to ~48 µm (5 times control) and crystal numbers reduced. Despite the impact at the higher concentration on the crystallisation of COM, at 0.1 g/L, the morphology of the COM crystals was unchanged. When comparing additive **11** to additive **9**, the only structural difference is the addition of the nitrogen into the aromatic ring (phenyl to pyridyl). Similar to **11**, additive **16** 1H-(5-(4-bromophenyl) tetrazole) considerably inhibited crystallisation of COM (***Figure 4.5c***), at 1.0 g/L with less than 7 crystals found across triplicate experiments. Particle size was increased to twice that of the control with the A.R. of the particles significantly altered to ~1.7. Although, on face value these results are promising, it is impossible to gauge results when very few or no crystals can be analysed, therefore, more data is required and nucleation data to follow in ***Chapter 5*** will help determine the potency of any tetrazole-containing inhibitors, particularly those, like **16** which impacted on the crystal numbers to such a degree.

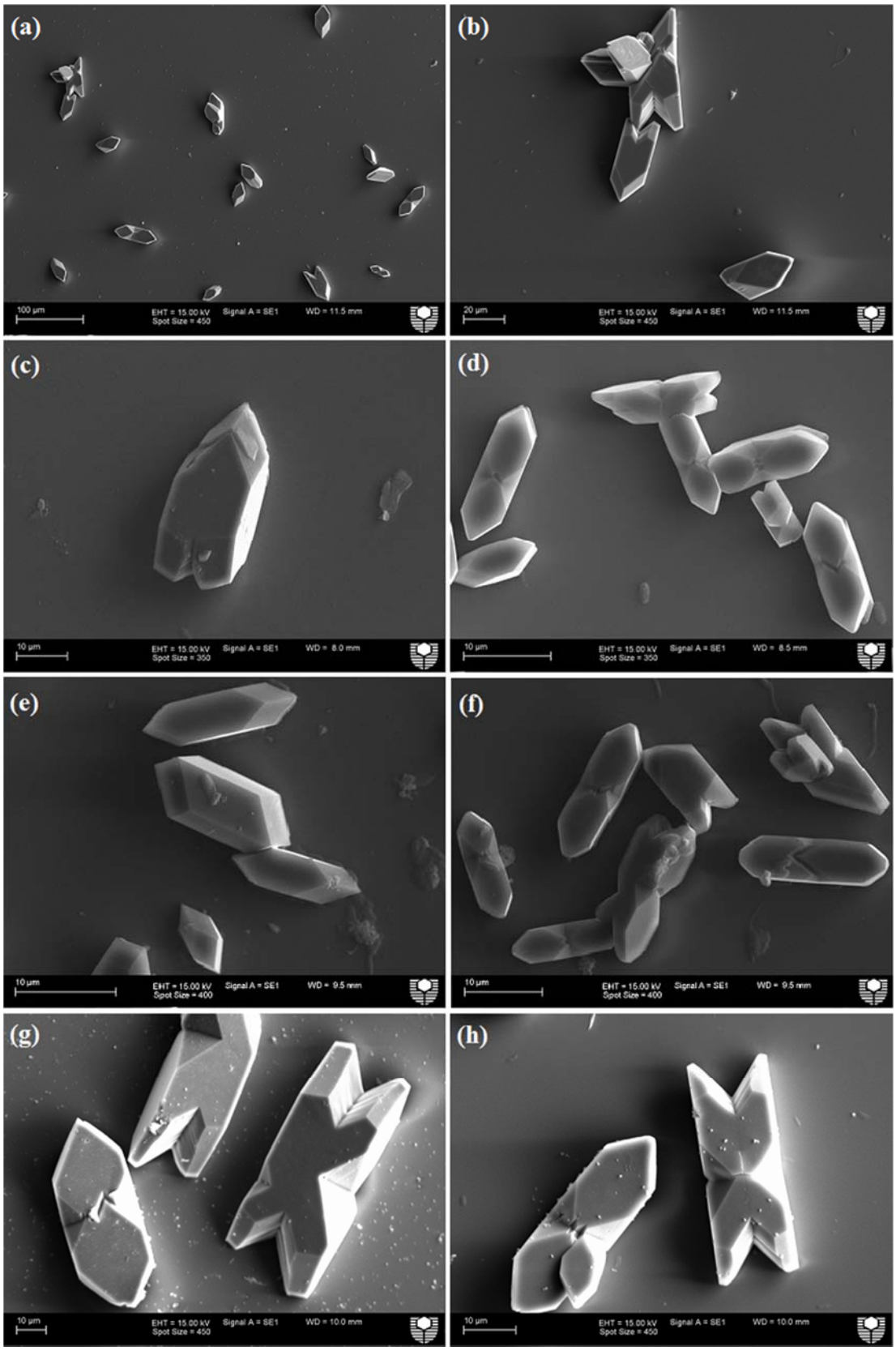


***Figure 4.5***: SEM micrographs of calcium oxalate (0.30 mM) crystal morphology in the presence of additives: (a) **11** at 0.46 mM, (b) **11** at 0.46 mM, (c) **16** at 4.44 mM, (d) **16** at 0.44 mM, (e) **18** at 5.29 mM, (f) **18** at 0.52 mM, (g) **20** at 4.42 mM, (h) **20** at 0.44 mM.

In the presence of additive **18**, crystal size was increased by twice the control average size with a slight increase in the A.R. of the crystals present. Little-to-no morphological changes were observed due to the presence of **18** during crystallisation. Additive **20** influenced COM particles in a similar manner to the majority of additives whereby the particle numbers has been suppressed and their size has been increased. No visible effects on the morphology can otherwise be determined from the micrographs (***Figure 4.5g***, ***Figure 4.5h***). However, with an average particle size of 67 μm, the COM particles grown in the presence of **20** are by far the largest seen in this study, along with the reduced numbers of COM crystals, this is an increasingly familiar trend seen across the tetrazole additives.

The majority of additives in ***Figure 4.6*** had little impact on the morphology of COM. Additive **7** and **17** (***Figure 4.6a, b, c*** *and* ***d***) decreased the number of particles present as indicated by ***Table 4.1***, substantially in the case of **7**, but as expected increased the particle size to ~2-2.5 times the control average size. Similar to additives (**8**, **9** and **10**, COM grown in the presence of **21** resulted in shortened, square or hexagonal particles. Comparing the aspect ratio, crystal sizes and numbers to the control, **21** had the lowest A.R. of any additive at 1.35 (***Table 4.1***) while still increasing the average particle size to 2.5 times the control size but having little impact on the overall nucleation of COM. Additives **19** and **26** had very little overall effect on the morphology and subsequently little effect on the crystallisation. This was indicated by the quantitative data, which suggests, as observed, that the crystals are very similar to the control COM with comparable A.R., and particle sizes in addition to insubstantial reduction of particles numbers based on the micrographs collected.

Investigating what may be considered as somewhat of a reference additive to compare within the tetrazole series itself additive **3**, 1H-5-phenyltetrazole, and additives with extended conjugation of the aromatic portion in tetrazole molecules **22**, **23** and **24** (***Figure 4.7***) may provide important comparisons in determining mechanistic differences across the entire series. All except **3** reduced the number of particles present to an appreciable degree, with all additives increasing the average size of COM crystals to twice the size for **3** and **23** while increases of four times as large compared to control crystal size for **22** and **24**, respectively.

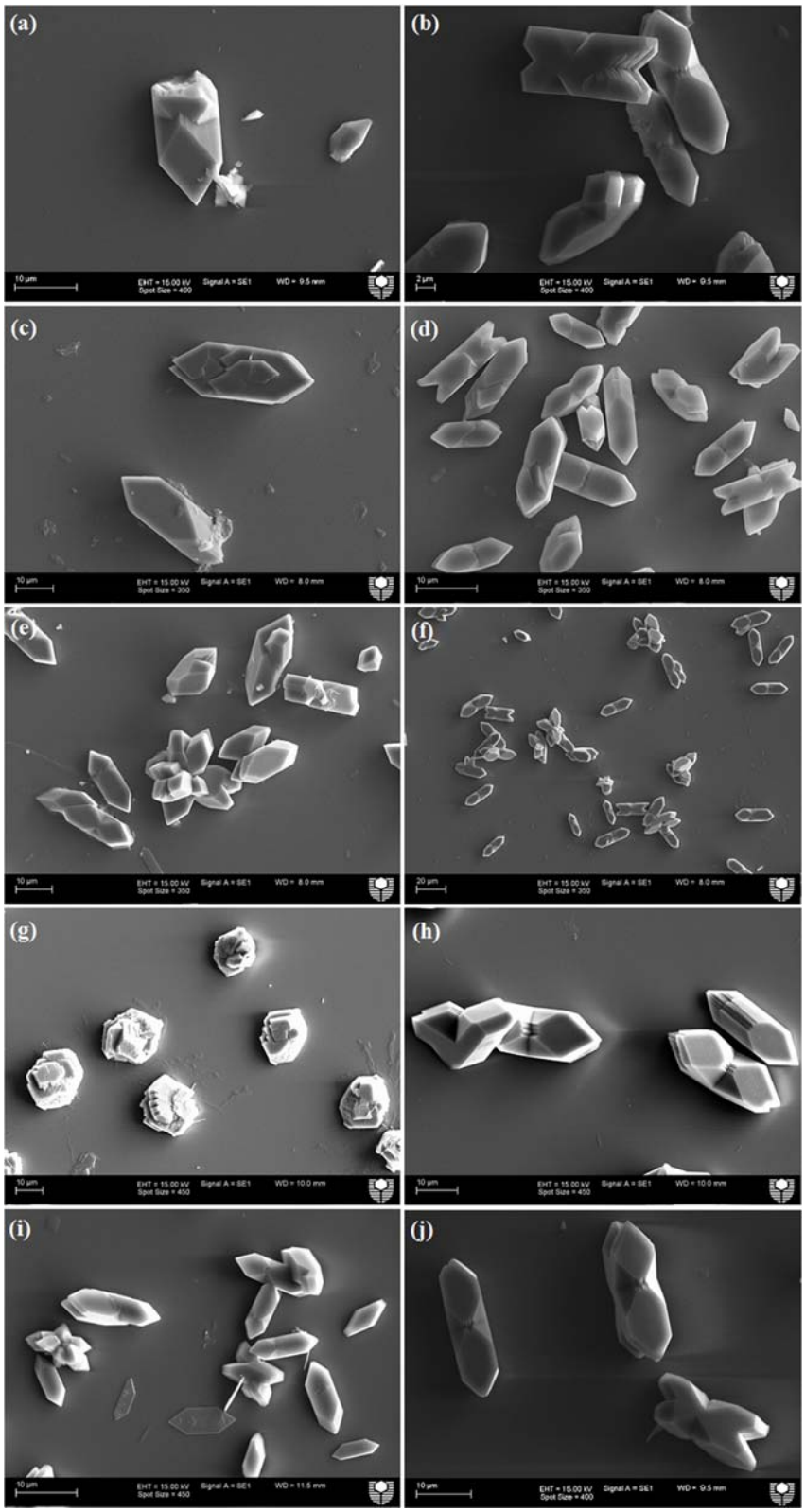


***Figure 4.6***: SEM micrographs of calcium oxalate (0.30 mM) crystal morphology in the presence of additives: (a) **7** at 4.90 mM, (b) **7** at 0.49 mM, (c) **17** at 5.68 mM, (d) **17** at 0.56 mM, (e) **19** at 6.17 mM, (f) **19** at 0.61 mM, (g) **21** at 5.31 mM, (h) **21** at 0.53 mM, (i) **26** at 6.17 mM, (j) **26** at 0.61 mM.

The aspect ratios in general stay relatively similar indicating that adsorption of additives on the common faces is equal among all faces or is not the main inhibiting mechanism. The aspect ratio should otherwise change upon adsorption of the tetrazole species selectively to a face of the crystal. For instance, in the case of additive **23** (1-(1H-tetrazol-5-yl) isoquinoline), the most promising additive featured in ***Figure 4.7***, the particles' aspect ratios were found to be 2.01 compared to the control (2.72) and subsequently as illustrated in ***Figure 4.7e***, the particles are appreciably altered in shape and size with respect to the control. The morphology of these particles is most likely due to **23** adsorbing preferentially to the (12-1), (1-2-1), (021) and (0-21) faces. The additive is thought to be more potent than most tetrazole molecules in the series, as even at the lower concentration crystallisation conditions (***Figure 4.7f***) the COM habit changes are still visible in the SEM micrographs. The majority of the tetrazole molecules' impact thus far is substantially reduced at the lower concentration, to the point where control-like crystals are typically formed at 0.1 g/L of additive. The crystals present in ***Figure 4.7f*** showed significant elongation of the (010) face, which may indicate promotion of growth in the [100] direction. Otherwise, the particles grown in the presence of **23** at 0.1 g/L had comparable quantitative parameters to the control (***Appendix 4***, ***Figure A4b***).

The final group of tetrazoles in the series included the nitrogen containing aromatic ring tetrazoles, additives **12**, **13**, **14**, **15** and **25**, similar to **3**, but with distinct structural changes in their aromatic backbones, these additives prove insightful in differentiating the effects on the morphology of COM crystals observed in ***Figure 4.8***. The most promising result of this subset of tetrazole molecules arose analysing **12**, 1H-5-(2-pyridyl) tetrazole, which had the highest impact on the numbers of particles, with less than 7 COM particles grown across multiple experiments (***Figure 4.8a***). Tetrazole **12** significantly reduced the A.R to 1.74 (Control 2.72), indicating a change of habit evidenced in the micrographs provided. Particle sizes of the crystals were increased as has been the trend across most tetrazoles, to ~19 μm, twice the size of the control COM. All other additives **13**, **14**, **15** and **25** had limited impact on both the morphology and particle numbers, apart from the general increase in crystal size (which could suggest promotion of crystal growth) and not inhibition.

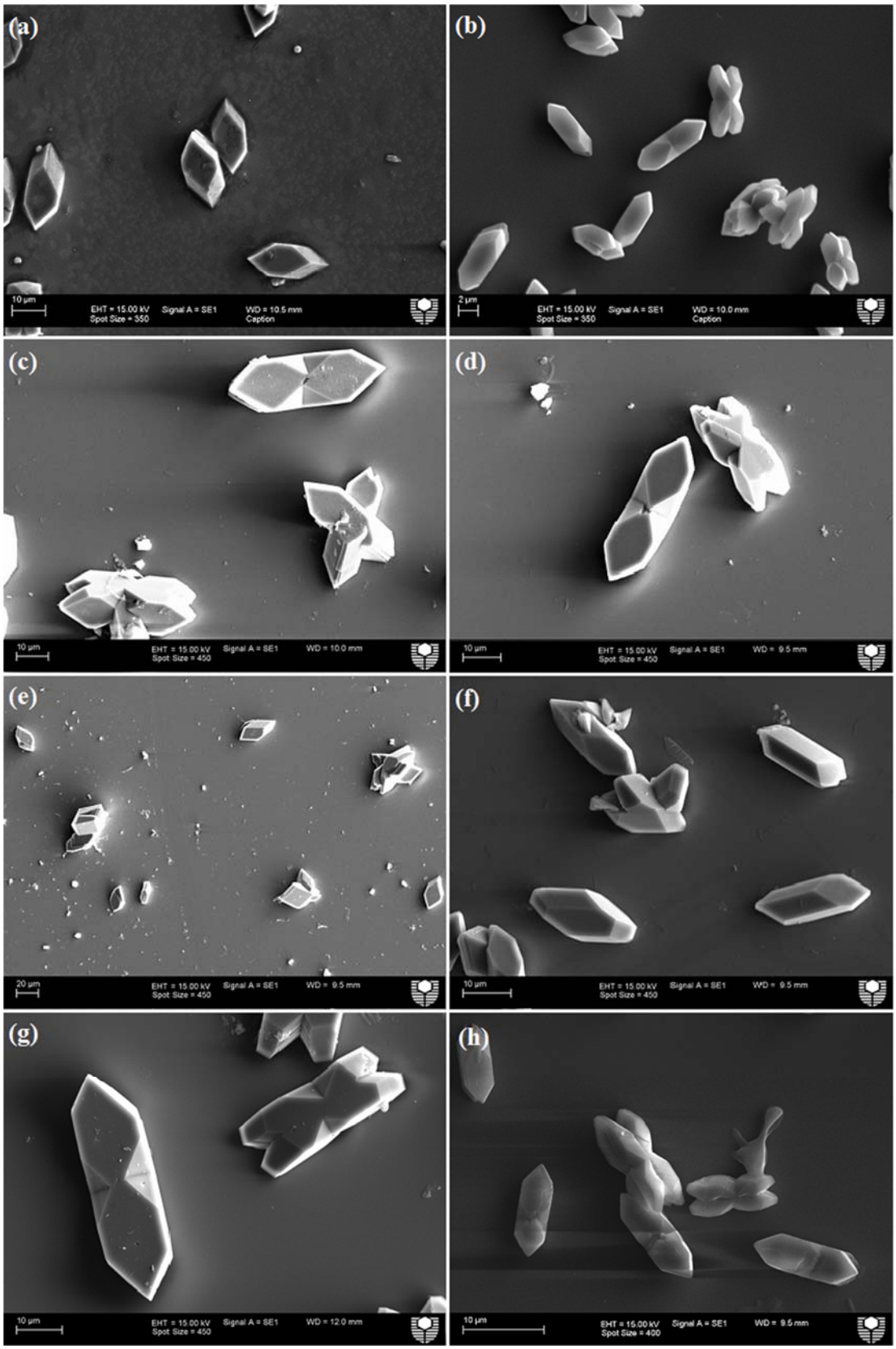


***Figure 4.7***: SEM micrographs of calcium oxalate (0.30 mM) crystal morphology in the presence of additives: (a) **3** at 6.84 mM, (b) **3** at 0.68 mM, (c) **22** at 5.07 mM, (d) **22** at 0.50 mM, (e) **23** at 5.10 mM, (f) **23** at 0.51 mM, (g) **24** at 5.10 mM, (h) **24** at 0.51 mM.

With a calcium oxalate concentration of 0.30 mM and a tetrazole additive concentration at 1.0 g/L (3 - 7 mM) and 0.1 g/L (0.3 - 0.7 mM) for the morphological experiments, the relative impacts of the tetrazole molecules are observed utilising SEM imaging to determine which COM crystal faces the tetrazole molecules adsorb strongly to. This was confirmed by visual changes in habit and morphology and quantified by the data obtained from the series of images seen throughout the chapter and ***Appendix 4***. The trends that were observed across the series included the definitive increase in crystal growth modification of COM in the presence of di-tetrazole species compared to mono-tetrazole-containing additives. Such di-tetrazole species included tetrazole molecules **8**, **9**, **10** and **11**. Interestingly among this small subset of tetrazole molecules, changes in structure quickly affected the impact of the additives on COM. This indicates that there is a direct link between the structure and the impact on COM crystallisation, in this particular subset the trend of impact follows **9** < **8** < **10** < **11**. Of particular note, **11** impacted the nucleation of COM greatest, while **10** changed the habit of COM from the typical 6-sided hexagon shape to a 4-sided square or diamond shape.

Aside from the di-tetrazole species, tetrazole molecules **17** and **21**, containing ether functional groups exhibited significant particle number inhibition and morphological impacts, respectively. As observed above for the di-tetrazole species, additives **12**, **13**, **14**, **15** and **25**, provided additional comparisons for the structural changes apparent in the series. The location of the nitrogen(s) on the aromatic backbone of the tetrazole compounds affected the final morphology and nucleation density of COM differently. The order of impact proceeded from **14** < **15** < **13** < **25** < **12**, with tetrazole **12** having the greatest overall impact. The nucleation, crystal growth rates and complexation of all tetrazole molecules will be conducted and discussed in the following chapters to further elucidate the impact of the tetrazole series structures.

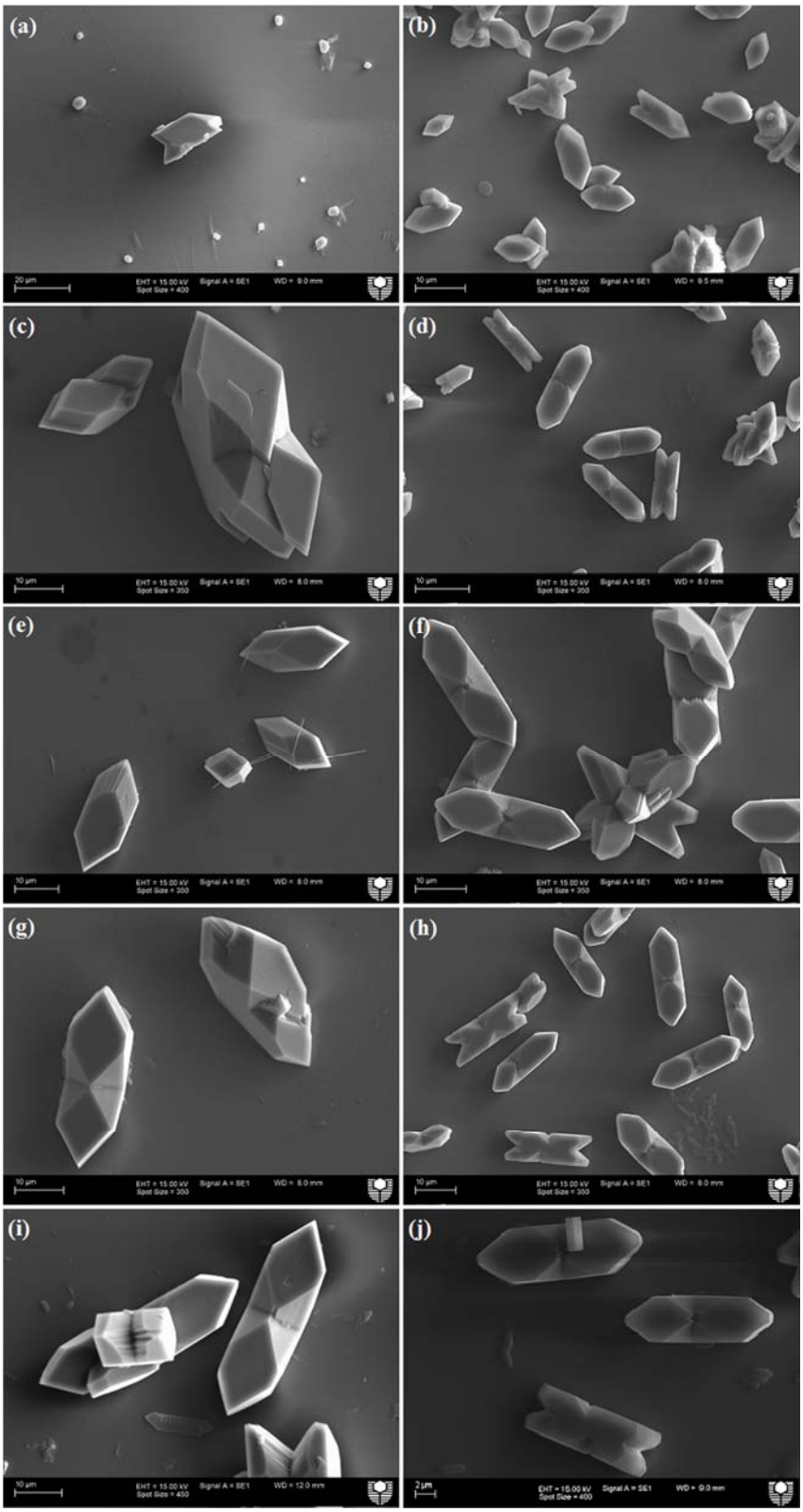


***Figure 4.8***: SEM micrographs of calcium oxalate (0.30 mM) crystal morphology in the presence of additives: (a) **12** at 6.80 mM, (b) **12** at 0.68 mM, (c) **13** at 6.80 mM, (d) **13** at 0.68 mM, (e) **14** at 6.80 mM, (f) **14** at 0.68 mM, (g) **15** at 6.75 mM, (h) **15** at 0.67 mM, (i) **25** at 6.75 mM, (j) **25** at 0.67 mM.

## 4.4 Artificial urine study

Developing artificial urine (AU) compositions to test particular effects and determining thresholds for each species present have been around for decades.[75,126,173,216] Crystallisation studies in AU's can help determine the potency of many potential additives in an environment more similar to physiological conditions and complexity. In this study the composition of Brown et al.[75] was used as it is well documented to crystallise calcium oxalate dihydrate (COD), a form of calcium oxalate not seen in the presence of our tetrazole additives during direct mixing experiments. As shown in ***Figure 4.9***, COD was indeed crystallised, indicated by its bipyramidal morphology, with the most common particle at a size of ~9 x 9 µm, however, fewer much larger particles (~40 x 40 µm) that were present were COM particles.

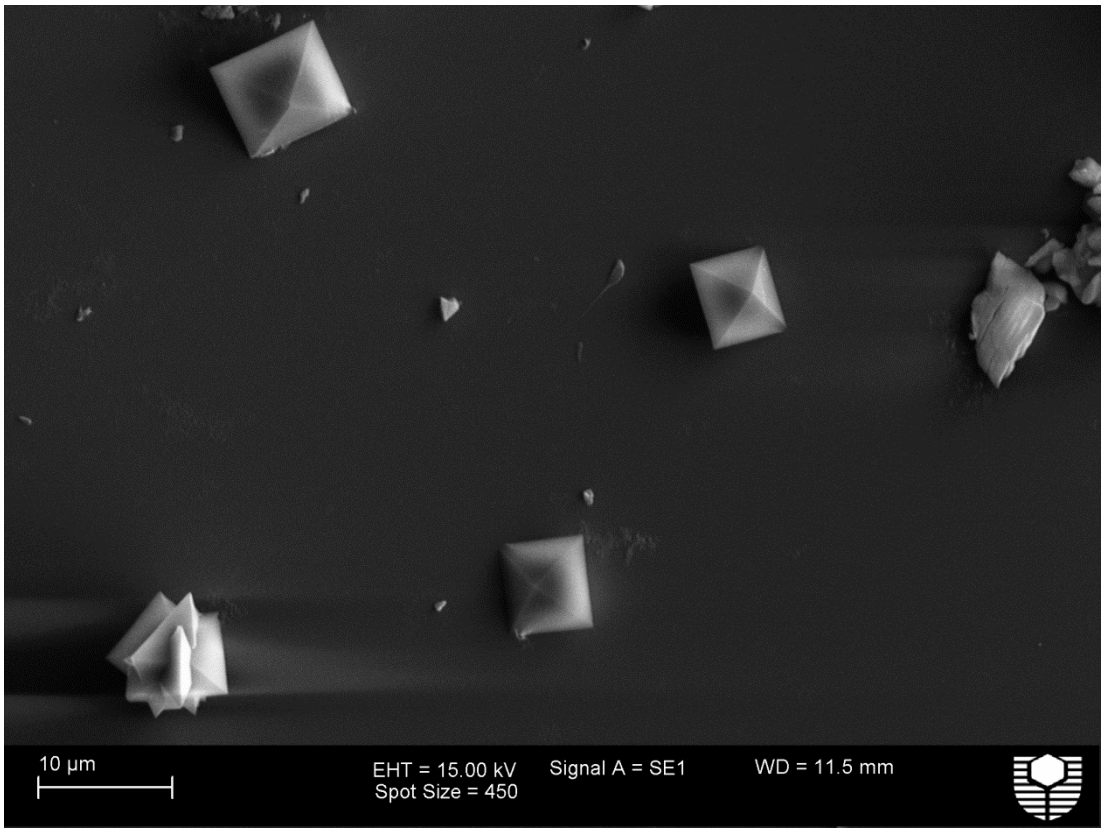


***Figure 4.9***: SEM micrograph of calcium oxalate control particles grown from A.U, without additives present.

Referring to ***Figures A4.7a*** and ***A4.7b*** in ***Appendix 4***, the analysis of the particles with energy dispersive x-ray spectroscopy (EDS) elucidated the composition of the larger particles as consisting of carbon, oxygen and calcium atoms, while the smaller particles had calcium, oxygen and calcium present with silicon also being detected, this is due to the glass discs on which the samples were grown on and was detected as the particles are quite small. Raman spectroscopy was performed on the particles found after crystallisation in the AU medium. The bipyramidal particles were found to be COD, based on literature,[217] which report a single characteristic peak at 1476 $cm^{-1}$, compared to COM, which is reported to have two peaks at 1474 and 1498 $cm^{-1}$. The spectrum shown in ***Figure 4.10*** represents the Raman frequencies of a COD particle grown as outlined above, without the presence of any additive species.

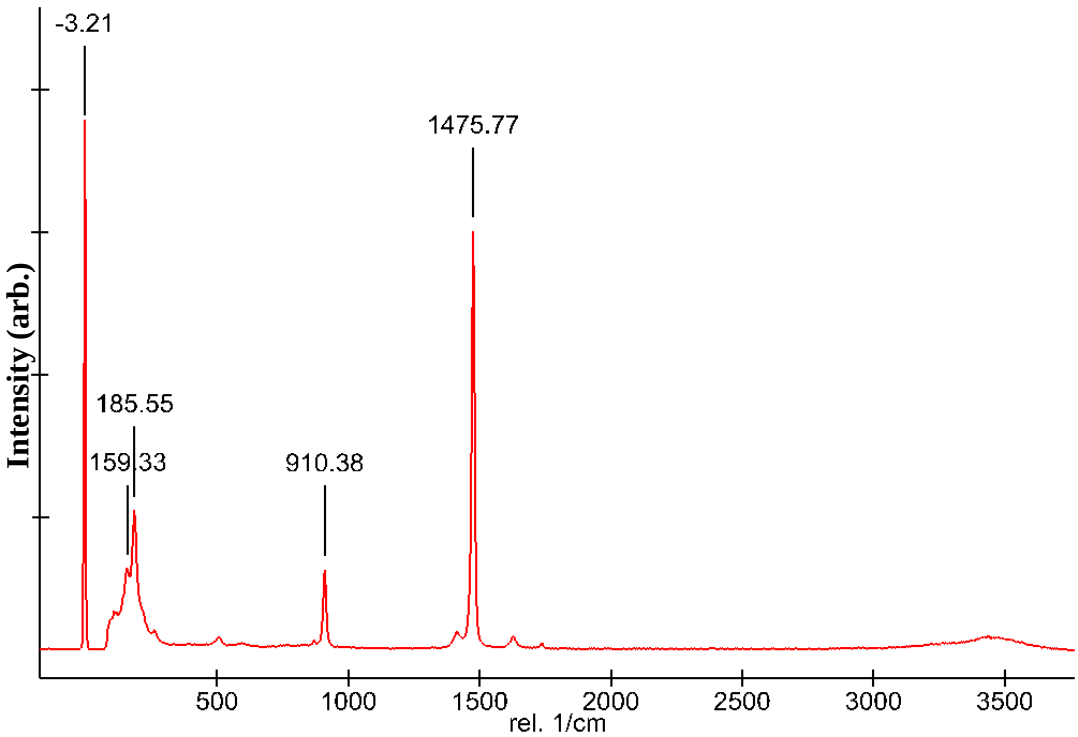


***Figure 4.10***: Raman Spectrum of COD particles grown in AU.

A baseline for the particles most likely to precipitate from AU has been determined. Addition of 6 of the tetrazole molecules from the series may provide insight into how potent they are at modifying the crystallisation of calcium oxalate in a slightly more complex mixture. The tetrazoles used for this series of experiments were, **4** (4-(1H-tetrazol-5-yl) benzaldehyde), **5** (4-(1H-tetrazol-5-yl) benzonitrile), **10** (1,4-bis-(1H-tetrazol-5-yl) benzene), **12** (1H-5-(2-pyridyl) tetrazole), **13** (1H-5-(3-

pyridyl) tetrazole) and **14** (1H-5-(4-pyridyl) tetrazole). The impacts of the additives were very similar across all 6 tetrazole species. SEM micrographs of the particles that remain after washing and air drying, as per the method described in ***Section 2.2.3***, are presented in ***Figure 4.11***. These tetrazoles were selected as an initial trial to determine whether modification was possible. Some structural similarities between the species chosen may have provided an avenue to continue research had any correlation been possible between the structure of the additives and the impact on the morphologies.

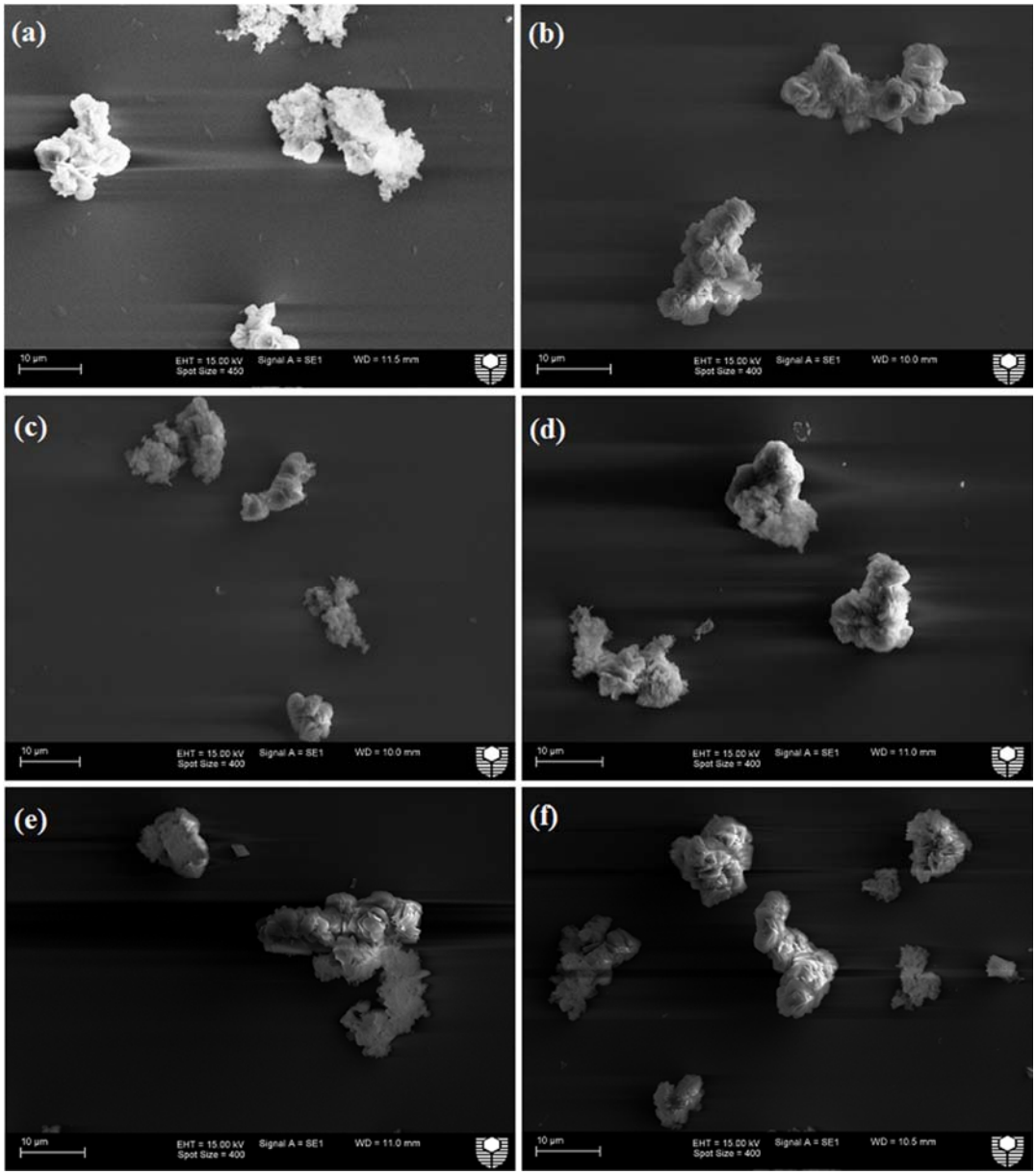


***Figure 4.11***: Calcium oxalate crystals grown in AU and in the presence of additives: (a) **4** at 5.74 mM, (b) **5** at 5.84 mM, (c) **10** at 4.67 mM, (d) **12** at 6.80 mM, (e) **13** at 6.80 mM and (f) **14** at 6.80 mM.

The particles present were either aggregates of plate-like crystals or a much rougher aggregate-like solid. All particles were analysed by EDS to clarify the constituents of each precipitate. Many different particles were analysed by EDS (refer to ***Appendix 4***, ***Figures A4.8-4.10***), while most of the plate-like crystals only contained calcium oxalate, many were aggregates containing the following species: sodium chloride, calcium phosphate, potassium chloride and calcium oxalates.

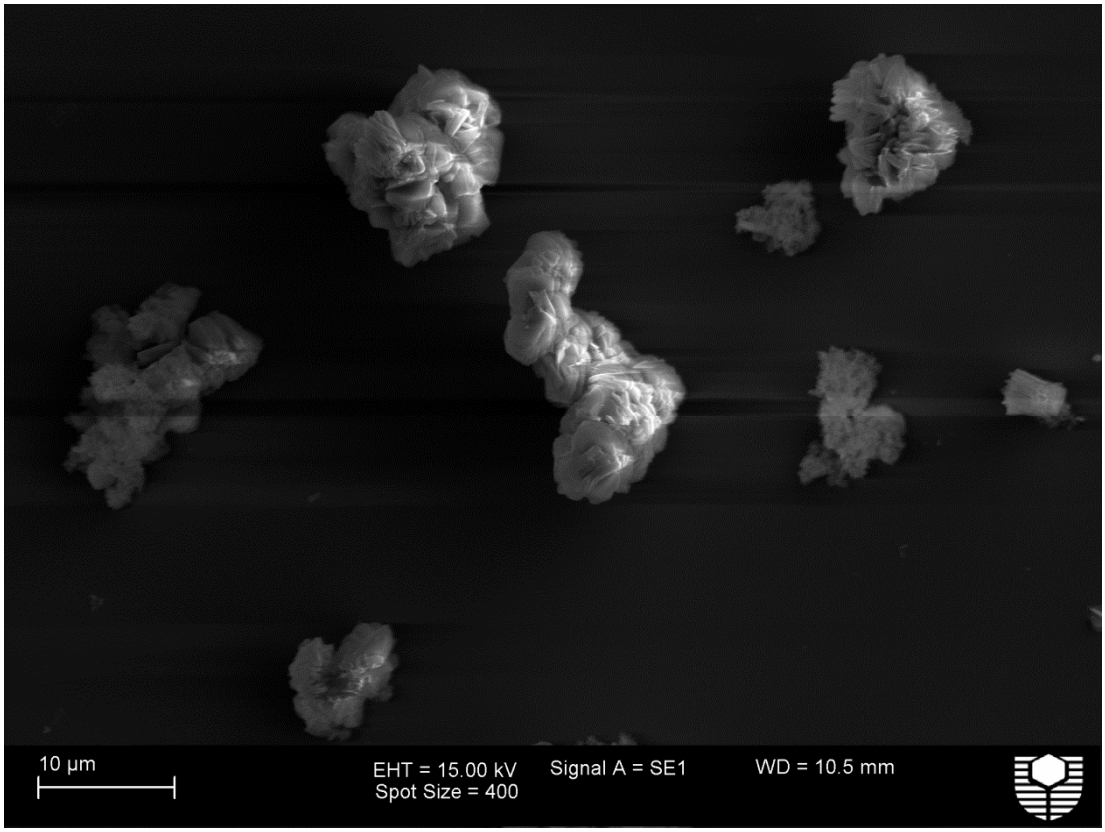


***Figure 4.12***: SEM micrographs of aggregate particles precipitated from AU in the presence of additive **14** (6.80 mM).

***Figure 4.12*** illustrates the calcium oxalate particles grown in the presence of **14**, clearly display the aggregate structure mentioned above. However, without distinct crystal faces to obs**e**rve it is extremely hard to determine how the crystals have been affected from the original COD particles observed in control experiments to the observed particles throughout the addition of the tetrazole molecules in the AU experiments. What can be stated from the images collected is thus: where once there

were predominantly COD particles in the control with much larger COM particles, now there are very few COD particles and no larger COM particles. Both have been replaced with aggregated particles, which consist of many salts present in the AU mixture, as confirmed by the EDS results. Raman analysis of the aggregates revealed little definitive structural information (***Appendix 4***, ***Figure A4.11***) with very low signal-to-noise ratios. The only distinct peak visible was at 960 $cm^{-1}$ and is close in frequency to the Raman vibration of both struvite and apatite,[218] (magnesium ammonium phosphate and calcium phosphate) respectively. Qualitatively, no magnesium was detected throughout EDS analysis of the particles, the conclusion can be made that the aggregates are calcium oxalate/phosphate mixtures predominantly.

## 4.5 Conclusion

The tetrazole additives **1-26**, all had some form of impact on the crystallisation of calcium oxalate. In particular, additives, **5**, **10**, **11**, **12**, **16**, **17**, **21** and **23** had the greatest impact on the morphology. Most tetrazole molecules influenced the crystal shape *via* adsorption onto the apical tips or (12-1), (1-2-1), (021) and (0-21) faces, this was indicated by those faces dominating the morphology of the crystals present in the micrographs. One face that was not impacted greatly throughout all additives (except additives **5** and **10**) was the (100) face, indicating that although it is by far the most prominent face (and therefore slowest growing) almost none of the tetrazole molecules had any interaction with it. Commonly used COM inhibitors, including carboxylic acid containing compounds such as citric acid,[68,142,150] have been shown to impede growth of COM *via* adsorption to both the (100) face, (010) face and (12-1), (1-2-1), (021), (0-21) faces. The key to inhibiting COM as strongly as citric acid, may rest in finding inhibitors that also strongly effect or can control growth of the prominent faces mentioned above.

Based upon the quantitative data obtained from the micrographs in ***Appendix 4***, trends are being formulated. Unfortunately, based solely on the morphology, it is extremely difficult to definitively say why some of the more potent tetrazole

molecules impacted to greater degrees than others. Thus, even though SEM investigations of COM in the presence of tetrazole molecules has given insight into which faces the tetrazoles interact strongly with COM, a deeper understanding of the interactions that take place during crystallisation and nucleation are required. Kinetic studies of the impact on nucleation by the tetrazole molecules, the extent of complexation to calcium atoms are to be investigated to further understand the mechanisms at play. In addition, AFM *in situ* growth measurements and Raman spectroscopy, with a photophysical study to investigate aggregation mechanisms observed, were undertaken to gather further information on the interactions of tetrazole molecules and COM crystals.

Although the AU experimentation did not provide much insight into the impact of the subset of tetrazoles species used, the modification of the crystalline species present shows promise for the use of tetrazoles as modifiers in more complex environments. Due to the stability of tetrazoles within the human body (resistance to biodegradation) the use of tetrazoles in medicine has grown rapidly, as this small study on the impact of some of the simple tetrazole species has shown, it is possible for modification to occur. Thus, further work in the future would include the expansion of the tetrazole species investigated as well as their concentration, in addition to investigating existing medicinal molecules with tetrazole functionality to bypass the need to determine their stability within more complex environments, i.e. the human renal system.

# 5 Nucleation and complexation behaviour

## 5.1 Introduction

Nucleation can be inhibited in the presence of additives, commonly nucleation is retarded by the action of additives binding strongly to the ions and clusters that grow in the supersaturated solution. Not surprisingly, nucleation can be retarded by the well-known COM crystal growth modifier, citrate[60] and other negatively charged species, such as phosphates,[219] have been proven to raise the soluble fraction of urinary calcium through complexation thus reducing crystal growth of COM. While the affinity of calcium and citrate has been measured to be higher than that of calcium and oxalate, the solubility of calcium citrate is 100 times more soluble than calcium oxalate; therefore, the precipitation of calcium oxalate is more likely to take place.[153] The capacity of tetrazole-containing molecules to complex calcium was studied to determine whether the additive series and their differing structures altered the supersaturation, S, of COM by lowering the available calcium and consequently lowering nucleation rates. In other words, removing calcium ions in the form of soluble complexes reduces the free ion activity, decreasing the supersaturation of calcium oxalate leading to fewer nucleation events. To measure the strength of complexation of the additives, dissolution experiments were conducted employing ICP-AES to measure the total calcium in solution. Increases in the total soluble calcium compared to the pure case directly infer that the tetrazole-containing molecules remove solute in the form of soluble complexes.

Carboxylic acid-containing molecules researched, such as potassium citrate,[62] have been shown to directly inhibit the nucleation of calcium oxalate crystals in urine. Thus, to determine if the 26 tetrazole molecules in this study also directly inhibit nucleation, dynamic light scattering (DLS) techniques were employed. Experimental results for both the dissolution and DLS studies will be discussed in this chapter and thus, in combination with the morphological study presented in ***Chapter 4*** will define which tetrazole molecules in the series impact nucleation, complex with calcium and to what degree.

## 5.2 Dynamic light scattering (DLS)

### 5.2.1 DLS methodology

To better determine the impact of the tetrazole molecules on the nucleation behaviour of calcium oxalate, dynamic light scattering (DLS) studies were undertaken to assess their impact on homogenous nucleation. DLS was used to monitor the onset of nucleation by determining the relative particle numbers, in turn this was then used to determine whether nucleation was promoted or impeded in the presence of each additive. The conditions described in ***Section 2.2.8***, were kept constant throughout all experiments with the only changing parameter being the additive present. The complete set of DLS data can be found below, each experiment was run in triplicate and the data averaged. All results (***Figures 5.1-5.6***) are presented with the averaged control measurements (without additives present) to provide a simple way of comparing and determining whether nucleation promotion or inhibition occurred in the presence of the tetrazole series.

Prepared solutions were added to a Teflon beaker covered by a watch glass to ensure no dust particles entered the solution during experimentation. Upon addition of the sodium oxalate solution to the solution of calcium chloride (with or without additive already present) an aliquot of ~3 mL was taken immediately and added to a plastic cuvette. The cuvette was placed into the Zetasizer and analysis of the particles begun. The number of integrations and readings performed was pre-set to ensure the time steps were always kept constant. This allowed for accurate measurements to be taken across 30 minutes, in 3 minute intervals with very little delay. The importance of consolidating the time of each recording was crucial for comparison and analysis of each time-steps' particle counts (kcps) across the 26 additives and control experiments. The following figures and discussion attempt to elucidate the data and trends seen therein. Each Figure is presented with the number of particles observed by the Zetasizer on the y-axis (in kcps) at a given time on the x-axis (in minutes) up to a total time of experimentation of 30 minutes. If the particle counts at a given time are higher than the control value, it can be said to have promoted nucleation, and *vice versa*.

### 5.2.2 DLS results and discussion

As was presented in ***Chapter 4***, the tetrazole molecules are similarly grouped throughout the DLS results. Nucleation data for tetrazole species **1**, **2**, **4** and **5** can be found in ***Figure 5.1***. Typically, it would be expected that nucleation of COM should be presented by a significant increase in particle numbers before the eventual plateau or flattening of the number of particles nucleating, indicating the point at which crystal growth of existing particles begins to dominate, in other words, the transition from the labile zone to the metastable zone. Longer experiment times were required to completely illustrate this transition from nucleation to crystal growth in the experiments shown here (presumable because nucleation was not a single event but continuously occurred during the experiment). However, comparison of the results in the pure system to the data collected in the presence of the 26 tetrazole-containing species can still be discussed to determine their impact on the early stages of nucleation. The trend discovered from the SEM studies, of tetrazoles **1**, **2**, **4** and **5** indicated that the morphology of COM was impacted upon, changing the habit of the crystals (***Figure 4.3***). The nucleation of COM was also inhibited by each compound, with tetrazole molecules **4** and **5** decreasing the number of particles nucleated by ~50%, while **1** inhibited less at ~35%, and **2** decreased the number by over 70%. Based upon the significant reduction in particle numbers, the strength of nucleation inhibition increases thus **1** < **5** < **4** < **2**. The most potent nucleation inhibitors will be compared to their dissolution (complexation) data obtained in ***Section 5.3*** to determine whether the results are due to supersaturation changes or surface energy changes, thereby refining the mechanism of interaction between the tetrazole series and COM crystals.

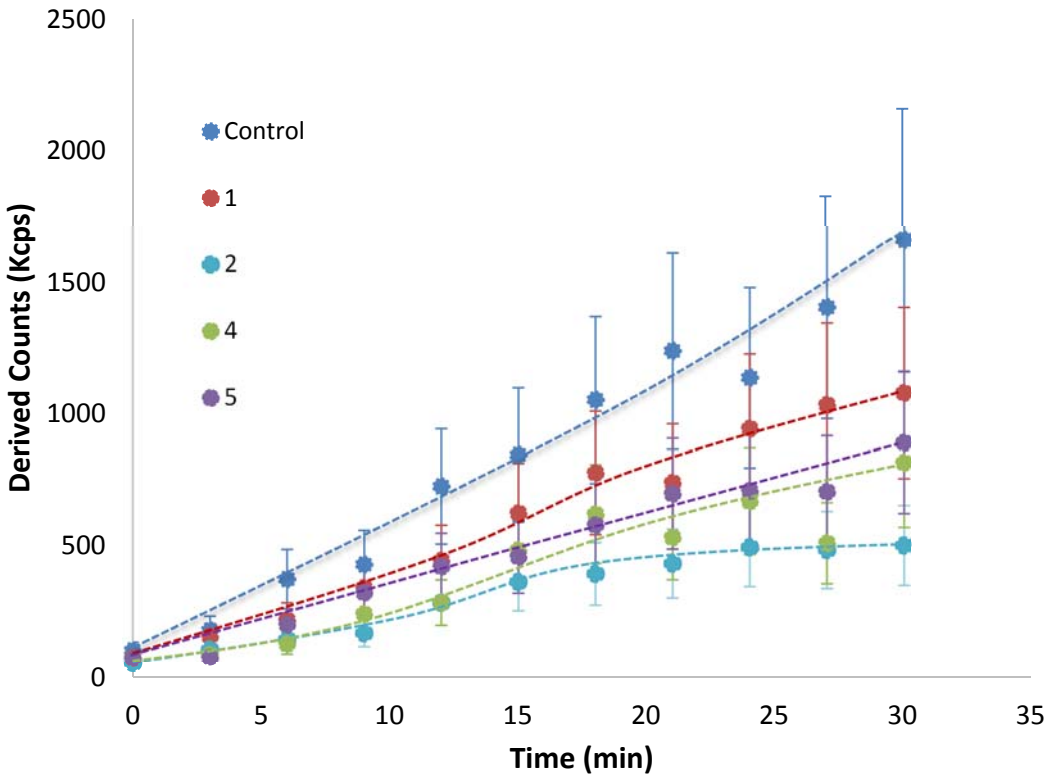


***Figure 5.1***: DLS data of control and in the presence of Tetrazoles **1**, **2**, **4** and **5**. Dotted lines are to guide reader only and do not represent a mathematical fit of any kind.

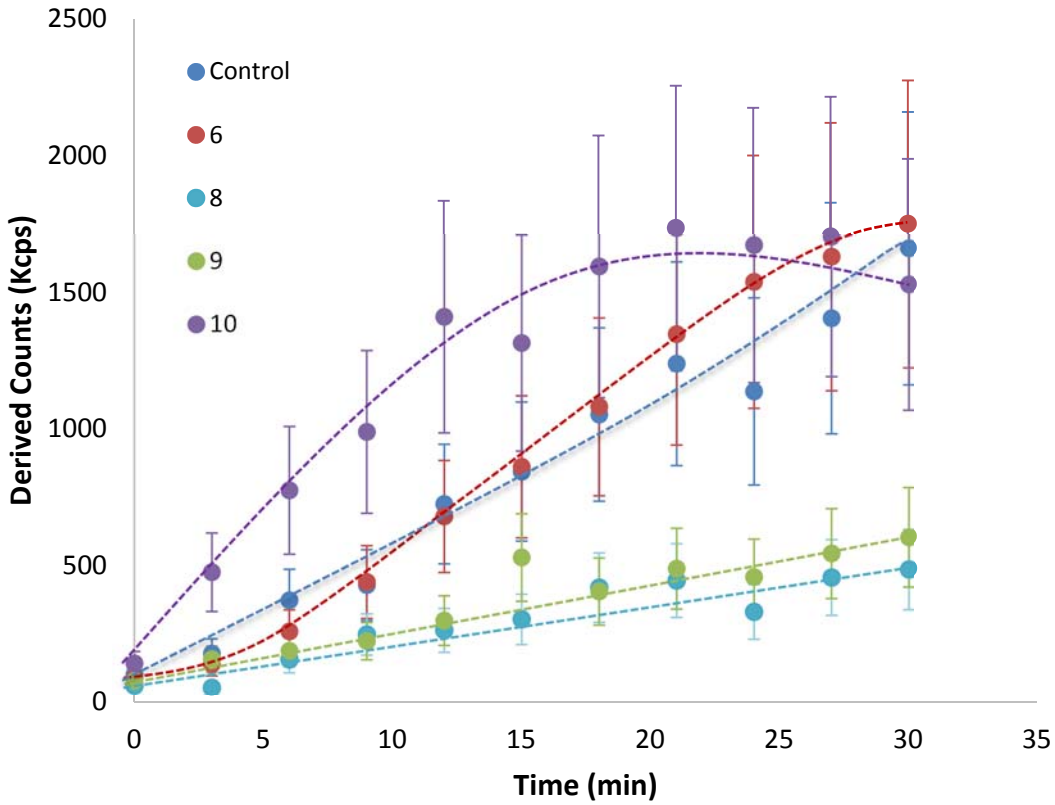


***Figure 5.2***: DLS data of control and in the presence of Tetrazoles **6**, **8**, **9** and **10**. Dotted lines are to guide reader only.

The morphological results from ***Chapter 4*** provided evidence that tetrazole **10** the *para* substituted bis-tetrazole was more potent at inhibiting COM than the structural isomers, *ortho* or *meta* bis-tetrazoles **8** and **9**. The DLS results however, indicated that **10**, in fact, promoted the nucleation (compared to control) in the earlier stages of nucleation before noticeably plateauing (***Figure 5.2***). Additives **8** and **9**, meanwhile, strongly reduced particle numbers by ~65%. This apparent discrepancy between the DLS results and morphological results will be further investigated in the complexation section to determine which data are consistent with each other and can be used for further mechanistic understanding. DLS results for **6** indicated a very similar nucleation to the control and thus had little impact on the nucleation. However, this result is in disagreement with the morphological study of COM in the presence of **6**, particles were much larger in size, and had significantly reduced particle numbers than the control. Again, complexation data will be used to try and resolve this discrepancy.

Most appropriately, the tetrazole that had the greatest impact on crystallisation throughout the morphological studies, 2,6-bis-(1H-tetrazol-5-yl) pyridine (**11**), also exhibited the greatest potency for nucleation inhibition (***Figure 5.3***). Tetrazole **11** reduced the number of particles by almost 90%, confirming the profound affect the tetrazole had indicated during crystallisation studies (***Chapter 4***). Accompanying **11**, tetrazoles **16** and **20** both strongly inhibited nucleation with reductions of ~80%. Based on the micrographs and their quantitative data from ***Appendix 4*** and presented in ***Table 4.1*** (***Chapter 4***), the results undeniably confirm the strength of inhibition of tetrazoles **11**, **16** and **20**. Following this, additive **18**'s DLS data showed it reduced COM crystal numbers by ~50%, and had subsequently less impact on the crystal numbers (***Figure A4.3***) when compared to SEM micrographs for COM grown in the presence of **11**, **16** or **20**.

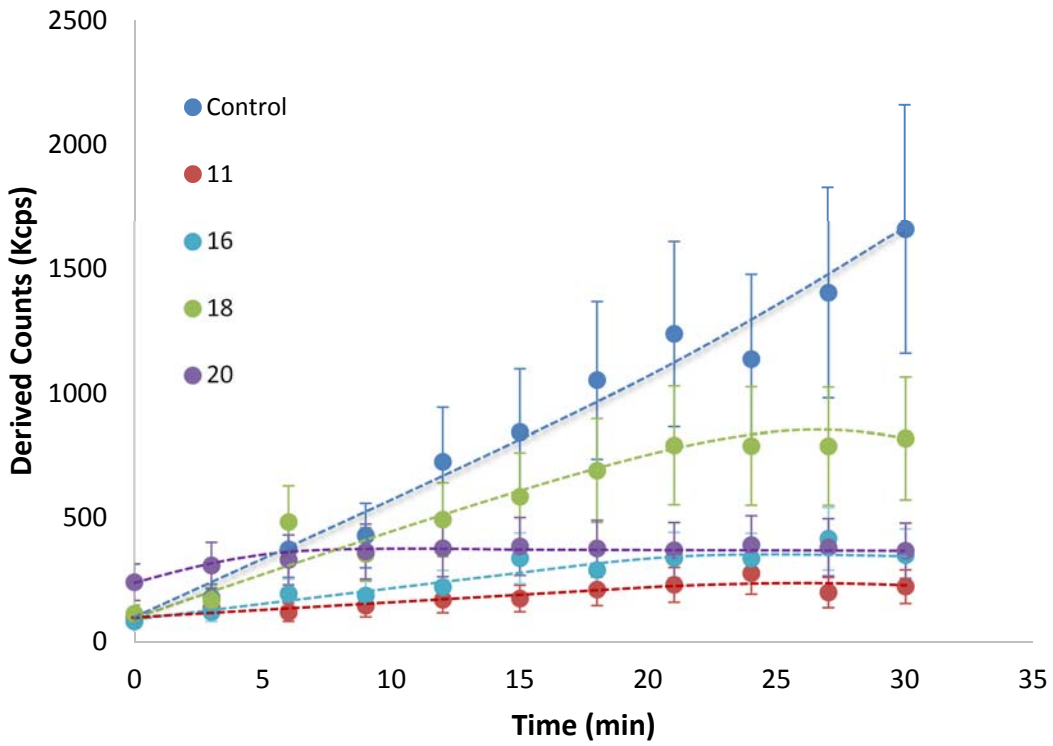


***Figure 5.3***: DLS data of control and in the presence of Tetrazoles **11**, **16**, **18** and **20**. Dotted lines are to guide reader only.

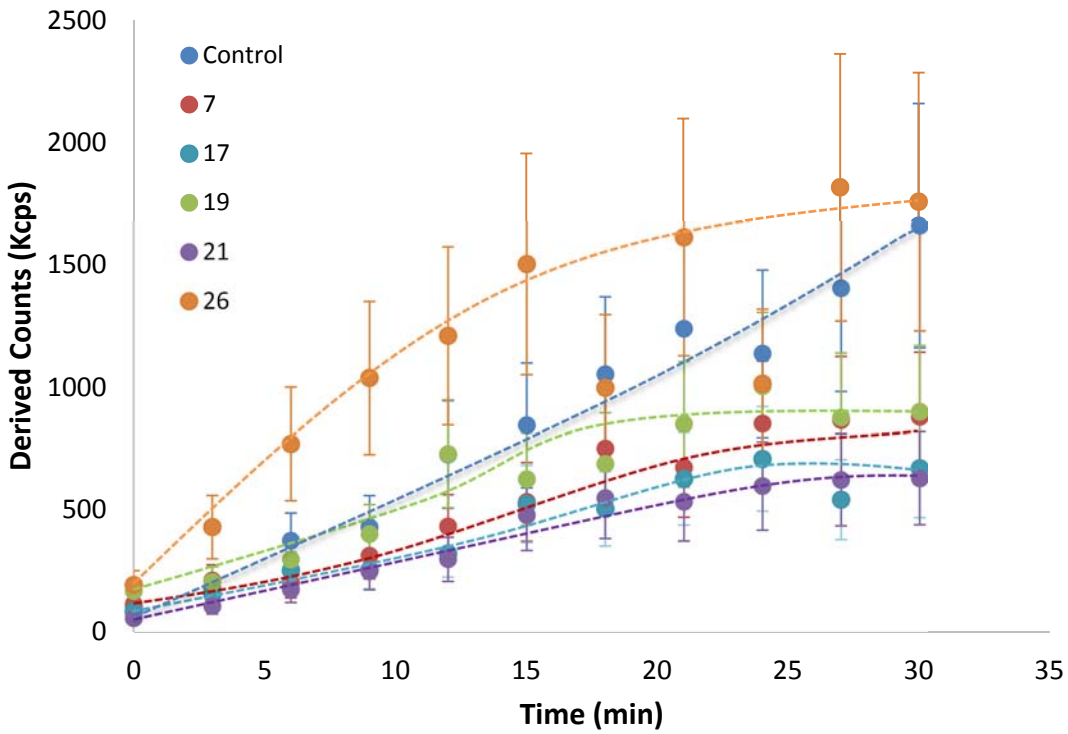


***Figure 5.4***: DLS data of control and in the presence of Tetrazoles **7**, **17**, **19**, **21** and **26**. Dotted lines are to guide reader only.

Featured in ***Figure 5.4***, tetrazole molecules **7**, **17**, **19**, **21** and **26**, generally inhibited COM nucleation, ranging in particle number reductions from 50% to 60% (**7**, **19** and **17**, **21**, respectively). Unlike the other additives in ***Figure 5.4***, tetrazole **26**'s DLS data indicated that it promoted the nucleation of COM slightly (5% by experiment end). However, molecule **26** promoted particle numbers by almost 2.5 times at the maximum difference to the control (9 minutes into the experiment). Shortly thereafter, the nucleation of COM in the presence of **26** became sporadic, increasing and decreasing over time but mostly probably plateauing to a constant value. Longer experimental times would have resulted in the convergence of the particle numbers as the concentration decreased into the metastable zone from the labile zone.

***Figure 5.5***, the phenyl and conjugated aromatic ring tetrazole molecules, **3**, **22**, **23**, and **24**, all exhibited moderate to strong inhibition of COM nucleation. Tetrazole **3**, the in-series tetrazole comparison, due to the common phenyl group and singular tetrazole moiety, exhibited strong nucleation inhibition at ~65%. All other additives compared to **3** had additional functionality and in the case of the additives in ***Figure 5.5***, additional conjugation. **22**, **23** and **24** each had an additional ring and conjugation, increasing aromaticity. **24**, the next simplest molecule in this subset of tetrazole molecules, further increased the nucleation inhibition to a reduction of ~75% of particle numbers. However, additives **22** and **23** both had a lessened impact on the nucleation at particle number reductions of 35% and 48%, respectively. From these results, structure and steric effects appear to play much larger roles in nucleation inhibition, including the involvement of further complexation sites present in **22** and **23** for the quinolone or isoquinoline aromatic tetrazoles. Competing interactions between nucleation of calcium oxalate and complexation of free $Ca^{2+}$ forming insoluble complexes by the tetrazole molecules may be the cause of the reduced nucleation potency compared to the simpler phenyl and naphthalene structures, which do not offer further positions for calcium complexation or hydrogen bonding.

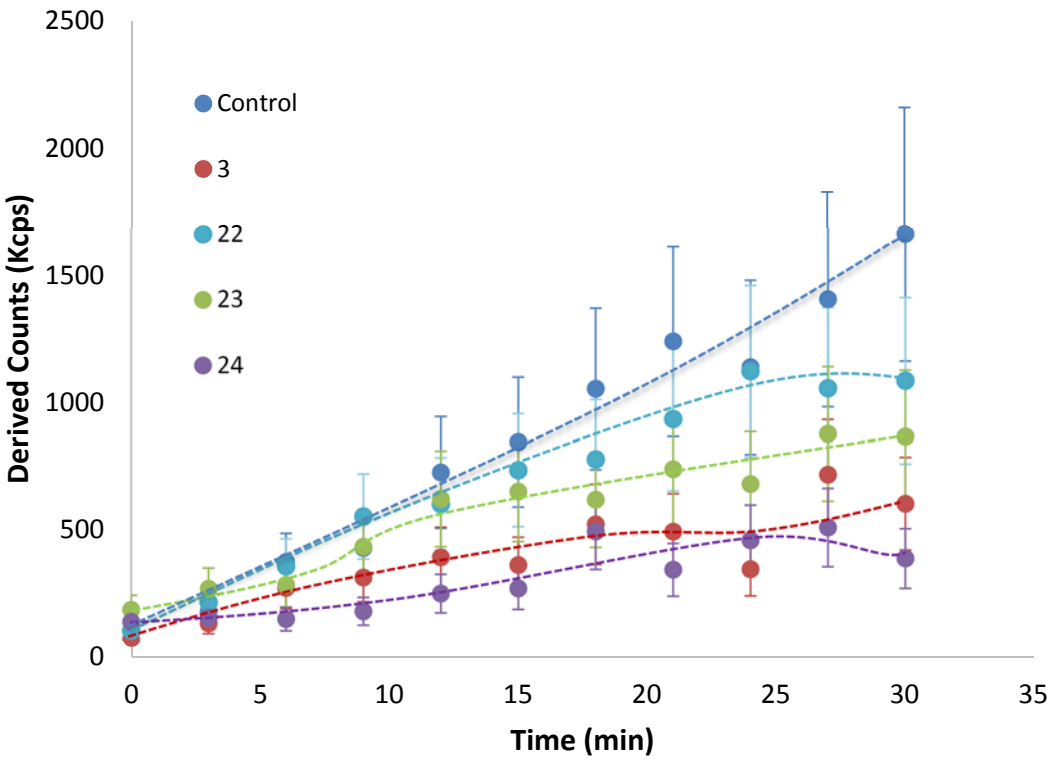


***Figure 5.5***: DLS data of control and in the presence of Tetrazoles **3**, **22**, **23** and **24**. Dotted lines are to guide reader only.

Lastly and similarly to the previous set of tetrazole molecules, **12**, **13**, **14**, **15** and **25** all contain nitrogen atoms in their aromatic rings, potentially strengthening the complexation possible in this subset of tetrazole molecules. Although morphologically, **12** had the greatest impacting from ***Chapter 4***, each tetrazole molecule except **25** impacted nucleation with equal strength, unsurprisingly, due to their structural similarity. While **25** marginally (5% increase) promoted nucleation it can be considered to have had control-like nucleation values, additives **12-15** all inhibited COM nucleation by ~45% with extremely similar plots as seen in ***Figure 5.6***. The structures of the tetrazole molecules change only by the position of the nitrogen in the pyridyl aromatic ring from *ortho*, *meta* to *para*, while **15** has an additional nitrogen atom at the *meta* position (refer to ***Scheme 3.3***, ***Section 3.5.1***). Thus, even though the structural isomers and addition of the extra nitrogen in the pyrazine tetrazole case (**15**), little impact on the nucleation potency occurred.

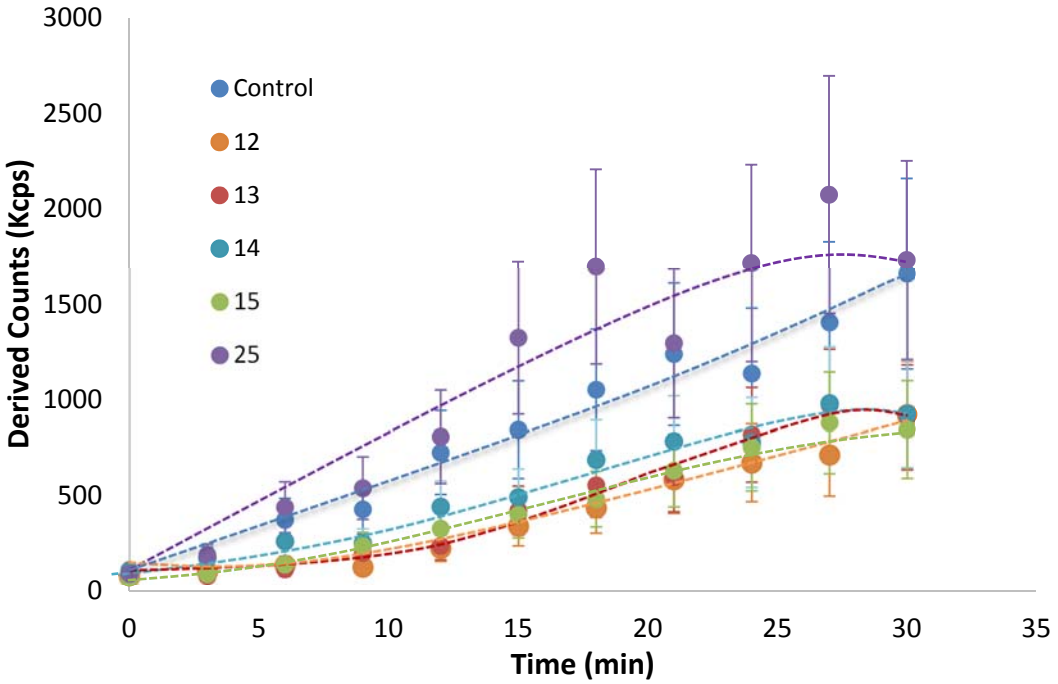


***Figure 5.6***: DLS data of control and in the presence of Tetrazoles **12**, **13**, **14**, **15** and **25**. Dotted lines are to guide reader only.

Each tetrazole molecule presented in ***Figure 5.6*** was equipotent at reducing particle nucleation as the simplest tetrazole in the series, 1H-5-phenyltetrazole (**3**). This result could indicate that although the tetrazole moiety can directly inhibit the nucleation, the addition of more complex structures (additional complexation positions) provided by nitrogen atoms on the aromatic backbones do not have the binding strength to directly impact nucleation. The impacts from the additional electronegative atoms are proposed to inhibit *via* the complexation of $Ca^{2+}$, reducing the supersaturation and thus inhibiting the nucleation. Importantly, this hypothesis can be tested in ***Section 5.3***. Additionally, though structural isomerism and functionality changes may have produced observable effects on the morphology and crystal growth, DLS results of the nucleation do not equally present the same trends. The interactions of the tetrazole molecules on the forming nuclei and supersaturation currently appear to be different mechanisms. Thus, further elucidation of these mechanisms should present clearer trends of how to determine the strength of each tetrazole molecule to inhibit COM nucleation. Dissolution experiments between the

tetrazole series COM powder should help illustrate the contribution of the tetrazole molecules' complexation to $Ca^{2+}$ during nucleation and crystal growth. Currently, the impacts each tetrazole molecule has on COM include multiple mechanisms of interaction simultaneously from adsorption interactions on the nuclei and crystal surfaces *via* hydrogen bonding or electrostatic interactions to the tetrazole functionality. Trends within subsets of tetrazole molecules indicate that the tetrazole functional group can directly inhibit the nucleation of COM, while other portions of the structures, particularly the nitrogen atoms in several molecules may only inhibit through complexation mechanisms. Comparison of all results is therefore extremely important in determining the strongest mechanism for each tetrazole in the series.

### 5.2.3 Conclusion

Throughout the DLS results shown in ***Figures 5.1-5.6***, the majority of tetrazole molecules were shown to inhibit the number of particles nucleated. In total only 4 tetrazole molecules of the total 26 showed promotion of the nucleation, these included tetrazole molecules **6**, **10**, **25** and **26**. Of the tetrazoles that inhibited COM nucleation, the strongest (>70% reduction of particles counted) included tetrazole molecules **2**, **11**, **16**, **20** and **24**. Structurally, two of the tetrazole molecules, **16** and **20**, both contained bromine atoms in the *para* position with the only other difference being the nitrogen atom in **20** making the backbone a pyridyl ring instead of a phenyl ring. As seen throughout this thesis, tetrazole **11** continues to exhibit strong inhibition of COM, in this case with the highest reduction in particle numbers of any tetrazole molecule in the series. Interestingly, tetrazole molecule **8** and **9** showed a decrease in the nucleation numbers of ~65% each, while **11** reduced particle numbers by almost 90%. The addition of the nitrogen atom on the aromatic pyridyl backbone or the change in the stereochemistry of the molecule can result in large changes in the overall potency of the tetrazole molecule on nucleation.

Comparing now the nitrogen containing aromatic ring tetrazole molecules **11**, **12**, **13**, **14**, **15**, **20**, **22**, **23** and **25**, it was observed that the extended conjugation of the aromatic rings in **22** and **23** resulted in an increase in particle numbers when compared to single ring counterparts. Thus, access to the nitrogen atom of the ring

(steric effects) is necessary to keep in mind for the interactions required for inhibition of nucleation. Interestingly tetrazole **25**, (2-(1H-tetrazol-5-yl) pyrimidine) containing two nitrogen atoms both *ortho* to the tetrazole resulted in a promotion of the particle numbers. In comparison, tetrazole **15** (1H-5-(2-pyrazine) tetrazole) containing two nitrogens at *ortho* and *meta* positions to the tetrazole produced equal inhibition of COM to that of the *ortho*, *meta* and *para*-pyridine tetrazoles (**12**, **13** and **14**). It is becoming increasingly clear that additive structure can have a profound effect on the potency of COM nucleation inhibition.

## 5.3 Complexation behaviour

### 5.3.1 Introduction

The ability of organic molecules to bind cations of interest is commonly utilised to inhibit crystallisation[47,64,220–222]. The reactions involved during this process are twofold. First, the cations and anions from dissolution of the solid equilibrate in the system. During this process calcium in solution is available for binding with the additive. In this case, calcium ions are bound by tetrazole molecules to form a Ca-Tetrazole complex. During nucleation and crystal growth the tetrazole species can bind with $Ca^{2+}$ ions due to their increased affinity. The decrease of available cations for oxalate anions to form calcium oxalate results in the reduction of the supersaturation, S. The degree of the tetrazole species complexing with calcium can be measured *via* the dissolved calcium in solution. Assuming the tetrazole-calcium complex is still soluble, a measure of the total soluble calcium will give an indication of the degree of complexation occurring. That is an increase of the dissolved calcium present in solution compared to the control without tetrazole molecules present directly reflects the strength of the tetrazole species to complex calcium ions during nucleation and crystal growth. Complexation occurs by the following chemical reactions:

$$CaC_2O_4.\ H_2O_{(s)} \rightleftharpoons Ca^{2+}_{(aq)} + C_2O_4^{2-}{}_{(aq)} + H_2O_{(l)} \quad (5.1)$$

$$\text{Tetrazole(H)}_{(aq)} + Ca^{2+}_{(aq)} \rightleftharpoons \left[\text{Ca-Tetrazole(H)}_{(aq)}\right]^{2+} \quad (5.2)$$

The ability of the entire tetrazole series to complex calcium was undertaken by measuring the dissolution of commercially obtained COM powder, in ultrapure water and the presence of the particular tetrazole of interest. The dissolved calcium content after one week was analysed by ICP-AES, of which the normalised data is presented (***Figure 5.7***) by dividing each result by the average control value to determine the relative strength of each additive in the series. Dissolved calcium for each tetrazole additive at 0.1 g/L, 1.0 g/L and 5.0 g/L concentrations were analysed. The following trends were observed; in general across the three concentrations, the dissolved calcium values increased, as expected. However, in several cases this trend was reversed, most probably due to the complexes being insoluble and precipitating out of solution. Thus, when the value for the dissolved calcium followed the expected trend (increased dissolved calcium with increased tetrazole molecule concentration), this implies the assumption of a soluble complex is true, while the opposite trend may indicate the insolubility of the complex rather than the tetrazole molecules' ability to complex $Ca^{2+}$. In general across the three concentrations (0.1, 1.0 and 5.0 g/L) the normalised and averaged dissolved calcium values increased from ~1.5 to ~1.8 and lastly ~2.0 times the pure or control calcium value indicating that most tetrazole-calcium complexes were soluble and did not precipitate from solution.

Firstly, tetrazole molecules **3**, **4**, **5**, and **24** exhibited similar dissolved calcium concentration compared to the control. Based on the structures, this is unsurprising, as they do not have additional complexation positions or tetrazole moieties. Thus, the strength of complexation of the additives relies greatly on the number of anionic and strongly calcium binding functional groups in the structure. In comparison, the dissolution values for additives **12**, **13**, **14**, **15** and **25** (the singular tetrazoles containing molecules) where each has extra nitrogen atoms in their structures, on average dissolved twice the amount of calcium as **3**, **4**, **5**, and **24**, indicating that

complexation plays more of an effect in these tetrazole molecule's structures. Based on the first two subsets of tetrazole molecules, and taking into account the recently discussed DLS results, which indicated that tetrazole molecules **3**, **4**, **5** and **24** all inhibited nucleation strongly; this suggests that these tetrazole molecules impacted on the surface free energy rather the supersaturation (based on the nucleation rate equation and the lack of impact on S inferred from these results). Meanwhile, tetrazole molecules **12-15** had moderate nucleation inhibition and even promoted nucleation in the case of **25**. In this case, apart from **25**, it is clear the nucleation inhibition is most likely due to a decreased supersaturation cause by the complexation of calcium with the tetrazole molecule.

Tetrazole molecules in the series that had multiple negatively charged moieties showed some of the highest levels of dissolved calcium values (***Figure 5.7***). These tetrazoles included **6**, **8**, **9**, **10** and **11**. Though each was structurally different, all contained either 2 tetrazole functional groups except for **6** which contained a tetrazole and carboxylate group. This subset of tetrazole molecules had average dissolved calcium values of 1.2, 2.0 and 3.0 times the control value across the three concentrations (0.1, 1.0 and 5.0 g/L, respectively). Tetrazole **11**, 2,6-bis (1H-tetrazol-5-yl) pyridine, as shown in previous chapters had the strongest effect on COM morphology and nucleation and is also, as shown here, one of the strongest calcium binders. Its structure, in fact, is not much different to tetrazole **9**, 1,3-bis (1H-tetrazol-5-yl) benzene, yet additive **9** has much lower inhibitory strength as evidenced by the previous three investigations. Tetrazole molecules by the additional nitrogen atom (**11**) instead of the carbon atom (**9**) in their aromatic rings, according to the results in ***Figure 5.7***, accounts for a doubling of the amount of calcium dissolved and therefore could account for the disparity in the two tetrazole molecules' DLS results. While **11** suppressed nucleation numbers to ~200 kcps (***Figure 5.3***, 30 mins), **9** though it inhibited nucleation, only inhibited numbers to ~600 kcps (***Figure 5.2***, 30 min), a threefold decrease in particle density in the presence of **11**. Structurally, small changes like the above example make huge differences in COM crystal modification, and although some trends are more difficult to ascertain, complexation can account for a substantial amount of the impact observed. Interestingly, **10** predicted lower nucleation numbers

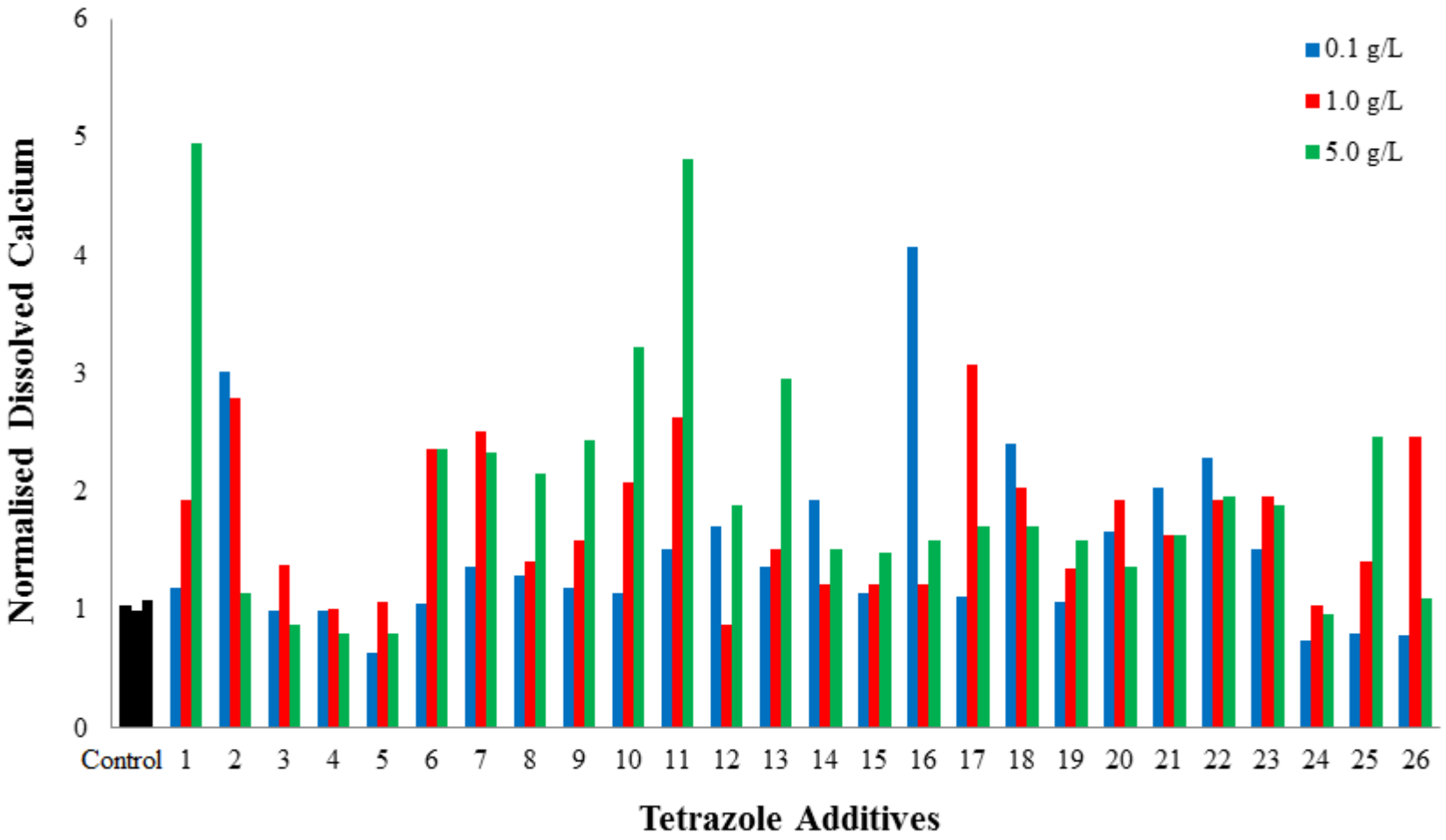


***Figure 5.7***: Normalised dissolved $Ca^{2+}$ results from dissolution experiments

from ***Chapter 4*** results (***Table 4.1***, ***Figure 4.4***). DLS however, did not reflect this result as the tetrazole had similar nucleation impact as the control (it even promoted nucleation in the initial stages). The quantitative data measured and presented in ***Table 4.1*** reports control-like potency, however, as the average crystal size is comparable to that of the control COM particles. The decreased particle numbers can therefore be accounted for the due to the decreased supersaturation caused by affinity for **10** to complex calcium ions (***Figure 5.7***).

Ignoring momentarily the additives that had multiple tetrazole functional groups, tetrazole **1**, methyl 4-(1H-tetrazol-5-yl) benzoate, had the strongest calcium dissolution across all tetrazole molecules. Tetrazole additives **2, 4**, **6**, **7** and **18**, similar to **1** all had carbonyl (C=O) groups in their structures. Of these, **4** showed very little calcium complexation, while the others did have improved calcium uptakes, none were to the same extent as **1**. Tetrazole **1** had a dissolved calcium value of 5 times the control and 2.5 times the value of the next closest carbonyl-containing-tetrazole molecules (**6**, **7** and **18**). As of yet, this dramatic increase in dissolution cannot be accounted for. The only difference between these molecules is the presence of the ester functionality, which is unique within the series. Though complexation may account for some of the nucleation decreases presented throughout the DLS results, it clearly does not account for the majority of the inhibition observed in the morphology or nucleation data, which is thought to be due to the direct inhibition of the nuclei, by altering the surface free energy of the nuclei. In particular the proposed mechanisms by which the aforementioned tetrazole molecules impede crystallisation are presumed to be *via* adsorption, electrostatic interactions and hydrogen bonding between COM and the tetrazole functionality.

## 5.4 Conclusion

DLS and dissolution data have clarified the strength of inhibition each tetrazole has on nucleation and their capabilities to interact with calcium during nucleation and crystal growth. From the DLS data, nucleation rate was analysed, the result supported the morphology data where the tetrazole molecules that impeded nucleation considerably were also those that impacted morphology the greatest as shown by results from ***Chapter 4***, (these included tetrazoles **11**, **16** and **21**). Though

many others inhibited nucleation strongly, this was not always reflected in the morphology of the crystals. Likewise, dissolution results indicated that those with the strongest complexation of calcium also impacted on the nucleation significantly, which in a cascade effect, was reflected in the morphological study, tetrazole **11**, again was the standout amongst these.

The general trend of increased dissolved calcium as concentration of tetrazole increases during dissolution experiments permits confidence in the results. The lowering of the supersaturation due to complexation of $Ca^{2+}$ from solution that would reacted to form COM crystals can be observed in many of the morphological studies in C***hapter 4***. However, as mentioned previously, an atypical trend can also be seen across several tetrazole molecules in ***Figure 5.7***, such as tetrazole molecules **2**, **18** and **21**. In these tetrazole molecules as additive concentration increased, the dissolved calcium found in solution by ICP-AES decreased. The formation of less soluble Ca-Tetrazole complexes may precipitate from solution, thus resulting in the removal of dissolved calcium species (***Figure 5.7***). The functional groups that inhibited strongest were found to be the bis-tetrazole containing species **8**, **9** and **11**, with some potent calcium complexation also seen for those without multiple tetrazole moieties, such as tetrazoles **1**, **6** and **16.** These molecules are believed to impact on the surface free energy of the nuclei and thereby impact nucleation rates. However, what is clear is that each of the tetrazole species can impact on nucleation of COM directly, with minor structural additions potentially substantially changing the potency of inhibition. Specifically, the inclusion of nitrogen atoms into the aromatic structure of the additives can improve the complexation and adsorption mechanisms resulting in stronger nucleation inhibition. The tetrazole compounds and their varying structures are vital in defining the mechanisms at play and their relative strengths. Once all the mechanisms have been discussed, including aggregation mechanisms in ***Chapter 6***, and direct observations of crystal growth in ***Chapter 7***, *via* an AFM investigation, the SAR study will be complete.

# 6 Aggregation mechanism investigation of tetrazoles within calcium oxalate crystals

## 6.1 Introduction

Raman spectroscopy is commonly utilised for investigating crystalline materials and is complementary with infrared spectroscopy as vibrational spectroscopies have the capability of determining crystal compositions. In this study, Raman is used to discriminate between the two most common forms of calcium oxalate found in kidney stones, COM (whewellite) and COD (weddellite). Thus the technique can be extremely useful for determining whether crystals grown in the presence of all tetrazole molecules in the series are in fact COM or COD. In addition, as determined in ***Chapter 3***, each tetrazole species also has a unique Raman spectrum, and this spectrum can change with respect to changes such as adsorption or aggregation state. This makes Raman an ideal method for determining the impact of the tetrazole species on calcium oxalate crystals.

## 6.2 Dissolution of COM in the presence of 1H-5-phenyltetrazole

SEM micrographs of COM grown in the presence of **3** showed signs of "hollowed out" crystals after the standard 3 day crystallisation time period. The dissolution occurred (***Figure 6.1***) at the largest surface, the (100) face. To investigate this effect, crystals were grown at increasing crystallisation time periods, both for the control and in the presence of **3**, 1H-5-phenyltetrazole. Prolonged time periods (up to 30 days with intervals of 3 days) were conducted to determine the following:

i) Whether in the presence of the additive **3**, the crystals grew in the hollowed out manner

ii) And after the COM dissolved whether some other solid phase re-precipitated.

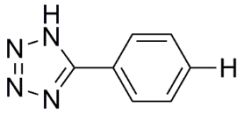


3

***Figure 6.1***: SEM micrographs of COM grown in the presence of **3** (6.84 mM) and its structure.

Firstly, control experiments were examined to determine whether the prolonged crystallisation time affected the thermodynamically stable species that precipitated throughout the experiments or led to microbial growth that would explain the hollowing out. The control crystallisation of COM did not show signs of "hollowing out". ***Figure 6.2a*** and ***Figure 6.2b*** display SEM micrographs of COM crystals after 3 days and 21 days without additives, respectively. At no point through the analysis of the COM crystals with optical microscopy, were other species of calcium oxalate present, only COM precipitated through experimentation (***Appendix A5.1***).

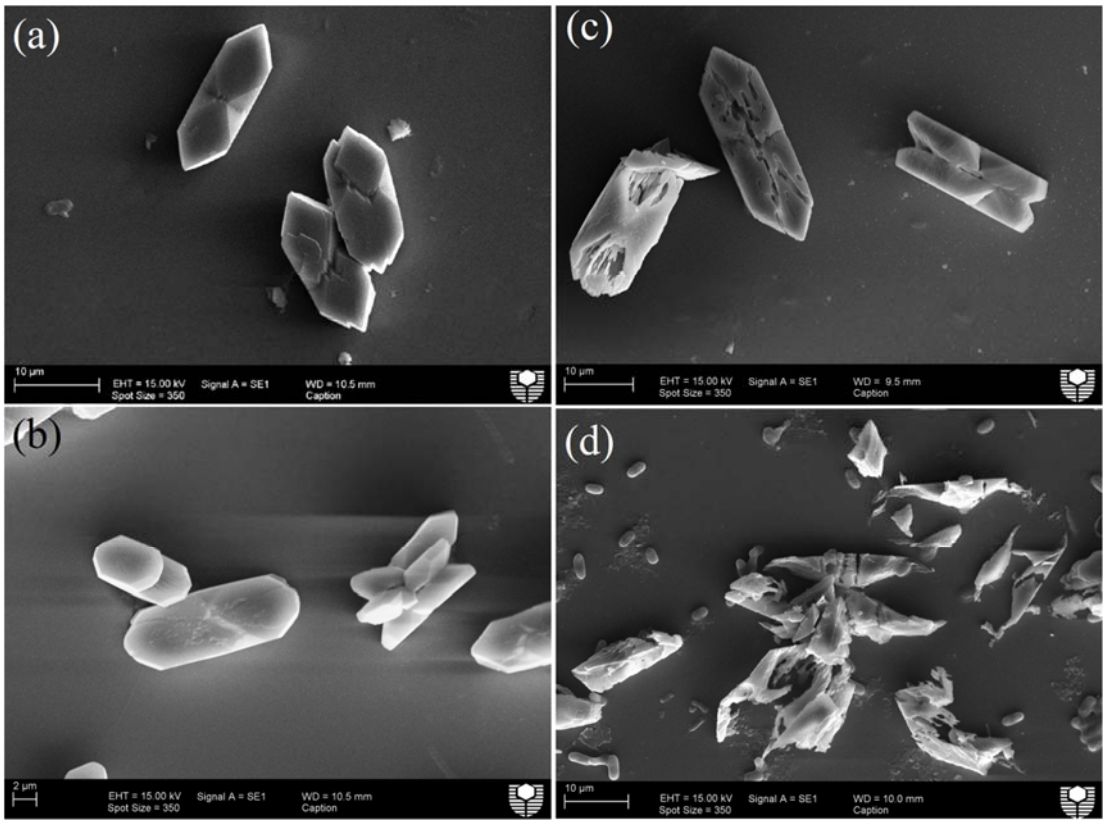


***Figure 6.2***: SEM micrographs of COM crystals grown (a) without additives after 3 days, (b) without additives after 21 days, (c) in the presence of tetrazole **3** (6.84 mM) after 3 days, and (d) in the presence of tetrazole **3** (6.84 mM) after 21 days.

Secondly, crystals grown in the presence of **3** were examined over the 30 day experimentation time. Initially, the majority of particles formed were the thermodynamically stable COM with morphologies that were also equivalent to the control particles but from 3 days and onwards, dissolution of the interior of the particles can be observed (as shown in ***Figure 6.2c***) and is a reproducible effect in the presence of **3**. After 19 days few particles with COM shape remained (***Figure 6.2d***), and there was microbial action evident as the laboratory conditions were not sterile. This issue persisted even when we attempted to sterilise by filtration (filtering all solutions using a 0.2 µm pore membrane). Finally, experiments with sodium azide (1% w/v) present, which acts as a biocide, prevented the action of microbes and resulted in the elimination of all hollowed crystals (***Appendix A5.2***), with crystals returning to control-like morphology (***Figure 6.3***). Thus the presence of microbes

was confirmed as the source of the dissolution mechanism in the presence of **3**. No other tetrazole molecules in the entire series interacted in the same way.

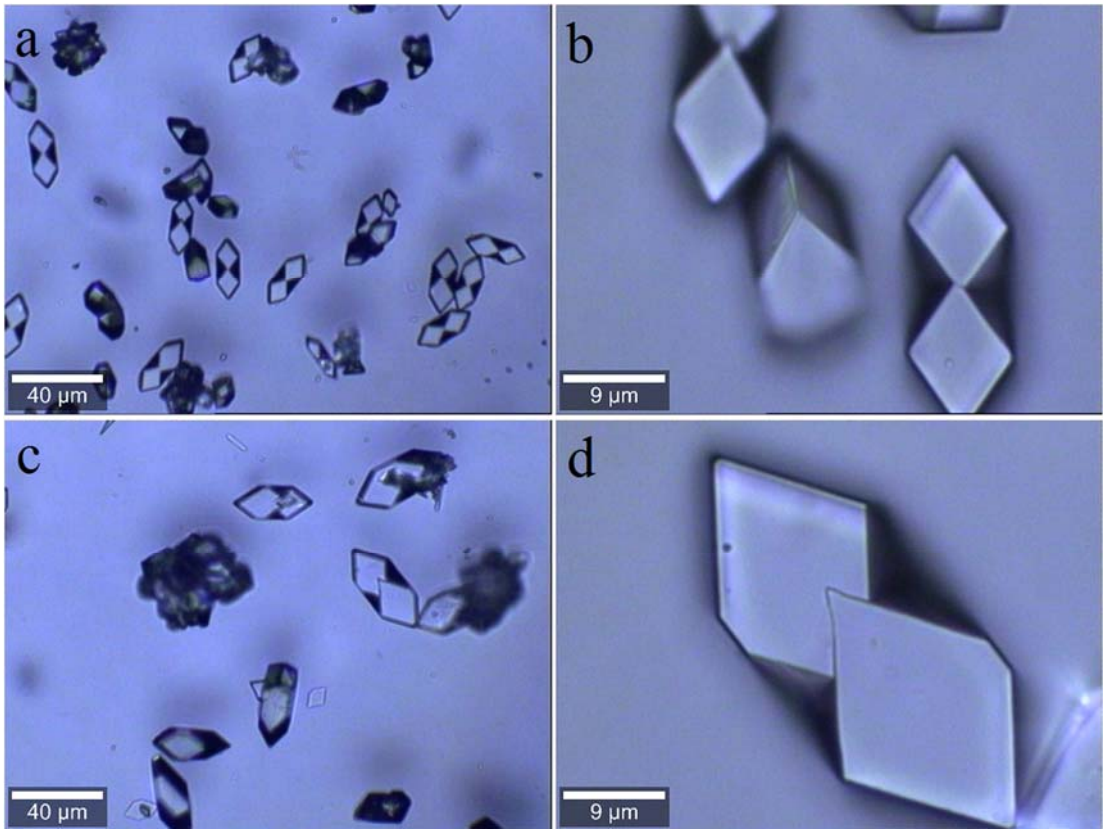


***Figure 6.3***: Optical images of COM crystals grown with sodium azide (1% w/v) in the presence of **3** (6.84 mM) after (a) 3 days, 20x magnification, (b) 3 days, 100x magnification, (c) 30 days, 20x magnification, and (d) 30 days, 100x magnification.

The prolonged experimentation in the presence of sodium azide (1% w/v) removed all trace of hollowed particles and thus the possibility that the dissolution was solely due to the additives adsorption mechanisms affecting the formed crystals can be ruled out. Sodium azide has been used for decades as a biocide in crystallisation due to its predictable impact and almost insignificant effects on the crystallisation of materials.[223] Over the 30 day experiment in the presence of **3**, no evidence of calcium oxalate re-precipitation was observed (of any form), with or without azide present. The mechanism of interaction between the microbes and COM is therefore believed to occur *via* consumption of the tetrazole species and oxalate,

which resulted in the weakened crystal structure and subsequent dissolution of calcium (and oxalate) ions back into solution. Consumption of the oxalate by microbial action meant no re-precipitation was observed. Additionally, the presence of **3** does not lead to COM particles growing in this hollowed out fashion and that therefore the most likely mechanism is that the tetrazole molecule is incorporated in the crystal. However, the reason or reasons behind the microbes' affinity for tetrazole **3**, 1H-5-phenyltetrazole (which was not observed under control conditions), is still unknown.

## 6.3 Confocal Raman microscopy (CRM) of COM

To confirm that the tetrazole molecules were incorporated into the crystal structure and that the microbes were affecting the crystals in this extremely specific way and, further to investigate the interactions of the other tetrazole molecules within the series with COM, CRM was utilised. As confocal Raman has the capability to image cross sections of the crystals' depth, analysis of crystals without "hollowing out" at <3 days was attempted. These particles showed Raman spectra (***Figure 6.4***) with a significant degree of fluorescence. Further investigation found that this fluorescence only occurred when COM was grown in the presence of tetrazole molecules, compared to control crystallisations experiments.

The peaks located at 499 and, the main characteristic peaks for pure tetrazole **3** (***Figure 6.4a***) at 1411 and 1608 $cm^{-1}$ represent stretching frequencies of the tetrazoles N-N and N=N bonds. Likewise the characteristic peaks of COM (***Figure 6.4b***) at 504, 895, doublet 1462, 1489 and 1629 $cm^{-1}$ correspond to C-O and C=O stretching frequencies and can be used to compare with the peaks of COM crystals grown in the presence of **3** (***Figure 6.4c***). The peak at 892 $cm^{-1}$ pertains to COM only (***Figure 6.4c***). While the signals at 1352, 1622 $cm^{-1}$, including the general fluorescence observed throughout the spectrum belong to tetrazole **3**. The frequencies of the characteristic peaks from the tetrazole shown in ***Figure 6.4a*** are

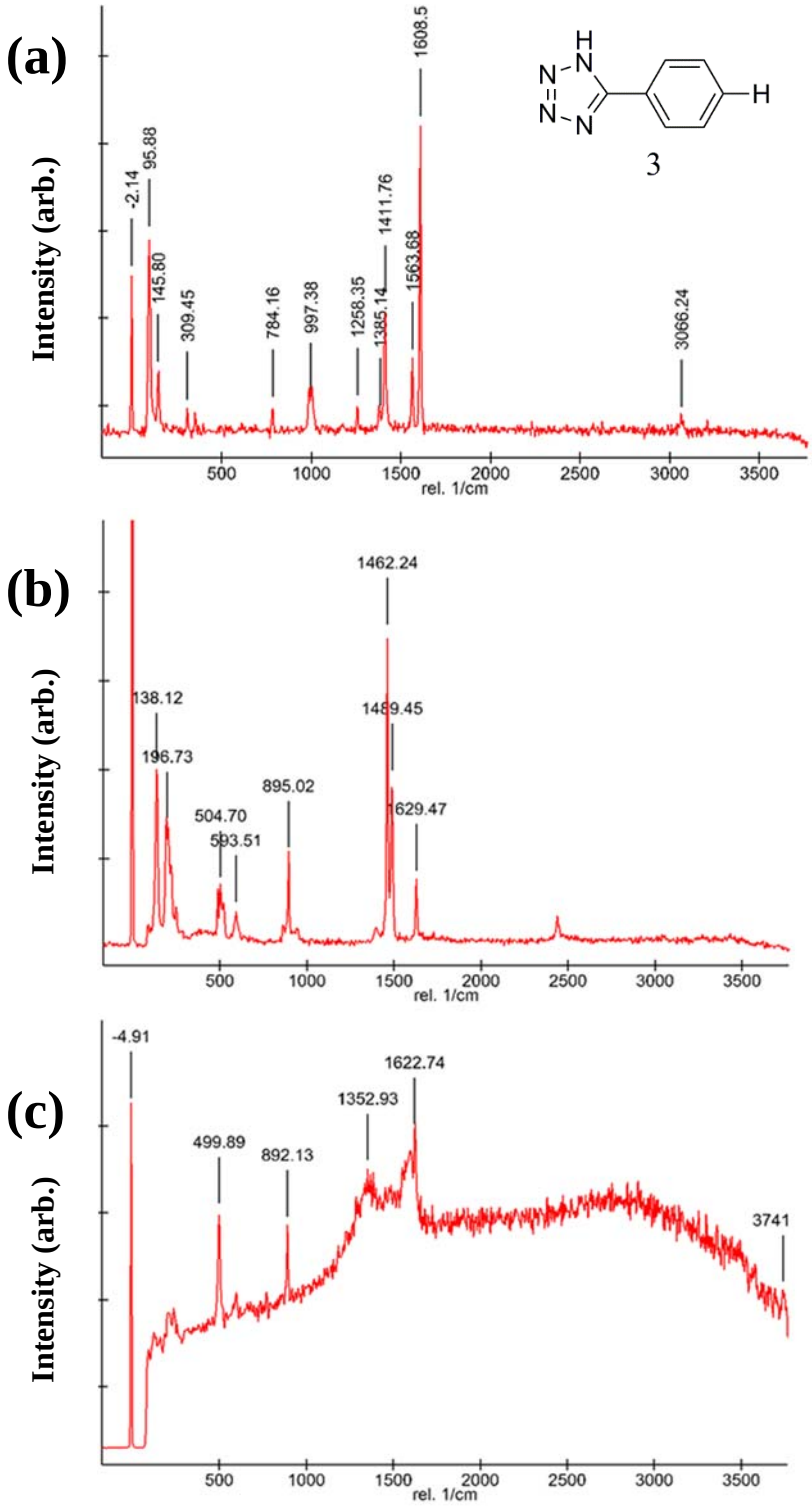


***Figure 6.4***: Raman spectra of (a) Tetrazole **3** synthesised in-house, (b) Control COM at crystal surface, and (c) COM grown in the presence of **3** (6.84 mM).

believed to be modified by the impact of the fluorescence and its bonding environment and are therefore shifted in ***Figure 6.4c***.[224] The bands at 1352 and 1622 $cm^{1}$ are different to the control COM crystal's Raman spectrum (***Figure 6.4b***), which

show the expected doublet for the monohydrate and does not emit such broad fluorescence. This implies that the tetrazole species is present in the crystal prior to hollowing occurring. Thus, the data suggests that it was the incorporation of tetrazole **3** that, in conjunction with the interaction of the microbes, causes the "hollowing out".

COM grown in the presence of the entire series of tetrazole molecules were analysed to determine whether incorporation within COM was limited to tetrazole **3**. CRM, in combination with a photophysical investigation has been employed to give insight into the interactions between COM and each tetrazole. Significant interactions were observed between the tetrazole species themselves during crystal growth. These interactions were sufficiently strong for aggregation of the tetrazole molecules to one another to occur within the crystal during crystallisation (***Figure 6.5***). Initially, it would be expected that tetrazole molecules would adsorb to the surface of COM, which has been observed for the majority of tetrazole molecules *via* electrostatic interaction, hydrogen bonding or chemical bonds (calcium complexation). The subsequent change in the Raman frequencies reflect the change in bonding environment (***Figure 6.5b***) compared to the pure tetrazole molecule. This includes the interactions of the tetrazole molecule with calcium oxalate and the subsequent fluorescence, which leads to broad feature being observed rather than distinct bands. Thus, the continued crystal growth of COM further surrounds the adsorbed tetrazole molecules and based on the results observed *via* CRM (***Figures 6.4*** and ***6.5***); the bonding is sufficiently strong enough that the tetrazole molecules become completely embedded within the crystal.

Raman spectra presented in ***Figure 6.5*** correspond to COM formed in the presence of **17**. In the spectra provided, the evidence of the interaction between COM and the tetrazole species will be elucidated. The characteristic peaks for COM are still present (***Figure 6.5a***) but the signals are diminished in intensity due to the lowering of laser intensity to avoid excessively exciting the tetrazole species (which fluoresces quite strongly in the regions where the characteristic peaks are visible). In ***Figure 6.5a*** the spectrum was taken at the surface of the crystal, which in contrast to ***Figure 6.5b*** illustrates the capabilities of CRM. This spectrum was taken a few micrometres within the crystal using the confocal ability of the instrument and allows for the observation of the fluorescence and Raman signals from the tetrazole at subsurface

layers. The presence of these Raman vibrational frequencies indicates that the tetrazole species were present within the crystals and not solely adsorbed to the surface, otherwise the Raman spectra within the crystal would have reflected the presence of COM only.

For all the Raman spectra collected of COM containing tetrazole molecules, the main signals for the tetrazole species are found at ~1340 $cm^{-1}$ and 1620 $cm^{-1}$, these peaks are believed to belong to either the C-N or N-N stretching frequencies of the tetrazole, see ***Figure A1.17*** for the Raman of pure **17**. The process of adsorption and fluorescence changes the characteristic peaks to different positions and broadens them relative to those shown in ***Figure A1.17***. As mentioned above, the laser intensity was reduced in order to see the structure of these bands better and upon increasing the intensity of the laser the fluorescent properties of the tetrazole species mask the peaks for both the tetrazole molecule and COM. As presented, the Y-axis indicates the intensity of the chosen Raman signals monitored during collection of the spectrum against the distance through the crystal (in micrometres, on the X-axis). CRM enables the illustration of the intensity of the characteristic signal for the COM (blue trace – 1470 $cm^{-1}$) and the tetrazole (red trace – 1340 $cm^{-1}$) allowing for a comparison between the two species' intensities with respect to the position inside the COM crystal. Thus determination of the location of the tetrazole-containing species within the crystal itself can be achieved quite simply. The tetrazole species have been found to reside closer to the surface of the COM crystals and relatively less found towards the centre of the crystal, the working hypothesis for this observation is that at the early stages of crystallisation:

i) the crystal faces of COM are not well developed for the tetrazole molecule to adsorb onto specific faces and

ii) during this time competition between the oxalate and tetrazole species occurs, the competition favours the oxalate species due to the initial high supersaturation.

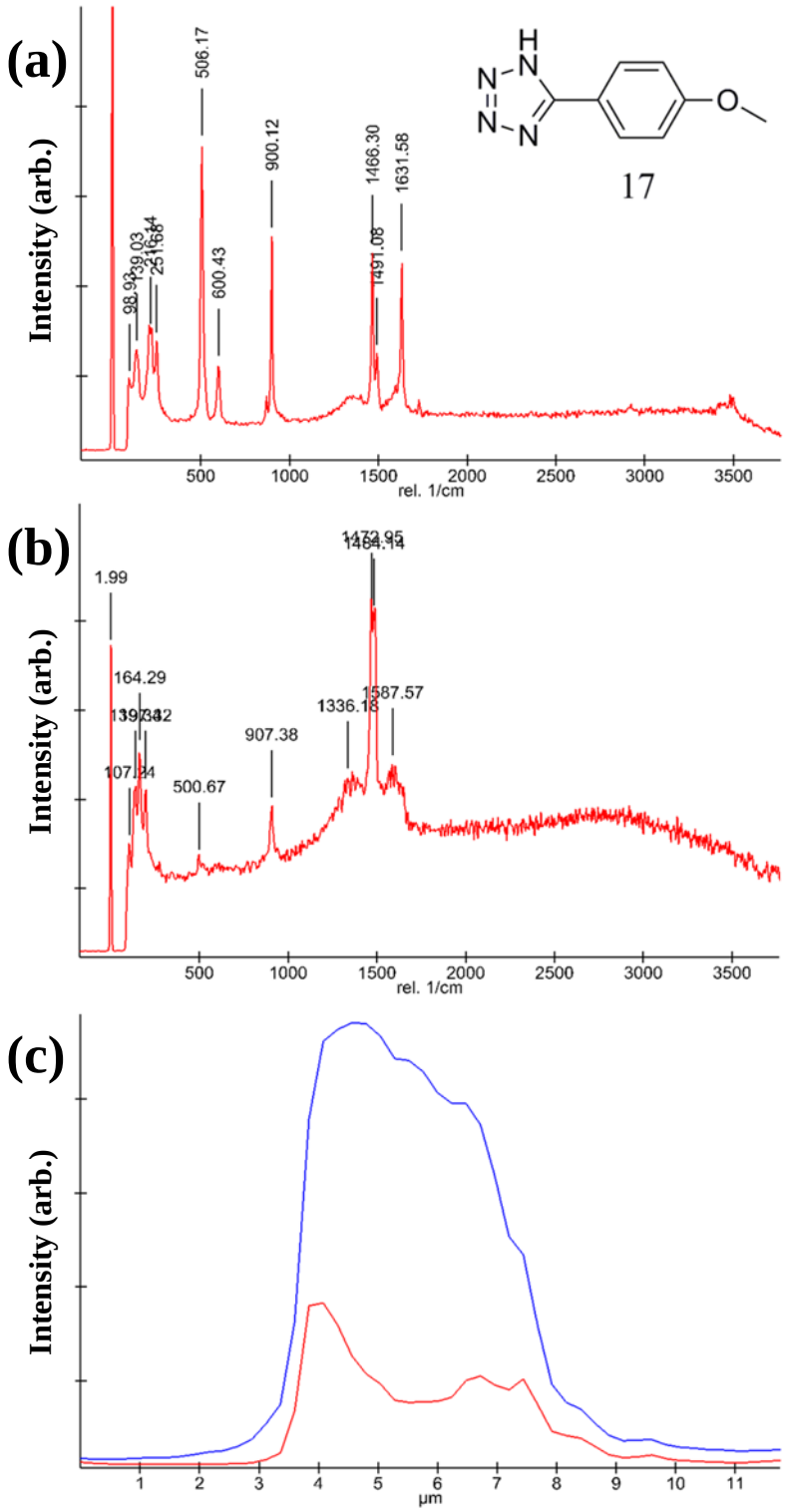


***Figure 6.5***: Confocal Raman spectra of COM grown in the presence of **17** (5.78 mM) imaged (a) at the COM crystal surface, (b) within COM crystal (~4 µm beneath crystal surface), and (c) intensity of Raman signals *vs* their position within crystal (µm), COM peak (1470 $cm^{-1}$, blue trace), tetrazole peak (1340 $cm^{-1}$, red trace), and the location of the crystal surfaces lie at ~3.5 µm (top surface) and ~8.0 µm, the bottom of the crystal. Structure of **17** shown top right. Refer to ***Appendix A5*** for micrographs taken of crystals before analysis.

The interaction between the tetrazole molecule and crystal is believed to occur *via* adsorption to the surface and subsequent growth of COM around the tetrazole species resulting in what is observed in our system. The tetrazole species are included into the crystal itself as verified by CRM. Almost every tetrazole molecule in the series was found to be included into COM after analysis by confocal Raman, the only exceptions to this included tetrazoles **11**and **12**, which significantly inhibited crystal nucleation, leaving few COM particles to analyse. Additionally, tetrazole **10** impacted the morphology of COM resulting in extremely thin crystals (***Figure 4.4***) with no tetrazole signals observed within the crystals themselves, only surface adsorbed tetrazole was present.

## 6.4 Photophysical investigation of tetrazoles within COM

What was common across the series of tetrazole molecules was the presence of very fluorescent Raman signals when the crystals were not washed before Raman analysis. This led to the subsequent washings of the crystals with water before analysis. In all cases this removed the majority of surface Raman signal observed, which corresponds to the removal of surface adsorbed (physi-sorbed) tetrazolate species. What was more surprising was that employing CRM to determine the confocal properties of the Raman spectrometer to probe the crystal, what was found indicated that significant Raman signals from tetrazole species were still present. This structure-less Raman signal is proposed to be due to the presence of pi-stacked tetrazolate species within the COM crystal. The presence of the tetrazole species within the crystals was investigated further through a photophysical investigation (as tetrazoles are known to be emissive) and the results are as follows.

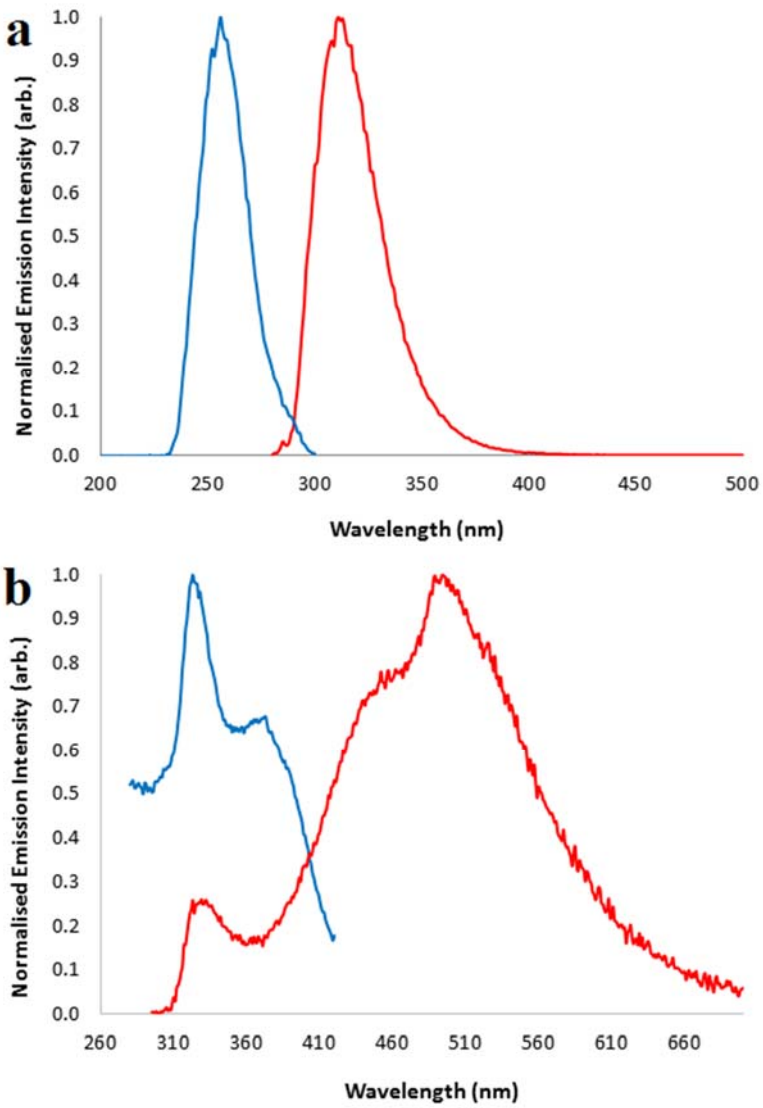


***Figure 6.6***: Excitation (blue) and emission (red) profiles of tetrazole **17** in (a) solution (water) at $10^{-6}$ M concentration, and in (b) the solid state (both shown in ***Appendix 3***).

The excitation and emission spectra are presented in each figure for tetrazole **17** in several different environments. ***Figure 6.6a*** represents the tetrazole species alone in an aqueous solution with one emission band, that of the $\pi\pi^*$ transition, which is common for species with extended interannular conjugation (covered in more detail in ***Section 3.2.3***). The solid state tetrazole provided the emission and excitation profiles shown in ***Figure 6.6b***. It can clearly be seen that this is very similar to the emission profile seen when the COM crystals are grown in the presence of the tetrazole molecule (***Figure 6.7a***). Minor differences in the intensity

of the aggregated peaks and the ππ* transition are thought to be due to the different environments in which they are situated. Emission of COM crystals alone were also examined and found not to emit at all, ruling out emission from the crystals accounting for any change observed in ***Figure 6.7a***.

Finally, to verify that the aggregated emission profile was not due to a possible protonated-deprotonated interaction of the tetrazole species, several molecules from the series were dispersed in PMMA polymers in their protonated or deprotonated states. The results are shown for the tetrazolate species **17** in ***Figure 6.7b***, while the protonated species was found to be identical (***Figure 6.7c***). In the case of the COM crystal the tetrazole species must therefore be aggregated. A lack of an aggregated state in the protonated and deprotonated species in PMMA verifies that the aggregation phenomenon is solely related to the interaction of the tetrazole additives functionalities to one-another. This aggregation mechanism of the tetrazole molecules' aromatic and π system to stack within COM is seen in all of the tetrazole species investigated.

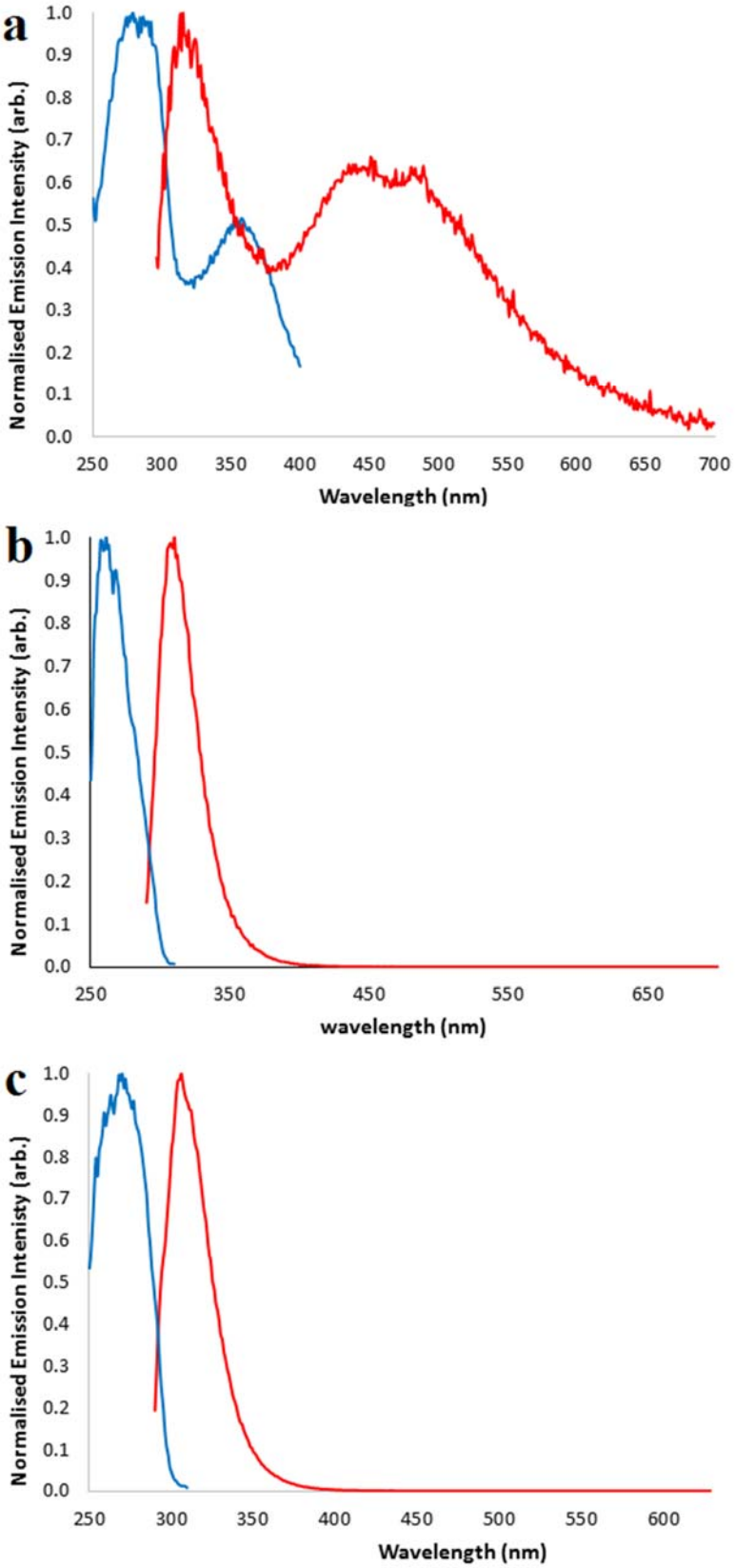


***Figure 6.7***: Excitation (blue) and emission (red) profiles of tetrazole **17** (a) within COM crystals grown in the presence of **17**, (b) within PMMA in the deprotonated form, and (c) within PMMA in its protonated form.

## 6.5 Conclusion

The interpretation of the confocal Raman microscopy (CRM) results indicates that the technique is extremely useful in determining interactions of additive species within the crystals. This includes the ability of CRM to probe and locate additive species within the crystal structure based on their interactions with the crystalline material and their own unique vibrational modes. This technique has proven to be extremely efficient in determining the hydration state of calcium oxalate crystals grown in the presence of 26 tetrazole molecules, in addition to characterising the additive species and their environments within COM. It was determined that the tetrazole molecules can adsorb onto COM and be subsequently incorporated into the crystal structure.

The photophysical investigation and exploration using CRM facilitated in probing the interactions between the tetrazole series and COM crystals. More importantly, it was determined that the strong adsorption interactions allow for aggregation of the tetrazole molecules within the crystal during crystal growth. This is a unique mechanism of interaction which still has many aspects to be fully understood. An AFM investigation to directly observe the adsorption will be discussed next to try to further elucidate this mechanism. Understanding of all the interactions involved will allow for much clearer determination of the extent of the morphological impact the adsorption process has alone, with or without the aggregation occurring.

# 7 Growth studies of calcium oxalate utilising atomic force microscopy (AFM)

## 7.1 Introduction

*In situ* AFM was used to elucidate the effects of inhibitors (or promoters) on the crystal growth of COM surfaces at a microscopic level. AFM has proven to be a valuable tool for investigating growth kinetics on a near molecular resolution.[144,225,226] In this chapter, the technique is used to collect time-resolved images of step advancement in the supersaturated solutions described in ***Section 2.2.5*** (S = 6.8) in the absence or presence of several tetrazole molecules in the series. All AFM imaging was performed on the crystallographic (010) surface of COM, all snapshots in the figures throughout this chapter use the AFM height sensor channel, and thus the brightest areas represent the higher surfaces while the darker shaded areas are lower surfaces. The main scanning mode utilised in this AFM study was ScanAsyst®, a PeakForce Tapping® mode. This tapping mode allows for measurement and capture of high resolution images in both air and fluid. In this mode the AFM is able to continuously self-adjust the forces responsible for the sample tapping interaction, keeping the force minimal, and reduces sample-cantilever impact.

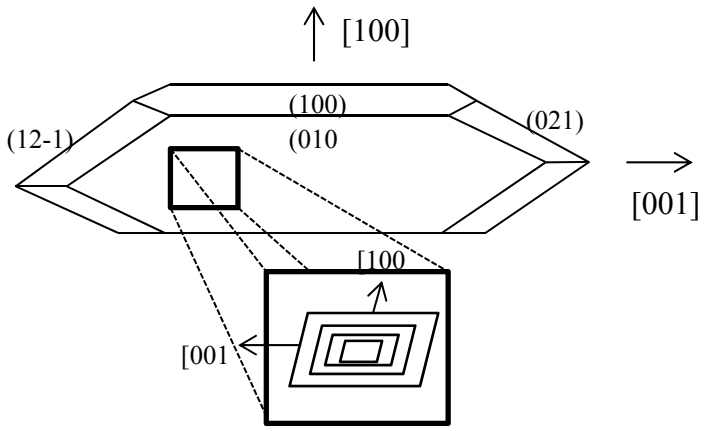


***Figure 7.1***: COM crystal with the respective faces labelled. AFM imaging occurred on the (010) face throughout experimentation, the growth hillock shown in enlarged section presents the typical shape of hillocks on the (010) face with the [001] and [100] growth directions of the steps labelled.

## 7.2 Results and Discussion

### 7.2.1 *In situ* AFM imaging of control COM

In the early stages of growth, COM (010) surfaces are composed of square hillocks (***Figure 7.2***) bound by the (120), (02-1), (-120) and (021) faces.[68] After ~15 minutes of a constant flow of growth solutions (supersaturated after mixing), the square or parallelogram shaped hillock becomes much more rounded and the steps become more uniform. Growth directions can be referred to from ***Figure 7.1***. Images from 0 minutes through to 30 minutes of control crystal growth with screw dislocations defined by the [100] and [001] steps are observed. The step that propagates along the [100] direction is thus labelled [100] (***Figure 7.1***), while the other step of interest, which propagates along the [001] direction is labelled so. The rates of growth for the steps were calculated by measuring the step progression in one direction, with either upwards or downwards scan directions. In this case, upwards scans were arbitrarily chosen with which to measure step velocities. The centre of the screw dislocation was used as the reference point from which the measurements were made. The velocities of the [100] growth direction in the presence of pure calcium chloride and sodium oxalate solutions was determined to be $0.07 \pm 0.03$ nm $s^{-1}$ while the [001] growth direction grew at a rate of $0.21 \pm 0.10$ nm $s^{-1}$. The average step height across all control COM samples was measured and determined to be $1.20 \pm 0.08$ nm. The value for the step heights measured corresponds to multiple unit-height steps, in this case triple steps. The formation of these multi-unit steps is commonly referred to as step interlacing or macrosteps.[227] The values mentioned above for the "control" experiments can be used to compare to the values of crystal growth obtained in the presence of an additive, and thus whether the organic molecules affected the growth rates can be determined.

In addition to the step growth velocities and step height parameters with which the results of the *in situ* AFM experiments can be compared, once inhibitors are added to the solutions, visual impacts should also be observable. The growth mechanisms most evident upon inhibition of the growth steps include, step bunching (which will be reflected by step height increases) and step pinning (reflected by growth velocity suppression and curvature or scalloping of the step).[100]

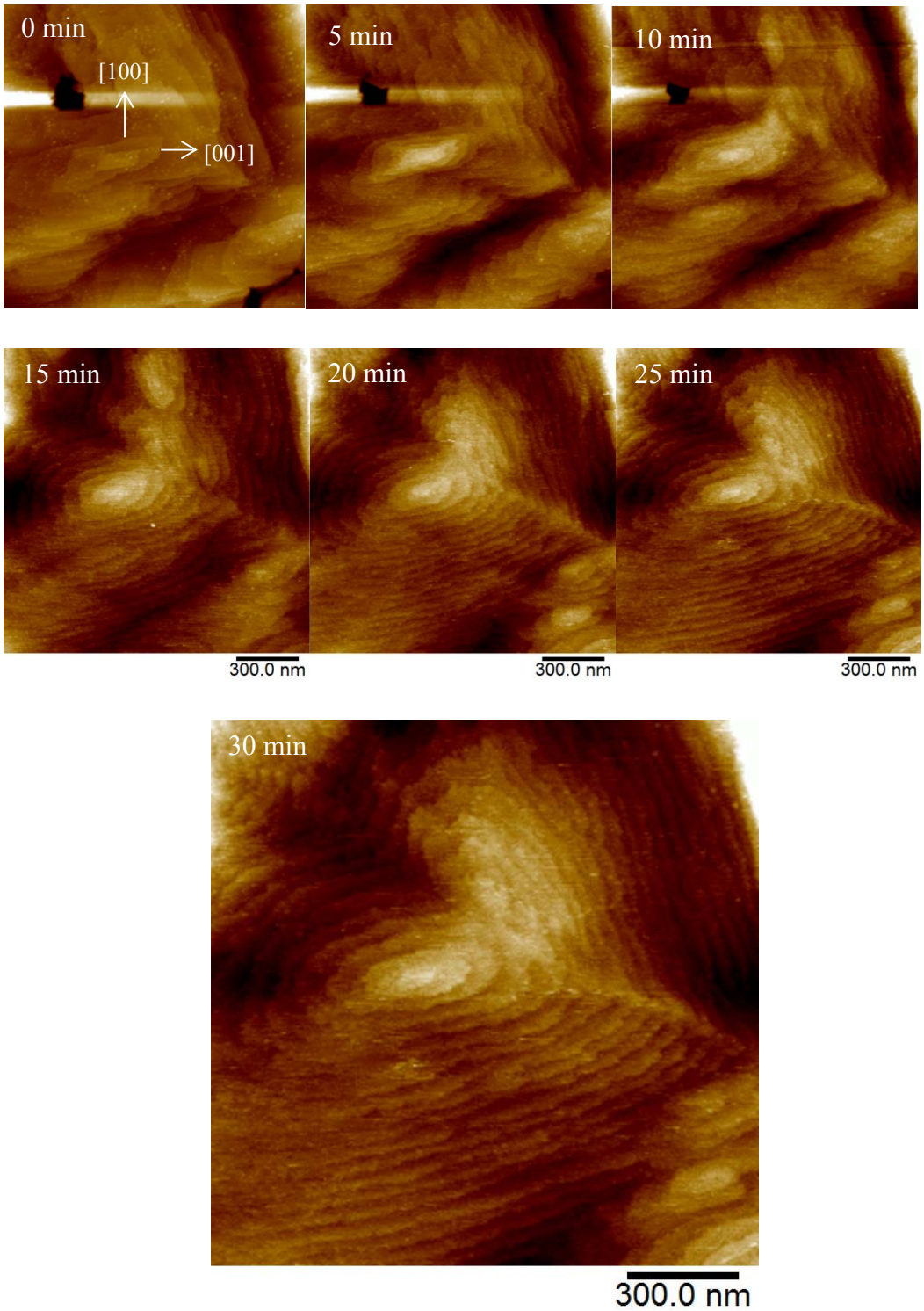


***Figure 7.2***: Snapshots from time-resolved *in situ* AFM imaging of hillock growth on the COM (010) face in supersaturated CaOx solutions without additives.

Step pinning and step bunching can be directly observed with AFM in the presence of additives throughout this chapter. Based on the results of each tetrazole

molecules' impact on the crystal growth of the COM (010) face, mechanisms previously discussed in ***Chapters 4***, ***5*** and ***6*** such as complexation will be further expanded on in order to elucidate their importance. All growth rates in the presence of the tetrazole molecules will be compared to the control values to determine whether individual faces are inhibited or promoted and whether any step specificity occurs related to the tetrazoles structures. All *in situ* AFM snapshots presented have been clipped into video files and can be found in ***Appendix 6***.

### 7.2.2 *In situ* AFM imaging in the presence of tetrazoles

For all AFM experiments conducted, measurement of the pure control system preceded each run in the presence of tetrazole molecules. This ensured several factors, first that growth of the COM surface was proceeding at a controllable rate using the "pure" supersaturated solutions. Secondly, that the PeakForce Tapping® mode was sufficiently stable and resolution of captured images adequate to observe the required mechanisms upon subsequent addition of the tetrazole molecules to the *in situ* system. Lastly, the measured growth rates before addition of the tetrazole molecules are compared to the rates of pure solution after the addition of the tetrazole molecules to determine whether surface poisoning was recoverable. In addition, each crystal may contain different numbers of defects and other factors which may alter the growth rates measured.

As investigated by De Yoreo et al.,[68,228] citrate, a dicarboxylic acid containing COM inhibitor, is much more potent at inhibiting the (-101) face compared to the (010) face for two reasons. First, the orientation of the oxalate groups on the (010) surface can repel the strongly electrostatic dicarboxylic acid ends of citrate. Secondly, the configuration of calcium sites of a growing step (presented in ***Figure 7.3***) are present on the [-100] step of the (010) face and can act as a site for adsorption. As citrate has a nonplanar conformation, the molecules are relatively rigid and thus the three carboxylic acids cannot easily rotate to bind to the surface. The issues faced by citrate may be lessened in the case of our tetrazole series as the tetrazole molecules are planar molecules and thus could be relatively have greater geometric relationships to the crystal steps and terraces. Additionally, none of the

tetrazole molecules in the series have three strongly electrostatic functional groups with which the surface oxalate groups on the (010) surface would repel. The tetrazole molecules in the series investigated to promote or inhibit crystal growth with AFM of the COM (010) surface include tetrazole molecules **5**, **6**, **10**, **12**, **13**, **14**, and **17**. These tetrazoles were chosen due to the slight changes in structure (**12**, **13** and **14**) as well as **6** and **10**. As such the slight changes may provide clues as to the types of mechanisms of crystal growth inhibition including binding interactions between the different functional groups present in the subset.

The graphic (***Figure 7.***3) from De Yoreo *et al.*[68] illustrates the binding of a citrate molecule on the [100] step on the (010) face, of particular note are oxalate species extending beyond the terrace of the (010) plane. In this case the citrate is repelled due to the electrostatic interactions between the citrate molecule and the oxalate's carboxylate functionality. The citrate molecules were found to have much weaker surface binding energy for the [-100] step on the (010) face at -90.2 kJ/mol, compared to the [101] step on the (-101) face at a much higher -166.5 kJ/mol.[68] Based on these molecular interactions, the tetrazole molecules measured are presumed to bind more strongly to steps on the (010) face than citrate molecules, as measure by De Yoreo and co-workers. It is assumed that the tetrazoles studied (**5**, **6**, **10**, **12**, **13**, **14** and **17** are either repelled less by the oxalate species or the attraction of the tetrazole functionality to $Ca^{2+}$ ions is sufficiently strong to overcome the repulsive forces of the oxalate ions exposed on the (010) face. Due to the strength of the molecules to complex calcium as discussed in ***Chapter 5***, it is believed that the interactions of the tetrazole molecules are sufficiently strong to adsorb to the COM (010) surfaces steps. The relative strengths of the tetrazole molecules above to complex calcium increased from **5** < **14** < **12** < **13** < **17** < **6** < **10** (***Figure 5.7***). Additionally, the tetrazole molecules in this study in general, have fewer negatively charged functional groups with which to repel the oxalate rich surface, and consequently are more likely to be able to adsorb to the surface of COM.

Crystal poisoning in the presence of impurities such as magnesium,[229,230] zinc and iron ions or in the presence of organic/inorganic molecules inhibits crystal growth *via* competition at growth sites (kinks, step edges). The following work with the aforementioned seven tetrazoles, show various levels of crystal poisoning. Adsorption of the tetrazoles onto the kink and edges of the steps can occur by both

physisorption and chemisorption. Dissolution of the surface *via* complexation of the tetrazole molecule to calcium ions in the solute can also account for the COM crystal growth rate changes. ***Figure 7.4*** shows images of *in situ* AFM experiments on the [001] step on the COM (010) face in the presence of tetrazole **5** and **10**.

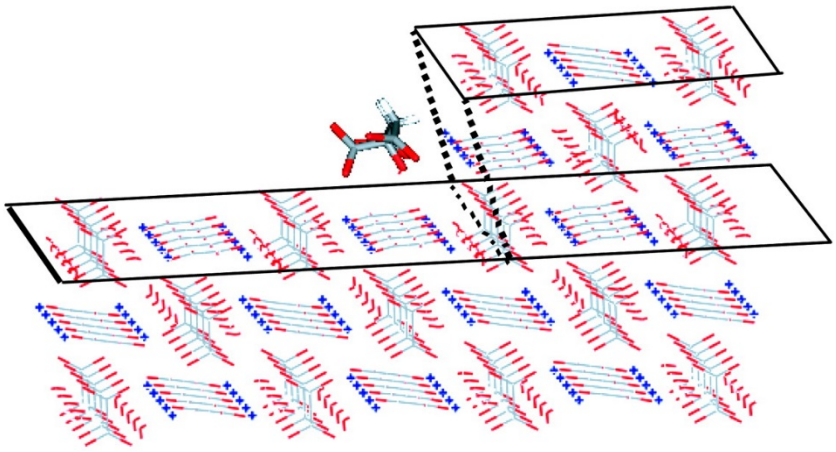

***Figure 7.3***: Geometry of a citrate molecule binding to the [100] step in the minimum energy configuration on the (010) face. Reproduced with permission from the work of De Yoreo *et al.*[68]

As no hillocks were observed in ***Figure 7.4a***, growth rates of the [100] step were impossible to measure. Initially, the growth rate of the [001] step was measured at 0.19 ± 0.10 nm $s^{-1}$ (control average of 0.21 ± 0.10 nm $s^{-1}$) while injecting additive-free supersaturated growth solutions resulting in macrostep heights of 1.25 nm (***Figure 7.4a***). After 20 minutes of control growth, tetrazole **5** (0.42 mg/mL) was added for 30 minutes resulting in the promotion of the growth rate of the [001] step to 0.43 ± 0.09 nm $s^{-1}$, twice the growth rate compared to the rate in the absence of **5** (***Figure 7.4b***). Upon increasing the concentration of **5** in solution from 0.42 mg/mL to 2.72 mg/mL for a period of 60 minutes (***Figure 7.4c***) the crystal growth in the [001] direction returned to a control-like rate of 0.26 ± 0.12 nm $s^{-1}$. Additionally, visible recession of steps was evident believed to be due to dissolution of the crystal surface by the additive. ***Figure 7.4b*** shows mostly steps in the [001] direction, upon the addition of **5** at higher concentration, receding [100] steps are produced (***Figure 7.4c***). After subsequent removal of the tetrazole inhibitor from growth solutions (40 minutes later) the steps in the [001] direction return to those observed before introduction of the tetrazole species, with slightly elongated terraces between steps

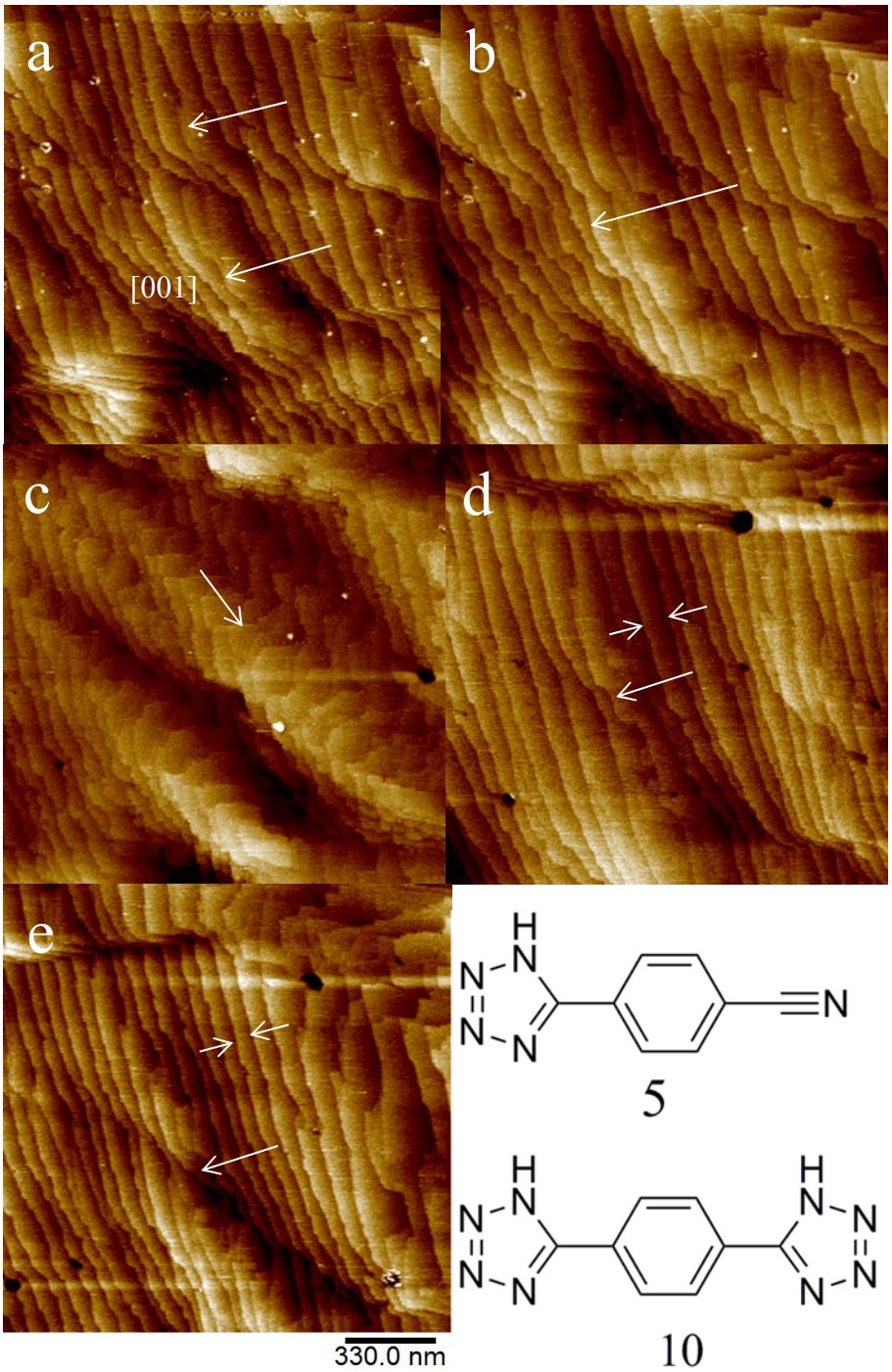


***Figure 7.4***: Snapshots from time resolved *in situ* AFM imaging of COM steps at constant supersaturation (a) without additives at 20 minutes, (b) in the presence of **5** (0.42 mg/mL) after 30 minutes, (c) in the presence of **5** (2.72 mg/mL) after 60 minutes, (d) regrowth without additives- 40 minutes after pumping with tetrazole **5** finished, and (e) in the presence of **10** (2.85 mg/mL) after 40 minutes.

(***Figure 7.4d***). The extension of the distance between steps is a result of the adsorption of the tetrazole species to the surface still impacting the step progression. This is evidenced by the suppressed step velocity in the [100] direction to 0.06 ± 0.04 nm $s^{-1}$ after 40 minutes. Although the adsorption was not sufficiently strong to completely stop re-growth in pure solutions, adsorption of the tetrazole molecule on the COM (010) face has been shown to occur as has been observed through these AFM results. Furthermore, this adsorption is irreversible and can account for the morphologies of COM crystals observed in ***Chapter 4***. In the presence of tetrazole **5**, COM crystals were fewer in number and square or diamond-like in shape (***Figure 4.3***) that were thinner in the [100] direction. This thinning of the crystals was measured by the AFM imaging in ***Figure 7.4***, as **5** reduced the crystal growth in the [100] step direction.

As mentioned in ***Chapter 4***, the morphology of COM crystals can be changed due to the tetrazole molecules adsorbing to the crystal surfaces. Crystals grown in the presence of additives **5** and **10** for instance, resulted in a 4-sided diamond-like COM crystal habit. Additives **5** and **10**, therefore, can be said to adsorb strongly to the (100), (120), (02-1), (-120) and (021) faces, which results in the change in habit of the COM crystals and thinning in the [100] direction. Tetrazole **5** was shown to have insignificant complexation to calcium (***Figure 5.7***) and thus the mechanism for the suppression of crystal growth occurs predominantly by the adsorption of the molecule to the crystal surface and not due to complexation. After 40 minutes of growth under control conditions tetrazole **10**, 1, 4-bis (1H-tetrazol-5-yl) benzene (2.85 mg/mL) was added to one of the solutions being pumped into the system to determine the molecule's effects on the crystal growth rate and steps. Moderate promotion of the [001] step was observed in the presence of **10** with a step rate of 0.28 nm ± 0.05 $s^{-1}$ compared to the control at a rate of 0.21 nm $s^{-1}$ (a 25% increase). The steps were observed to become more closely grouped, an indication that step bunching occurs despite the increase in the step velocity, while no change to the step heights were seen across ***Figure 7.4***. This would suggest that some layers of the steps grow faster than others and are limited by the slow growing layers. Comparing the morphology of the crystals in ***Figure 4.4g*** in the presence of **10**, the average crystal length was slightly increased compared to the control crystals.

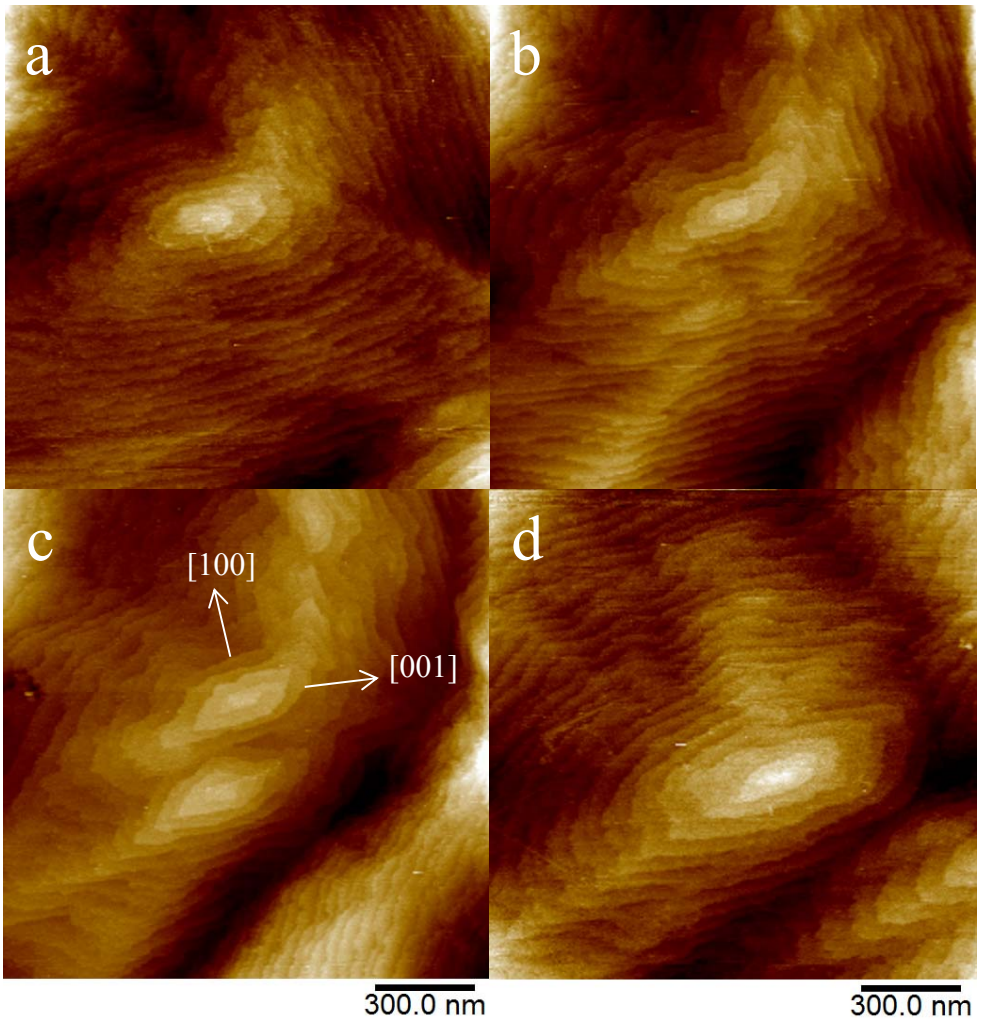


***Figure 7.5***: Snapshots from time resolved *in situ* AFM imaging of hillock growth on the COM (010) face in supersaturated CaOx solutions (a) without additives after 35 minutes, (b) in the presence of **12** (3.03 mg/mL) after 25 minutes (c) in the presence of **12** (3.03 mg/mL) after 45 minutes, and (d) regrowth without additives after 25 minutes.

The promotion of the crystal growth in the [001] direction that occurs when **10** is added may account for the increase in particle size measured in ***Chapter 4***. The mechanisms, which result in the crystals featured in ***Figure 4.4g*** however, must also account for the thinning of the crystals in the [100] direction. Nucleation-related mechanisms observed from the DLS data can be ruled out as these effects are growth related. However, complexation of calcium in the presence of **10** was determined to be one of the strongest in the tetrazole series, thus it is highly likely to contribute to the reduction in the thickness of COM crystals in the [100] direction. Thus adsorption mechanisms of the tetrazole molecules to calcium in the COM (100)

surface by electrostatic interactions results in the lowering of the local supersaturation, decreasing the growth rates in that direction, perhaps even leading to dissolution and this can account for the morphology observed.

Following the control growth hillocks featured in ***Figure 7.2***, tetrazole **12** was added to determine whether it affected the (010) face crystal growth (***Figure 7.5***). With step growth rates of 0.15 ± 0.03 nm $s^{-1}$ and 0.23 ± 0.03 nm $s^{-1}$ for the [100] and [001] steps, respectively. The control growth solutions were recorded for 35 minutes before addition of **12**. Upon addition of **12** the oval shaped uniform steps seen in ***Figure 7.5a*** become roughened (***Figure 7.5b***) after 25 minutes. After 45 minutes of injecting **12** (3.03 mg/mL) the hillock became parallelogram shaped (***Figure 7.5c***), with measured step velocities becoming 0.14 ± 0.001 nm $s^{-1}$ and 0.21 ± 0.02 nm $s^{-1}$ for the [100] and [001] step directions, respectively. Control supersaturated solution was subsequently injected (***Figure 7.5d***) to determine the relative strength of the additives adsorption to the surface. After 25 minutes, the oval shaped hillock began to take shape again. However, step velocities of the [100] and [001] steps during this period were 0.05 ± 0.002 nm $s^{-1}$ and 0.07 ± 0.002 nm $s^{-1}$, respectively. This indicates that tetrazole **12** molecules are still strongly adsorbed and competing with the newly injected supersaturated solution, impeding the growth on the (010) face.

Comparing the observed impact of **12** on the crystal growth on the COM (010) face to previous results in ***Chapters 4-6***, a significant reduction in the nucleation of COM particles was observed (***Chapter 5***, ***Figure 5.6***). This is reflected in the morphological study from ***Chapter 4*** (***Figure 4.8***) and the quantitative data obtained in the presence of **12**, where only 7 particles were observed. This indicates that adsorption of tetrazole molecules during crystal growth can be considered less impactful than the adsorption that occurs during nucleation. The complexation of **12** determined in ***Chapter 5*** and the aggregation of tetrazole species within COM particles (C***hapter 6***) were not considered as potent interactions, however they do contribute to the overall inhibition of the COM crystals. This suggests the main impact of **12** is to alter the surface free energy of the nuclei.

In order to further understand the structure activity relationships of the tetrazole structures (***Figure 7.6***) and their impact on COM crystallisation, tetrazole

molecules **13** and **14**, were investigated by *in situ* AFM experiments (***Figure 7.7***) to complement **12**. ***Figure 7.7a-c*** corresponds with the growth of COM under control conditions, the introduction of **13** and subsequent regrowth using control conditions, respectively. Likewise for ***Figure 7.7d-e***, except in the presence of **14**, AFM imaging was conducted and the growth rates of the respective steps were determined. The growth rate of the [100] step initially (***Figure 7.7a***) was 0.07 ± 0.01 nm $s^{-1}$, while the rate of growth for the [001] direction was 0.29 ± 0.07 nm $s^{-1}$. Upon addition of tetrazole **13** (3.33 mg/mL) the rate of growth in the [100] and [001] step directions were both reduced to 0.03 ± 0.05 nm $s^{-1}$ and -0.03 ± 0.05 nm $s^{-1}$, respectively (***Figure 7.7b***). While the [100] steps halved in growth rate, the [001] steps experienced negative growth rates or recession of the steps towards the growth hillock. Thus **13** impacts strongly on the crystal growth of the COM (010) face in both directions. After injection of **13**, control solutions were pumped to regrow the surface, in which time (***Figure 7.7c***) the steps' growth rates began to normalise. While the growth for the [001] steps returned to a control rate of 0.22 ± 0.11 nm $s^{-1}$ after 30 minutes, the [100] step growth remained similar to the rate during additive injection at 0.04 ± 0.02 nm $s^{-1}$. Thus, tetrazole molecule **13** appears to be reversibly adsorbed.

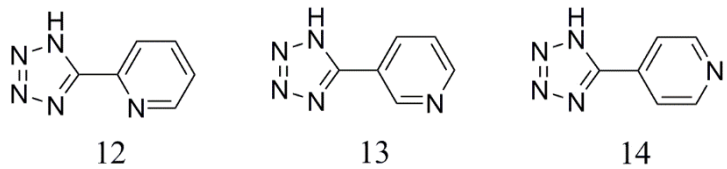


***Figure 7.6***: Structures of additives **12**, **13** and **14** for AFM experimentation.

***Figure 7.7d-f*** included the controlled growth of steps on the COM (010) face, in the presence of additive **14** and regrowth using supersaturated control solutions. The rate of step progression of the [100] and [001] faces were measured to be 0.04 ± 0.10 nm $s^{-1}$ and 0.12 ± 0.27 nm $s^{-1}$ initially (***Figure 7.7d***), however, the standard deviation for the measured rates indicates that the growth rates fluctuated excessively before the addition of **14** (3.12 mg/mL) which reduced the growth rates effectively to zero (0.002 ± 0.03 nm $s^{-1}$) for the [100] face and 0.09 ± 0.08 nm $s^{-1}$ for the [001] steps (***Figure 7.7e***). Where initially rectangular shaped hillocks were present,

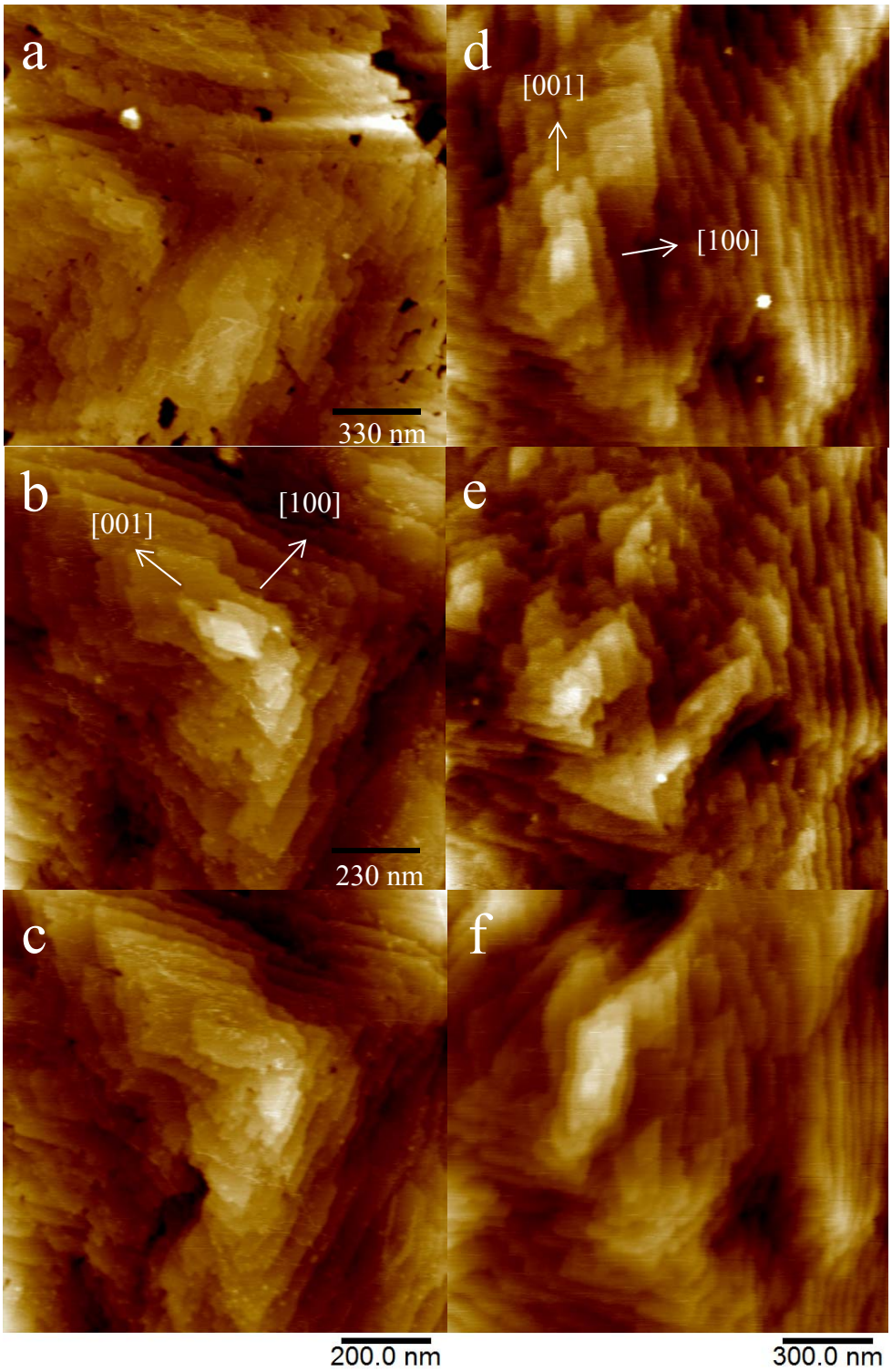


***Figure 7.7***: Snapshots from time resolved *in situ* AFM imaging of hillock growth on the COM (010) face in supersaturated CaOx solutions. (a) Growth: 20 minutes no additives, (b) Inhibition: 40 minutes with tetrazole **13** (3.33 mg/mL) present, and (c) Regrowth: 30 minutes without additives. (d) Growth: 30 minutes without additives, (e) Inhibition: 23 minutes with tetrazole **14** (3.12 mg/mL) present, and (f) Regrowth: 50 minutes without additives.

addition of **14** resulted in roughened steps, particularly in the [001] direction. As has been shown in the results thus far, for most tetrazole species, subsequent regrowth yields growth hillocks comparable to the initial state before addition of the tetrazole additive. Tetrazole **14** follows this trend (***Figure 7.7f***) with growth rates of the [100] and [001] faces found to be 0.09 ± 0.04 nm $s^{-1}$ and 0.27 ± 0.11 nm $s^{-1}$, respectively. Thus, again for **14**, adsorption appears to be reversible. The tetrazole molecules **12**, **13** and **14** result in the following inhibition trends on the COM (010) surface; the *para*-pyridyl tetrazole (**14**) showed greater inhibitory impact in the [100] direction, while the *meta*-pyridyl species (**13**) impacted more strongly on the steps growing in the [001] direction. In comparison, **12** had little impact on either step direction but did, however, change the growth hillocks step spacing as discussed previously indicating a step bunching mechanism occurs in the presence of **12**. The relatively low impact of **12** seems counterintuitive to the strength of the adsorption as indicated by the step bunching. The interaction of the nitrogen on the pyridine ring located nearby the tetrazole functional group (***Figure 7.6***), may account for its limited growth inhibition *vis-a-vis* steric affects.

Meanwhile, due to the increased distance of the nitrogen in the pyridine ring for both **13** and **14**, the structure of both is likely preferable for interactions between the nitrogen atom and COM surface to occur. These interactions include hydrogen bonding between the nitrogen atoms of both the tetrazole and pyridine with the water molecules of COM or lone pair electrons from the pyridine ring nitrogen atom to calcium ions. Comparing the morphology of the COM crystals grown in the presence of these additives (***Chapter 4***, ***Figure 4.8***) each tetrazole increased the mean particle size to at least twice that of the control. Additionally, the DLS results indicated that all three pyridine tetrazoles inhibited the nucleation of COM strongly.

Lastly, tetrazoles **6** and **17**, were further investigated with *in situ* AFM imaging to determine the structure activity relationships of the carboxylic acid and methoxy functionality, as the carboxylic acid groups are electron withdrawing (like additive **5**, the cyano-tetrazole) while **17** is strongly electron donating, the structures of which can be seen in ***Figure 7.8***. Outside of the additives' similarities, the relationship between the *para*-substituted functional group chemistry is of great interest. Thus the results of the snapshots from the AFM studies for the two tetrazole species are presented in ***Figure 7.9***.

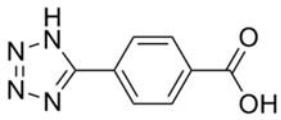

6

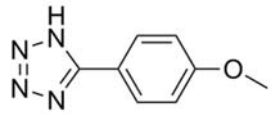

17

***Figure 7.8***: Structures of additives **6** and **17**.

The growth hillock featured in ***Figure 7.9a*** is again rectangular in shape, with a screw dislocation evident in the centre of the image. The crystal growth rate of the steps of interest were determined to be initially 0.02 ± 0.01 nm $s^{-1}$ for the [100] step. Likewise, the growth rate for the [001] step was found to be 0.11 ± 0.06 nm $s^{-1}$. Additive **6** (3.12 mg/mL) was injected and the crystal growth rates increased compared to the initial values (***Figure 7.9b***). The growth rates of 0.07 ± 0.01 and 0.17 ± 0.04 nm $s^{-1}$ were found for the [100] and [001] step directions in the presence of **6**, respectively. Thus the additive promoted both steps to grow rather than inhibited them (at this concentration). However, both values are still within the error of the average control growth rates for both steps. After this, pure solutions of calcium oxalate were injected to determine whether the additive adsorbed to the (010) surface strongly and if returning to control growth rates could be achieved (***Figure 7.9c***). In both step directions growth rates were measured at a 0.04 ± 0.07 nm $s^{-1}$. This indicates that although the tetrazole promoted crystal growth, the molecules still adsorb strongly to the surface, particularly on the [001] step as it exhibited the greatest rate reduction. Upon subsequent growth using calcium oxalate supersaturated solutions, resistance to growth was measured due to the irreversibility of the surface adsorbed additives. Now that tetrazole **6** has been shown to slightly promote the growth of the COM (010) surface, comparisons to the morphology of the final crystals observed in ***Chapter 4*** (***Figure 4.4***) and the underlying mechanism responsible can be determined. Based on the quantitative data for the crystals grown in the presence of the inhibitor at the higher concentration, the mean particle size was increased by 5 times COM control crystals.

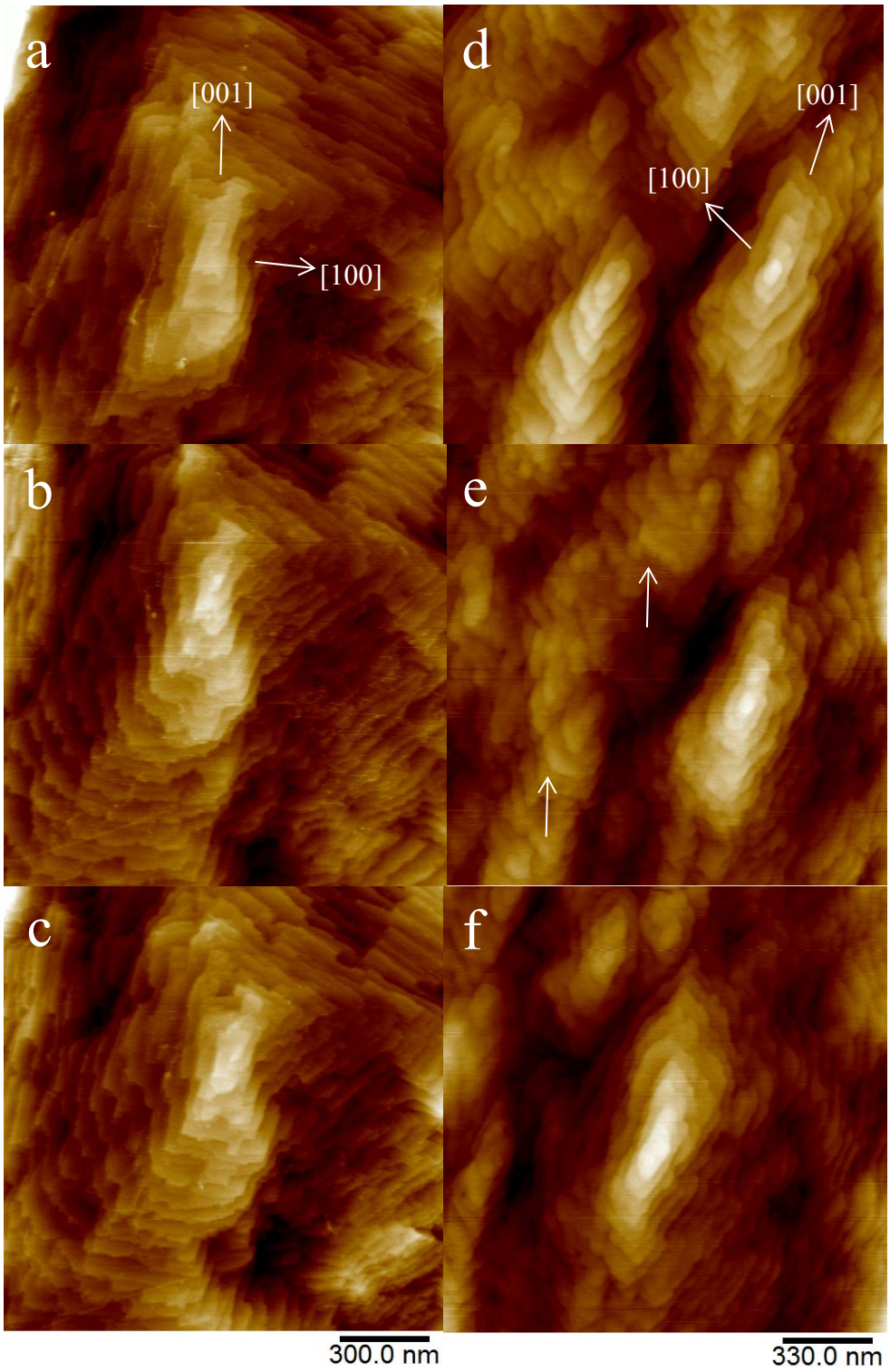


***Figure 7.9***: Snapshots from time resolved *in situ* AFM imaging of hillock growth on the COM (010) face in supersaturated CaOx solutions. (a) Growth: 20 minutes no additives, (b) Inhibition: 40 minutes with tetrazole **6** (3.12 mg/mL) present, and (c) Regrowth: 33 minutes without additives. (d) Growth: 60 minutes without additives, (e) Inhibition: 20 minutes with tetrazole **17** (5.00 mg/mL) present, and (f) Regrowth: 24 minutes without additives.

Results indicate **6** did not have significant complexation above the control, while the DLS results indicated that the additive promoted nucleation. As has been seen for many of the tetrazole species, adsorption of the functional groups to the crystal surface *via* electrostatic interactions or hydrogen bonding are the most common mechanisms responsible for the morphology of the crystals observed in ***Chapter 4***. In this case the carboxylic acid and tetrazole moieties present in **6** provide multiple strong binding functionalities with which to adsorb to COM surfaces, most likely the (100), (12-1), (021), (1-2-1) and (0-21) faces. The promotion of crystal growth and nucleation observed in the presence of tetrazole **6**, may be explained by mechanisms observed previously for COM.[66] It is proposed enhanced rates of crystal growth result from two possible mechanisms, both of which facilitate attachment of solute to growth sites on the COM crystal surface. Firstly, promoters may increase the local supersaturation of calcium or oxalate ions near the crystal surface; secondly, promoters may disrupt solvent structuring close to the crystal surface, decreasing the barriers for solute diffusion from the solution to the crystal surface.[211] However, the exact mechanism of growth promotion is unknown and remains a topic of ongoing investigation.

The final tetrazole molecule employed to impact the crystal growth of the COM (010) face is **17** (***Figure 7.8*** and ***Figures 7.9d-f***). Snapshots from time resolved *in situ* AFM images of spiral dislocations are presented after 60 minutes of supersaturated calcium oxalate solution injection. The growth rates of the labelled steps (***Figure 7.8d***) were measured to be 0.08 ± 0.02 nm $s^{-1}$ and 0.34 ± 0.06 nm $s^{-1}$ for the [100] and [001] directions. Step pinning was noticeable immediately after injection of **17** (5.00 mg/mL) to the growth solution (***Figure 7.9e***) and resulted in more rounded and roughened step edges. The growth rates of the individual steps were subsequently suppressed due to the presence of the additive. Growth rates in the [100] and [001] directions were measured to be 0.06 ± 0.01 and 0.15 ± 0.05 nm $s^{-1}$, respectively. Removal of the tetrazole additive from solution and regrowth of the steps was attempted (***Figure 7.9f***). After 24 minutes of pure solution injection, the growth rate in the [001] step direction was still lower than the control at 0.13 ± 0.11 nm $s^{-1}$. The growth rate of the [100] step returned to 0.09 ± 0.02 nm $s^{-1}$.

The effects observed in the presence of **17** illustrate that both electron withdrawing and donating functional groups *para* to the tetrazole can impact the crystal growth on the (010) face of COM. In the two cases just observed, tetrazole **17** inhibited the growth compared to the control by reducing the growth rate by 50%. Tetrazole **6** on the other hand promoted crystal growth by 50% when added to the growth solution. The difference in functional groups in the *para* positions obviously accounting for the different growth rates and adsorption mechanisms seen between the two additives, tetrazole **6** was found to be irreversibly adsorbed while **17** has reversible adsorption. Tetrazole **6** has a carboxylate moiety *para* to the tetrazole group, while **17** has methoxy (ether) functional group *para* to its tetrazole group. As mentioned for the pyridine series in this chapter, the adsorption of the tetrazole molecules and consequently the strength of inhibition of the COM crystal morphology increases with the increasing alignment of the lattice ions with the structure of the tetrazole functional groups. However, without computational modelling to determine how the tetrazole molecules and crystal surfaces of COM interact only generalisations can be made as to the alignment and binding to specific steps and ions of the COM lattice based on literature. What can be elaborated on is the types of interactions present in each additive, for instance in the case of tetrazole **6**, *para* to the tetrazole group, the carboxylate functionality has additional capability to adsorb to the surface by hydrogen bonding. Similarly, pyridine tetrazoles **12**, **13** and **14** have nitrogen atoms present in their aromatic rings and are capable of hydrogen bonding to the COM surface.

The mechanisms additive **17** inhibited COM includes the directly observed adsorption to the crystal steps on the (010) face *via* the AFM study as shown by step pinning (***Figure 7.9e***). Tetrazole **17** also displayed strong nucleation inhibition, complexation of calcium and was observed to reside within the crystal lattice of the COM solid *via* an aggregation mechanism (***Chapter 6***). Based on the abovementioned mechanisms involving **17**, the morphology of the final crystals displayed in ***Chapter 4***, (***Figure 4.6***) and the quantitative data obtained from the SEM micrographs, it can be concluded that the crystals were significantly inhibited by **17**. The nucleation rate was directly inhibited by this tetrazole molecule and this effect could be understood by the significant complexation of the molecule to calcium ions, lowering the supersaturation and consequently the nucleation rate. The

combination of these mechanisms resulted in the morphologically observed results in ***Chapter 4***, illustrating that very few COM crystals were left to image. While the morphology of the crystals was unchanged, compared to the control, nucleation mechanisms have played a larger role in the inhibition between COM and tetrazole **17** than adsorption mechanisms. However, the lack of morphological change observed (***Figure 4.6***) may be a result of the equally strong adsorption to multiple different faces of COM by **17**, yielding somewhat control-like crystals. A table of the combined results of this chapter is illustrated in ***Table 7.1***. The results include the relative crystal growth rates in the [100] and [001] directions once each of the additives was injected and their concentrations.

***Table 7.1***: Summary of AFM crystal growth rate experiments.

| Additive | Additive Concentration (mg/mL) | [001] Direction (nm/s) | [100] Direction (nm/s) | Figure |
|---|---|---|---|---|
| ***Control*** | 0.00 | 0.21 | 0.07 | ***7.2*** |
| ***5*** | 0.42 | 0.43 | - | ***7.4*** |
| ***5*** | 2.72 | 0.26 | - | ***7.4*** |
| ***10*** | 2.85 | 0.28 | - | ***7.4*** |
| ***12*** | 3.03 | 0.21 | 0.14 | ***7.5*** |
| ***13*** | 3.33 | -0.03 | 0.03 | ***7.7*** |
| ***14*** | 3.12 | 0.09 | 0.002 | ***7.7*** |
| ***6*** | 3.12 | 0.17 | 0.07 | ***7.9*** |
| ***17*** | 5.00 | 0.15 | 0.06 | ***7.9*** |

"-"represents data from ***Figure 7.4*** which could not be calculated as spiral growth was not formed during this experiment.

## 7.3 Conclusion

Across the seven tetrazole-containing molecules studied with *in situ* AFM imaging, several trends were elucidated with many that can be applied to the remaining series. The mechanism in focus in this chapter was the adsorption of the tetrazole moiety and other functional groups to the COM (010) surface to promote or inhibit crystal growth. In the cases investigated, each additive contained a tetrazole, and *para* to that for **5**, **6**, **10**, and **17** each had a cyano, carboxylic acid, tetrazole and methoxy functional group, respectively. While, additives **12** (*ortho*), **13** (*meta*) and **14** (*para*) all had pyridine functional groups attached to the tetrazole moiety, each was structurally different and the binding therefore was also different. The 4 *para* substituted tetrazole-containing compounds, additives **5**, **6** and **10**, all promoted crystal growth of the (010) face in the [001] direction with respect to the control growth rate, leaving only **17** to inhibit the rate of crystal growth. Meanwhile, each of the pyridine tetrazoles inhibited COM crystal growth to varying degrees, **12** was discovered to have the weakest impact although it was the strongest inhibitor of COM morphology form ***Chapter 4***. Tetrazole **13** was shown to inhibit the crystal growth in the [001] directions very strongly, enough in fact to reverse the direction of growth. Lastly, tetrazole **14** was measured to inhibit the crystal growth more so in the [100] step direction. Each had unique crystal growth inhibition despite their structural similarities. The reasons behind these differences in inhibition are discussed in this chapter in more detail, however it was concluded that the adsorption strength to the surface of COM through hydrogen bonding and electrostatic interactions can account for some of the differences observed. In addition, contributions from complexation were discussed and related to the structure of the molecules.

# 8 Conclusions and Future directions

This study has investigated 26 tetrazole molecules with various structures and functional groups to determine their impacts on calcium oxalate monohydrate crystallisation. To do this, several different techniques were employed to characterise and describe the results for calcium oxalate nucleation, crystal growth, complexation behaviour and aggregation behaviour. The techniques utilized included optical microscopy, SEM, AFM, CRM, ICP-AES, DLS and a photophysical investigation employing spectroscopy. The first step in studying the calcium oxalate system required the development of reliable and reproducible techniques in a pure system without additives. This was essential in determining a control result to which the effect(s) of each tetrazole molecule across several techniques can be compared and contrasted. Even before this, ***Chapter 3***, the synthesis and characterisation of the tetrazole series were performed employing known safe, simple reactions and purification methods to obtain the tetrazole-containing species.[174] Once each tetrazole molecule was synthesised and purified, characterisation by NMR, IR spectroscopy, melting point, Raman spectroscopy, absorption, excitation and emission spectroscopy were performed. The characterisation by Raman spectroscopy, for many of the tetrazole molecules in the series, are the first to be measured and recorded, despite the common use of Raman in other fields for functional group characterisation.

In ***Chapter 4***, morphological changes to the COM crystals by the tetrazole species were attributed in the most part to the adsorption of the tetrazole-containing species to particular surfaces of calcium oxalate monohydrate crystals. In many cases, this resulted in a significant change of habit of the crystals, directly viewed by optical and scanning electron microscopy (SEM), a powerful technique for determining morphological changes to the crystals. Quantitative data of the crystal experiments also provided extremely useful in determining preliminary trends in nucleation inhibition, which was then used to formulate initial impacts of the structures of each tetrazole-containing molecule in the series. Trends based on the visual and numerical data obtained allowed for the identification of initial structure-activity relationships between COM crystal morphology and tetrazole structure.

Changes in aspect ratio (l/w) of each crystal, standard deviation in mean crystal length and particle numbers were extracted from the SEM micrographs. The results of which indicated that the additives that adsorbed strongest to the calcium oxalate crystal surfaces, greatly slowed the growth rates of the crystals formed, reflected by the quantitative data collected for the entire series. Structurally, the tetrazole molecules with multiple tetrazole functional groups were discovered to be the most potent, often altering the habit of COM from the typical 6-sided elongated hexagonal shape to a shortened 4-sided diamond shape. The underlying mechanism responsible for the observed change in habit of the crystals being due to the strength of the tetrazole moiety to bind selectively to specific crystallographic faces of COM. The most commonly affected surfaces were found to be the apical tips or (12-1), (1-2-1), (021) and (0-21) faces of COM, resulting in shortened crystals in the [001] direction.

In ***Chapter 5***, dynamic light scattering (DLS) techniques were employed to understand the nucleation impacts of the additives on calcium oxalate monohydrate. What was discovered was that the majority of the tetrazole-containing additives inhibited the nucleation density, some weakly (<20% reduction of nuclei) some very strongly (>70% reduction nuclei). Among these, typically the di-tetrazole-containing species impacted with greater potency than mono-tetrazole-containing molecules. Of the 26 tetrazoles, only 5 were found to promote the nucleation density, thus the tetrazole functional group typically inhibits calcium oxalate nuclei forming. Differences in nucleation inhibition between molecules of similar structures were also observed, indication that structure can strongly impact the strength of inhibition; moreover this is typically thought to be *via* the charge of the inhibiting species and the addition of further complexation sites in each structure.

To extend on the nucleation study, the complexation of the additive series to $Ca^{2+}$ in solution was studied to determine the impact on the supersaturation and consequently, nucleation inhibition potency of each tetrazole in the series. Removal of free calcium from solution subsequently lowers the supersaturation due to the decrease in available calcium ions, thus, complexation can have a pronounced effect on calcium oxalate nucleation. The dissolved calcium was measured using ICP-AES with results reflecting the strength of di-tetrazole-containing molecules to both complex $Ca^{2+}$ ions and inhibit calcium oxalate nucleation more potently. In this case, di-tetrazole molecules complexed calcium ions much more strongly than many

mono-tetrazole molecules in the series, up to 5 times relative to the control. Thus, complexation of the tetrazole molecules to $Ca^{2+}$ can significantly impact on the supersaturation and contributes to the nucleation inhibition of COM.

Interestingly, a unique interaction of the tetrazole species occurred with COM during investigations with confocal Raman microscopy (CRM) and the photophysical investigation. In ***Chapter 6***, CRM was employed to determine adsorption interactions. What was discovered was that the additives adsorbed strongly enough to calcium oxalate monohydrate crystal surface through, most likely hydrogen bonding, strong enough to be embedded in the crystal lattice during growth. Incorporation of additives into crystal lattices during growth occurs routinely,[64,145,231] however in the case of the tetrazole molecules studied; the overlap of $\pi$ orbitals once incorporated within the crystal lattice enabled an aggregated emission mechanism to be observed using the excitation and emission properties of the tetrazole molecules *via* the photophysical investigation. This implies that while the tetrazole molecules may adsorb individually, there is significant intermolecular interactions with other tetrazole molecules, leading to tetrazole aggregates being incorporated into the crystal. Additionally, the additives location and intensity embedded within the crystals could be ascertained with CRM. It is thought this mechanism of aggregation could be used to further investigate the interactions of inhibitory molecules on COM crystals.

Lastly, in ***Chapter 7***, atomic force microscopy (AFM) was attempted to directly observe the crystal growth inhibition of tetrazole-containing additives on calcium oxalate monohydrate crystals, for the first time. 7 of the 26 tetrazoles of varying degrees of inhibition were selected to use in *in situ* AFM growth experiments due to their structural similarities and impact on crystal growth (based on the previous chapter's results). Spiral crystal growth was achieved first, in the absence of additives, to measure the control growth rate before exposing the crystals to the tetrazole-containing molecules and determining their impact. The additives were found to inhibit the growth rate of calcium oxalate steps on the (010) crystal face in supersaturated conditions. Most tetrazoles reduced the crystal growth rates of the [001] and [100] steps found on the (010) COM face. The underlying mechanism of the reduced growth rates was observed to be *via* step pinning, where molecules adsorbed to the surface interfere with the step growth. Step pinning is typically

indicated by the roughening of the COM crystal step edges. The aforementioned results include the first measurements and research on the effects of tetrazole-containing molecules on calcium oxalate crystallisation. The work conducted indicates that the tetrazole functionality can be used in crystal growth modifiers to inhibit calcium oxalate monohydrate crystallisation and may provide a new promising moiety for the control of crystal growth and morphology. However, further investigation of many more tetrazoles with potential for greater potency is required to find a cure for these pathological mineralization events which affects more than 10% of the global population during their lifetime.

Given the opportunity, further study into the impacts of the entire series of tetrazole molecules on calcium oxalate solids grown in artificial urine (AU) could have provided further information on the strength and structural impacts of each tetrazole additive in a more complex medium. Additionally, expanding on the AFM study to include all tetrazole molecules in the series could have provided additional indications to which functional groups and structures adsorb to the surface of COM and therefore inhibit COM crystal growth more strongly. Similarly, expansion of the tetrazole series to investigate the more potent tetrazole molecules by altering structures and addition functionality to improve inhibition strength of the molecules at much lower concentrations, would be particularly important for future works for tetrazole molecules as crystal growth modifiers. Current concentrations of the tetrazole series in this study are much higher than COM macromolecule inhibitors, which typically exhibit inhibition in part per million (ppm) concentrations and lower. Thus, the improvement of the potency of the additives compounds is of high priority. Simultaneously, the inhibitory affects need to be maintained and improved upon for the eventual use of tetrazole-containing molecules for kidney stone inhibition. Hand-in-hand with further investigations into tetrazole molecules, mechanisms of interaction believed to be most prevalent for the reduction of kidney stone formation are essential for future work in pathological mineral control. Mechanisms investigated in this work such as additive-crystal adsorption and complexation interactions may provide avenues to explore in more detail to determine the extent of their effects on forming and formed COM-containing kidney stones.

# 9 References


(1) Baeuerlein, E. *Biomineralization: Progress in biology, Molecular biology and Application, 2nd ed*, 2nd ed.; Wiley-VCH Verlag GmbH: Weinheim, 2004.

(2) Mann, S. *Biomineralization: Principles and Concepts in Bioinorganic Materials Chemistry*; Oxford University Press, 2002.

(3) Lowenstam, H.; Weiner, S. *On Biomineralization*; Oxford University Press: New York, 1989.

(4) Addadi, L.; Weiner, S. Crystals, asymmetry and life. *Nature* **2001**, *411* (6839), 753–755.

(5) Van Cappellen, P. Biomineralization and Global Biogeochemical Cycles. *Rev. Mineral. Geochemistry* **2003**, *54* (1), 357–381.

(6) Addadi, L.; Weiner, S. Biomineralization: mineral formation by organisms. *Phys. Scr.* **2014**, *89* (9), 1–13.

(7) Lowenstam, H. Minerals Formed by Organisms. *Science.* **1981**, *211*, 1126–1131.

(8) Simkiss, K.; Wilbur, K. . *Biomineralization: Cell Biology and Mineral Deposition*; Academic Press: New York, 1989.

(9) Behrens, P.; Baeuerlein, E. Biomimetic and Bioinspired Chemistry. In *Handbook of Biomineralization*; Wiley-VCH Verlag GmbH and Co. KGaA: Weinheim, 2007.

(10) Epple, M.; Baeuerlein, E. Medical and Clinical Aspects. In *Handbook of Biomineralization*; Wiley-VCH Verlag GmbH and Co. KGaA: Weinheim, 2007.

(11) He, G.; Gajjeraman, S.; Schultz, D.; Cookson, D.; Qin, C.; Butler, W. T.; Hao, J.; George, A. Spatially and temporally controlled biomineralization is facilitated by interaction between self-assembled dentin matrix protein 1 and calcium phosphate nuclei in solution. *Biochemistry* **2005**, *44* (49), 16140–16148.

(12) Lakshminarayanan, R.; Loh, X. J.; Gayathri, S.; Sindhu, S.; Banerjee, Y.; Kini, R. M.; Valivaveettil, S. Formation of transient amorphous calcium carbonate precursor in quail eggshell mineralization: An in vitro study. *Biomacromolecules* **2006**, *7* (11), 3202–3209.

(13) Hernzandez-Hernandez, A.; Gomez-Morales, J.; Rodriguez-Navarro, A.R.; Gautron, J.; Nys, Y.; Garcia-Ruiz, J. . Identification of Some Active Proteins in the Process of Hen Eggshell Formation. *Cryst. Growth Des.* **2008**, *8* (12), 4330–4339.

(14) Falini, G.; Albeck, S.; Weiner, S.; Addadi, L. Control of Aragonite or Calcite Polymorphism by Mollusk Shell Macromolecules. *Science.* **1996**, *271* (5245), 67–69.

(15) Meldrum, F. C.; Cölfen, H. Controlling mineral morphologies and structures in biological and synthetic systems. *Chem. Rev.* **2008**, *108* (11), 4332–4432.

(16) Nudelman, F.; Gotliv, B. A.; Addadi, L.; Weiner, S. Mollusk shell formation: Mapping the distribution of organic matrix components underlying a single aragonitic tablet in nacre. *J. Struct. Biol.* **2006**, *153* (2), 176–187.

(17) Gotliv, B. A.; Addadi, L.; Weiner, S. Mollusk shell acidic proteins: In search of individual functions. *ChemBioChem* **2003**, *4* (6), 522–529.

(18) Lowenstam, H.; Weiner, S. Transformation of amorphous calcium phosphate to crystalline dahllite in the radular teeth of chitons. *Science.* **1985**, *227*, 51–53.
(19) Henriksen, K.; Stipp, S. L. S.; Young, J. R.; Marsh, M. E. Biological control on calcite crystallization: AFM investigation of coccolith polysaccharide function. *Am. Mineral.* **2004**, *89* (11–12), 1709–1716.
(20) Henriksen, K.; Stipp, S. L. S. Controlling Biomineralization : The Effect of Solution Composition on Coccolith Polysaccharide Functionality Controlling Biomineralization : The Effect of Solution Composition on Coccolith Polysaccharide Functionality. *Cryst. Growth Des.* **2009**, *9* (5), 2088–2097.
(21) Henriksen, K.; Stipp, S. L. S.; Young, J. R.; Bown, P. R. Tailoring calcite: Nanoscale AFM of coccolith biocrystals. *Am. Mineral.* **2003**, *88* (11–12 PART 2), 2040–2044.
(22) Aizenberg, J.; Tkachenko, A.; Weiner, S.; Addadi, L.; Hendler, G. Calcitic microlenses as part of the photoreceptor system in brittlestars. *Nature* **2001**, *412* (6849), 819–822.
(23) Beniash, E.; Aizenberg, J.; Addadi, L.; Weiner, S. Amorphous calcium carbonate transforms into calcite during sea urchin larval spicule growth. *Proc. R. Soc. B Biol. Sci.* **1997**, *264* (1380), 461–465.
(24) Sumper, M.; Brunner, E.; Lehmann, G. Biomineralization in diatoms: Characterization of novel polyamines associated with silica. *FEBS Lett.* **2005**, *579* (17), 3765–3769.
(25) Iijima, M.; Onuma, K.; Tsuji, T. Biomineralization: Tooth Enamel Formation. In *Bioinspiration: From Nano to Micro Scales*; Springer New York Heidelberg Dordrecht London: New York, 2012; pp 161–188.
(26) Simmer, J. P.; Richardson, A. S.; Hu, Y.-Y.; Smith, C. E.; Ching-Chun Hu, J. A post-classical theory of enamel biomineralization… and why we need one. *Int. J. Oral Sci.* **2012**, *4* (3), 129–134.
(27) Dorozhkin, S. V; Epple, M. Biological and medical significance of calcium phosphates. *Angew. Chemie Int. Ed.* **2002**, *41* (17), 3130–3146.
(28) Addadi, L.; Weiner, S. Kontroll-und Designprinzipien bei der Biomineralisation. *Angew. Chemie* **1992**, *104* (2), 159–176.
(29) Zaremba, C. M.; Belcher, A. M.; Fritz, M.; Li, Y.; Mann, S.; Hansma, P. K.; Morse, D. E.; Speck, J. S.; Stucky, G. D. Critical Transitions in the Biofabrication of Abalone Shells and Flat Pearls. *Chem. Mater.* **1996**, *8* (3), 679–690.
(30) D'Souza, S. M.; Alexander, C.; Carr, S. W.; Waller, A. M.; Whitcombe, M. J.; Vulfson, E. N. Directed nucleation of calcite at a crystal-imprinted polymer surface. *Nature* **1999**, *398* (6725), 312–316.
(31) Li, X.; Zhang, W.; Lu, J.; Huang, L.; Nan, D.; Webb, M. A.; Hillion, F.; Wang, L. Templated biomineralization on self-assembled protein nanofibers buried in calcium oxalate raphides of musa spp. *Chem. Mater.* **2014**, *26* (12), 3862–3869.
(32) Metzler, R. A.; Kim, I. W.; Delak, K.; Evans, J. S.; Zhou, D.; Beniash, E.; Wilt, F.; Abrecht, M.; Chiou, J. W.; Guo, J.; et al. Probing the organic-mineral interface at the molecular level in model biominerals. *Langmuir* **2008**, *24* (6), 2680–2687.
(33) Dey, A.; Bomans, P. H. H.; Müller, F. A.; Will, J.; Frederik, P. M.; de With, G.; Sommerdijk, N. A. J. M. The role of prenucleation clusters in surface-induced calcium phosphate crystallization. *Nat. Mater.* **2010**, *9* (12), 1010–

1014.
(34) Mann, S. *Biomimetic Materials Chemistry*, First.; VCH Publishers, Inc.: New York, 1996.
(35) Mann, S. Biomineralization and Biomimetic Materials Chemistry. *J. Mater. Chem.* **1999**, *5* (7), 935–946.
(36) Jones, F.; Ogden, M. I. Controlling crystal growth with modifiers. *CrystEngComm* **2010**, *12* (4), 1016.
(37) Smeets, P. J. M.; Cho, K. R.; Sommerdijk, N. A. J. M.; De Yoreo, J. J. A Mesocrystal-Like Morphology Formed by Classical Polymer-Mediated Crystal Growth. *Adv. Funct. Mater.* **2017**, *1701658*, 1701658.
(38) De Yoreo, J. J.; Gilbert, P. U. P. A.; Sommerdijk, N. A. J. M.; Penn, R. L.; Whitelam, S.; Joester, D.; Zhang, H.; Rimer, J. D.; Navrotsky, A.; Banfield, J. F.; et al. Crystallization by particle attachment in synthetic, biogenic, and geologic environments. *Science.* **2015**, *349* (6247), aaa6760.
(39) Gebauer, D.; Kellermeier, M.; Gale, J. D.; Bergström, L.; Cölfen, H. Pre-nucleation clusters as solute precursors in crystallisation. *Chem. Soc. Rev.* **2014**, *43* (7), 2348–2371.
(40) Gebauer, D.; Voelkel, A.; Coelfen, H. Stable Prenucleation Calcium Carbonate Clusters. *Science.* **2008**, *120* (December), 1819–1823.
(41) Gebauer, D.; Cölfen, H. Prenucleation clusters and non-classical nucleation. *Nano Today* **2011**, *6* (6), 564–584.
(42) Vekilov, P. G. Dense liquid precursor for the nucleation of ordered solid phases from solution. *Cryst. Growth Des.* **2004**, *4* (4), 671–685.
(43) Anwar, J.; Boateng, P. K. Computer simulation of crystallization from solution. *J. Am. Chem. Soc.* **1998**, *120* (37), 9600–9604.
(44) Bonnett, P. E.; Carpenter, K. J.; Dawson, S.; Davey, R. J. Solution crystallisation via a submerged liquid–liquid phase boundary: oiling out. *Chem. Commun.* **2003**, *13* (6), 698–699.
(45) Suzuki, M.; Saruwatari, K.; Kogure, T.; Yamamoto, Y.; Nishimura, T.; Kato, T.; Nagasawa, H. An Acidic Matrix Protein, Pif, Is a Key Macromolecule for Nacre Formation. *Science.* **2009**, *325* (5946), 1388–1390.
(46) Masica, D.; Schrier, S.; Specht, E. De Novo Design of Peptide− Calcite Biomineralization Systems. *J. Am.* **2010**, No. 14, 12252–12262.
(47) Lyons Ryall, R.; Fleming, D. E.; Doyle, I. R.; Evans, N. A; Dean, C. J.; Marshall, V. R. Intracrystalline proteins and the hidden ultrastructure of calcium oxalate urinary crystals: implications for kidney stone formation. *J. Struct. Biol.* **2001**, *134* (1), 5–14.
(48) Jones, F.; Rohl, A. L.; Ogden, M. I.; Parkinson, G. M. Scale formation and inhibition. *Mater. Forum* **2001**, *25*, 116–135.
(49) Weiner, S. An Overview of Biomineralization Processes and the Problem of the Vital Effect. *Rev. Mineral. Geochemistry* **2003**, *54* (1), 1–29.
(50) Gebauer, D.; Cölfen, H.; Verch, A.; Antonietti, M. The multiple roles of additives in CaCO3 crystallization: A quantitative case study. *Adv. Mater.* **2009**, *21* (4), 435–439.
(51) Colfen, H.; Qi, L. A Systematic Examination of the Morphogenesis of Calcium Carbonate in the Presence of a Double-Hydrophilic Block Copolymer. *Chem. - A Eur. J.* **2001**, *7* (1), 106–116.
(52) Olszta, M. J.; Cheng, X.; Jee, S. S.; Kumar, R.; Kim, Y.-Y.; Kaufman, M. J.; Douglas, E. P.; Gower, L. B. Bone Structure and Formation: a New Perspective. *Mater. Sci. Eng. Reports* **2007**, *58*, 77–116.

(53) Brown, W. E.; Chow, L. C. Chemical Properties of Bone Mineral. *Annu. Rev. Mater. Sci.* **1976**, *6*, 213–236.
(54) Foley, R. N.; Collins, A. J.; Ishani, A.; Kalra, P. A. Calcium-phosphate levels and cardiovascular disease in community-dwelling adults: The Atherosclerosis Risk in Communities (ARIC) Study. *Am. Heart J.* **2008**, *156* (3), 556–563.
(55) Coe, F. L.; Evan, A. P.; Worcester, E. M.; Lingeman, J. E. Three pathways for human kidney stone formation. *Urol. Res.* **2010**, 147–160.
(56) Anjos, A. J.; Nolasco, P.; Aquino Marques, J. M.; Cabrita, F.; Pereira, M. F. C.; Alves de Matos, A. P.; Carvalho, P. A. On oral calcifications: sialoliths, dental calculi and tonsilloliths. *Microsc. Microanal.* **2013**, *19* (S4), 23–24.
(57) Smith, L. The many roles of oxalate in nature. *Trans. Am. Clin. Climatol. Assoc.* **2002**, *113*, 1–20.
(58) Pearle, M. S.; Calhoun, E. A.; Curhan, G. C. Urolithiasis. In *Urological Diseases in America*; 2007; pp 283–319.
(59) Uribarri, J.; Oh, M. S.; Carroll, H. J. The first kidney stone. *Ann. Intern. Med.* **1989**, *111* (12), 1006–1009.
(60) Moe, O. W. Kidney stones: pathophysiology and medical management. *Lancet* **2006**, *367* (9507), 333–344.
(61) Moe, O. W.; Pearle, M. S.; Sakhaee, K. Pharmacotherapy of urolithiasis: evidence from clinical trials. *Kidney Int.* **2011**, *79* (4), 385–392.
(62) Kirk, C. A.; Bartges, J. W. *Dietary Considerations for Calcium Oxalate Urolithiasis*, Fifth Edit.; Elsevier Inc., 2005.
(63) Boyce, W. H.; Garvey, F. K. The amound and nature of the organic matrix in urinary calculi: a review. *J. Urol.* **1956**, *76* (3), 213–227.
(64) Fleming, D. E.; Van Riessen, A; Chauvet, M. C.; Grover, P. K.; Hunter, B.; van Bronswijk, W.; Ryall, R. L. Intracrystalline proteins and urolithiasis: a synchrotron X-ray diffraction study of calcium oxalate monohydrate. *J. Bone Miner. Res.* **2003**, *18* (7), 1282–1291.
(65) Ryall, R. L. Urinary inhibitors of calcium oxalate crystallization and their potential role in stone formation. *World J. Urol.* **1997**, *15*, 155–164.
(66) Farmanesh, S.; Chung, J.; Sosa, R. D.; Kwak, J. H.; Karande, P.; Rimer, D. Natural Promoters of Calcium Oxalate Monohydrate Crystallization. *J. Am. Chem. Soc.* **2014**.
(67) Farmanesh, S.; Ramamoorthy, S.; Chung, J.; Asplin, J. R.; Karande, P.; Rimer, D. Specificity of Growth Inhibitors and their Cooperative Effects in Calcium Oxalate Monohydrate Crystallization. *J. Am. Chem. Soc.* **2014**.
(68) Qiu, S. R.; Wierzbicki, A; Orme, C. A; Cody, A. M.; Hoyer, J. R.; Nancollas, G. H.; Zepeda, S.; De Yoreo, J. J. Molecular modulation of calcium oxalate crystallization by osteopontin and citrate. *Proc. Natl. Acad. Sci. U. S. A.* **2004**, *101* (7), 1811–1815.
(69) Wesson, J. A.; Ward, M. D. Pathological biomineralization of kidney stones. *Elements* **2007**, *3* (6), 415–421.
(70) Fleming, D. E.; van Bronswijk, W.; Ryall, R. L. A comparative study of the adsorption of amino acids on to calcium minerals found in renal calculi. *Clin. Sci. (Lond).* **2001**, *101* (2), 159–168.
(71) Ryall, R. L. Glycosaminoglycans, proteins, and stone formation: adult themes and child's play. *Pediatr. Nephrol.* **1996**, *10* (5), 656–666.
(72) Kim, K. Mulberry Particles Formed by Red Blood Cells in Human Weddelite Stones. *J. Urol.* **1983**, *129* (4), 855–857.
(73) Khan, S. R.; Shevock, P. N.; Hackett, R. L. Presence of lipids in urinary

stones: Results of preliminary studies. *Calcif. Tissue Int.* **1988**, *42* (2), 91–96.
(74) Tazzoli, V.; Domeneghetti, C. The crystal structures of whewellite and weddellite : re-examination and comparison. *Am. Mineral.* **1980**, *65*, 327–334.
(75) Brown, P.; Ackermann, D.; Finlayson, B. Calcium Oxalate Dihydrate (Weddellite) precipitation. *J. Cryst. Growth* **1989**, *98*, 285–292.
(76) Deganello, S.; Kampf, A. R.; Moore, P. B. The crystal structure of calcium oxalate trihydrate : Ca(H2O)3 ( C2O4 ). *Am. Mineral.* **1981**, *66*, 859–865.
(77) Tomazic, B. B.; Nancollas, G. H. A study of the phase transition of calcium oxalate trihydrate-monohydrate. *Invest. Urol.* **1979**, *16* (5), 329–335.
(78) Echigo, T.; Kimata, M.; Kyono, A.; Shimizu, M.; Hatta, T. Re-investigation of the crystal structure of whewellite [Ca(C2O4)H2O] and the dehydration mechanism of caoxite [Ca(C2O4)3H2O]. *Mineralogical Magazine*. 2005, pp 77–88.
(79) Deganello, S. The Structure of Whewellite CaC2O4.H2O, at 328 K. *Acta Crystallogr. Sect. B* **1981**, *2* (1947), 826–829.
(80) Dhanaraj, G.; Byrappa, K.; Prasad, V.; Dudley, M. *Springer Handbook of Crystal Growth*; 2010.
(81) Ihli, J.; Wang, Y.-W.; Cantaert, B.; Kim, Y.-Y.; Green, D. C.; Bomans, P. H. H.; Sommerdijk, N. A. J. M.; Meldrum, F. C. Precipitation of Amorphous Calcium Oxalate in Aqueous Solution. *Chem. Mater.* **2015**, *27* (11), 3999–4007.
(82) Hajir, M.; Graf, R.; Tremel, W. Stable amorphous calcium oxalate: synthesis and potential intermediate in biomineralization. *Chem. Commun.* **2014**, *50* (49), 6534–65366.
(83) Hochrein, O.; Thomas, A.; Kniep, R. Revealing the crystal structure of anhydrous calcium oxalate, Ca[C2O4], by a combination of atomistic simulation and rietveld refinement. *Zeitschrift fur Anorg. und Allg. Chemie* **2008**, *634* (11), 1826–1829.
(84) Schubert, G.; Ziemer, B. A New Calcium Oxalate Monohydrate Produced by Thermal Dehydration of Weddellite. *Cryst. Res. Technol.* **1981**, *16* (9), 1025–1031.
(85) Millan, A. Crystal Growth Shape of Whewellite Polymorphs : Influence of Structure Distortions on Crystal Shape 2001. *Cryst. Growth Des.* **2001**, *1* (3), 245–254.
(86) Aquilano, D.; Franchini-Angela, M. Twin Laws of Whewellite, CaC204 • H20. A Structural and Growth Approach. *Phys. Chem. Miner.* **1981**, *7*, 124–129.
(87) Cody, A. M.; Cody, R. D. Contact and Penetration Twinning of Calcium Oxalate Monohydrate. *J. Cryst. Growth* **1987**, *83*, 485–498.
(88) Gault, C. D. Weddellite : a new occurrence. *Mineral. Magaz* **1983**.
(89) Arnott, H. J. Calcium oxalate (weddellite) crystals in forest litter. *Scan. Electron Microsc.* **1982**, *3*, 1141–1149.
(90) Bárcenas-Argüello, M. L.; Gutiérrez-Castorena, M. C. de. C.; Terrazas, T. The polymorphic weddellite crystals in three species of Cephalocereus (Cactaceae). *Micron* **2015**, *77* (2015), 1–8.
(91) Poloni, L. N.; Ward, M. D. The Materials Science of Pathological Crystals. *Chem. Mater.* **2013**.
(92) Tomazic, B.; Nancollas, G. H. The Kinetics of Dissolution of Calcium Oxalate Hydrates. *J. Cryst. Growth* **1979**, *46* (1979), 355–361.
(93) Zhao, W.; Sharma, N.; Jones, F.; Raiteri, P.; Gale, J. D.; Demichelis, R.

Anhydrous Calcium Oxalate Polymorphism: A Combined Computational and Synchrotron X-ray Diffraction Study. *Cryst. Growth Des.* **2016**, *16* (10), 5954–5965.
(94) Gibbs, J.W.; Smith, A. W. On the Equilibrium of Heterogeneous Substances. *Trans. Connect. Acad. Arts Sci.* **1878**, *3* (10), 343–524.
(95) Becker, R.; Döring, W. Kinetische Behandlung der Keimbildung in übersättigten Dämpfen. *Ann. Phys.* **1935**, *416* (8), 719–752.
(96) Mullin, J. W. *Crystallization*, 4th ed.; Butterworth-Heinemann, 2001.
(97) Kostorz, G. *Phase Transformations in Materials*; Kostorz, G., Ed.; Wiley-VCH Verlag GmbH: Weinheim, 2001.
(98) Kashchiev, D. Thermodynamically consistent description of the work to form a nucleus of any size. *J. Chem. Phys.* **2003**, *118* (4), 1837–1851.
(99) De Yoreo, J. J. A holistic view of nucleation and self-assembly. *MRS Bull.* **2017**, *42* (7), 525–536.
(100) DeYoreo, J. J.; Vekilov, P. G. Principles of Crystal Nucleation and Growth. *Rev. Mineral. Geochemistry* **2003**, *54* (1), 57–93.
(101) Vekilov, P. G.; Vorontsova, M. A. Nucleation precursors in protein crystallization. *Acta Crystallogr. Sect. F Struct. Biol. Commun.* **2014**, *70* (3), 271–282.
(102) Cölfen, H.; Antonietti, M. *Mesocrystals and Nonclasical Crystallization*; John Wiley & Sons Australia, Ltd: San Francisco, 2008.
(103) Nielsen, M. H.; Aloni, S.; De Yoreo, J. J. In situ TEM imaging of CaCO3 nucleation reveals coexistence of direct and indirect pathways. *Science.* **2014**, *345* (6201), 1158–1162.
(104) Petsev, D. N.; Chen, K.; Gliko, O.; Vekilov, P. G. Diffusion-limited kinetics of the solution-solid phase transition of molecular substances. *Proc. Nat. Acad. Sci. USA* **2003**, *100* (3), 792–796.
(105) Giuffre, A. J.; Hamm, L. M.; Han, N.; De Yoreo, J. J.; Dove, P. M. Polysaccharide chemistry regulates kinetics of calcite nucleation through competition of interfacial energies. *Proc. Natl. Acad. Sci.* **2013**, *110* (23), 9261–9266.
(106) Smeets, P. J. M.; Cho, K. R.; Kempen, R. G. E.; Sommerdijk, N. A. J. M.; De Yoreo, J. J. Calcium carbonate nucleation driven by ion binding in a biomimetic matrix revealed by in situ electron microscopy. *Nat. Mater.* **2015**, *14* (4), 394–399.
(107) Dey, A.; de With, G.; Sommerdijk, N. A. J. M. In situ techniques in biomimetic mineralization studies of calcium carbonate. *Chem. Soc. Rev.* **2010**, *39* (2), 397–409.
(108) Patterson, J. P.; Xu, Y.; Moradi, M. A.; Sommerdijk, N. A. J. M.; Friedrich, H. CryoTEM as an Advanced Analytical Tool for Materials Chemists. *Acc. Chem. Res.* **2017**, *50* (7), 1495–1501.
(109) Demichelis, R.; Raiteri, P.; Gale, J. D.; Quigley, D.; Gebauer, D. Stable prenucleation mineral clusters are liquid-like ionic polymers. *Nat. Commun.* **2011**, *2*, 590.
(110) Smeets, P. J. M.; Finney, A. R.; Habraken, W. J. E. M.; Nudelman, F.; Friedrich, H.; Laven, J.; De Yoreo, J. J.; Rodger, P. M.; Sommerdijk, N. A. J. M. A classical view on nonclassical nucleation. *Proc. Natl. Acad. Sci.* **2017**, 201700342.
(111) Gibbs, J. W. *Thermodynamics*; 1948.
(112) Volmer, M.; Weber, A. Keimbildung in ubersattigten Gebilden. *Zeitschrift fur*

*Phys. chemie* **1926**, *119*, 277–301.
(113) Volmer, M. *Kinetik der Phasenbildung*; Theodor Steinkopf: Dresden, 1939.
(114) Frank, F. C. The influence of dislocations on crystal growth. *Discuss. Faraday Soc.* **1949**, *5*, 48–54.
(115) Kossel, W. Zur Theorie des Kristallwachstums. *Nachrichten von der Gesellschaft der Wissenschaften zu Göttingen, Math. Klasse* **1927**, *1927*, 135–143.
(116) Van der Eerden, J.; Bennema, P.; Cherepanova, T. Survery of Monte Carlo simulations of crystal growth surfaces and crystal growth. *Prog. Cryst. Growth Characterisation* **1978**, *1*, 219–264.
(117) Nielson, A. E. Electrolyte crystal growth mechanisms. *J. Cryst. Growth* **1984**, *67*, 289–310.
(118) Habraken, W. J. E. M.; Tao, J.; Brylka, L. J.; Friedrich, H.; Bertinetti, L.; Schenk, A. S.; Verch, A.; Dmitrovic, V.; Bomans, P. H. H.; Frederik, P. M.; et al. Ion-association complexes unite classical and non-classical theories for the biomimetic nucleation of calcium phosphate. *Nat. Commun.* **2013**, *4*, 1507.
(119) Cho, K. S.; Talapin, D. V.; Gaschler, W.; Murray, C. B. Designing PbSe nanowires and nanorings through oriented attachment of nanoparticles. *J. Am. Chem. Soc.* **2005**, *127* (19), 7140–7147.
(120) Xie, B.; Halter, T. J.; Borah, B. M.; Nancollas, G. H. Aggregation of calcium phosphate and oxalate phases in the formation of renal stones. *Cryst. Growth Des.* **2015**, *15* (1), 204–211.
(121) Dongsheng, L.; Nielsen, M. H.; Lee, J. R.; Frandsen, C.; Banfield, J. F.; De Yoreo, J. J. Direction-Specific Interactions Control Crystal Growth by Oriented Attachment. *Science.* **2012**, *336* (6084), 1014–1018.
(122) Gebauer, D.; Volkel, A.; Colfen, H. Stable Prenucleation Calcium Carbonate Clusters. *Science.* **2008**, *322* (5909), 1819–1822.
(123) Song, R. Q.; Cölfen, H.; Xu, A. W.; Hartmann, J.; Antonietti, M. Polyelectrolyte-directed nanoparticle aggregation: Systematic morphogenesis of calcium carbonate by nonclassical crystallization. *ACS Nano* **2009**, *3* (7), 1966–1978.
(124) Cölfen, H.; Mann, S. Higher-order organization by mesoscale self-assembly and transformation of hybrid nanostructures. *Angew. Chemie - Int. Ed.* **2003**, *42* (21), 2350–2365.
(125) Wulff, G. On the question of the rate of growth and dissolution of crystal surface. *Zeitschrift fuer Krist. und Mineral.* **1901**, *34*, 449–530.
(126) Laube, N.; Klein, F.; Bernsmann, F. Kinetics of calcium oxalate crystal formation in urine. *Urolithiasis* **2016**.
(127) Baumann, J. M.; Affolter, B.; Caprez, U.; Lauper, D.; Maier, F.; Siegrist, H. P.; Zysset, T. Nucleation and aggregation of calcium oxalate in whole urine; spectrophotometric sedimentation analysis: a new approach to study the aggregation of calcium oxalate dihydrate. *Urol. Res.* **2000**, *28* (3), 147–154.
(128) Liebman, M.; Chai, W. Effect of dietary calcium on urinary oxalate excretion after oxalate loads. *Am. J. Clin. Nutr.* **1997**, *65*, 1453–1459.
(129) Butz, M. Metabolic disorders in patients with calcium urolithiasis. *Int. Urol. Nephrol.* **1986**, *18* (2), 131–139.
(130) Robertson, W.; Peacock, M. Pathogenesis of urolithiasis. In *Urolithiasis, etiology, diagnosis*; Springer-Verlag: Berlin, 1985; pp 185–334.
(131) Pak, C. Y.; Pak, Y.; Skurla, C.; Harvey, J. Graphic display of urinary risk factors for renal stone formation. *J. Urol.* **1985**, *134* (5), 867–870.

(132) Riley, J. M.; Kim, H. J. H.; Averch, T. D.; Kim, H. J. H. Effect of Magnesium on Calcium and Oxalate Ion Binding. *J. Endourol.* **2013**, *27* (12), 1487–1492.
(133) Farmanesh, S.; Alamani, B. G.; Rimer, J. D. Identifying alkali metal inhibitors of crystal growth: a selection criterion based on ion pair hydration energy. *Chem. Commun.* **2015**, *51* (73), 13964–13967.
(134) Meyer, J. L.; Thomas, W. C. Trace metal-citric acid complexes as inhibitors of calcification and crystal growth. *J. Urol.* **1982**, *128* (6), 1376–1378.
(135) Sayan, P.; Sargut, S. T.; Kıran, B. Calcium oxalate crystallization in the presence of amino acids, proteins and carboxylic acids. *Cryst. Res. Technol.* **2009**, *44* (8), 807–817.
(136) He, J.; Lin, R.; Long, H.; Liang, Y.; Chen, Y. Adsorption characteristics of amino acids on to calcium oxalate. *J. Colloid Interface Sci.* **2015**, *454*, 144–151.
(137) Cody, A. M.; Cody, R. D. Calcium oxalate trihydrate phase control by structurally-specific carboxylic acids. *J. Cryst. Growth* **1994**, *135* (1–2), 235–245.
(138) Ouyang, J.; Duan, L.; Tieke, B.; Ko, D.-. Effects of Carboxylic Acids on the Crystal Growth of Calcium Oxalate Nanoparticles in Lecithin-Water Liposome Systems. *Langmuir* **2003**, No. 19, 8980–8985.
(139) Grases, F.; Millan, A.; Garcia-Raso, A. Polyhydroxycarboxylic acids as inhibitors of calcium oxalate crystal growth; relation between inhbitory capacity and chemical structure. *J. Cryst. Growth* **1988**, *89*, 496–500.
(140) Cowley, D. M.; McWhinney, B. C.; Brown, J. M.; Chalmers, a H. Effect of citrate on the urinary excretion of calcium and oxalate: relevance to calcium oxalate nephrolithiasis. *Clin. Chem.* **1989**, *35* (1), 23–28.
(141) Demko, Z. P.; Sharpless, K. B. An expedient route to the tetrazole analogues of alpha-amino acids. *Org. Lett.* **2002**, *4* (15), 2525–2527.
(142) Weaver, M. L.; Qiu, S. R.; Hoyer, J. R.; Casey, W. H.; Nancollas, G. H.; De Yoreo, J. J. Inhibition of calcium oxalate monohydrate growth by citrate and the effect of the background electrolyte. *J. Cryst. Growth* **2007**, *306* (1), 135–145.
(143) Wang, L.; Zhang, W.; Qiu, S. R.; Zachowicz, W. J.; Guan, X.; Tang, R.; Hoyer, J. R.; Yoreo, J. J. De; Nancollas, G. H. Inhibition of calcium oxalate monohydrate crystallization by the combination of citrate and osteopontin. *J. Cryst. Growth* **2006**, *291* (1), 160–165.
(144) Cho, K. R.; Salter, A.; Yoreo, J.; Wierzbicki, A.; Elhadj, S.; Huang, Y.; Qiu, R.; Salter, E. A.; De Yoreo, J. J.; Wierzbicki, A.; et al. Growth inhibition of calcium oxalate monohydrate crystal by linear aspartic acid enantiomers investigated by in situ force microscopy. *CrystEngComm* **2012**, No. 207890, 1–40.
(145) Touryan, L. A; Clark, R. H.; Gurney, R. W.; Stayton, P. S.; Kahr, B.; Vogel, V. Incorporation of fluorescent molecules and proteins into calcium oxalate monohydrate single crystals. *J. Cryst. Growth* **2001**, *233* (1–2), 380–388.
(146) Sheng, X.; Jung, T.; Wesson, J. A; Ward, M. D. Adhesion at calcium oxalate crystal surfaces and the effect of urinary constituents. *Proc. Natl. Acad. Sci. U. S. A.* **2005**, *102* (2), 267–272.
(147) Nene, S. S.; Hunter, G. K.; Goldberg, H. A.; Hutter, J. L. Reversible inhibition of calcium oxalate monohydrate growth by an osteopontin phosphopeptide. *Langmuir* **2013**, *29* (21), 6287–6295.
(148) Cerini, C.; Geider, S.; Dussol, B.; Hennequin, C.; Daudon, M.; Veesler, S.;

Nitsche, S.; Boistelle, R.; Berthézène, P.; Dupuy, P.; et al. Nucleation of calcium oxalate crystals by albumin: Involvement in the prevention of stone formation. *Kidney Int.* **1999**, *55* (5), 1776–1786.
(149) Farmanesh, S.; Chung, J.; Chandra, D.; Sosa, R. D.; Karande, P.; Rimer, J. D. High-throughput platform for design and screening of peptides as inhibitors of calcium oxalate monohydrate crystallization. *J. Cryst. Growth* **2012**, *373* (2013), 13–19.
(150) Chung, J.; Granja, I.; Taylor, M. G.; Mpourmpakis, G.; Asplin, J. R.; Rimer, J. D. Molecular modifiers reveal a mechanism of pathological crystal growth inhibition. *Nature* **2016**, *536* (7617), 1–5.
(151) Wesson, J. A.; Worcester, E. M.; Wiessner, J. H.; Mandel, N. S.; Kleinman, J. G. Control of calcium oxalate crystal structure and cell adherence by urinary macromolecules. *Kidney Int.* **1998**, *53* (4), 952–957.
(152) Govindaraj, A.; Selvam, R. Increased calcium oxalate crystal nucleation and aggregation by peroxidized protein of human kidney stone matrix and renal cells. *Urol. Res.* **2001**, *29* (3), 194–198.
(153) Christmas, K. G.; Gower, L. B.; Khan, S. R.; El-Shall, H. Aggregation and dispersion characteristics of calcium oxalate monohydrate: effect of urinary species. *J. Colloid Interface Sci.* **2002**, *256*, 168–174.
(154) Jung, T.; Sheng, X.; Choi, C. K.; Kim, W.-S. S.; Wesson, J. A.; Ward, M. D. Probing crystallization of calcium oxalate monohydrate and the role of macromolecule additives with in situ atomic force microscopy. *Langmuir* **2004**, *20* (20), 8587–8596.
(155) Thomas, A.; Rosseeva, E.; Hochrein, O.; Carrillo-Cabrera, W.; Simon, P.; Duchstein, P.; Zahn, D.; Kniep, R. Mimicking the growth of a pathologic biomineral: Shape development and structures of calcium oxalate dihydrate in the presence of polyacrylic acid. *Chem. - A Eur. J.* **2012**, *18* (13), 4000–4009.
(156) Bladin, J. . No Title. *Chem. Ber.* **1885**, *18*, 1544.
(157) Singh, H.; Chawla, A. S.; Kapoor, V. K.; Paul, D.; Malhotra, R. K. Medicinal Chemistry in Tetrazoles. *Prog. Med. Chem.* **1980**, *17*, 151–183.
(158) Wittenberger, S. J. Recent Developments in Tetrazole Chemistry. A Review. *Org. Prep. Proced. Int. new J. Org. Synth.* **2009**, *26* (5), 499–531.
(159) Benson, F. R. The Chemistry of the Tetrazoles. *Chem. Rev.* **1947**, *41* (1), 1–61.
(160) Rostom, S. A. F.; Ashour, H. M. A.; Razik, H. A. A. E.; Fattah, A. E. F. A. E. .; El-Din, N. N. Azole antimicrobial pharmacophore-based tetrazoles: Synthesis and biological evaluation as potential antimicrobial and anticonvulsant agents. *Bioorganic Med. Chem.* **2009**, *17* (6), 2410–2422.
(161) Ostrovskii, V. A.; Trifonov, R. E.; Popova, E. A. Medicinal chemistry of tetrazoles. *Russ. Chem. Bull.* **2012**, *61* (4), 768–780.
(162) Malik, M. A.; Wani, M. Y.; Al-Thabaiti, S. A.; Shiekh, R. A. Tetrazoles as carboxylic acid isosteres: Chemistry and biology. *J. Incl. Phenom. Macrocycl. Chem.* **2014**, *78* (1–4), 15–37.
(163) Holland, G. F.; Pereira, J. N. *Heterocyclic tetrazoles, a New Class of Lipolysis Inihibitors*; 1967; Vol. 10.
(164) Herr, R. J. 5-Substituted-1H-tetrazoles as carboxylic acid isosteres: medicinal chemistry and synthetic methods. *Bioorg. Med. Chem.* **2002**, *10* (11), 3379–3393.
(165) Butler, R. 4.17- Tetrazoles. In *Comprehensive Heterocyclic Chemistry II*; 1996; pp 621–678.

(166) Werrett, M. V.; Huff, G. S.; Muzzioli, S.; Fiorini, V.; Zacchini, S.; Skelton, B. W.; Maggiore, A.; Malicka, J. M.; Cocchi, M.; Gordon, K. C.; et al. Methylated Re(I) tetrazolato complexes: photophysical properties and Light Emitting Devices. *Dalt. Trans.* **2015**, *44* (18), 8379–8393.
(167) Werrett, M. V.; Muzzioli, S.; Wright, P. J.; Palazzi, A.; Raiteri, P.; Zacchini, S.; Massi, M.; Stagni, S. Proton-induced reversible modulation of the luminescent output of rhenium(I), iridium(III), and ruthenium(II) tetrazolate complexes. *Inorg. Chem.* **2014**, *53* (1), 229–243.
(168) Stagni, S.; Colella, S.; Palazzi, A.; Valenti, G.; Zacchini, S.; Paolucci, F.; Marcaccio, M.; Albuquerque, R. Q.; Cola, L. De; Fisica, C.; et al. Essential role of the ancillary ligand in the color tuning of iridium tetrazolate complexes. *Inorg. Chem.* **2008**, *47* (22), 10509–10521.
(169) Driscoll, C. R.; Skelton, B. W.; Massi, M.; Ogden, M. I. Structural characterisation and photophysical properties of lanthanoid complexes of a tetra-amide functionalised calix[4]arene. *Supramol. Chem.* **2016**, *278* (July).
(170) Massi, M.; Ogden, M. I.; Radomirovic, T.; Jones, F. Tetrazoles: a new class of compound for crystallization modification. *CrystEngComm* **2010**, *12* (12), 4205.
(171) McMulkin, C. J.; Massi, M.; Jones, F. Tetrazoles: calcium oxalate crystal growth modifiers. *CrystEngComm* **2015**, *17* (13), 2675–2681.
(172) McMulkin, C. J.; Massi, M.; Jones, F. Calcium oxalate crystal growth modification; investigations with confocal Raman microscopy. *J. Cryst. Growth* **2017**, *468*, 295–298.
(173) Chutipongtanate, S.; Thongboonkerd, V. Systematic comparisons of atrificial urine formulas for in vitro cellular study. *Anal. Biochem.* **2010**, *402*, 110–112.
(174) Koguro, K.; Oga, T.; Mitsui, S.; Orita, R. Novel Synthesis of 5-Substituted Tetrazoles from Nitriles. *Synthesis (Stuttg).* **1998**, No. 6, 910–914.
(175) Demko, Z. P.; Sharpless, K. B. Preparation of 5-substituted 1H-tetrazoles from nitriles in water. *J. Org. Chem.* **2001**, *66* (24), 7945–7950.
(176) Himo, F.; Demko, Z. P.; Noodleman, L.; Sharpless, K. B. Mechanisms of tetrazole formation by addition of azide to nitriles. *J. Am. Chem. Soc.* **2002**, *124* (41), 12210–12216.
(177) Rama, V.; Kanagaraj, K.; Pitchumani, K. Syntheses of 5-Substituted 1 H - Tetrazoles Catalyzed by Reusable CoY Zeolite. *J. Org. Chem. Org.* **2011**, No. 76, 9090–9095.
(178) Coca, A.; Turek, E. Synthesis of 5-substituted 1H-tetrazoles catalyzed by ytterbium triflate hydrate. *Tetrahedron Lett.* **2014**, *55* (16), 2718–2721.
(179) Das, B.; Reddy, C.; Kumar, D.; Krishnaiah, M.; Narender, R. A Simple, Advantageous Synthesis of 5-Substituted 1H-Tetrazoles[1]. *Synlett* **2009**, *2010* (3), 391–394.
(180) Zhong, D.-C.; Wen, Y.-Q.; Deng, J.-H.; Luo, X.-Z.; Gong, Y.-N.; Lu, T.-B. Uncovering the Role of Metal Catalysis in Tetrazole Formation by an In Situ Cycloaddition Reaction: An Experimental Approach. *Angew. Chemie Int. Ed.* **2015**, *54* (40), 11795–11799.
(181) Azides, O.; Aureggi, V.; Sedelmeier, G. 1 , 3-Dipolar Cycloaddition : Click Chemistry for the Synthesis of 5-substituted Tetrazoles from Organoaluminum Azides and Nitriles. *Angew. Chemie* **2007**, *46*, 8440–8444.
(182) Zhu, Y.; Ren, Y.; Cai, C. One-Pot Synthesis of 5-Substituted 1H-Tetrazoles from Aryl Bromides with Potassium Hexakis ( cyano-kC ) ferrate ( 4 À ) ( K 4 [ Fe ( CN ) 6 ]) as Cyanide Source. *Helv. Chim. Acta* **2009**, *92*, 171–175.

(183) Myznikov, L. V.; Efimova, Y. A.; Artamonova, T. V.; Koldobskii, G. I. Tetrazoles: LVI. Synthesis of 5-substituted tetrazoles under microwave activation in the presence of heterogeneous catalyst (zinc oxide). *Russ. J. Org. Chem.* **2011**, *47* (5), 728–730.
(184) Mohammed, A. Microwave Assisted Synthesis of New Heterocyclic Compounds : 1 , 2 , 3-Triazoles and Tetrazoles and Study of Their Biological Activity †. *Asian J. Chem.* **2012**, *24* (12), 5592–5596.
(185) Jaiswal, R. K.; Parmar, S. S.; Kumar, S.; James, E. C. Anticonvulsant property of substituted 5-aryltetrazol-2-ylacetylcarbamides. *Res. Commun. Chem. Pathol. Pharmacol.* **1983**, *37* (3), 499–502.
(186) Nagy, Z.; Tóth, M.; Czecze, L.; Nguyen, A.; Nhien, V.; Kun, S.; Docsa, T.; Gergely, P.; Charavgi, M.; Skourti, P. V; et al. Synthesis of variously coupled conjugates of D -glucose , 1 , 3 , 4-oxadiazole , and 1 , 2 , 3-triazole for inhibition of glycogen phosphorylase. *Carbohydr. Res.* **2011**, *346*, 1427–1438.
(187) Butler, R. N.; Garvin, V. C. A study of annular tautomerism, interannular conjugation, and methylation reactions of ortho-substituted-5-aryltetrazoles using carbon-13 and hydrogen-1 N.M.R spectroscopy. *J. Chem. Soc. Perkins Trans. I* **1981**, No. 390, 3–6.
(188) Butler, R. N.; Garvin, V. C.; Lumbroso, H.; Liegeois, C.; A Substituent Correlation and Medium Effects on the Annular Tautomerism of Substituted 5-Aryltetrazoles: the Nitrogen analogues of benzoic acids. A Carbon-13 NMR and dipole moment study. *J. Chem. Soc. Perkins Trans. II* **1984**, 721–725.
(189) Skoog, D. A.; Holler, F. J.; Crouch, S. R. *Principles of Instrumental Analysis*, 6th ed.; Brooks/Cole, 2007.
(190) Daimay, L.; Colthup, N. B.; Fately, W. G.; Grasselli, J. G. *The Handbook of Infrared and Raman Characterisistic Frequencies of Organic Molecules*; Academic Press: New York, 1991.
(191) Billes, F.; Endrédi, H.; Keresztury, G. Vibrational spectroscopy of triazoles and tetrazole. *J. Mol. Struct. Theochem* **2000**, *530* (1–2), 183–200.
(192) Hibben, J. H. Raman Spectra in Organic Chemistry. *Chem. Rev.* **1935**, *18* (1).
(193) Gómez-Zavaglia, A.; Ismael, A.; Cabral, L. I. L.; Kaczor, Aa.; Paixão, J. A.; Fausto, R.; Cristiano, M. L. S. Structural investigation of nitrogen-linked saccharinate–tetrazole. *J. Mol. Struct.* **2011**, *1003* (1–3), 103–110.
(194) Simpson, P. V.; Casari, I.; Paternoster, S.; Skelton, B. W.; Falasca, M.; Massi, M. Defining the Anti-Cancer Activity of Tricarbonyl Rhenium Complexes: Induction of G2/M Cell Cycle Arrest and Blockade of Aurora-A Kinase Phosphorylation. *Chem. - A Eur. J.* **2017**, *23* (27), 6518–6521.
(195) Fiorini, V.; Zanoni, I.; Zacchini, S.; Costa, A. L.; Hochkoeppler, A.; Zanotti, V.; Ranieri, A.; Massi, M.; Stefan, A.; Stagni, S. Methylation of Ir(III)-tetrazolato complexes: an effective route to modulate the emission outputs and to switch to antimicrobial properties. *Dalt. Trans.* **2017**, 12328–12338.
(196) Bader, C. A.; Sorvina, A.; Simpson, P. V.; Wright, P. J.; Stagni, S.; Plush, S. E.; Massi, M.; Brooks, D. A. Imaging nuclear, endoplasmic reticulum and plasma membrane events in real time. *FEBS Lett.* **2016**, *590* (18), 3051–3060.
(197) Werrett, M. V; Wright, P. J.; Simpson, P. V; Raiteri, P.; Skelton, B. W.; Stagni, S.; Buckley, A. G.; Rigby, J.; Massi, M. Rhenium tetrazolato complexes coordinated to thioalkyl-functionalised phenanthroline ligands: synthesis, photophysical characterisation, and incubation in live HeLa cells. *Dalt. Trans.* **2015**, *3* (44), 20636–20647.
(198) Song, Y. H.; Chi, Y.; Chiu, Y. C.; Chou, P. T.; Cheng, Y. M.; Lin, C. W.; Lee,

G. H.; Carty, A. J. Synthesis, characterization, and photophysical properties of luminescent gallium and indium complexes constructed using tridentate 6-azolyl-2,2'- bipyridine chelates. *Organometallics* **2008**, *27* (1), 80–87.
(199) Tang, H.; Zhang, Z.; Cong, C.; Zhang, K. Synthesis of a novel β-diketone containing carbazole and 2,5-diphenyl-1,3,4-oxadiazole fragments. *Russ. J. Org. Chem.* **2009**, *45* (4), 559–563.
(200) Sauer, J.; Huisgen, R.; Sturm, H. J. Ring-opening of azoles. III. Acylation of 5-aryl tetrazoles; a duplication procedure for preparation of polyaryls. *Tetrahedron* **1960**, *11* (4), 241–251.
(201) Chermahini, A. N.; Teimouri, A.; Moaddeli, A. Simple and Efficient Synthesis of 5-Substituted 1H-Tetrazoles Using Metal-Modified Clay Catalysts. *Heteroat. Chem.* **2011**, *22* (2), 168–173.
(202) Teimouri, A.; Najafi Chermahini, A. Zeolite and sulfated zirconia as catalysts for the synthesis of 5-substituted 1H-tetrazoles via [2+3] cycloaddition of nitriles and sodium azide. *Polyhedron* **2011**, *30* (15), 2606–2610.
(203) Aureggi, V.; Sedelmeier, G. 1, 3-dipolar cycloaddition: Click chemistry Supplementary Information. *Angew. Chem. Int. Ed. Engl.* **2007**, *46*.
(204) Brouwer-Van Straaten, B.; Solinger, D.; Van De Westeringh, C.; Veldstra, H. Tetrazole Analogues of Physiologically or Pharmacologically Active Carboxylic Acids. *Recueil* **1958**, *77*, 1129–1134.
(205) Fleming, A.; Kelleher, F.; Mahon, M. F.; Prajapati, V. Reactions of bis ( tetrazole ) phenylenes . Surprising formation of vinyl compounds from alkyl halides. **2005**, *61*, 7002–7011.
(206) Sreedhar, B.; Kumar, A. S.; Yada, D. CuFe 2 O 4 nanoparticles : a magnetically recoverable and reusable catalyst for the synthesis of 5-substituted 1 H -tetrazoles. *Tetrahedron Lett.* **2011**, *52* (28), 3565–3569.
(207) La, N. M.; Burgard, R.; Wentrup, C. Rearrangement of 2-Quinolyl- and 1-Isoquinolylcarbenes to. *J. Org. Chem.* **2004**, *69* (69), 2033–2036.
(208) Grohe, B.; O'Young, J.; Langdon, A.; Karttunen, M.; Goldberg, H. A.; Hunter, G. K. Citrate modulates calcium oxalate crystal growth by face-specific interactions. *Cells Tissues Organs* **2011**, *194* (2–4), 176–181.
(209) Hess, B.; Jordi, S.; Zipperle, L.; Ettinger, E.; Giovanoli, R. Citrate determines calcium oxalate crystallization kinetics and crystal morphology-studies in the presence of Tamm-Horsfall protein of a healthy subject and a severely recurrent calcium stone former. *Nephrol. Dial. Transplant* **2000**, *15* (3), 366–374.
(210) Titiz-Sargut, S.; Sayan, P.; Avcı, B. Influence of citric acid on calcium sulfate dihydrate crystallization in aqueous media. *Cryst. Res. Technol.* **2007**, *42* (2), 119–126.
(211) Chung, J.; Sosa, R.; Rimer, J. D. Elucidating the Effects of Polyprotic Acid Speciation in Calcium Oxalate Crystallization. *Cryst. Growth Des.* **2017**, acs.cgd.7b00608.
(212) Hug, S.; Grohe, B.; Jalkanen, J.; Chan, B.; Galarreta, B.; Vincent, K.; Lagugné-Labarthet, F.; Lajoie, G.; Goldberg, H. A.; Karttunen, M.; et al. Mechanism of inhibition of calcium oxalate crystal growth by an osteopontin phosphopeptide. *Soft Matter* **2012**, *8* (4), 1226–1233.
(213) Grohe, B.; Hug, S.; Langdon, A.; Jalkanen, J.; Rogers, K. A.; Goldberg, H. A.; Karttunen, M.; Hunter, G. K. Mimicking the biomolecular control of calcium oxalate monohydrate crystal growth: Effect of contiguous glutamic acids. *Langmuir* **2012**, *28* (33), 12182–12190.

(214) Bartlett, M. J.; Mocerino, M.; Ogden, M. I.; Oliveira, A.; Parkinson, G. M.; Petterson, J. K.; Reyhani, M. M. Amino acid modified calixarenes as crystal growth modifiers. *J. Mater. Sci. Technol.* **2005**, *21* (1), 1–5.
(215) Zhang, D.; Qi, L.; Ma, J.; Cheng, H. Morphological Control of Calcium Oxalate Dihydrate by a Double-Hydrophilic Block Copolymer. *Chem. Mater.* **2002**, No. 26, 2450–2457.
(216) Bretherton, T.; Rodgers, a. Crystallization of calcium oxalate in minimally diluted urine. *J. Cryst. Growth* **1998**, *192* (April), 448–455.
(217) Edwards, H. G. M.; Farwell, D. W.; Jenkins, R. Vibrational Raman Spectroscopic Studies of Calcium Oxalate Monohydrate and Dihydrate in Lichen Encrustations on Renaissance Frescoes. *J. raman Spectrosc.* **1992**, *23* (September 1991), 185–189.
(218) Paluszkiewicz, C.; Gałka, M.; Kwiatek, W.; Parczewski, A.; Walas, S. Renal stone studies using vibrational spectroscopy and trace element analysis. *Biospectroscopy* **1997**, *3* (5), 403–407.
(219) Letellier, S. R.; Lochhead, M. J.; Campbell, A. A.; Vogel, V. Oriented growth of calcium oxalate monohydrate crystals beneath phospholipid monolayers. *Biochim. Biophys. Acta* **1998**, *1380* (1), 31–45.
(220) Gutzow, I.; Atanassova, S.; Budevsky, G.; Neykov, K. Solubility, inhibited growth and dissolution kinetics of calcium-oxalate crystals in solutions, containing hippuric-acid. *Urol. Res.* **1993**, *21* (3), 181–185.
(221) Atanassova, S.; Neykov, K.; Gutzow, I. Solubility and dissolution kinetics of calcium oxalate renal calculi in solutions, containing DL-lysine: In vitro experiments. *J. Cryst. Growth* **2000**, *212*, 233–238.
(222) China, M.; Tsianou, M. Influence of Additives on Calcium Oxalate Crystallization in Solution. In *Mineral Scales in Biological and Industrial Systems*; 2013; pp 259–286.
(223) McPherson, A.; Gavira, J. A. Introduction to protein crystallisation. *Acta Crystallogr. Sect. F Struct. Biol. Commun.* **2014**, *70* (1), 2–20.
(224) Sherif, E.-S. M.; Erasmus, R. M.; Comins, J. D. Inhibition of copper corrosion in acidic chloride pickling solutions by 5-(3-aminophenyl)-tetrazole as a corrosion inhibitor. *Corros. Sci.* **2008**, *50* (12), 3439–3445.
(225) Rimer, J. D.; Rimer, J. D.; An, Z.; Zhu, Z.; Lee, M. H.; Goldfarb, D. S.; Wesson, J. A.; Ward, M. D. Crystal Growth Inhibitors for the Prevention of L-cystine Kidney Stones Through Molecular Design. *Science.* **2010**, *330* (6002), 337–341.
(226) Elhadj, S.; De Yoreo, J. J.; Hoyer, J. R.; Dove, P. M. Role of molecular charge and hydrophilicity in regulating the kinetics of crystal growth. *Proc. Natl. Acad. Sci. U. S. A.* **2006**, *103* (51), 19237–19242.
(227) Van Enckevort, W. J. P.; Bennema, P. Interlacing of growth steps on crystal surfaces as a consequence of crystallographic symmetry. *Acta Crystallogr. Sect. A Found. Crystallogr.* **2004**, *60* (6), 532–541.
(228) De Yoreo, J. J.; Chung, S.; Friddle, R. W. In Situ Atomic Force Microscopy as a Tool for Investigating Interactions and Assembly Dynamics in Biomolecular and Biomineral Systems. *Adv. Funct. Mater.* **2013**, *23* (20), 2525–2538.
(229) Gratz, A. J.; Hillner, P. E. Poisoning of calcite growth viewed in the atomic force microscope (AFM). *J. Cryst. Growth* **1993**, *129* (3–4), 789–793.
(230) Land, T. A.; Martin, T. L.; Potapenko, S.; Palmore, G. T.; De Yoreo, J. J. Recovery of surfaces from impurity poisoning during crystal growth. *Nature* **1999**, *399* (June), 442–445.

(231) Baynton, A.; Ogden, M. I.; Raston, C. L.; Jones, F. Barium sulfate crystallization dependence on upper rim calix[4]arene functional groups. *CrystEngComm* **2012**, *14*, 1057–1062.

Every reasonable effort has been made to acknowledge the owners of copyright material. I would be pleased to hear from any copyright owner who has been omitted or incorrectly acknowledged.

# Appendix

## A1 Raman Spectroscopy of Tetrazole Series

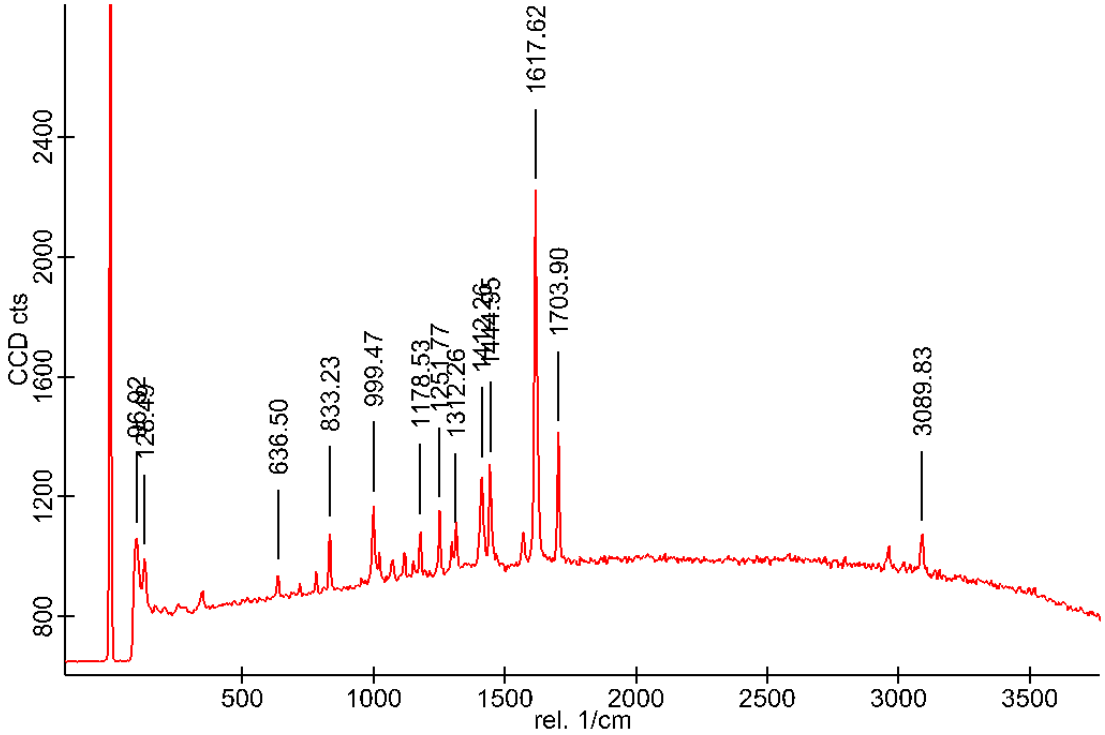


***Figure A1.1***: Raman spectrum of methyl 4-(1H-tetrazol-5-yl) benzoate (**Tzmeb**H, **1**).

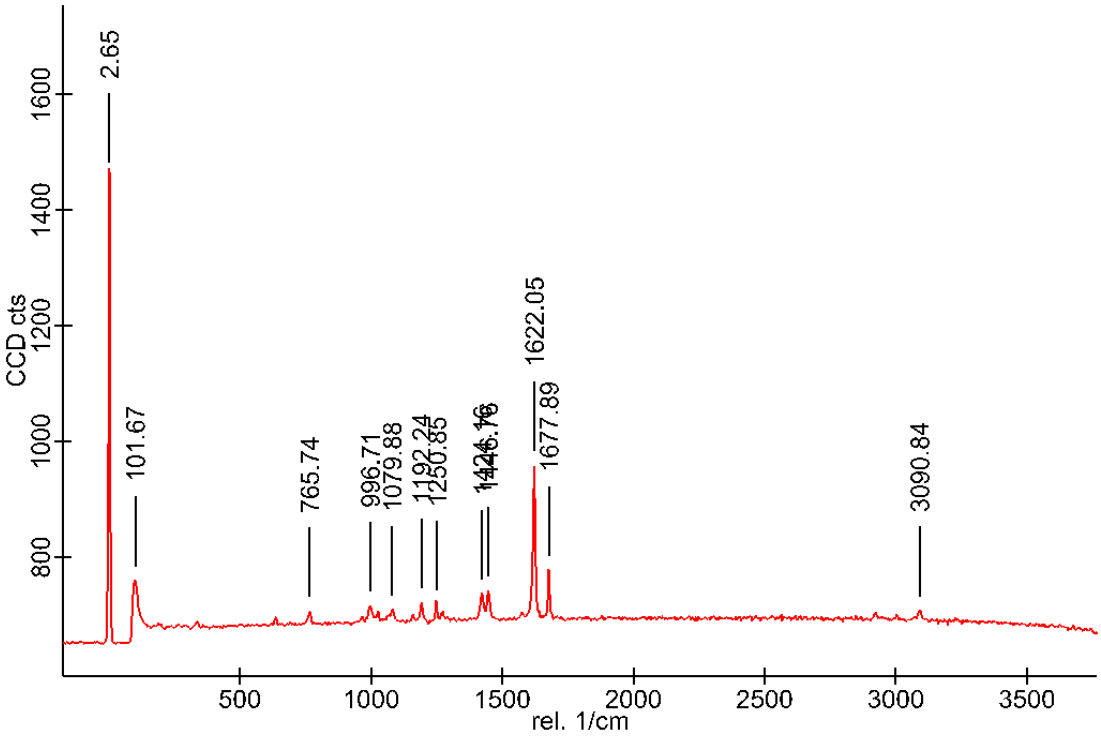


***Figure A1.2***: Raman spectrum of 4-(1H-tetrazol-5-yl) acetylbenzene (**Tzacb**H, **2**).

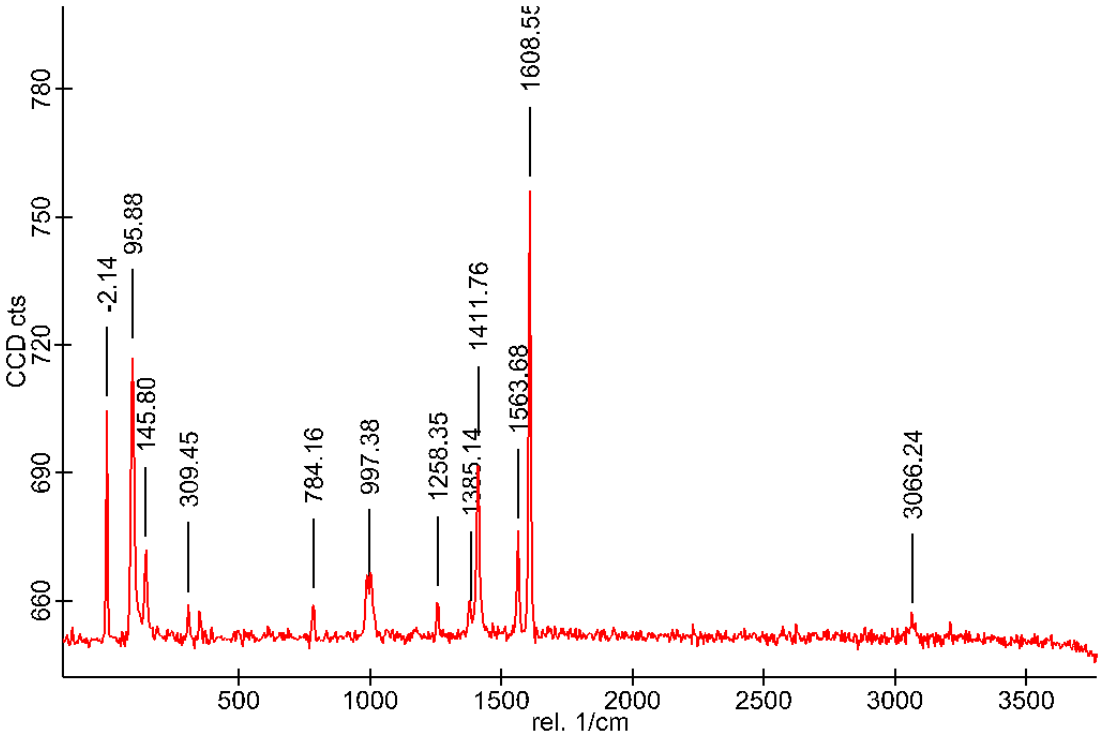


***Figure A1.3***: Raman spectrum of 1H-5-phenyltetrazole (**TzPh**H, **3**)

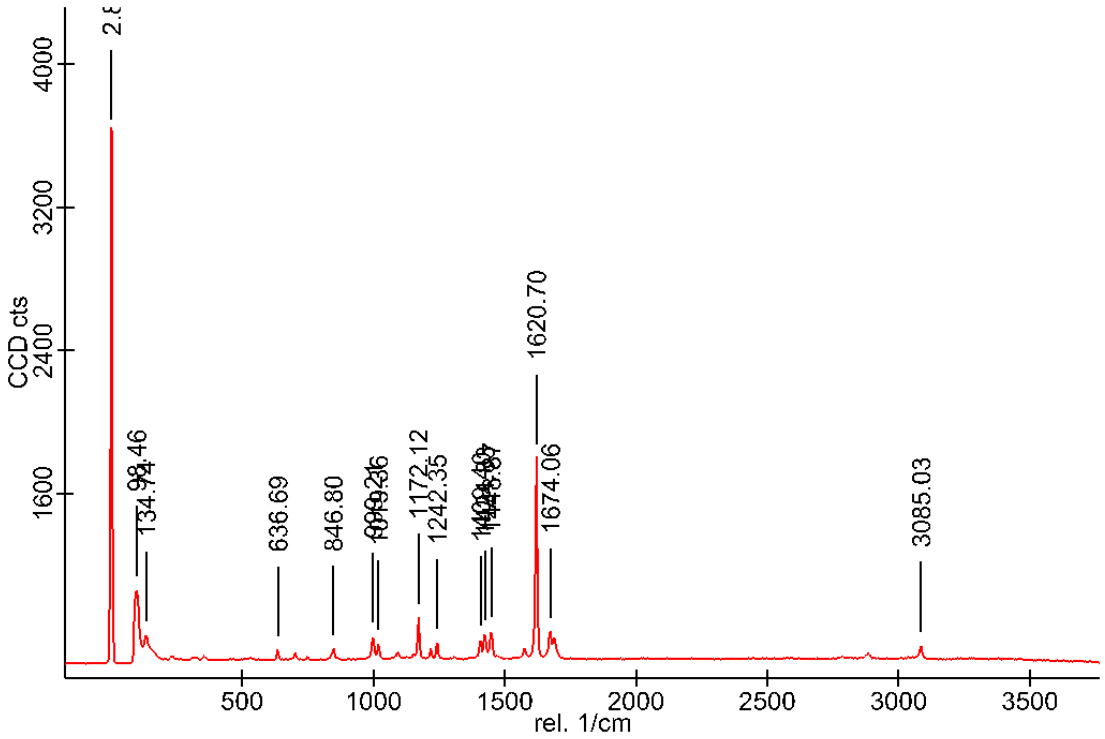


***Figure A1.4***: Raman spectrum of 4-(1H-tetrazol-5-yl) benzaldehyde (**TzPha**H, **4**).

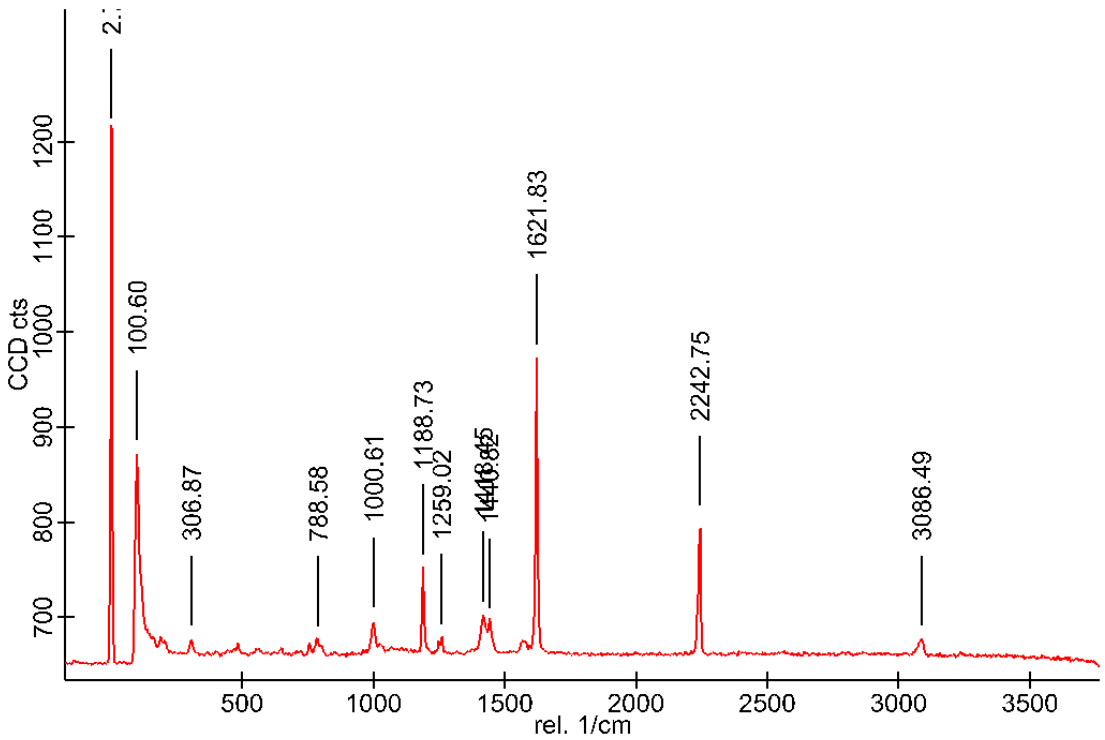


***Figure A1.5***: Raman spectrum of 4-(1H-tetrazol-5-yl) benzonitrile (**TzPhCN**H, **5**).

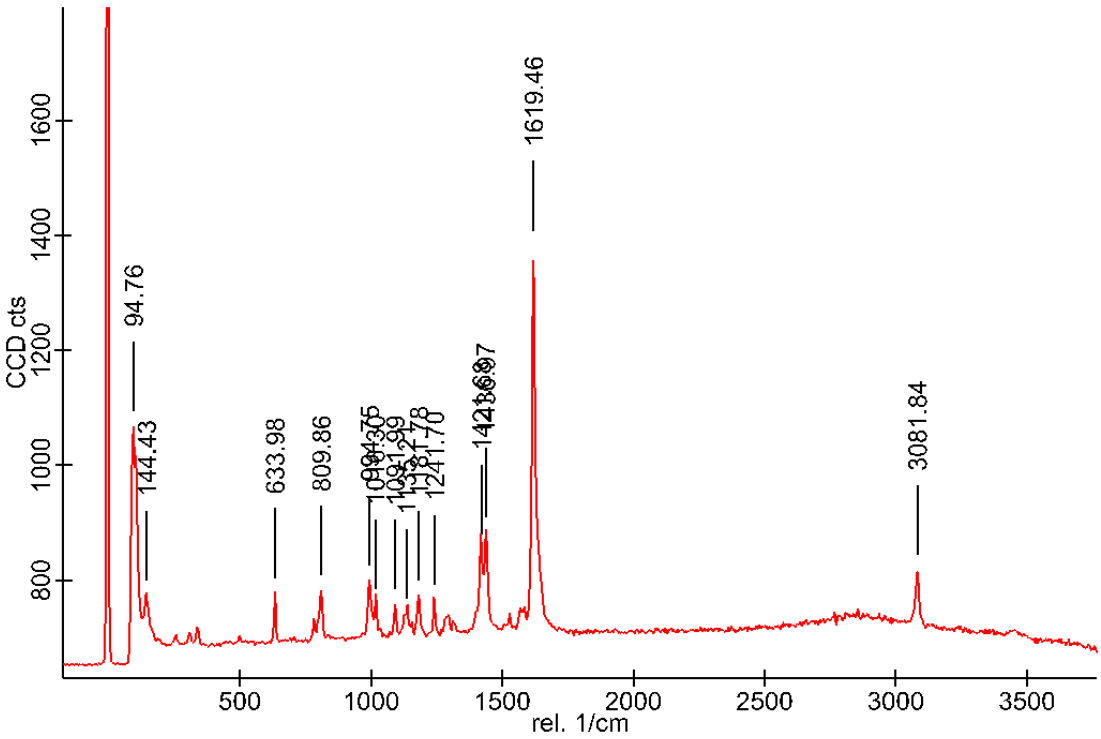


***Figure A1.6***: Raman spectrum of 4-(1H-tetrazol-5-yl) benzoic acid (**TzBa**H, **6**).

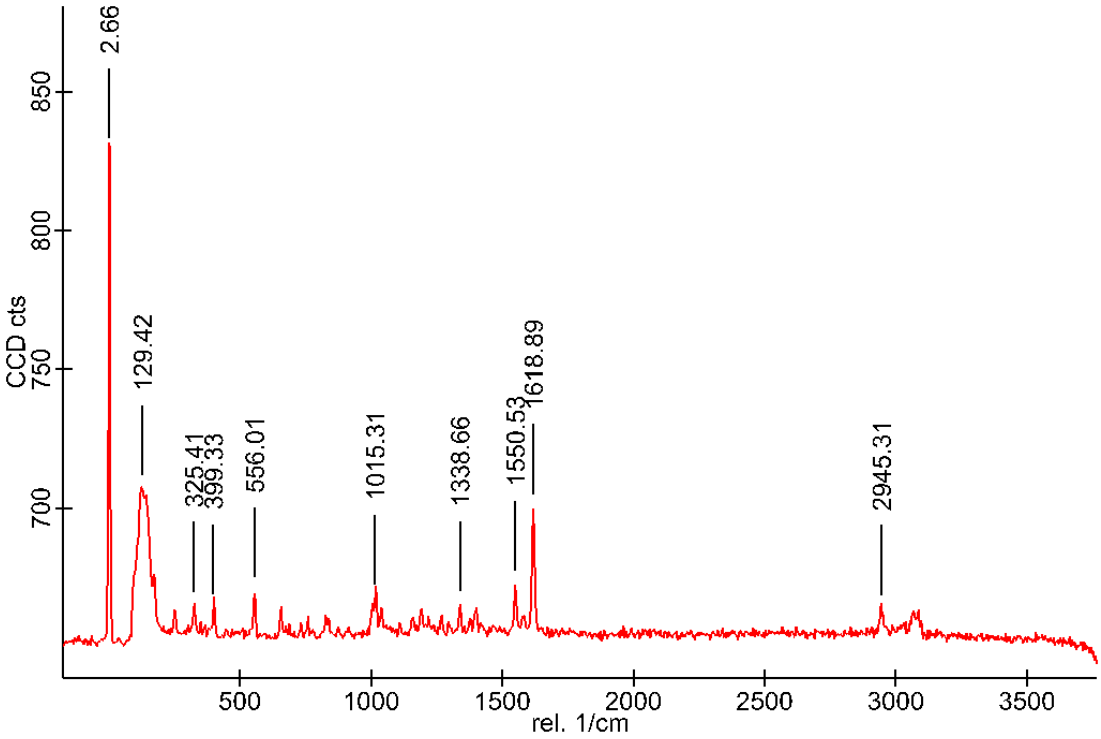


***Figure A1.7***: Raman spectrum of 5-(2-acetyloxyphenyl) tetrazole (**TzAcoPh**H, **7**).

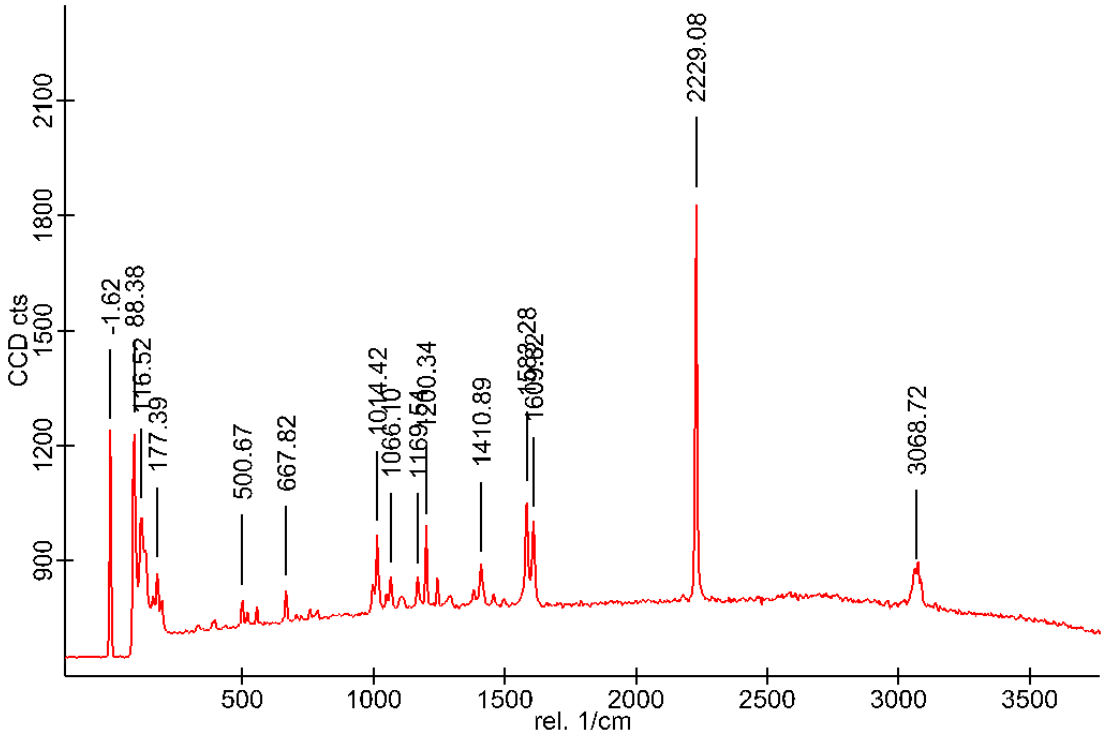


***Figure A1.8***: Raman spectrum of 1,2-bis (1H-tetrazol-5-yl) benzene (***o*TzTz**$H_2$, **8**).

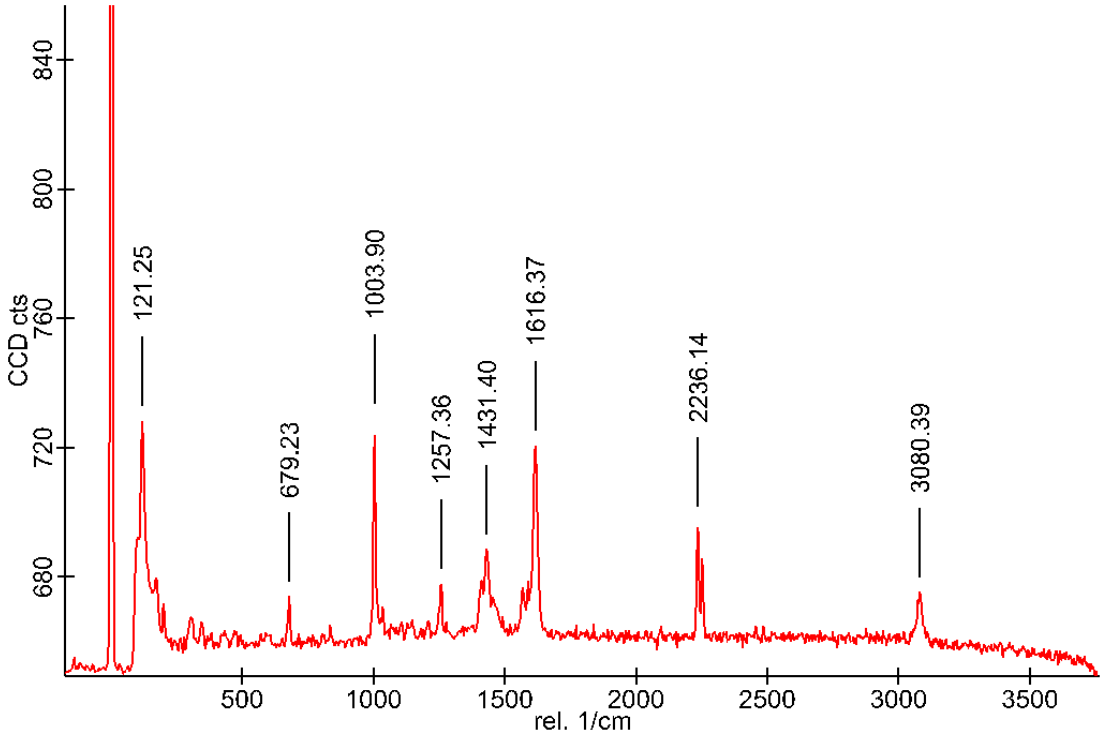


***Figure A1.9***: Raman spectrum of 1,3-bis (1H-tetrazol-5-yl) benzene (***m*TzTz**$H_2$, **9**).

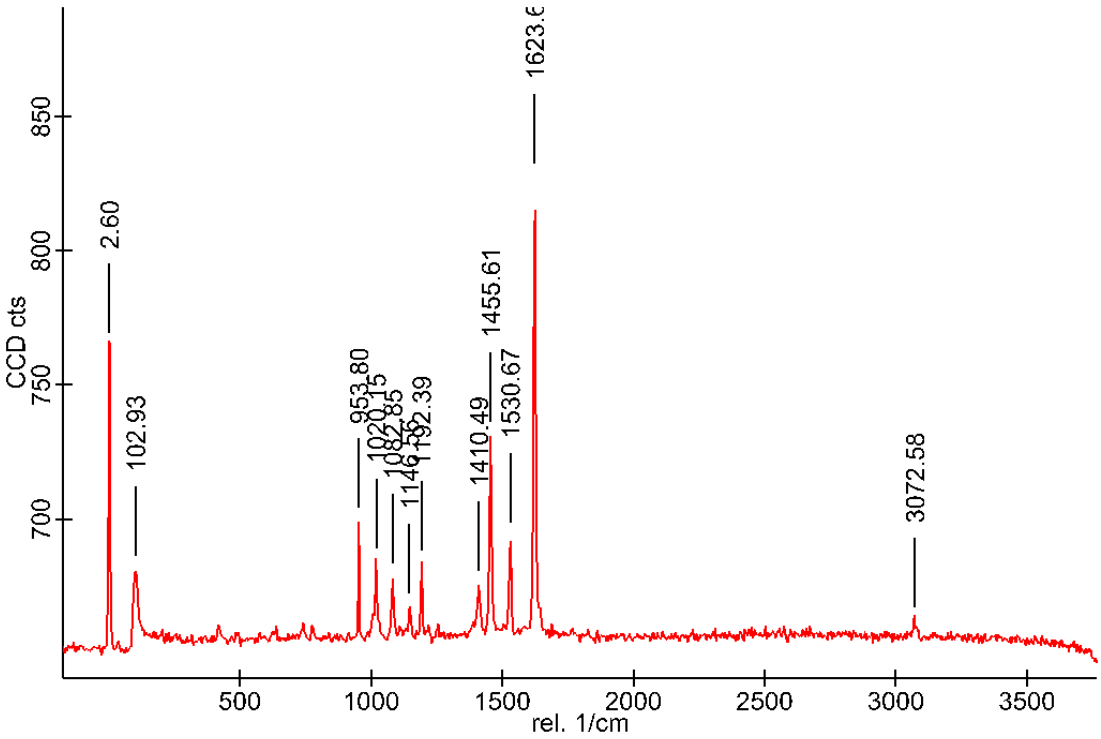


***Figure A1.10***: Raman spectrum of 1,4-bis (1H-tetrazol-5-yl) benzene (***p*TzTz**$H_2$, **10**).

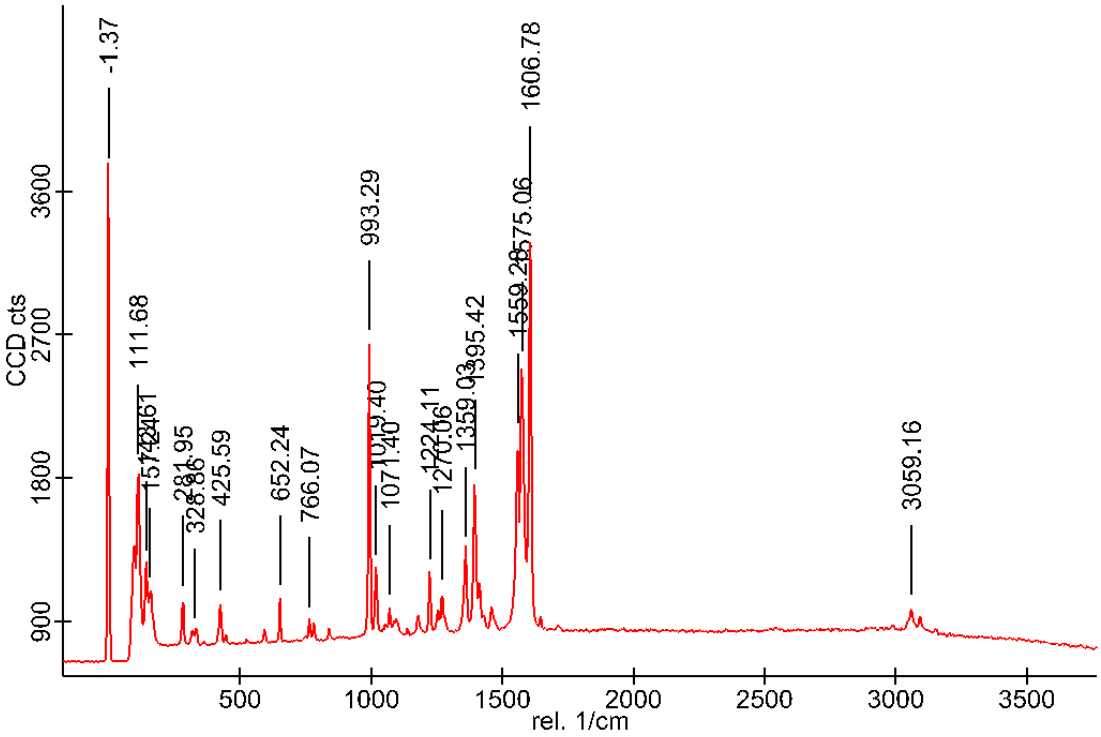


***Figure A1.11***: Raman spectrum of 2,6-bis (1H-tetrazol-5-yl) pyridine (**TzTzPyr**$H_2$, **11**).

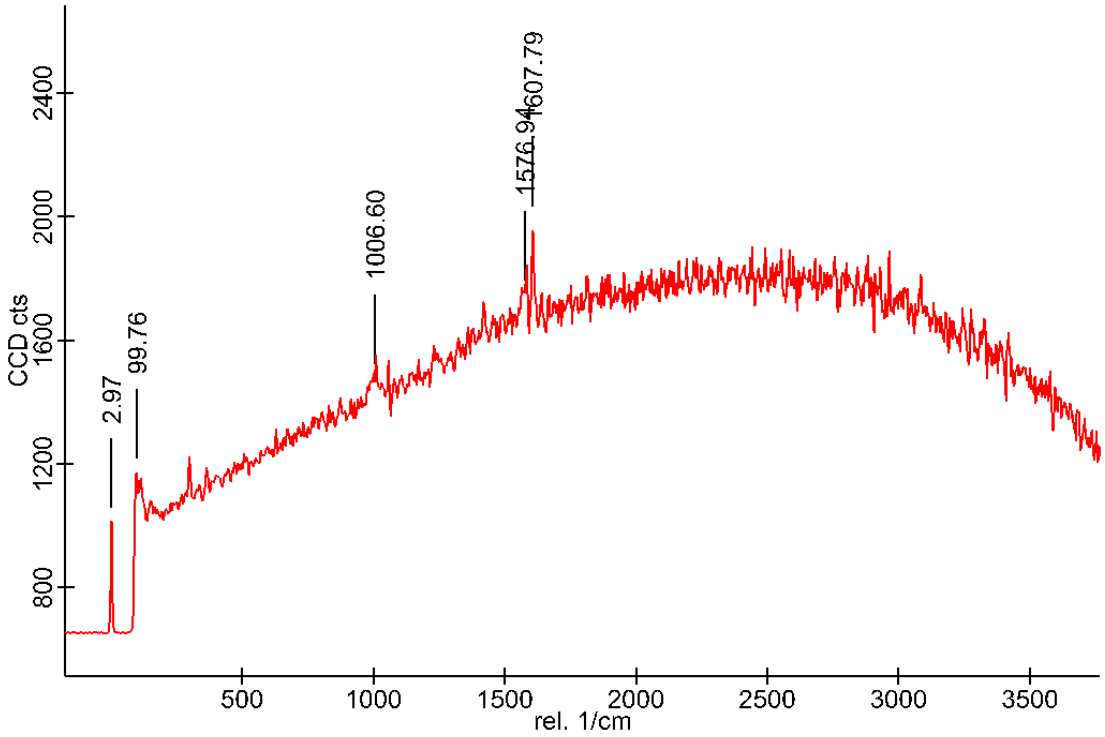


***Figure A1.12***: Raman spectrum of 1H-5-(2-pyridyl) tetrazole (***o*TzPyr**H, **12**).

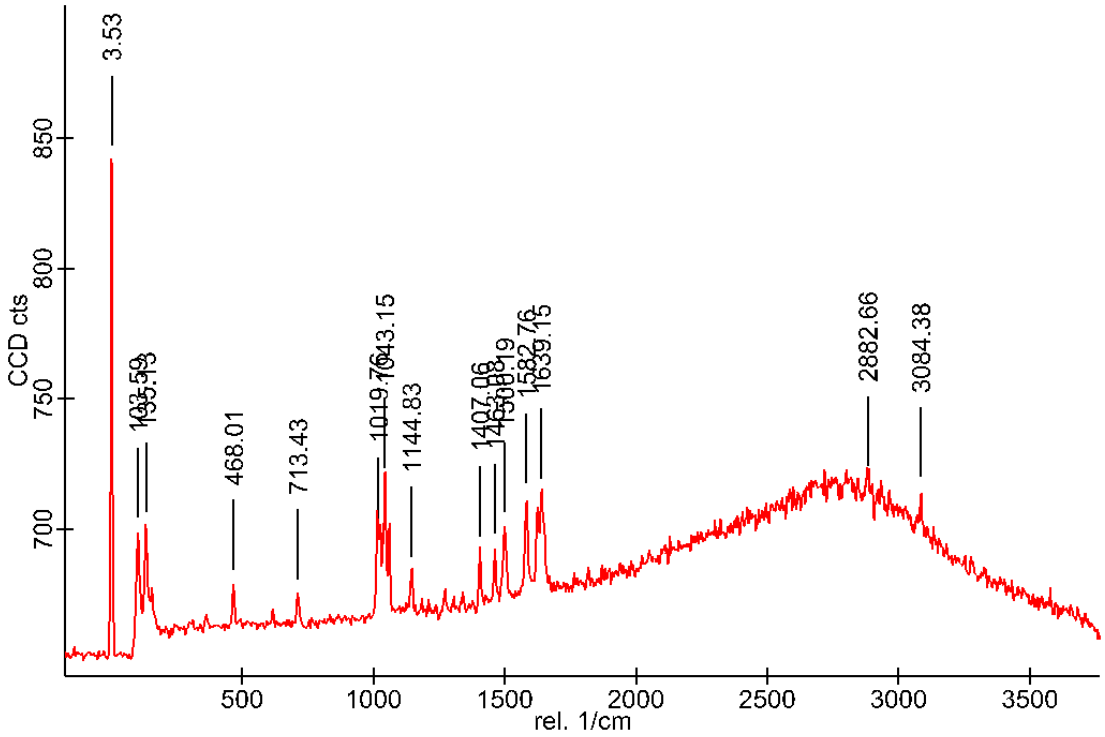


***Figure A1.13***: Raman spectrum of 1H-5-(3-pyridyl) tetrazole (***m*TzPyr**H, **13**).

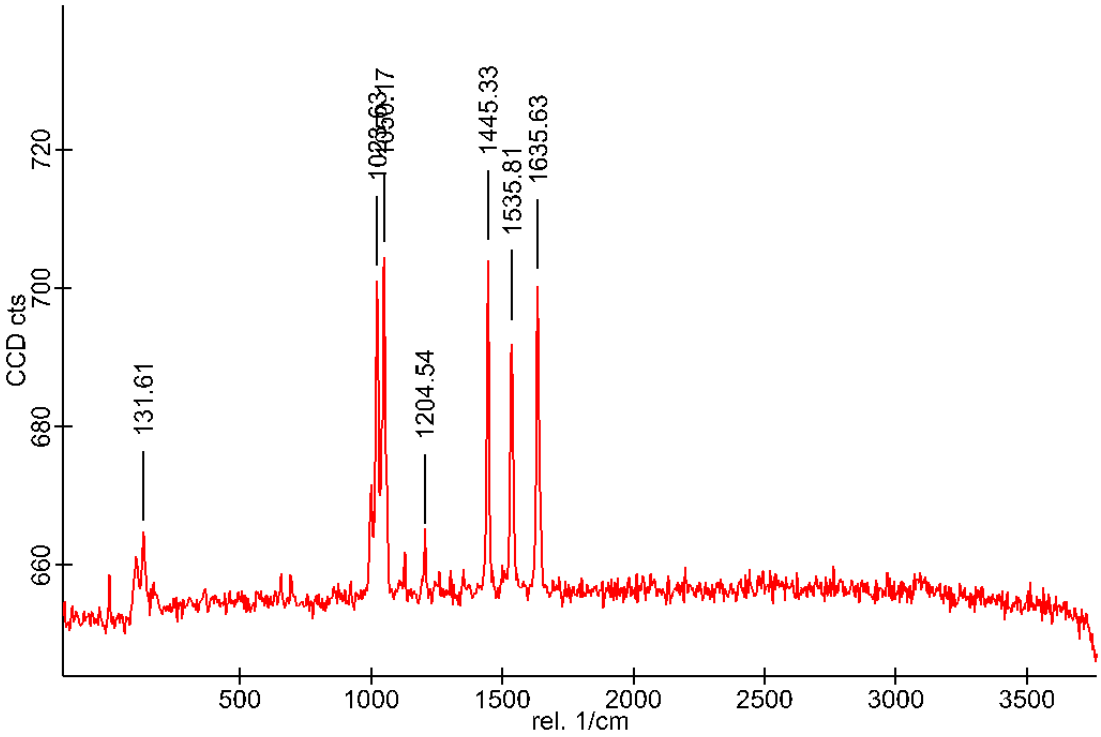


***Figure A1.14***: Raman spectrum of 1H-5-(4-pyridyl) tetrazole (***p*TzPyr**H, **14**).

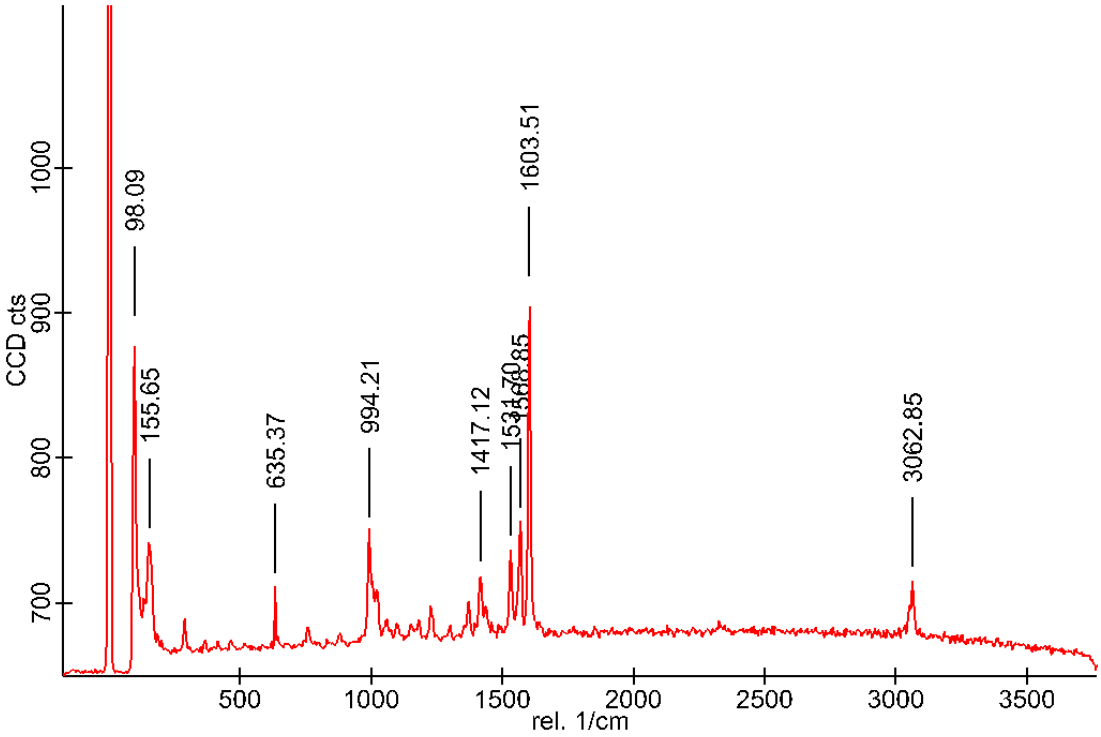


***Figure A1.15***: Raman spectrum of 1H-5-(2-pyrazine) tetrazole (**TzPyz**H, **15**).

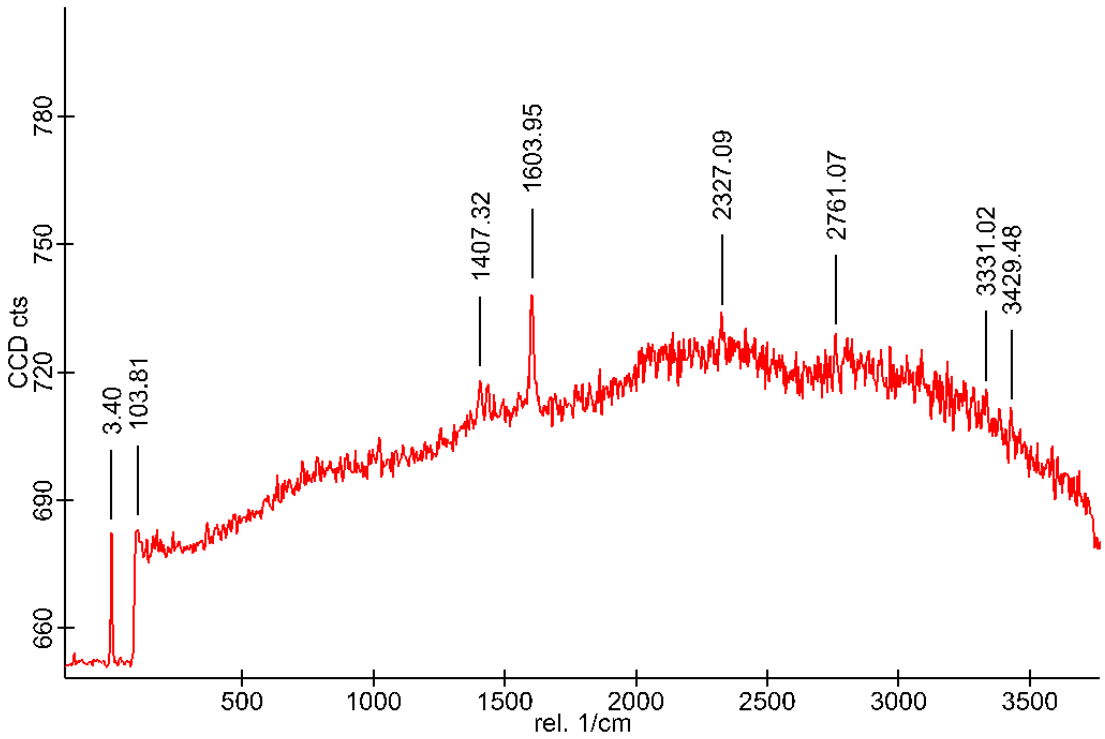


***Figure A1.16***: Raman spectrum of 1H-5-(4-bromophenyl) tetrazole (**TzBrPh**H, **16**).

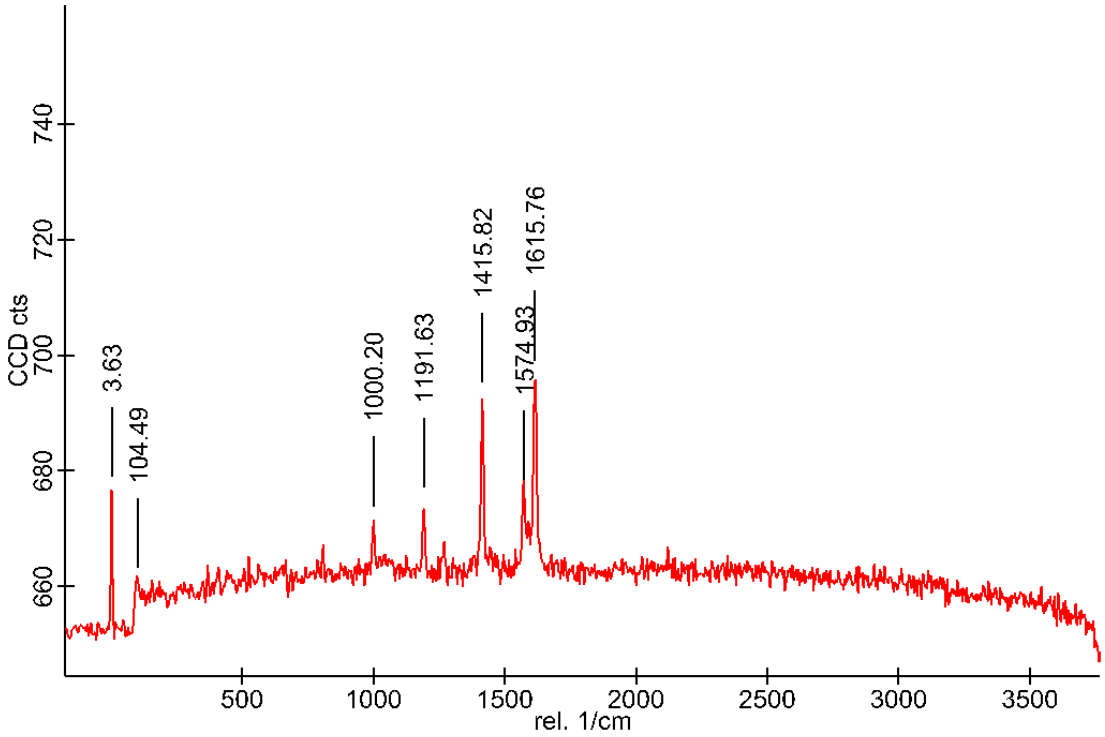


***Figure A1.17***: Raman spectrum of 1H-5-(4-methoxyphenyl) tetrazole (**TzmeoxPh**H, **17**).

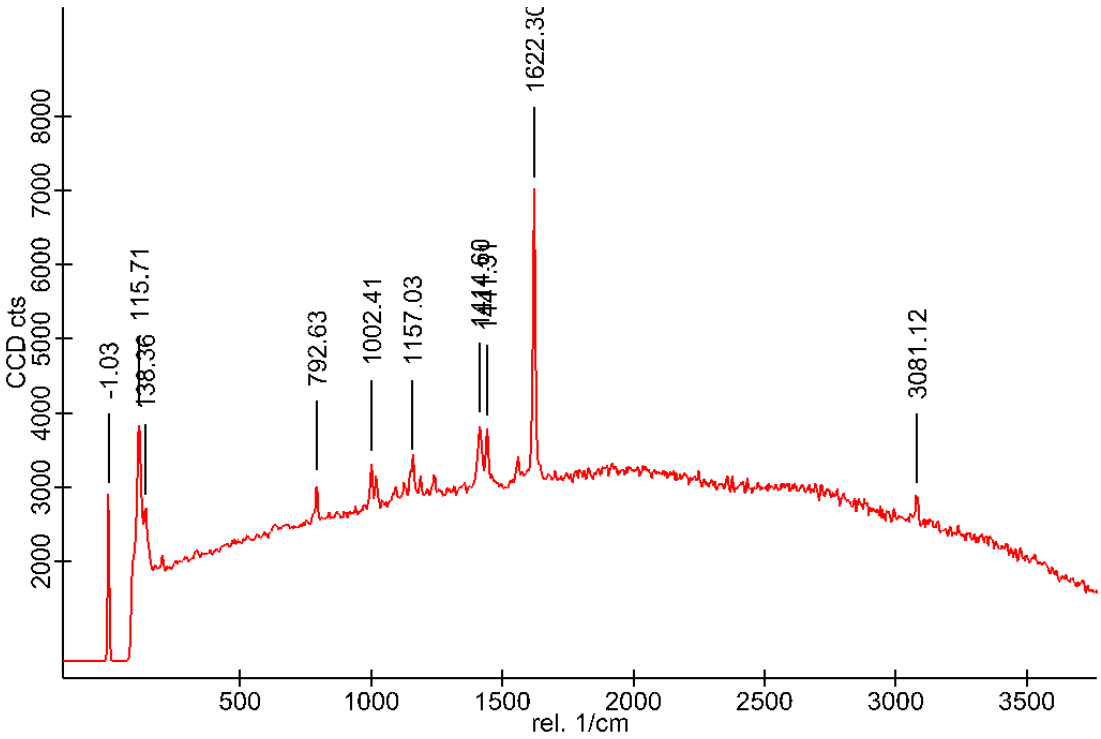


***Figure A1.18***: Raman spectrum of 4-(1H-tetrazol-5-yl) benzamide (**TzPham**H, **18**).

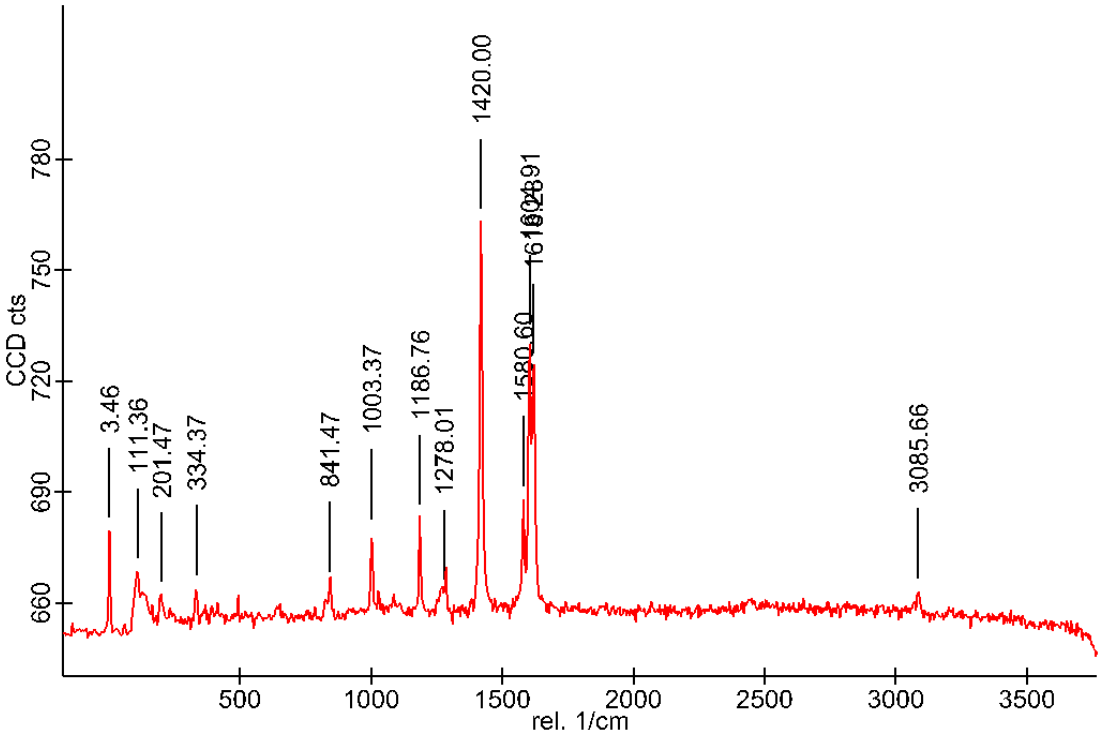


***Figure A1.19***: Raman spectrum of 4-(1H-tetrazol-5-yl) phenol (**TzPhOH**H, **19**).

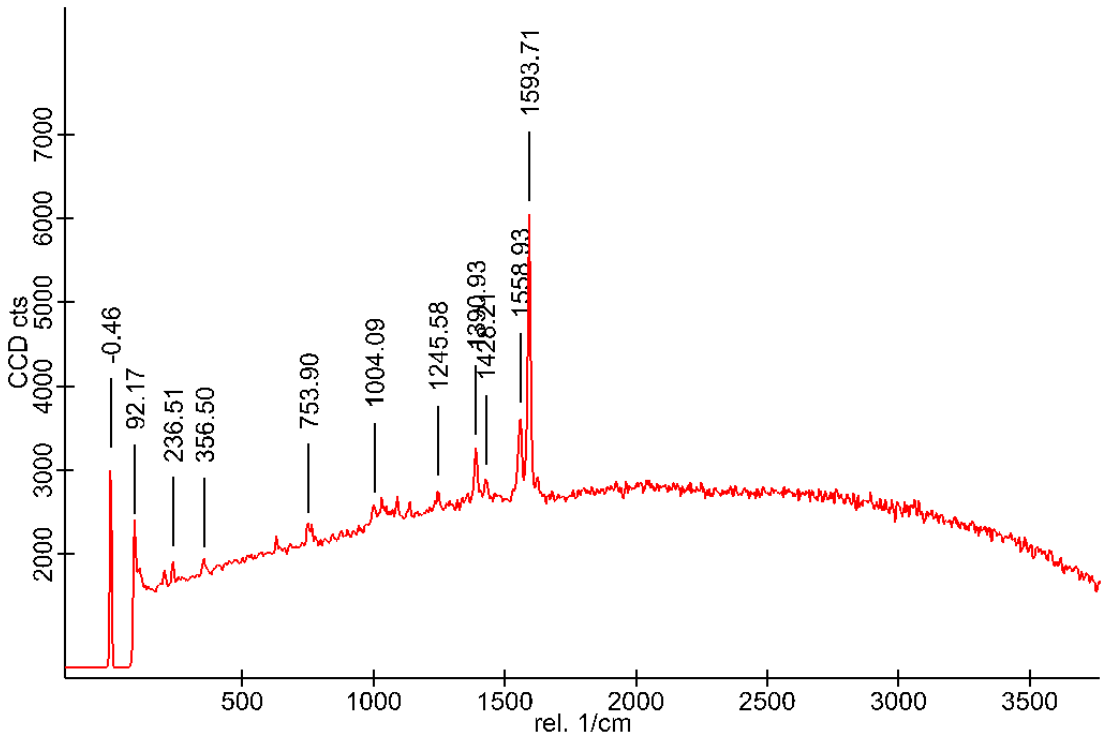


***Figure A1.20***: Raman spectrum of 1H-4-bromo-(2-pyridyl)-tetrazole (**TzBrPyr**H, **20**).

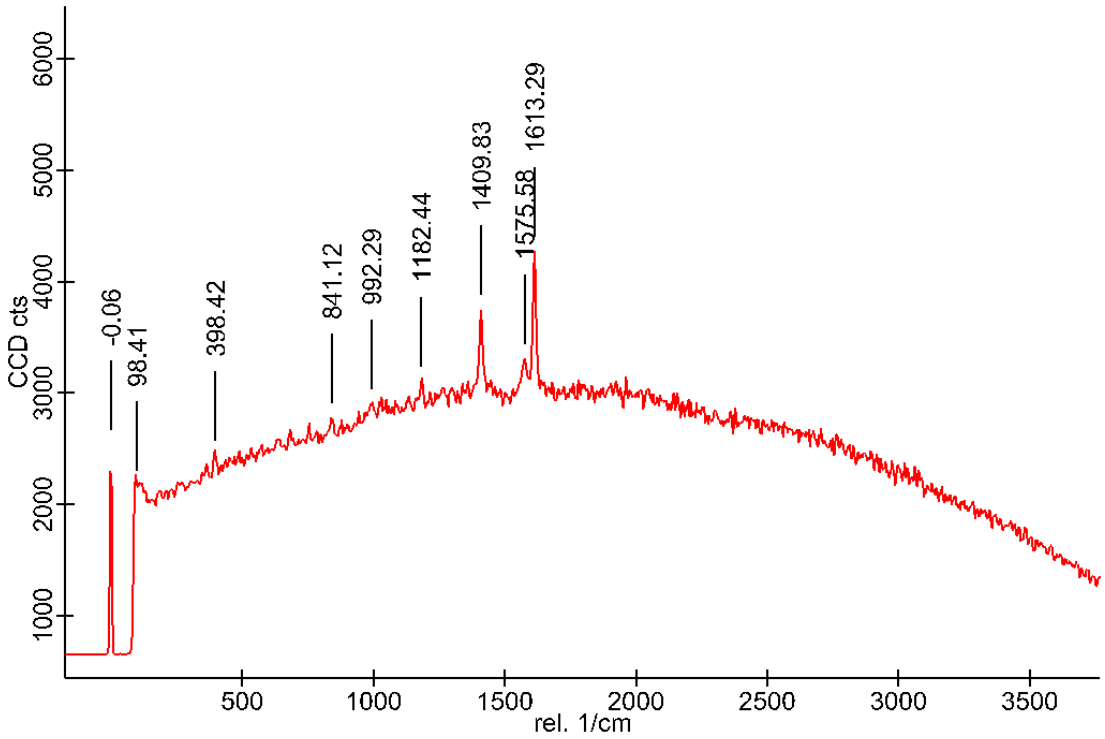


***Figure A1.21***: Raman spectrum of 1H-4-allylphenyl-tetrazole (**TzAlPh**H, **21**).

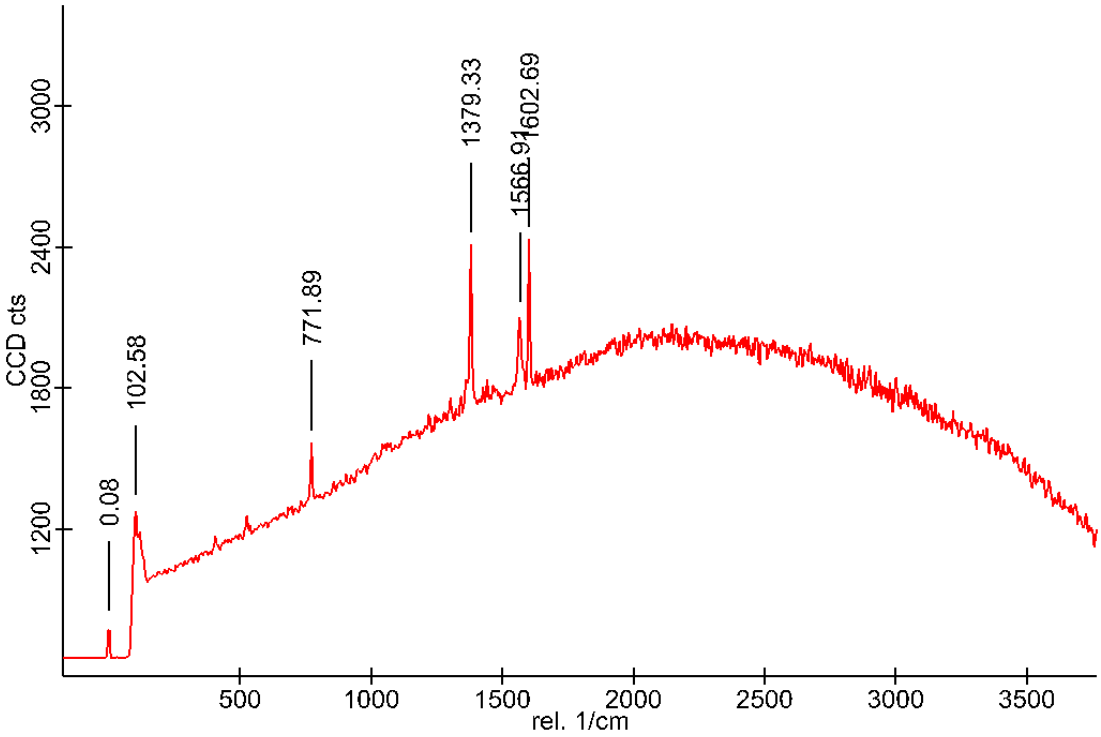


***Figure A1.22***: Raman spectrum of 2-(1H-tetrazol-5-yl) quinolone (**TzQn**H, **22**).

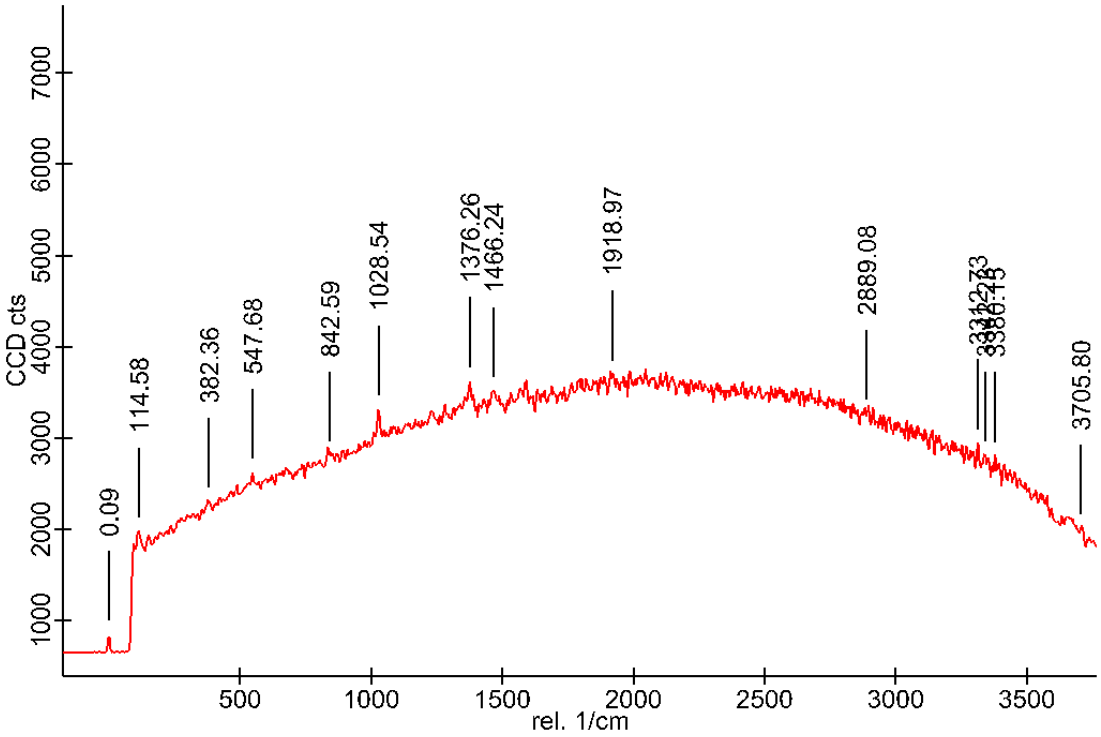


***Figure A1.23***: Raman spectrum of 1-(1H-tetrazol-5-yl) isoquinoline (**TzIsoQn**H, **23**).

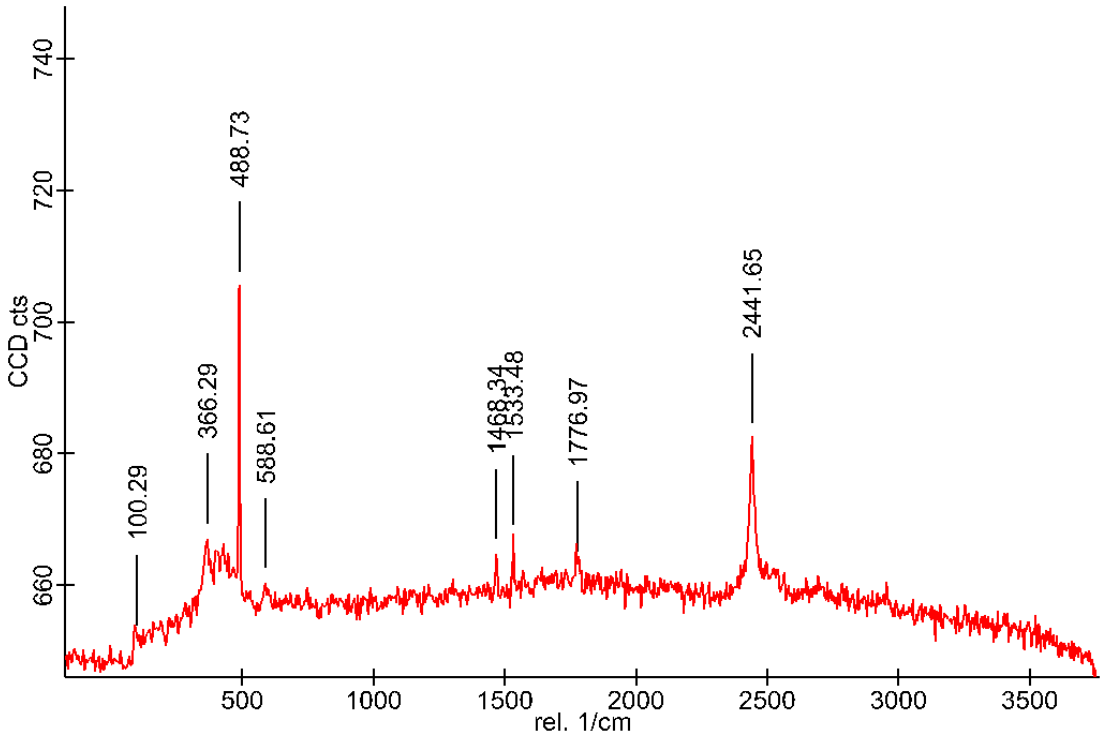


***Figure A1.24***: Raman spectrum of 1-(1H-tetrazol-5-yl) naphthalene (**TzNaph**H, **24**).

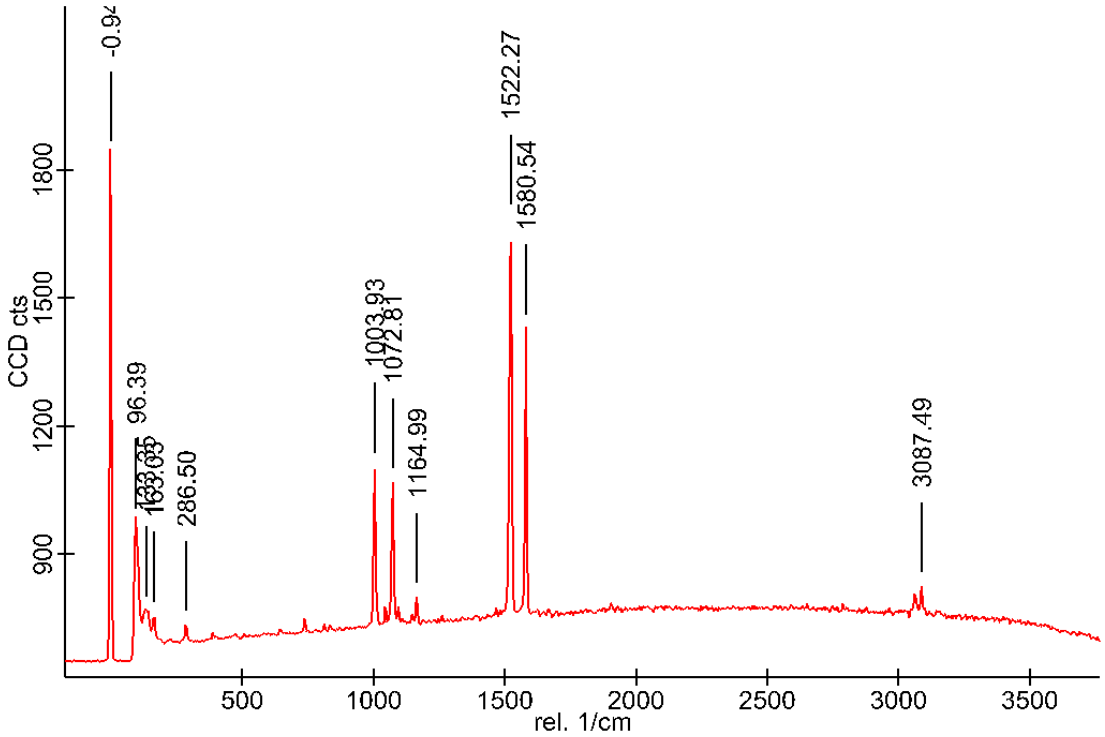


***Figure A1.25***: Raman spectrum of 2-(1H-tetrazol-5-yl) pyrimidine (**TzPyrm**H, **25**).

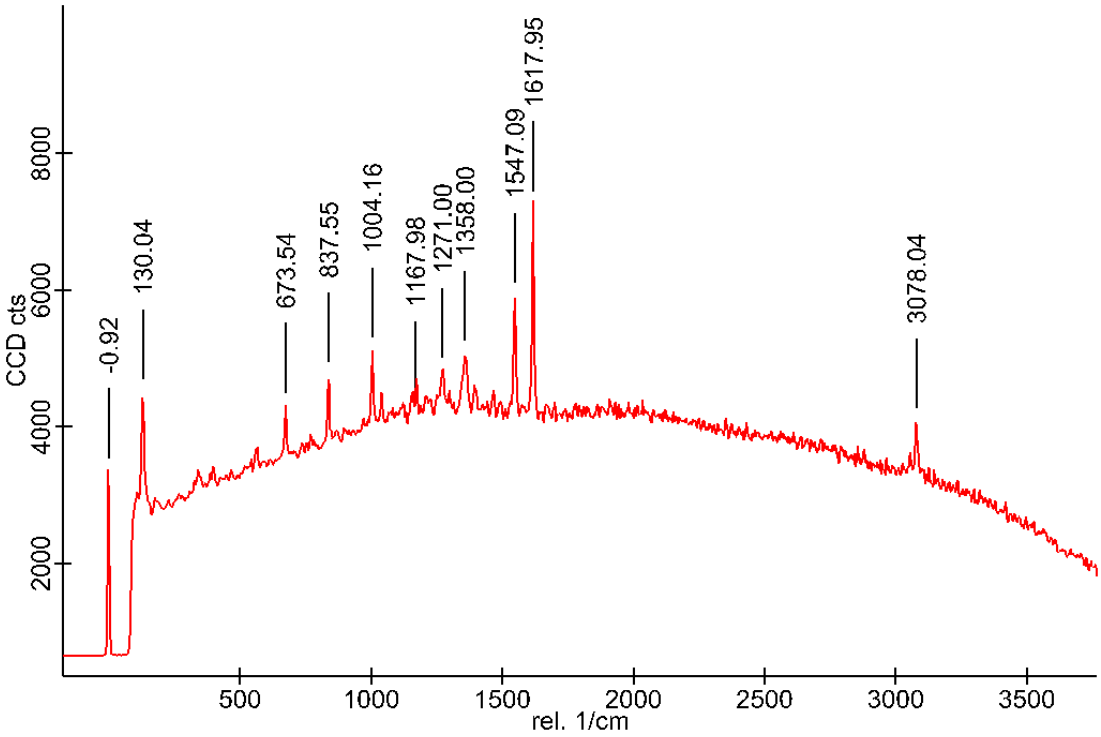


***Figure A1.26***: Raman spectrum of 2-(1H-tetrazol-5-yl) phenol (***o*TzPhOH**H, **26**).

## A1b Tetrazole Spectra not synthesised by Author

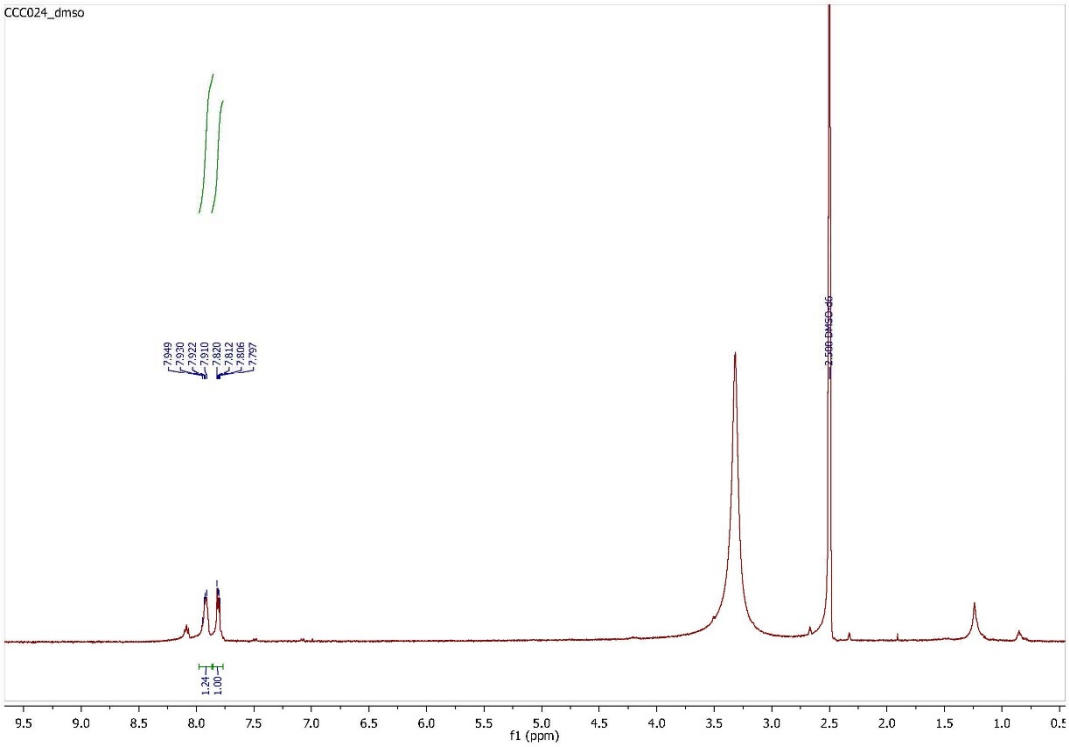


***Figure A1b.1***: NMR spectrum of 1,2-bis (1H-tetrazol-5-yl) benzene (***o*TzTz**$H_2$, **8**).

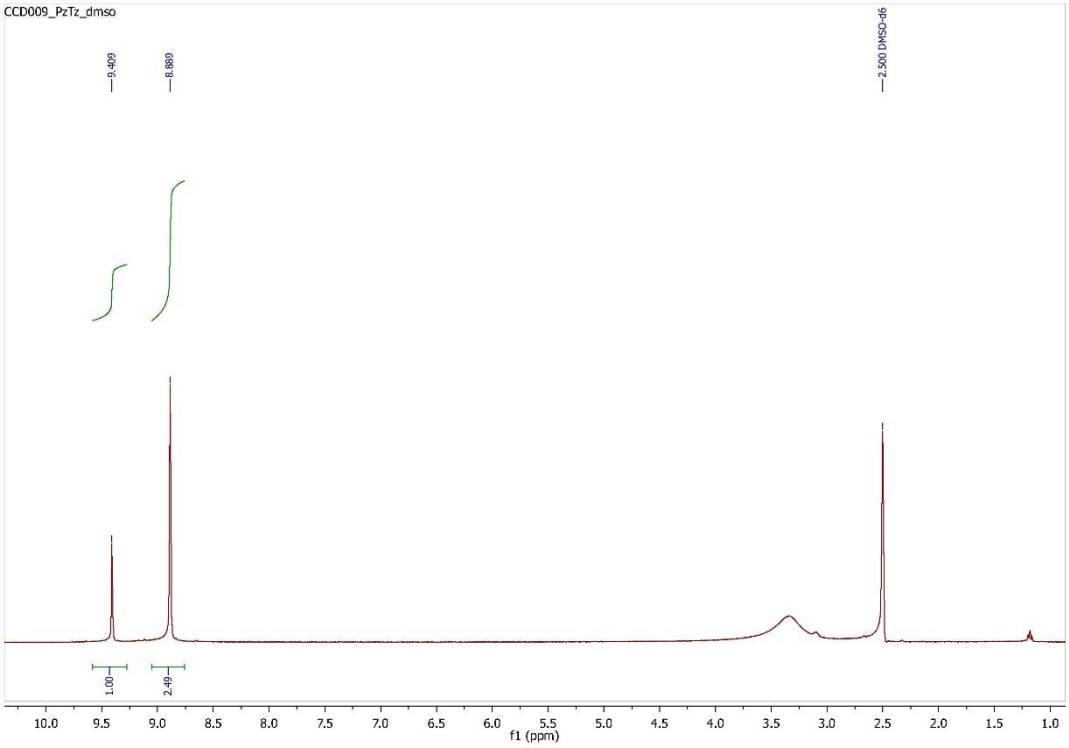


***Figure A1b.2***: NMR spectrum of 1H-5-(2-pyrazine) tetrazole (**TzPyz**H, **15**).

NMR signals reported for 1H-5-(4-bromophenyl) tetrazole (**TzBrPh**H, **16**) as synthesised by Melissa Werrett: $^{1}$H NMR (δ, ppm, DMSO-$d_6$): 7.98 (2H, d, *J*= 6.8 Hz, $CN_4$-$C_6H_4$-Br $H_{ortho}$), 7.83 (2H, d, *J*= 6.6 Hz, $CN_4$-$C_6H_4$-Br $H_{meta}$). $^{13}$C NMR (δ, ppm, DMSO-$d_6$): 155.1 (*C*$N_4$-$C_6H_4$-Br), 132.5, 128.9, 124.7, 123.6.

NMR signals reported for 4-(1H-tetrazol-5-yl) phenol (**TzPhOH**H, **19**) as synthesised by Philip Wright: $^{1}$H NMR (δ, ppm, DMSO-$d_6$): 10.1 (1H, br s), 7.85 (2H, d, *J*= 8.8 Hz), 6.94 (2H, d, *J*= 8.8 Hz). $^{13}$C NMR (δ, ppm, DMSO-$d_6$): 159.8, 155.1, 128.6, 116.0, 115.2.

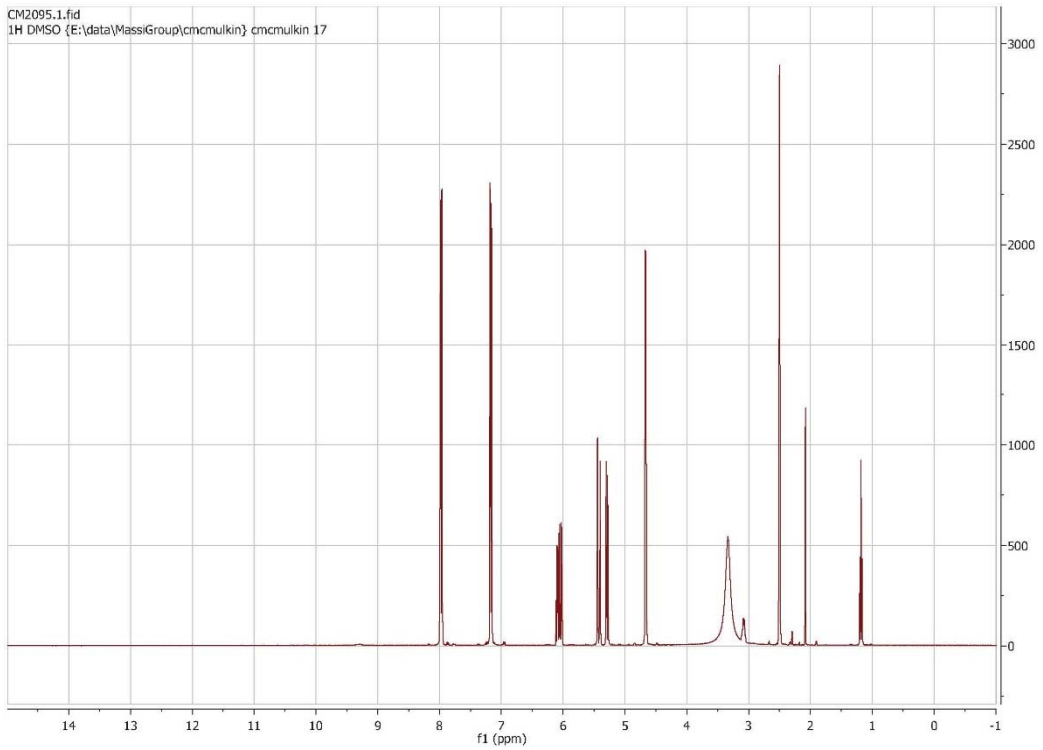


***Figure A1b.5***: NMR spectrum of 1H-4-allylphenyl-tetrazole (**TzAlPh**H, **21**).

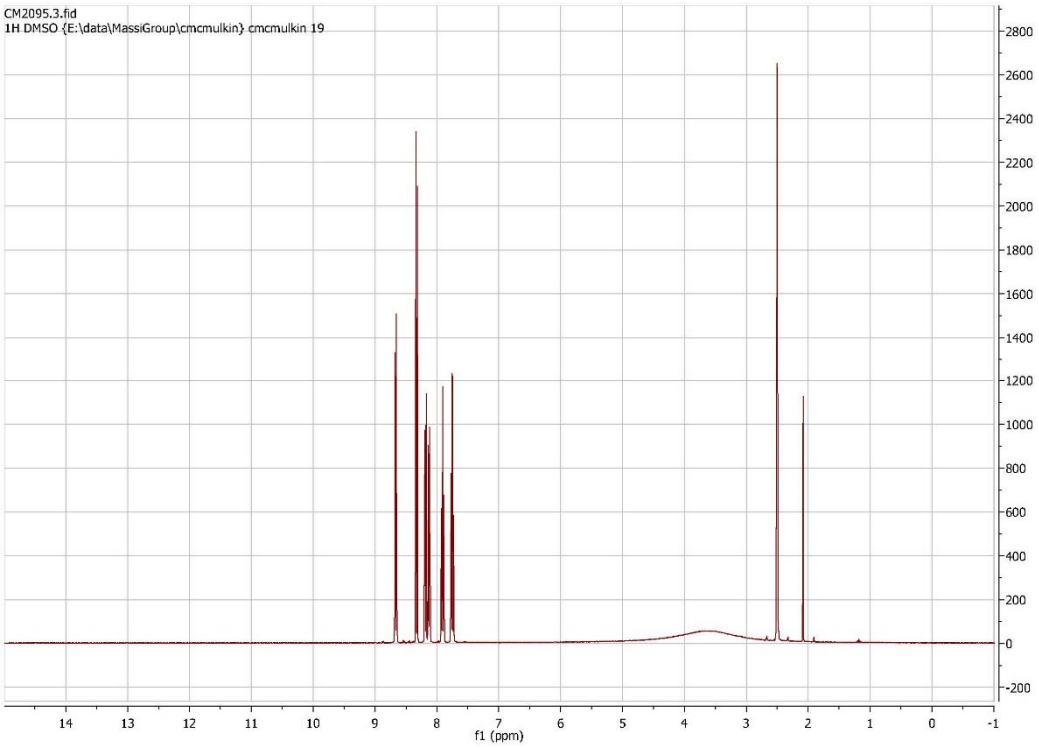


***Figure A1b.6***: NMR spectrum of 2-(1H-tetrazol-5-yl) quinolone (**TzQn**H, **22**).

## A2 Absorption of Tetrazole Series

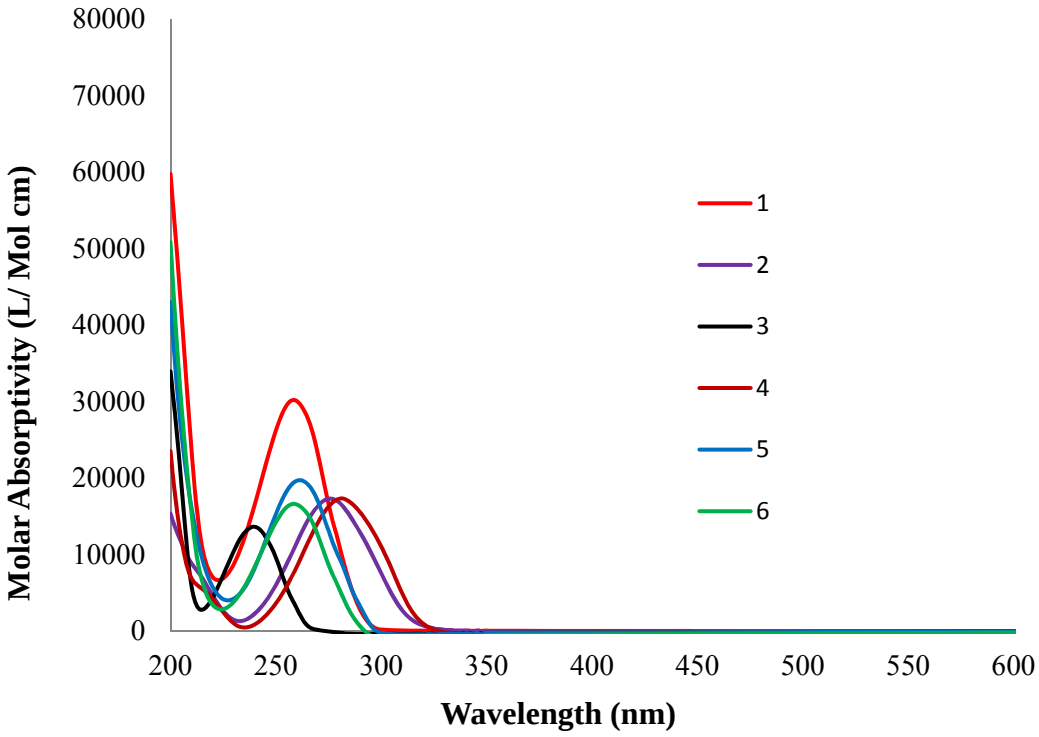


***Figure A2.1***: Absorption spectra of tetrazoles **1** to **6** in $H_2O$ ($10^{-6}$ M).

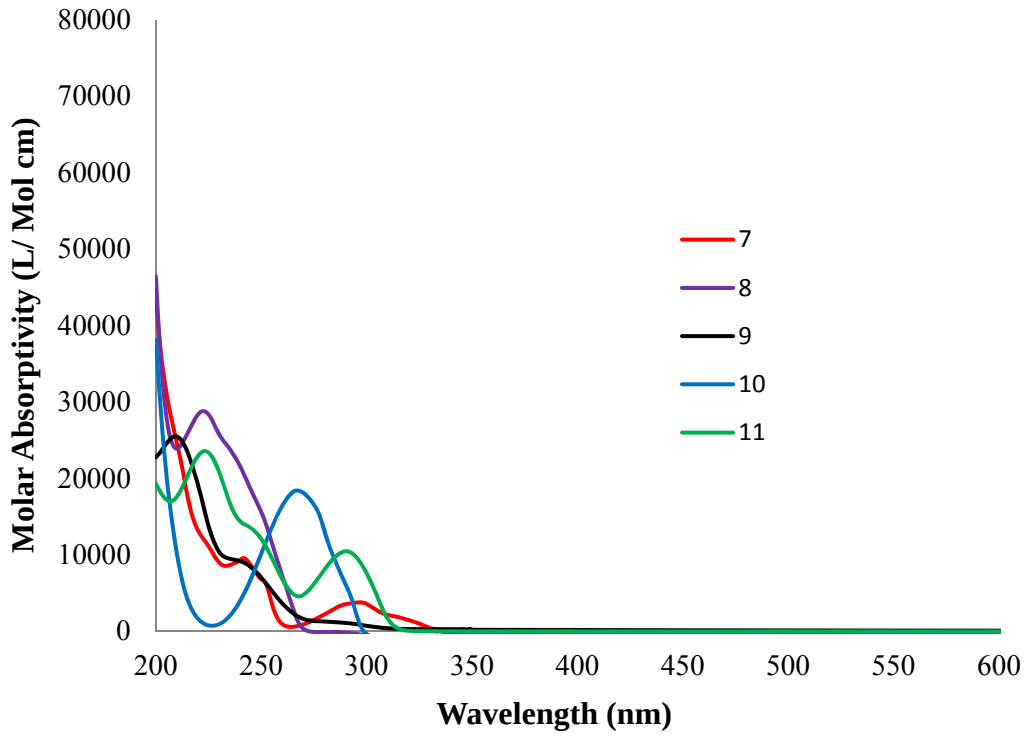


***Figure A2.1***: Absorption spectra of tetrazoles **7** to **11** in $H_2O$ ($10^{-6}$ M).

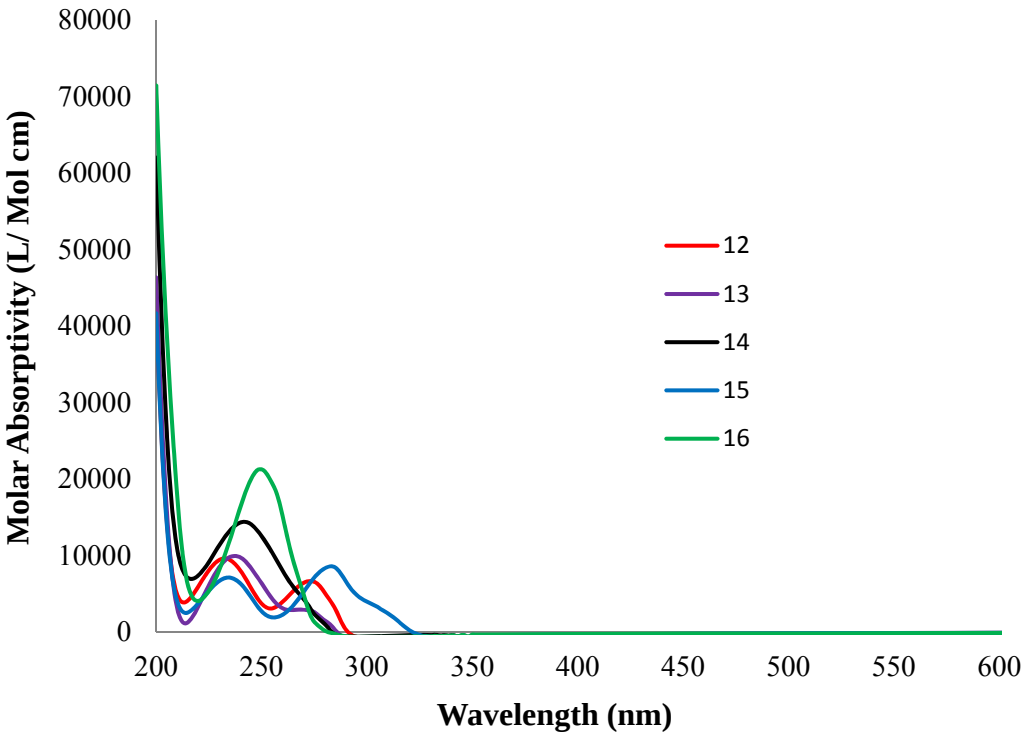


***Figure A2.2***: Absorption spectra of tetrazoles **12** to **16** in $H_2O$ ($10^{-6}$ M).

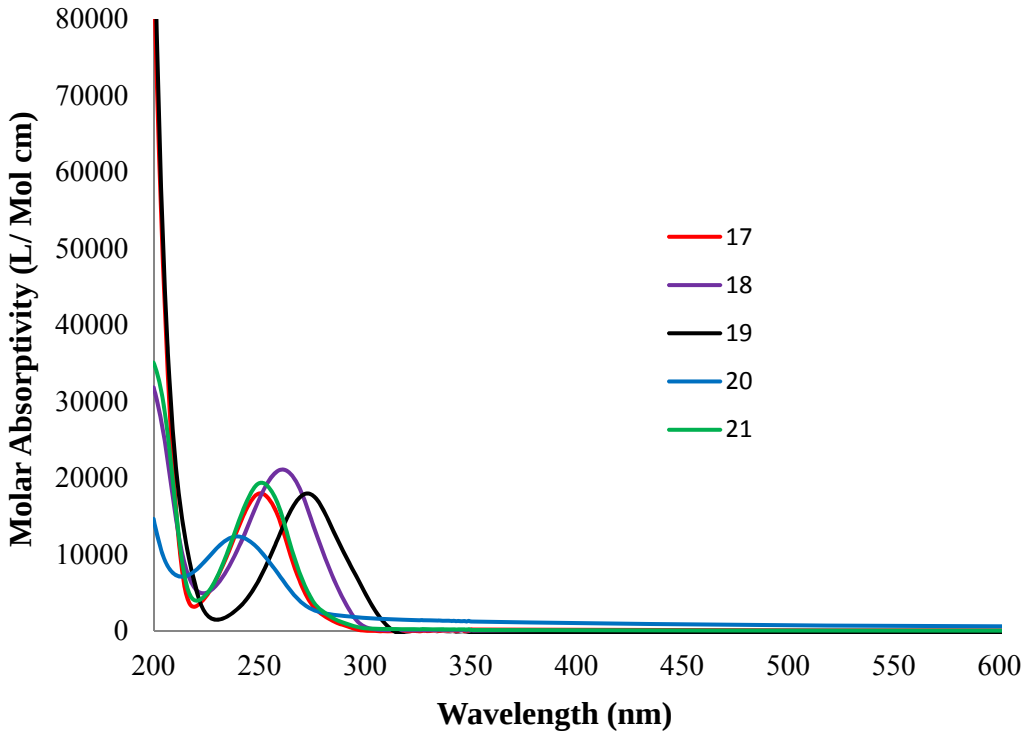


***Figure A2.3***: Absorption spectra of tetrazoles **17** to **21** in $H_2O$ ($10^{-6}$ M).

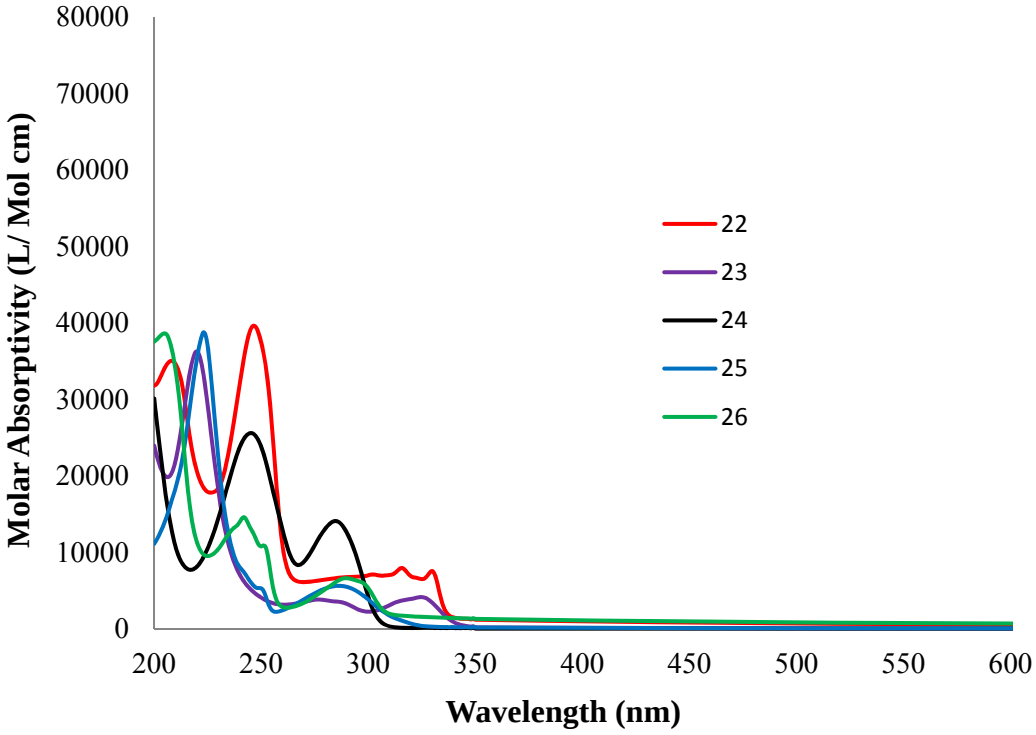


***Figure A2.4***: Absorption spectra of tetrazoles **22** to **26** in $H_2O$ ($10^{-6}$ M).

## A3 Emission and Excitation of Tetrazole Series

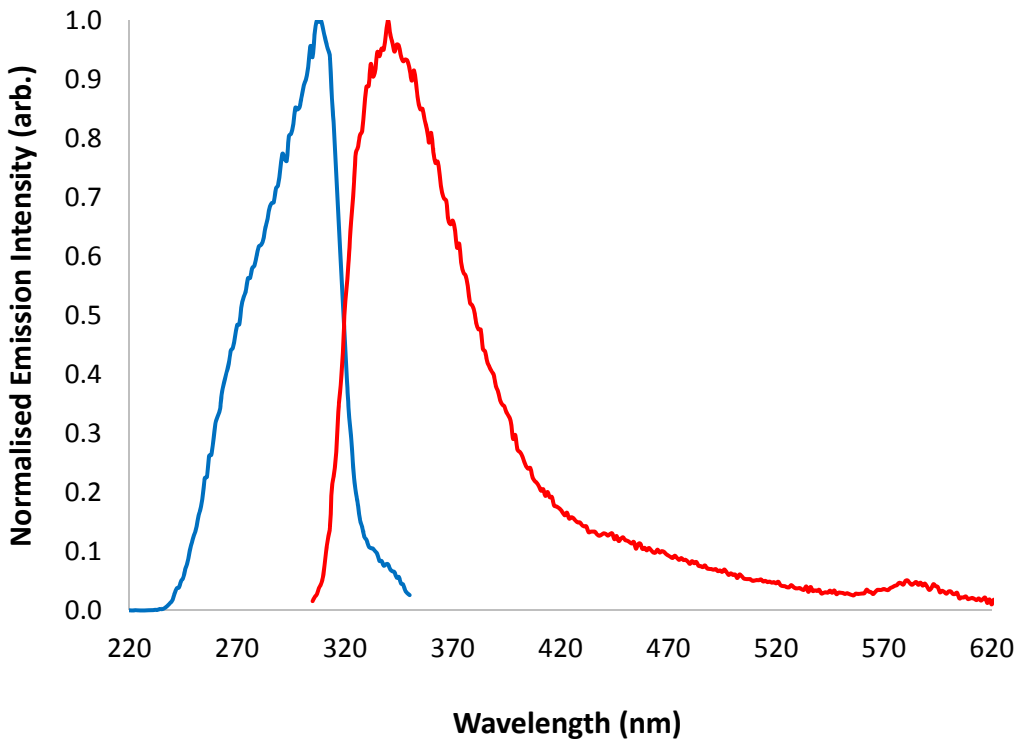


***Figure A3.1a***: Excitation and Emission profile of **1** in the solid state.

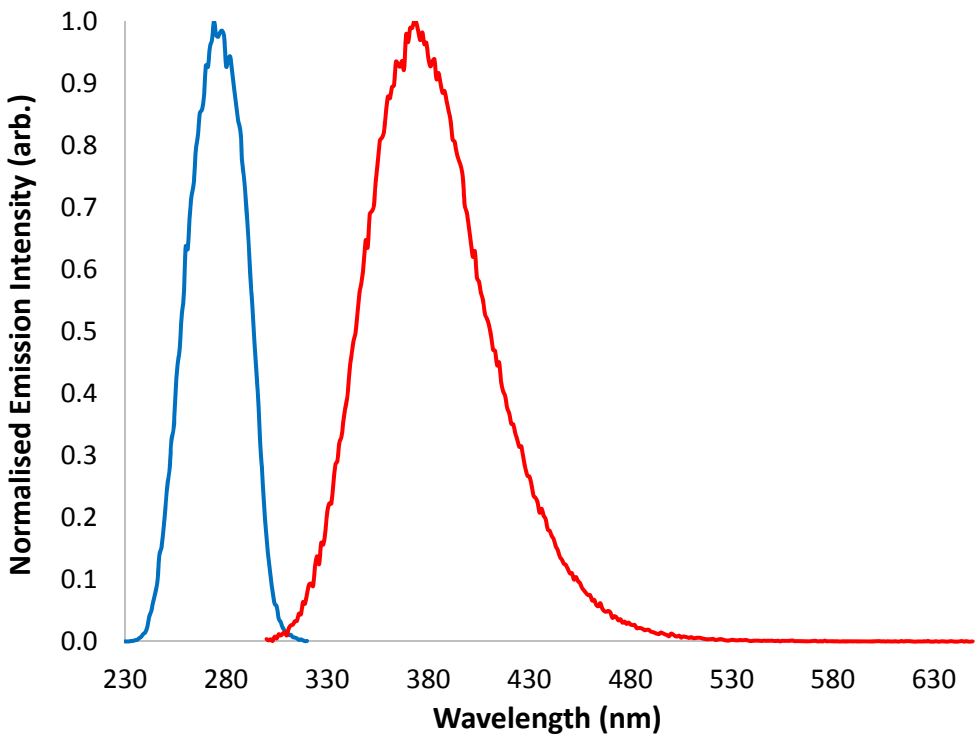


***Figure A3.1b***: Excitation and Emission profile of **1** in $H_2O$ ($10^{-6}$ M).

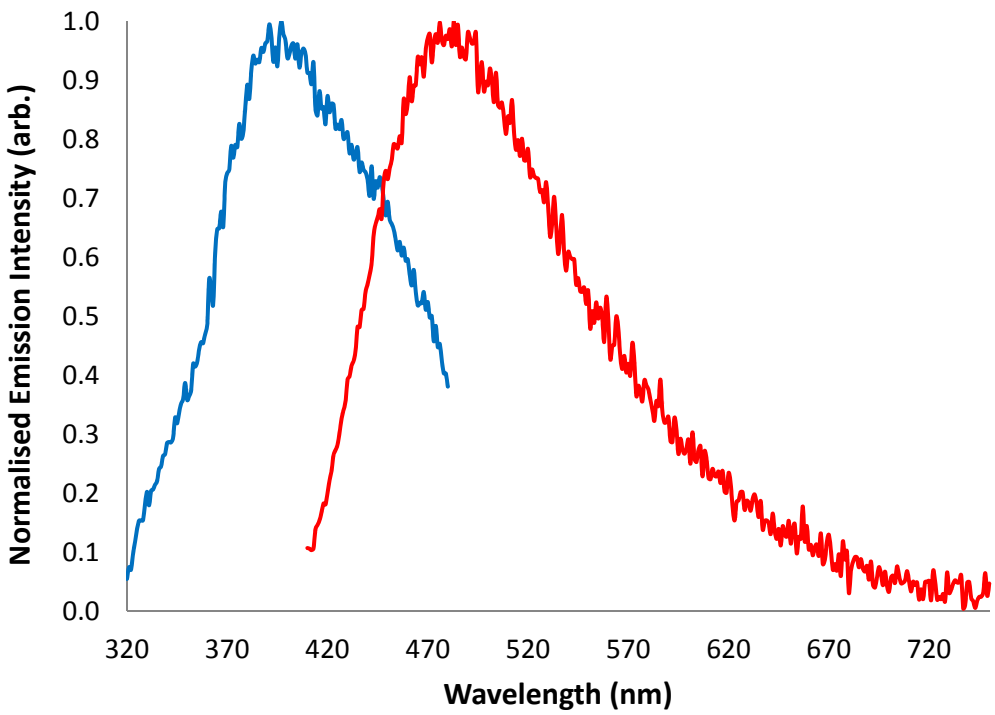


***Figure A3.2a***: Excitation and Emission profile of **2** in the solid state.

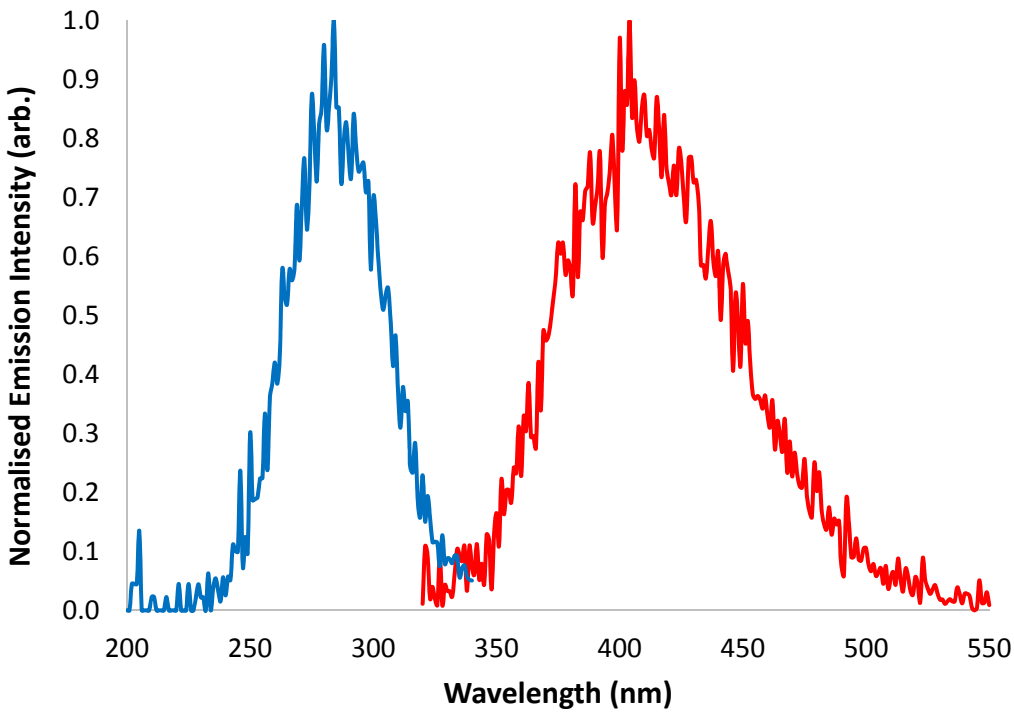


***Figure A3.2b***: Excitation and Emission profile of **2** in $H_2O$ ($10^{-6}$ M).

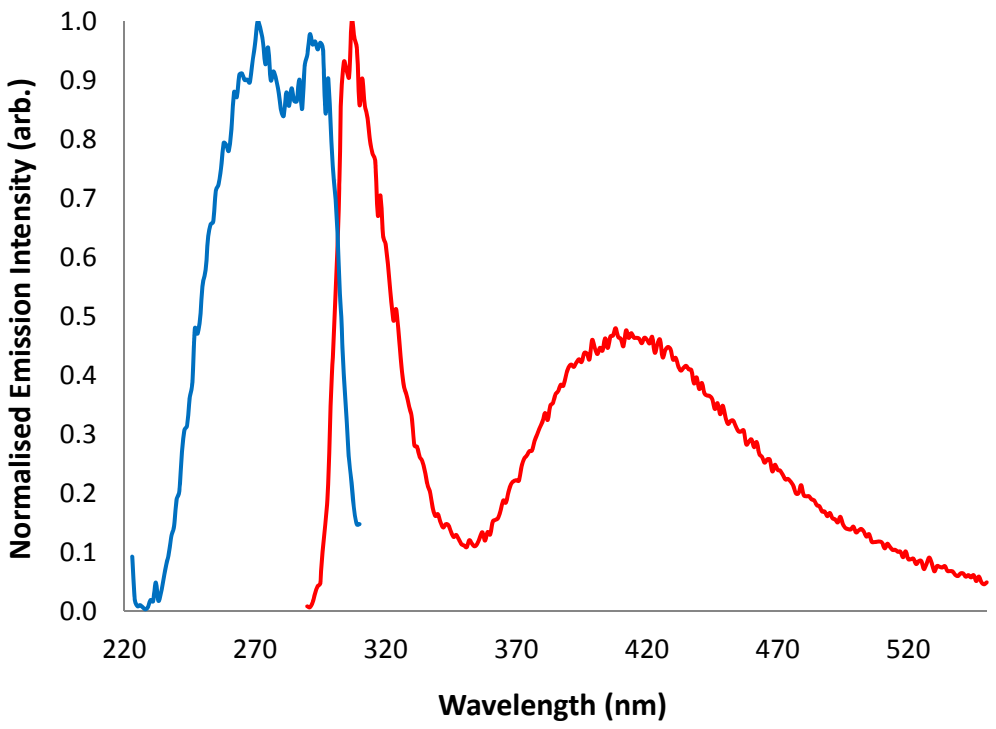


***Figure A3.3a***: Excitation and Emission profile of **3** in the solid state.

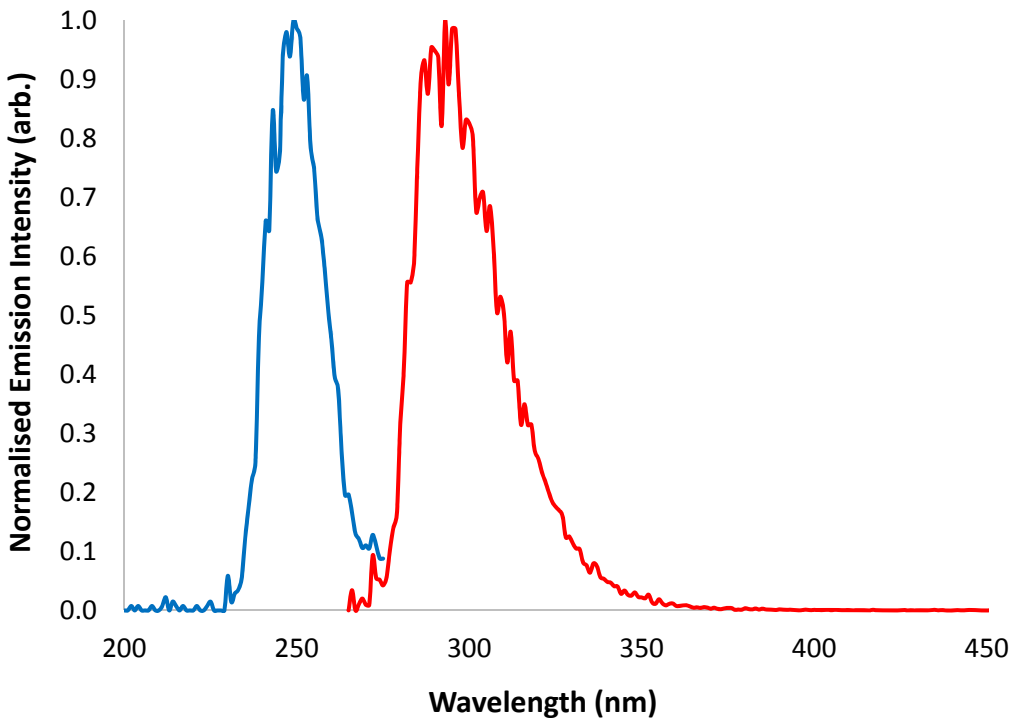


***Figure A3.3b***: Excitation and Emission profile of **3** in $H_2O$ ($10^{-6}$ M).

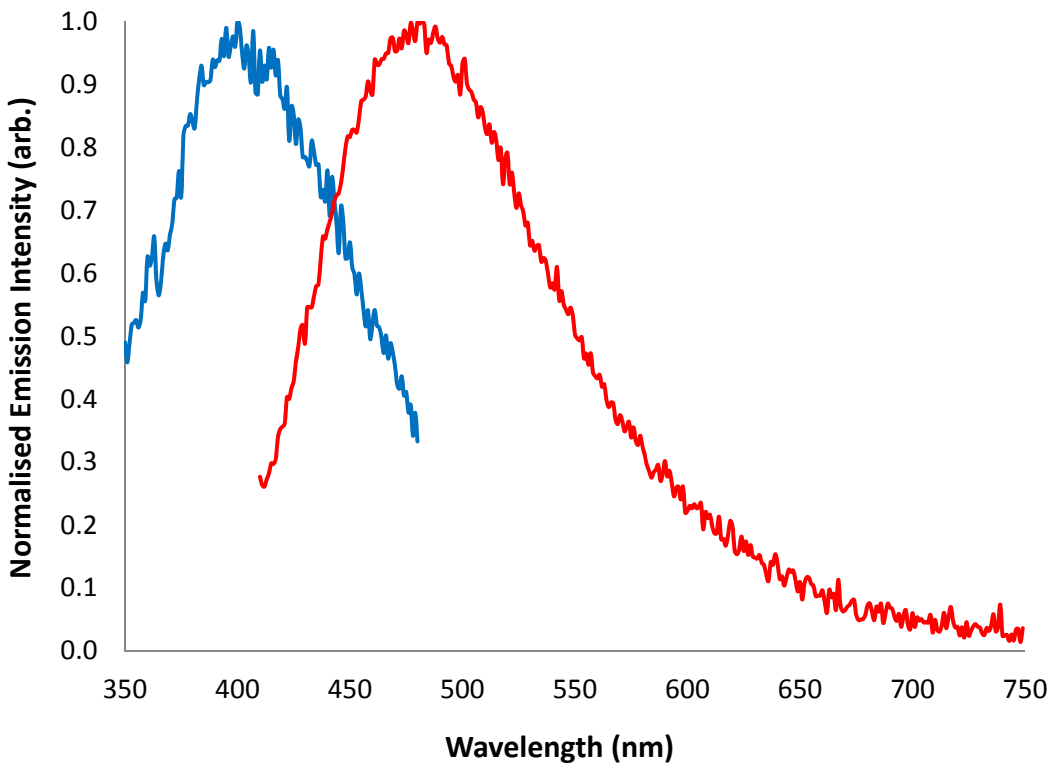


***Figure A3.4a***: Excitation and Emission profile of **4** in the solid state.

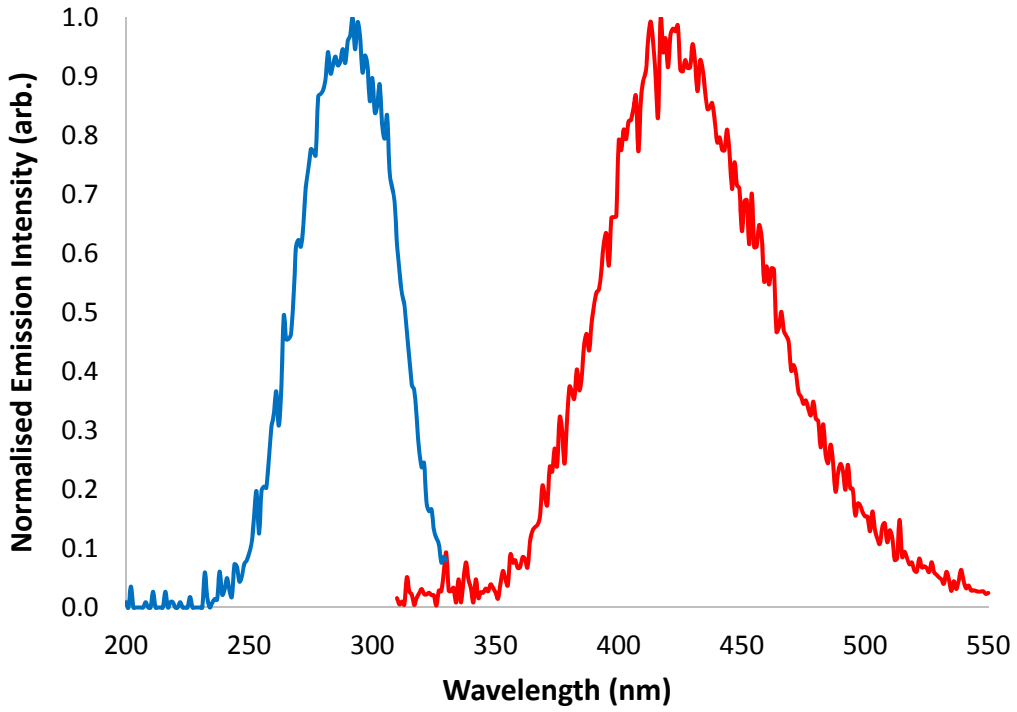


***Figure A3.4b***: Excitation and Emission profile of **4** in $H_2O$ ($10^{-6}$ M).

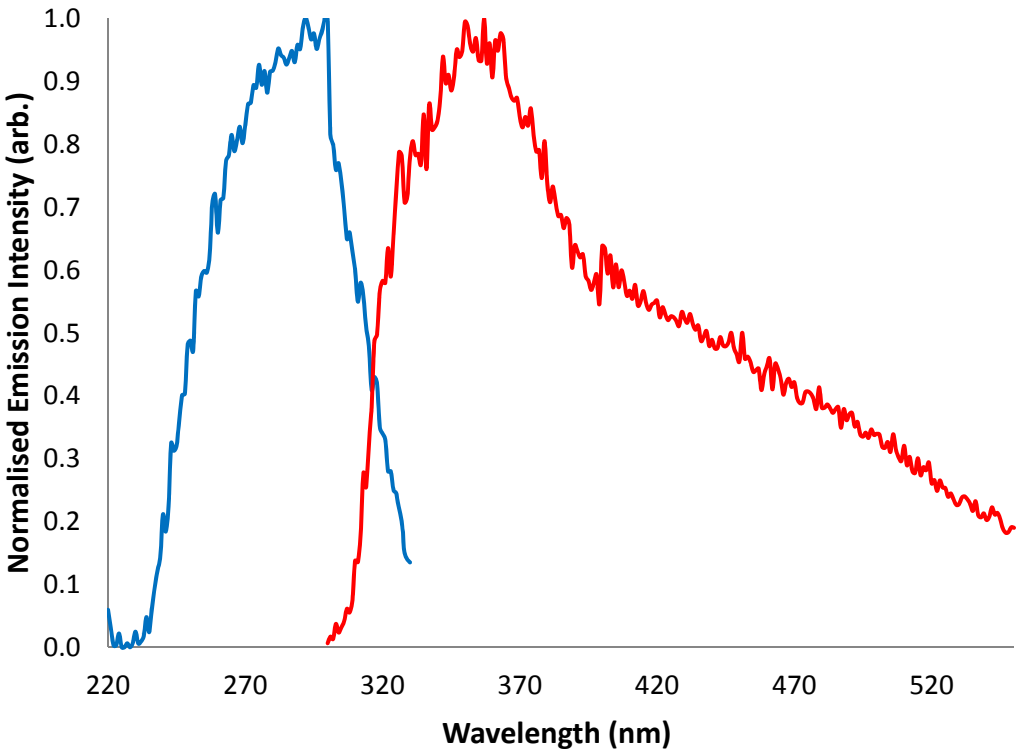


***Figure A3.5a***: Excitation and Emission profile of **5** in the solid state.

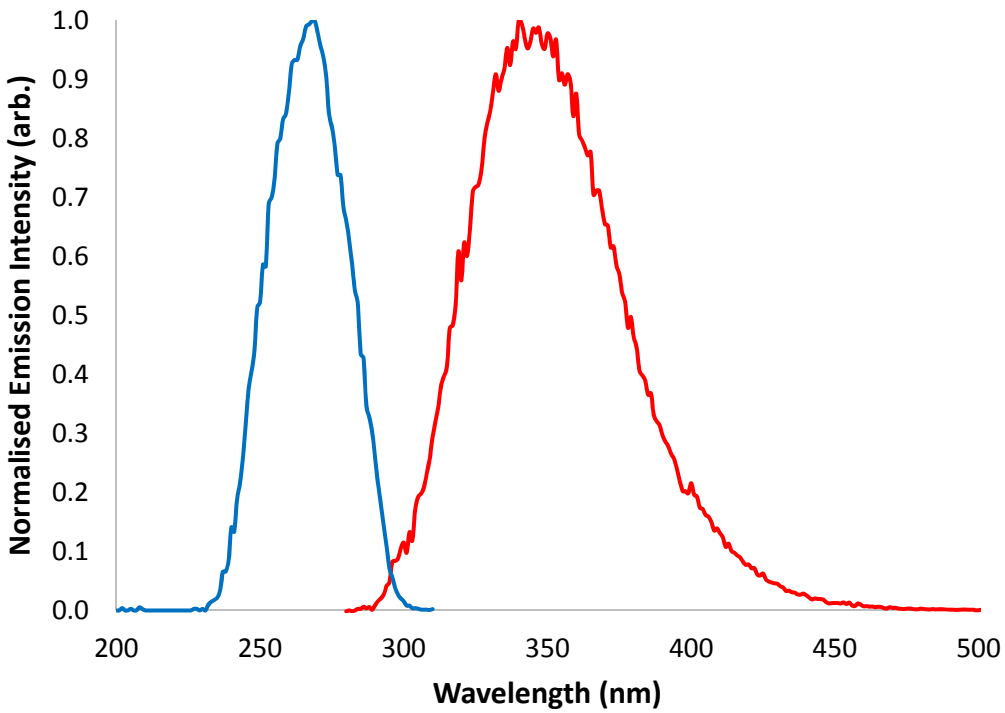


***Figure A3.5b***: Excitation and Emission profile of **5** in $H_2O$ ($10^{-6}$ M).

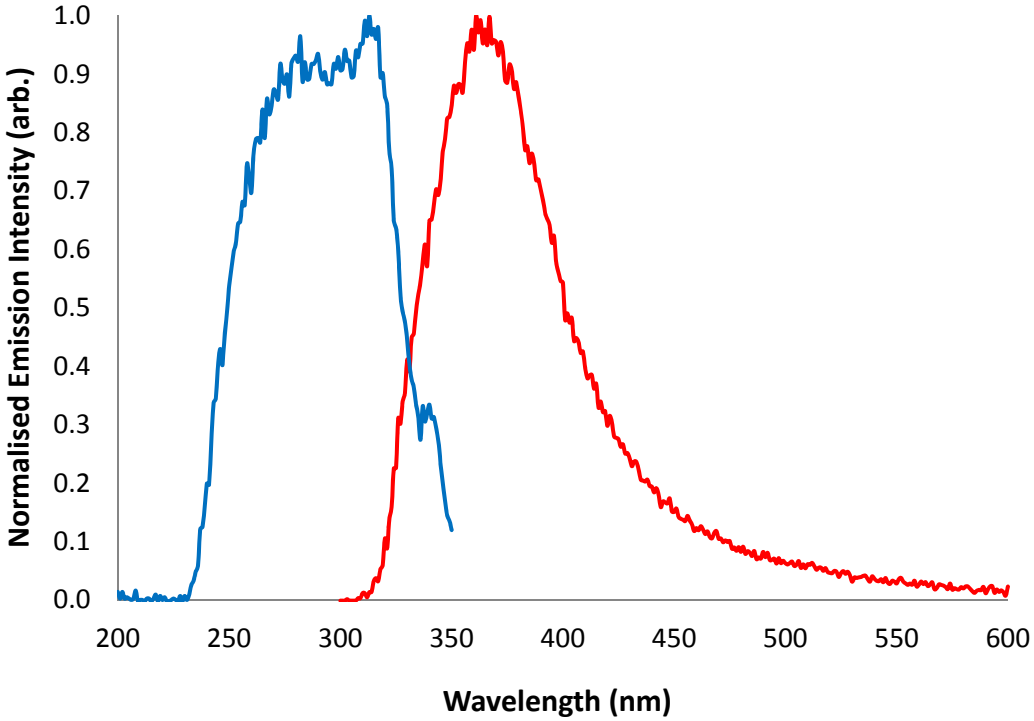


***Figure A3.6a***: Excitation and Emission profile of **6** in the solid state.

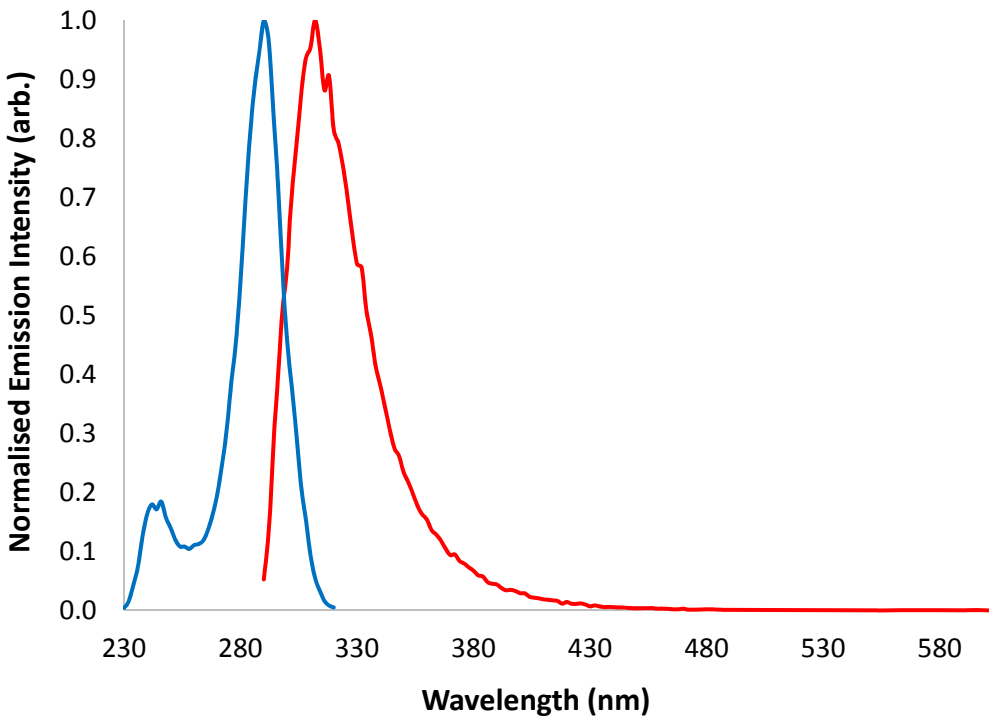


***Figure A3.6b***: Excitation and Emission profile of **6** in $H_2O$ ($10^{-6}$ M).

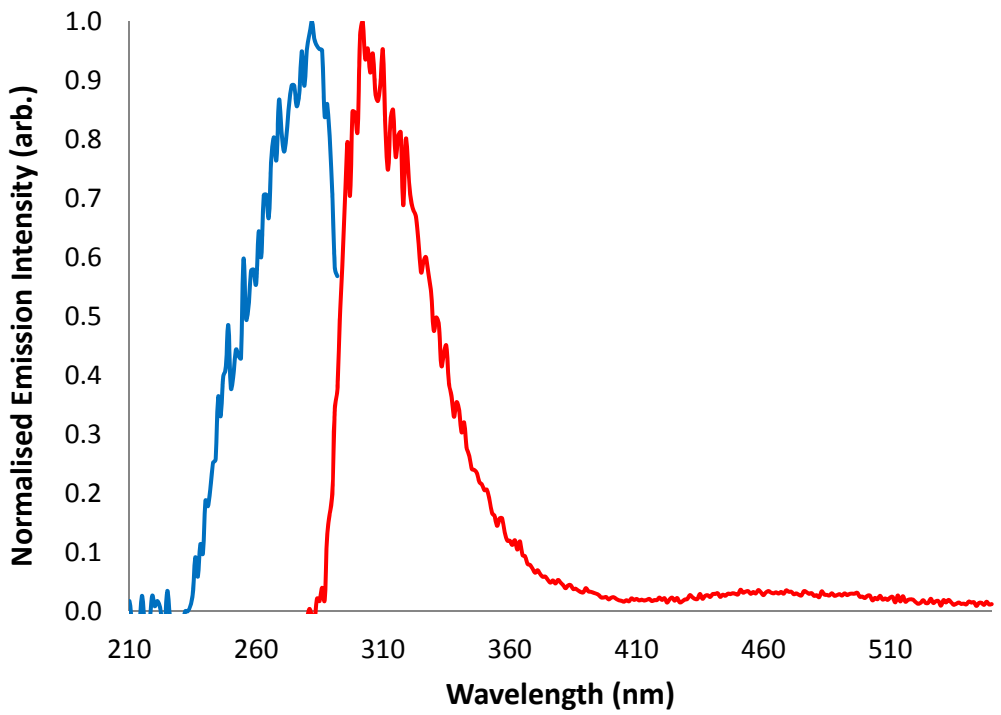


***Figure A3.7a***: Excitation and Emission profile of **7** in the solid state.

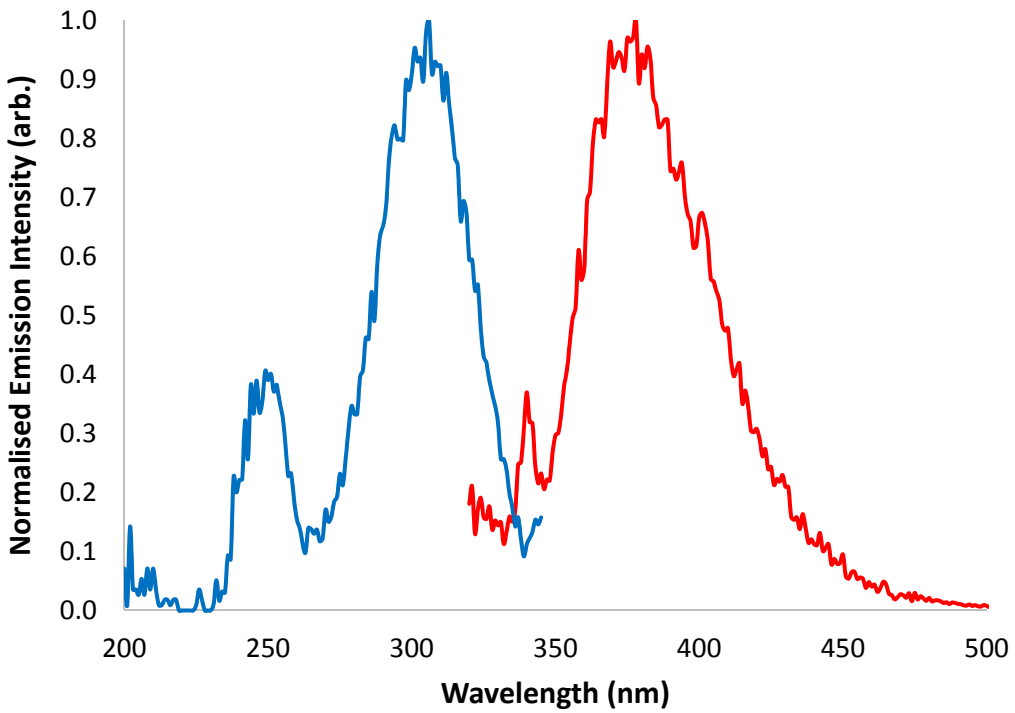


***Figure A3.7b***: Excitation and Emission profile of **7** in $H_2O$ ($10^{-6}$ M).

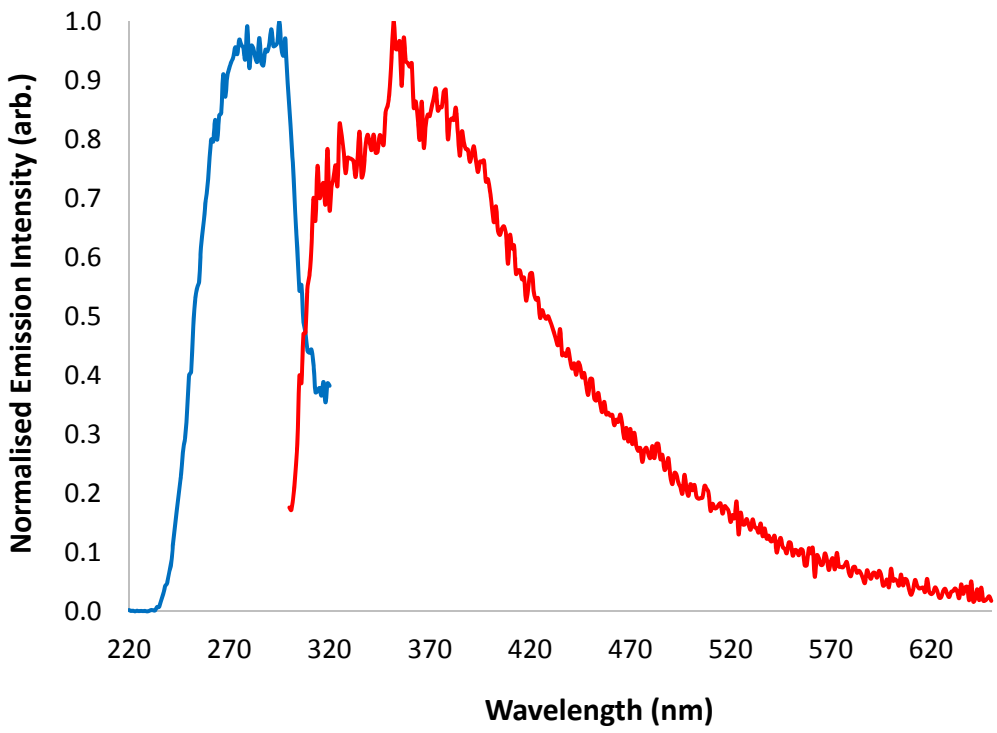


***Figure A3.8a***: Excitation and Emission profile of **8** in the solid state.

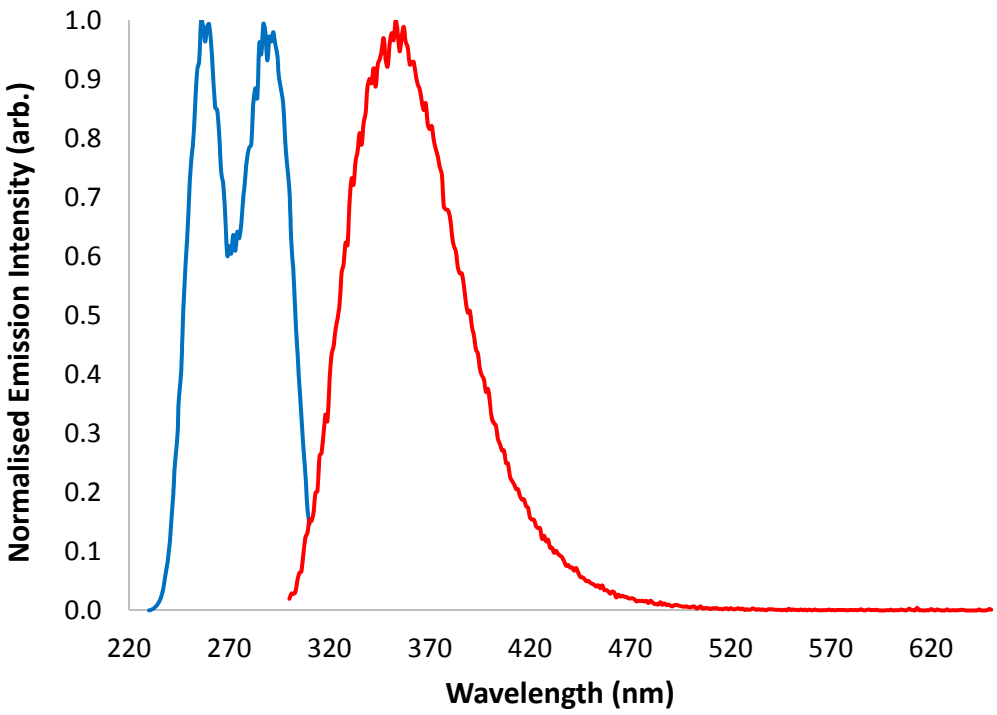


***Figure A3.8b***: Excitation and Emission profile of **8** in $H_2O$ ($10^{-6}$ M).

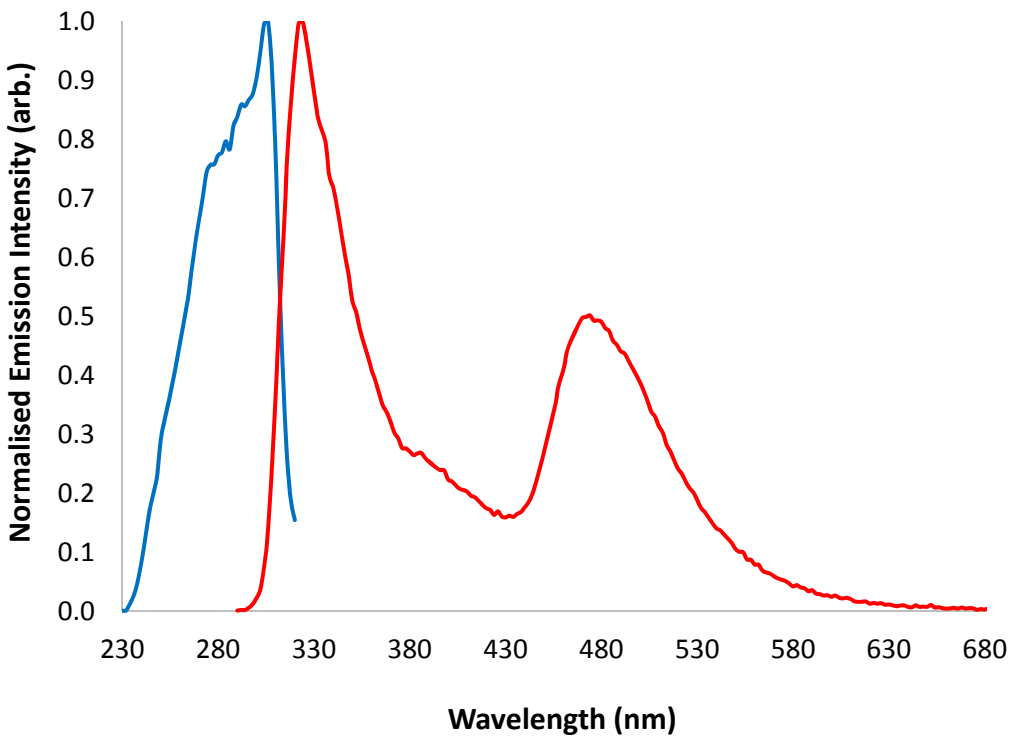


***Figure A3.9a***: Excitation and Emission profile of **9** in the solid state.

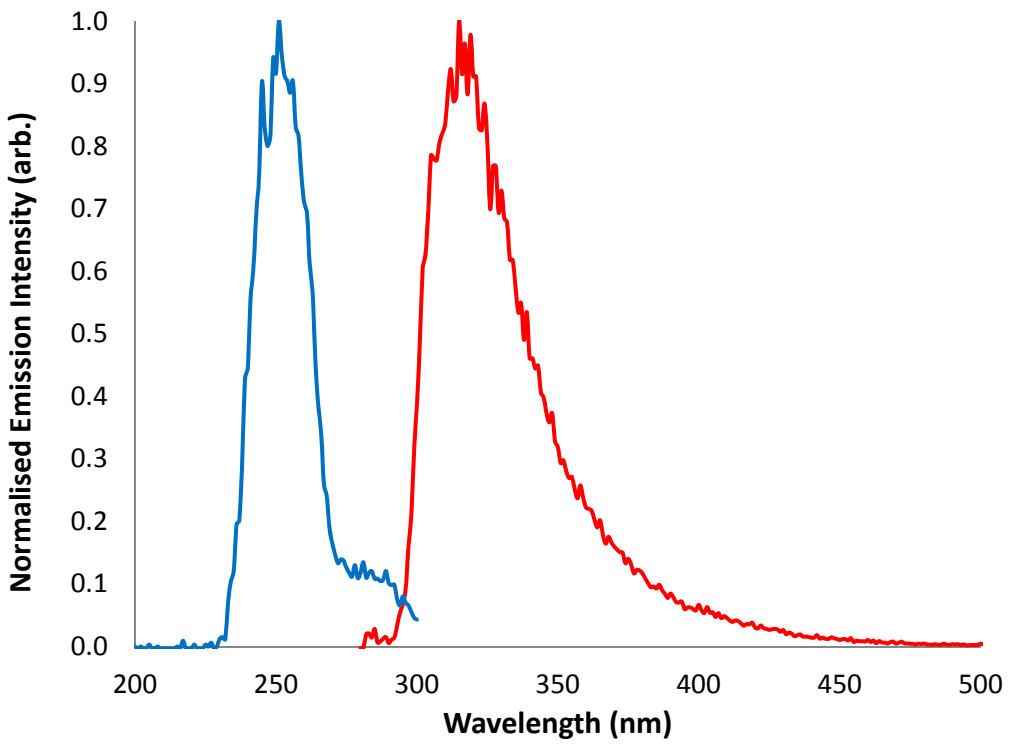


***Figure A3.9b***: Excitation and Emission profile of **9** in $H_2O$ ($10^{-6}$ M).

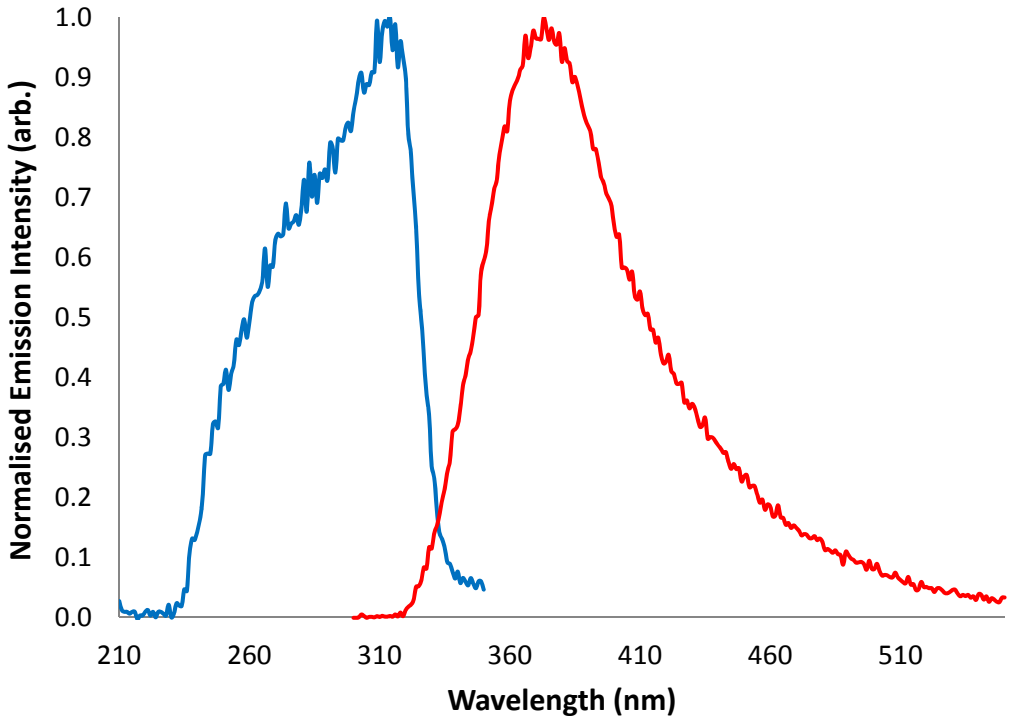


***Figure A3.10a***: Excitation and Emission profile of **10** in the solid state.

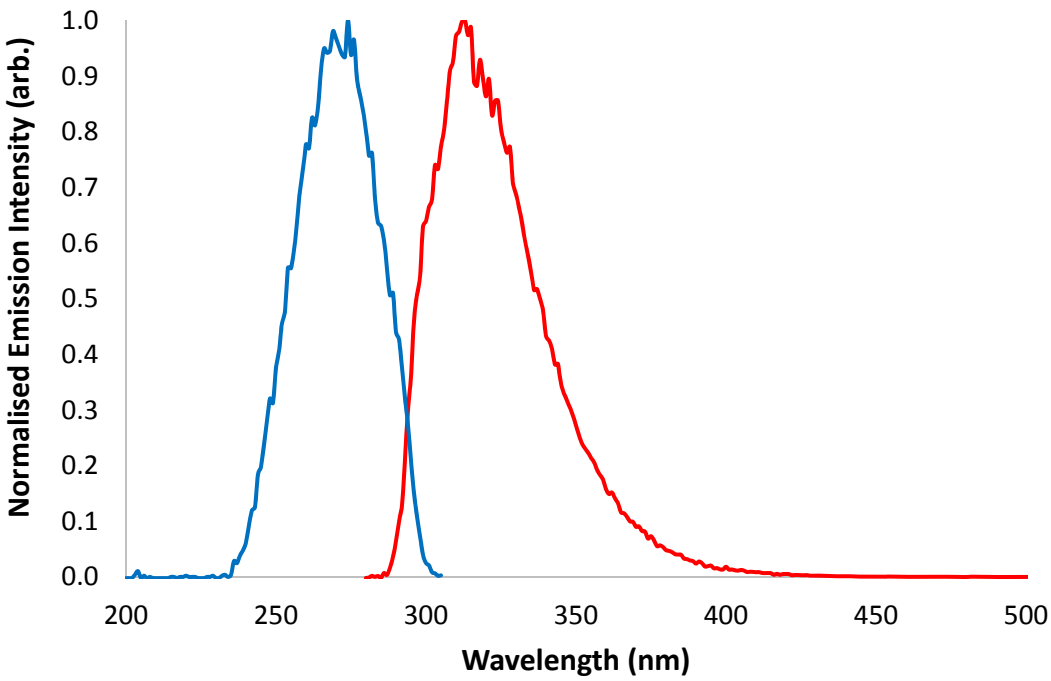


***Figure A3.10b***: Excitation and Emission profile of **10** in $H_2O$ ($10^{-6}$ M).

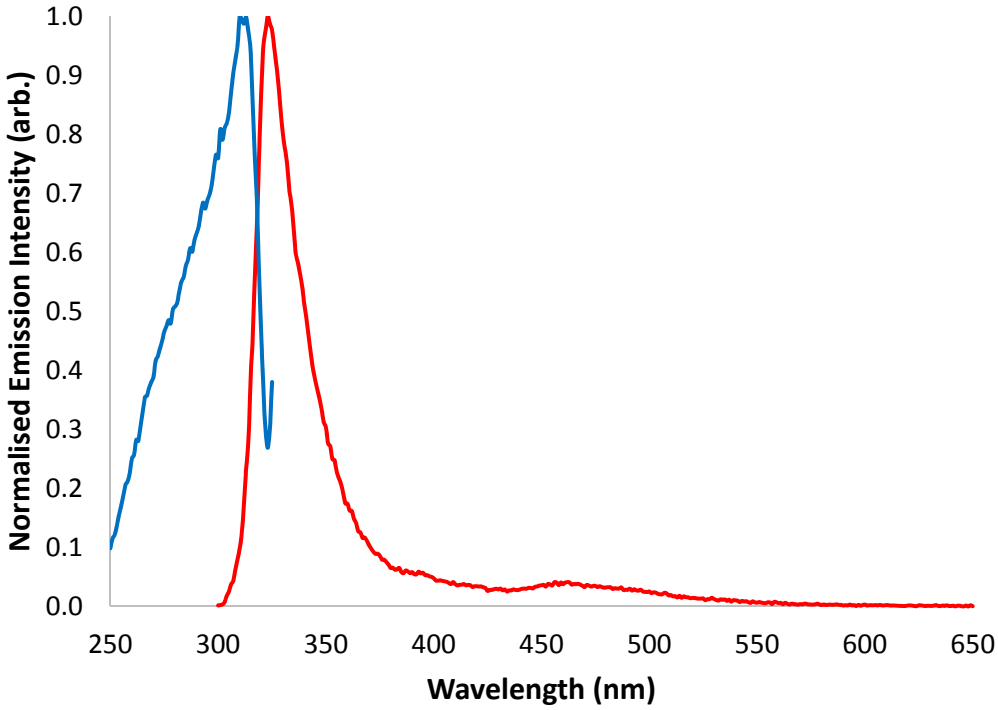


***Figure A3.11a***: Excitation and Emission profile of **11** in the solid state.

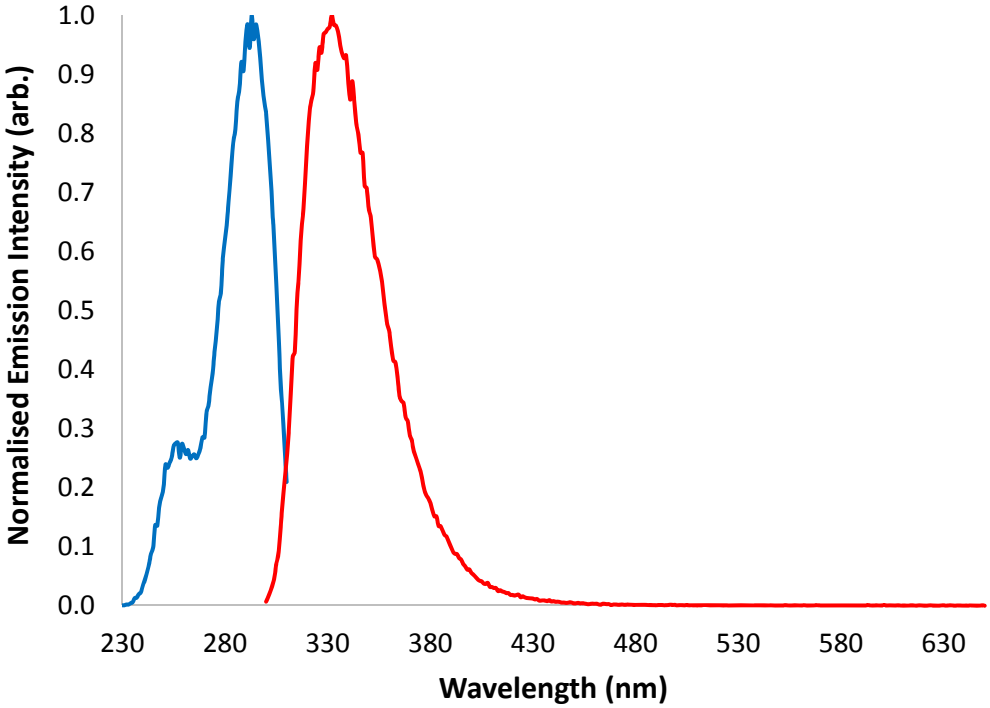


F***igure A3.11b***: Excitation and Emission profile of **11** in $H_2O$ ($10^{-6}$ M).

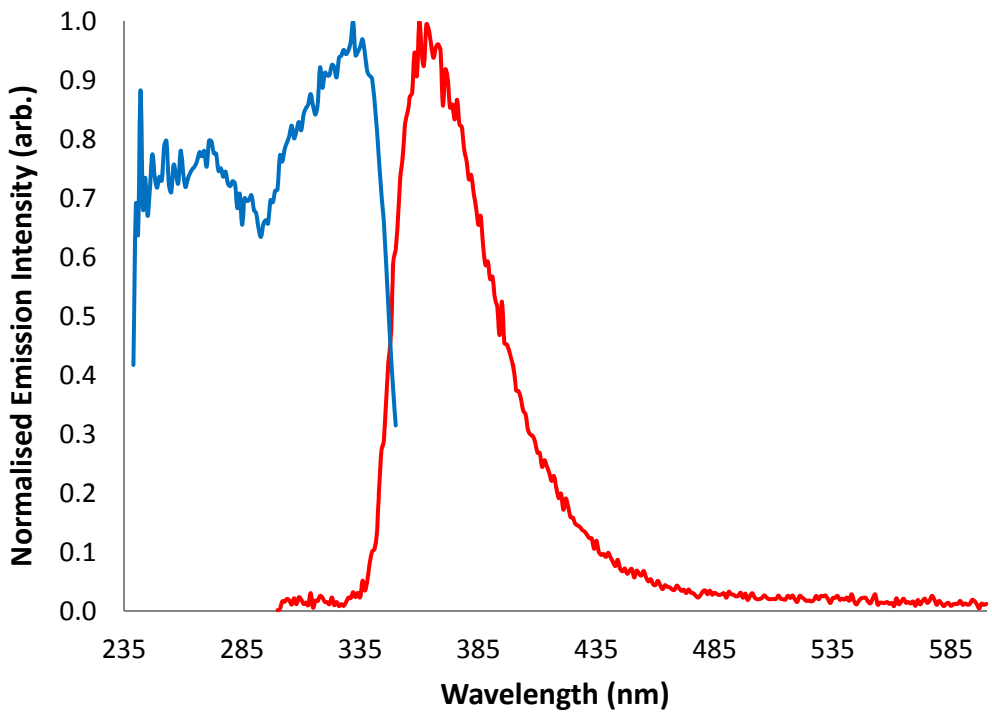


***Figure A3.12a***: Excitation and Emission profile of **12** in the solid state.

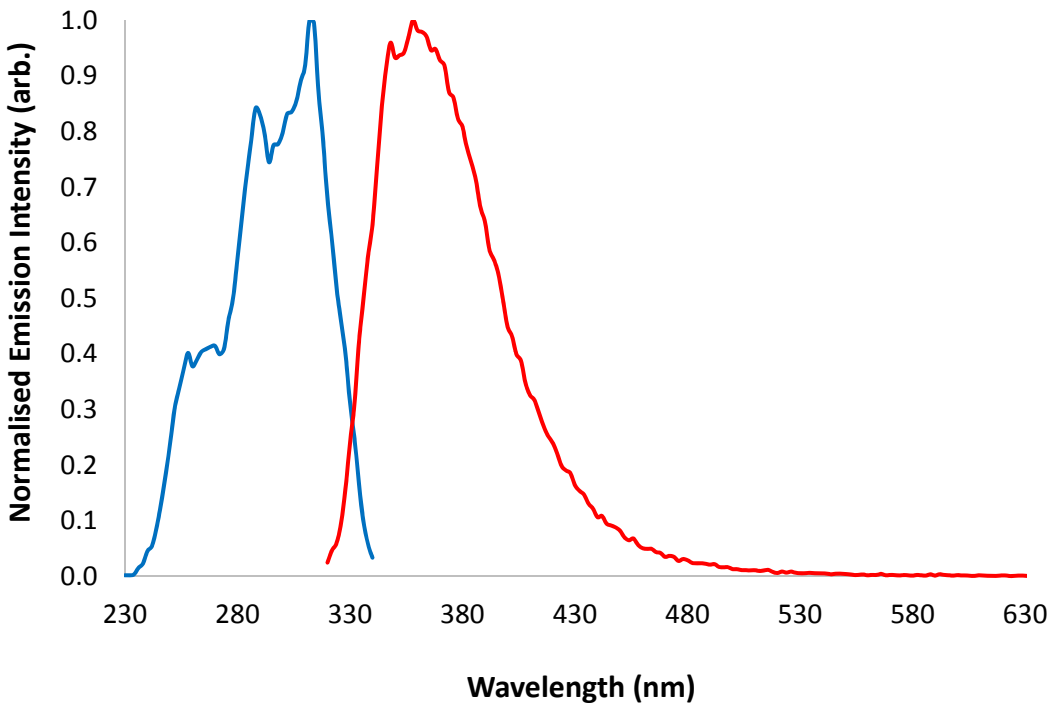


***Figure A3.12b***: Excitation and Emission profile of **12** in $H_2O$ ($10^{-6}$ M).

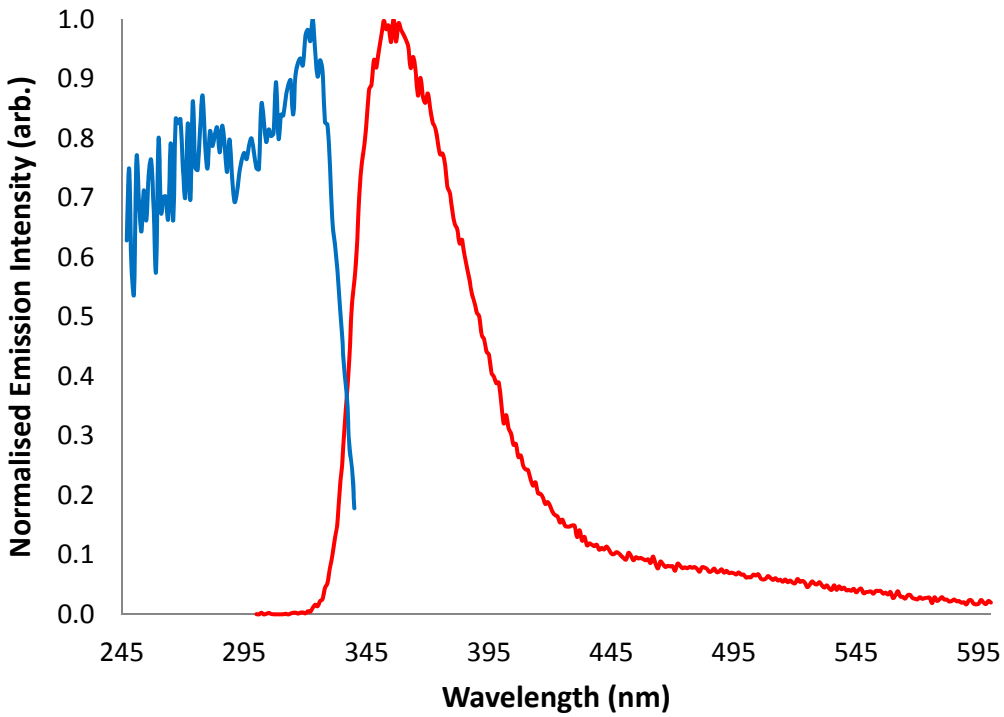


***Figure A3.13a***: Excitation and Emission profile of **13** in the solid state.

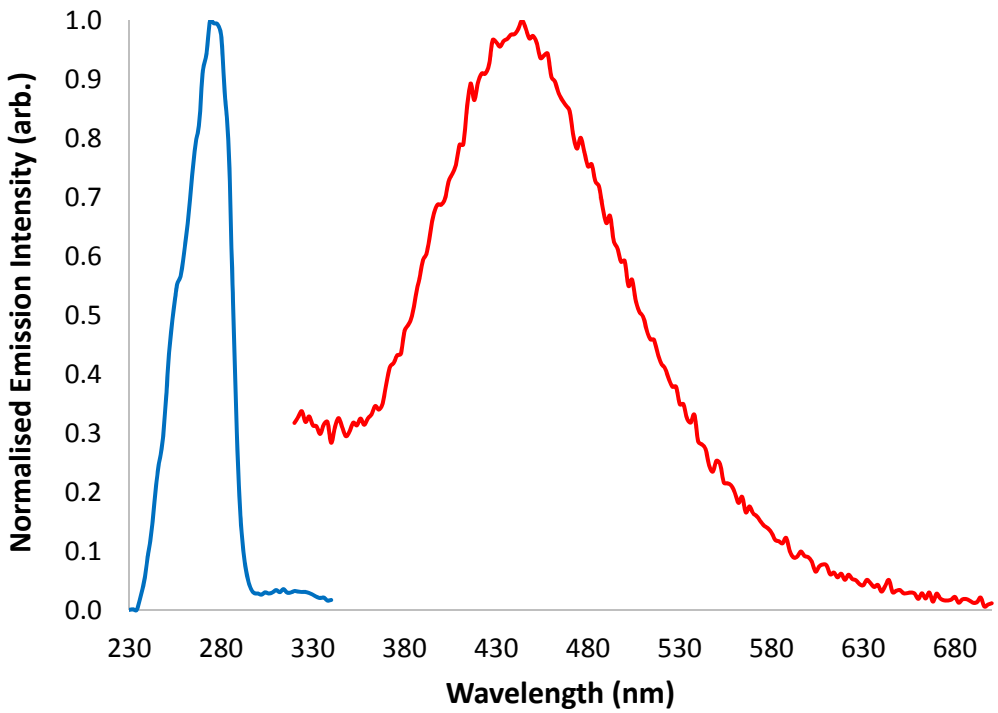


***Figure A3.13b***: Excitation and Emission profile of **13** in $H_2O$ ($10^{-6}$ M).

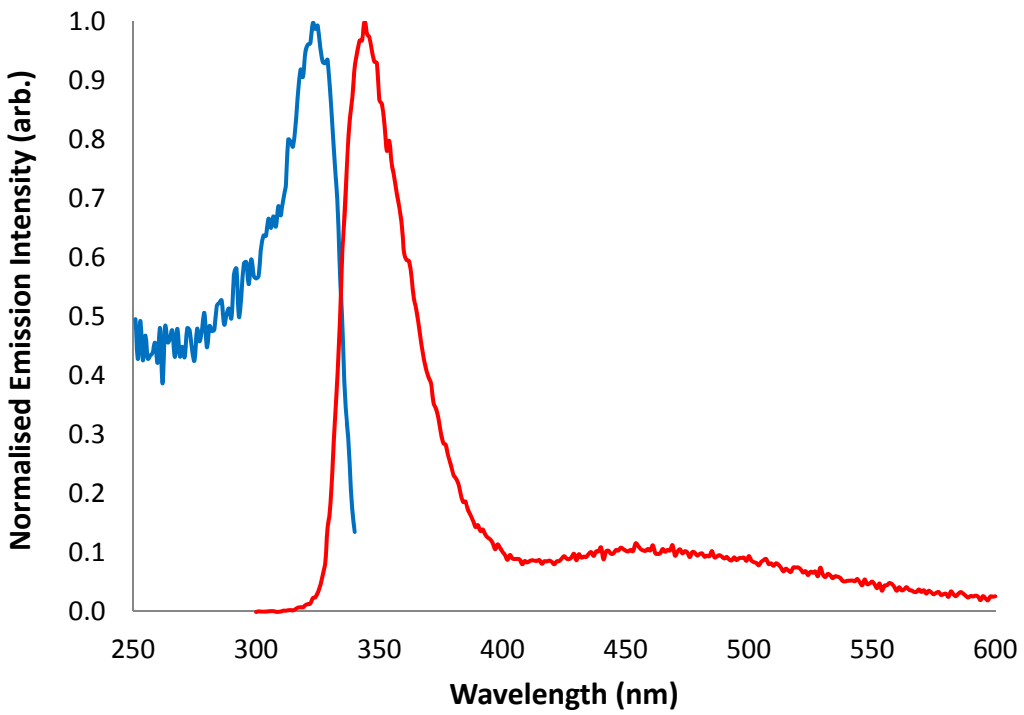


***Figure A3.14a***: Excitation and Emission profile of **14** in the solid state.

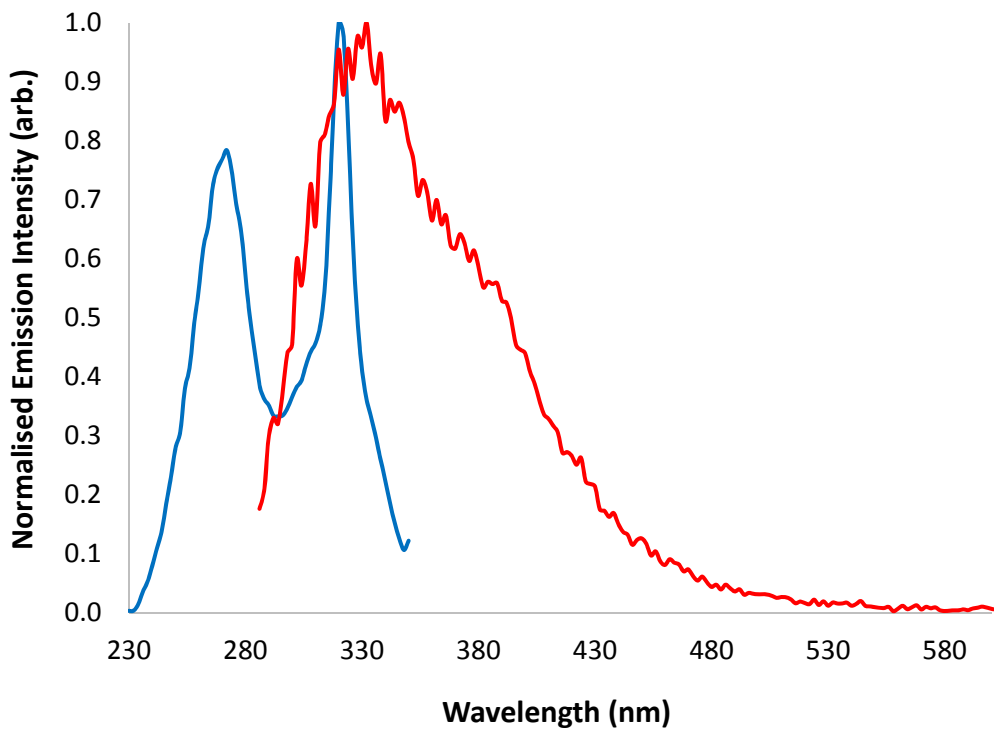


***Figure A3.14b***: Excitation and Emission profile of **14** in $H_2O$ ($10^{-6}$ M).

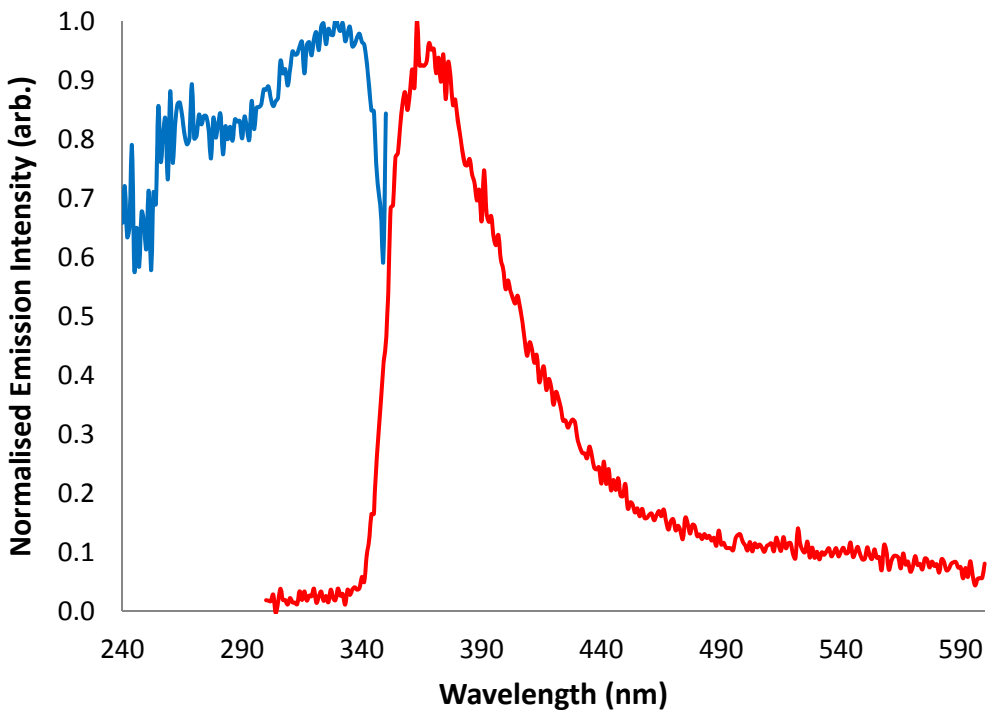


***Figure A3.15a***: Excitation and Emission profile of **15** in the solid state.

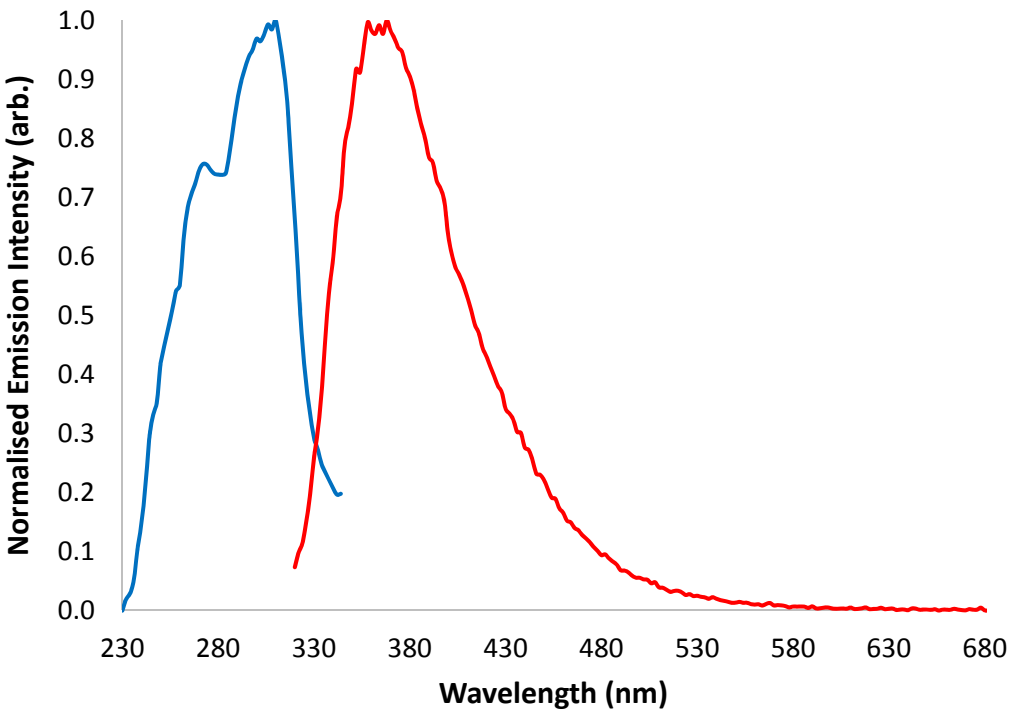


***Figure A3.15b***: Excitation and Emission profile of **15** in $H_2O$ ($10^{-6}$ M).

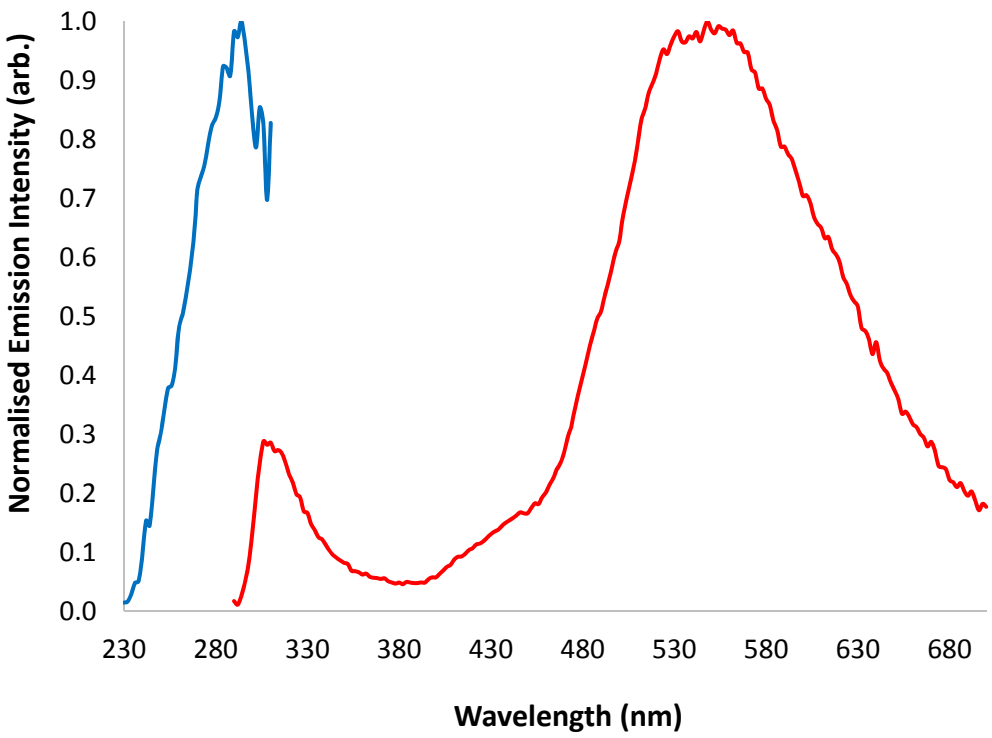


***Figure A3.16a***: Excitation and Emission profile of **16** in the solid state.

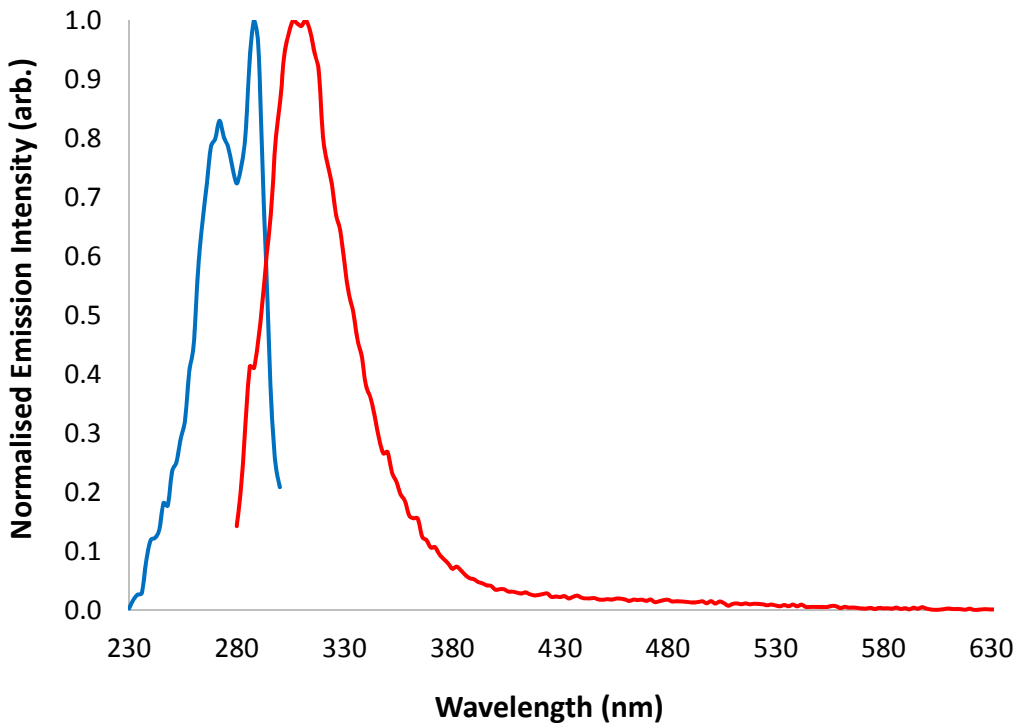


***Figure A3.16b***: Excitation and Emission profile of **16** in $H_2O$ ($10^{-6}$ M).

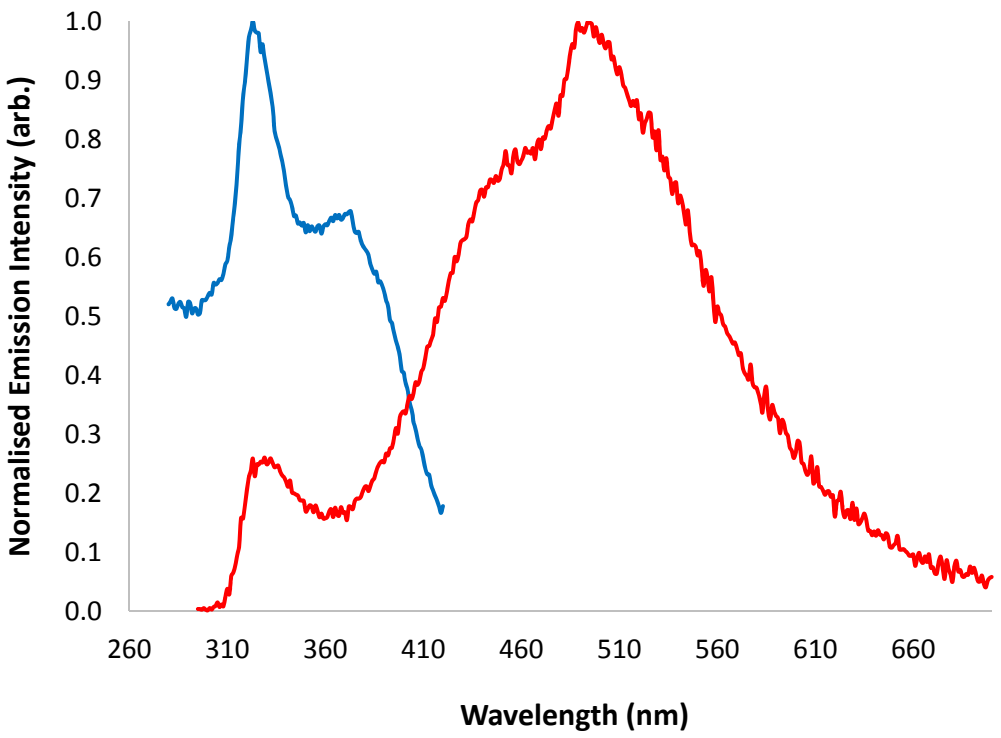


***Figure A3.17a***: Excitation and Emission profile of **17** in the solid state.

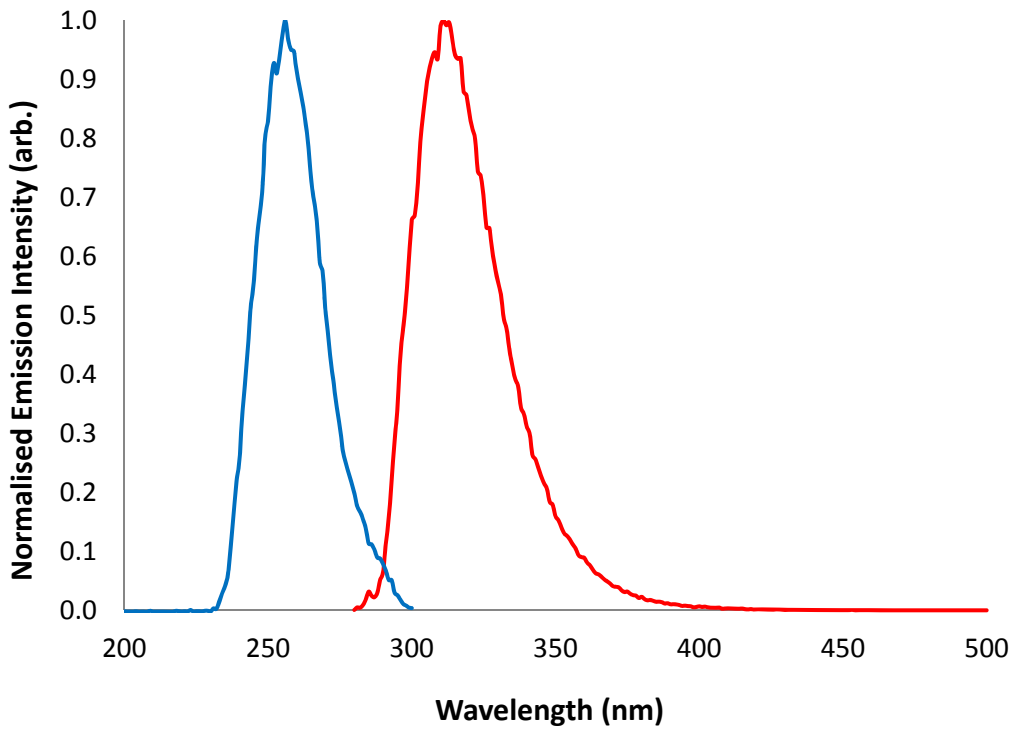


***Figure A3.17b***: Excitation and Emission profile of **17** in $H_2O$ ($10^{-6}$ M).

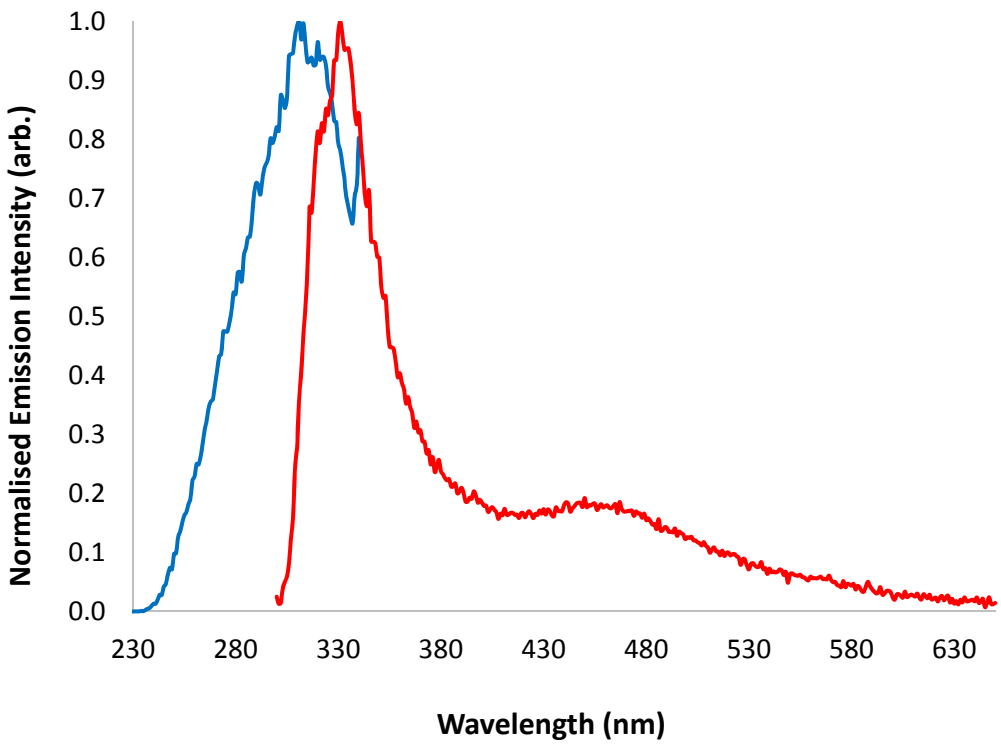


***Figure A3.18a***: Excitation and Emission profile of **18** in the solid state.

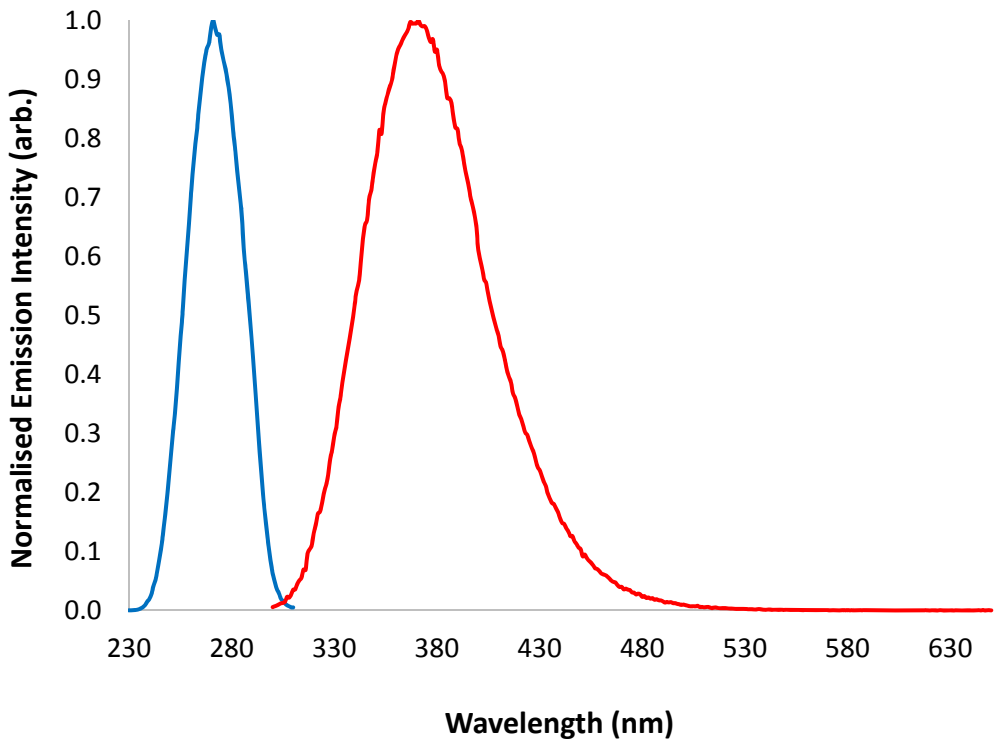


***Figure A3.18b***: Excitation and Emission profile of **18** in the solid state.

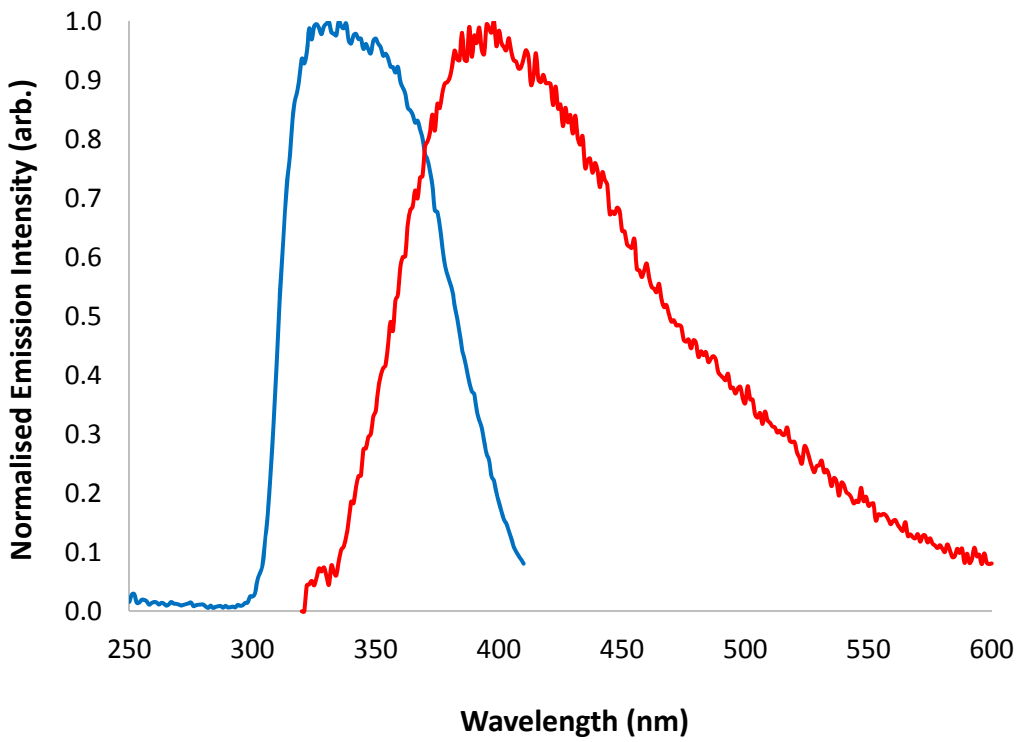


***Figure A3.19a***: Excitation and Emission profile of **19** in the solid state.

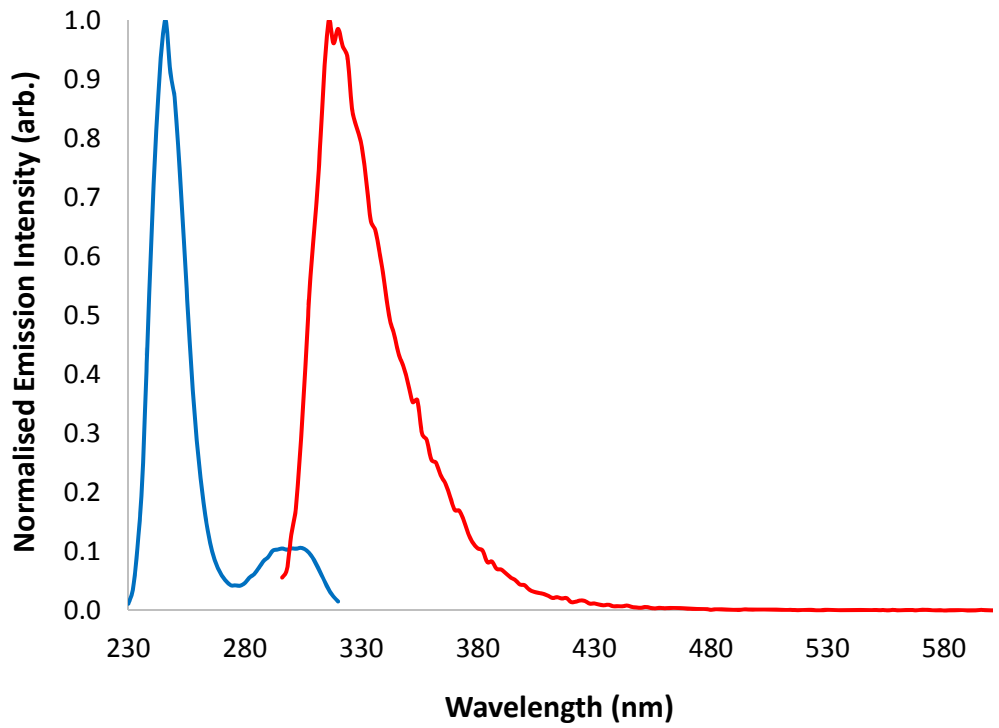


***Figure A3.19b***: Excitation and Emission profile of **19** in $H_2O$ ($10^{-6}$ M).

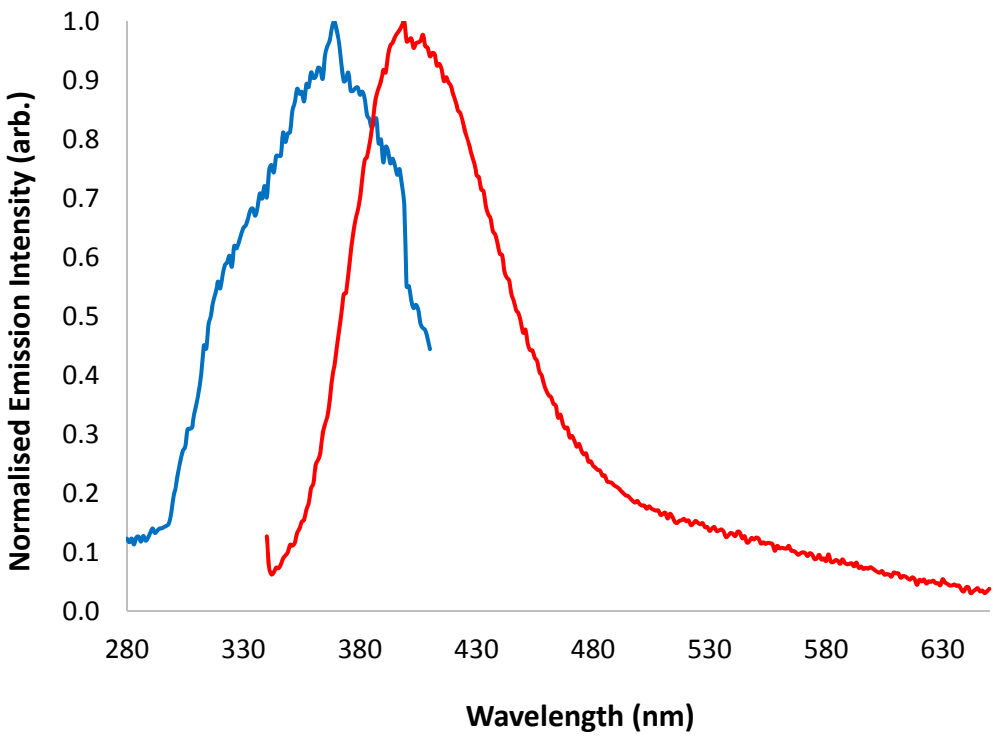


***Figure A3.20a***: Excitation and Emission profile of **20** in the solid state.

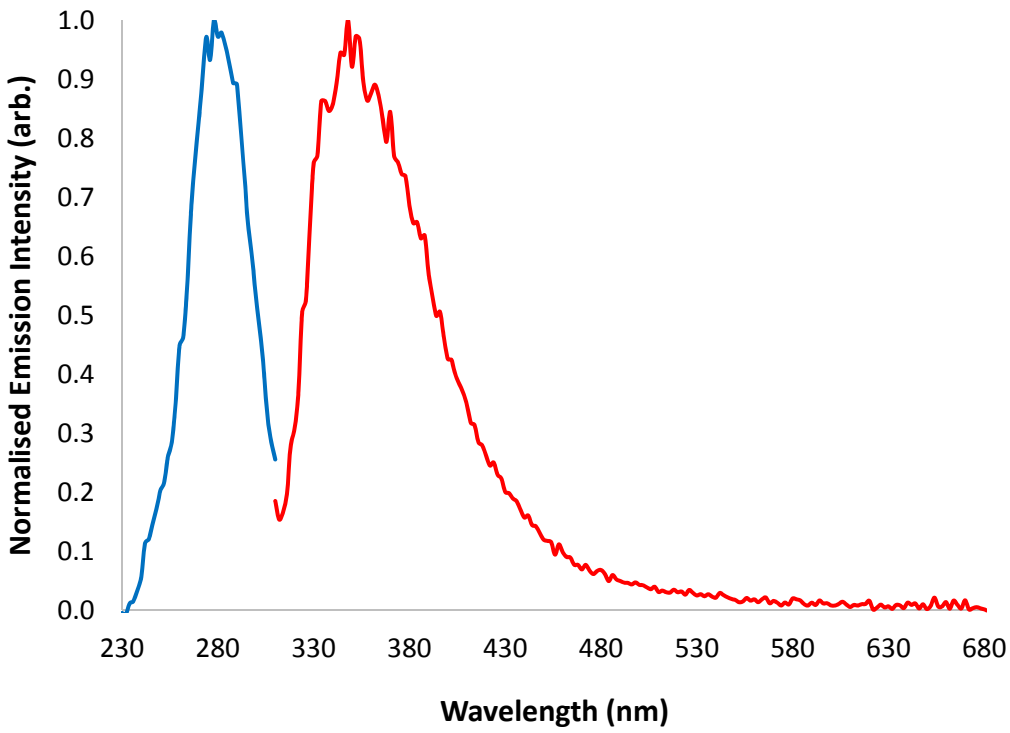


***Figure A3.20b***: Excitation and Emission profile of **20** in $H_2O$ ($10^{-6}$ M).

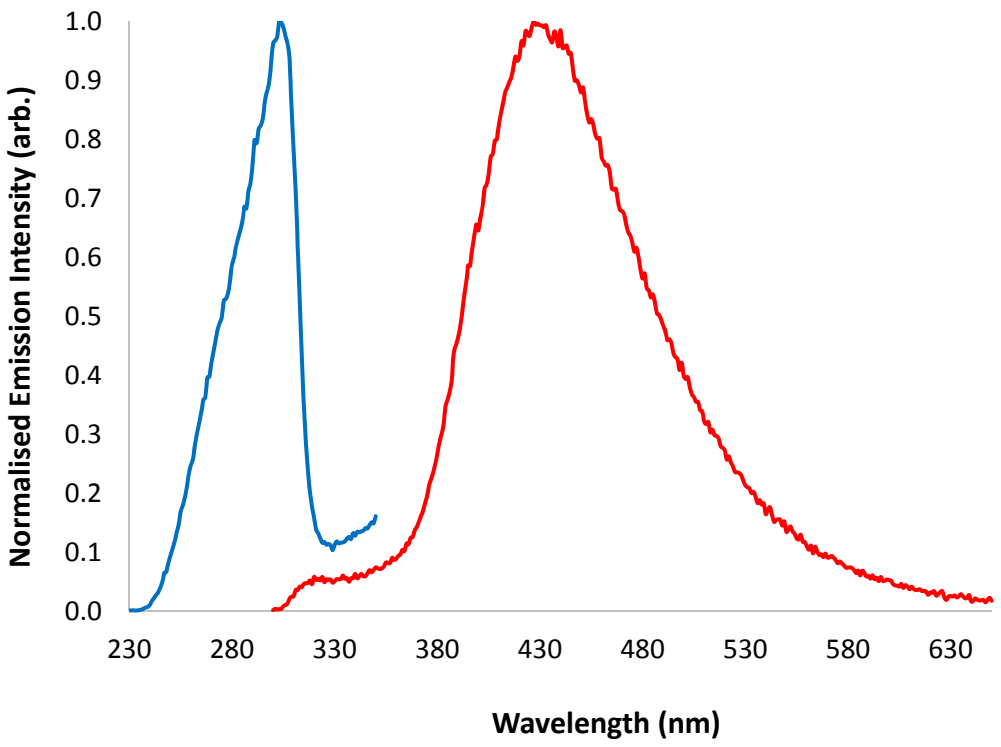


***Figure A3.21a***: Excitation and Emission profile of **21** in the solid state.

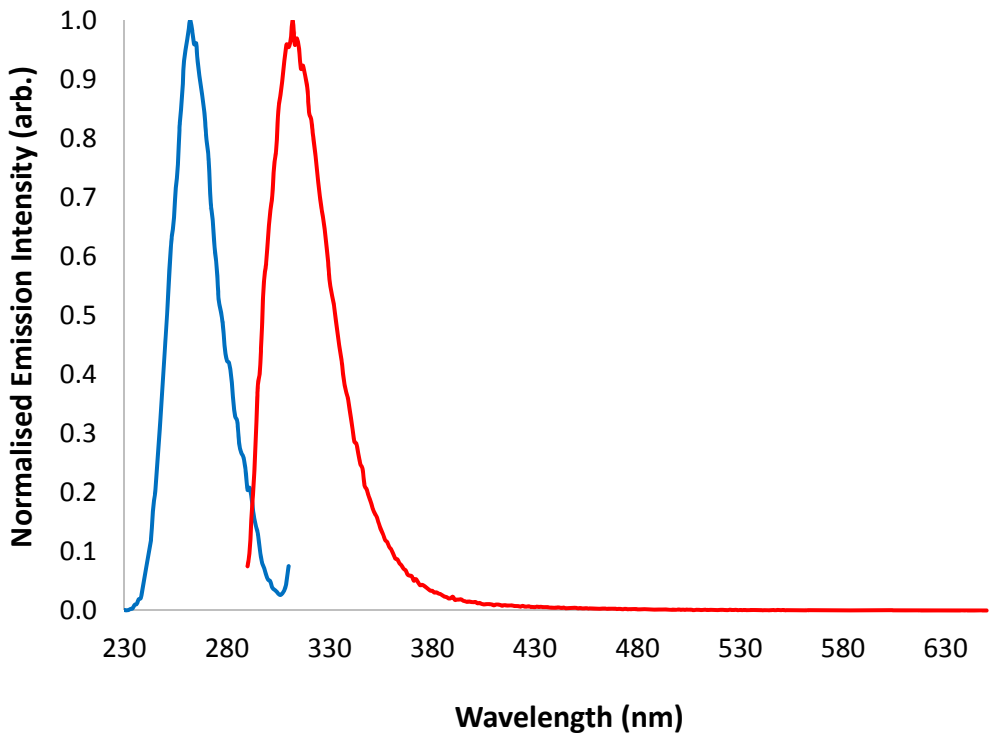


***Figure A3.21b***: Excitation and Emission profile of **21** in $H_2O$ ($10^{-6}$ M).

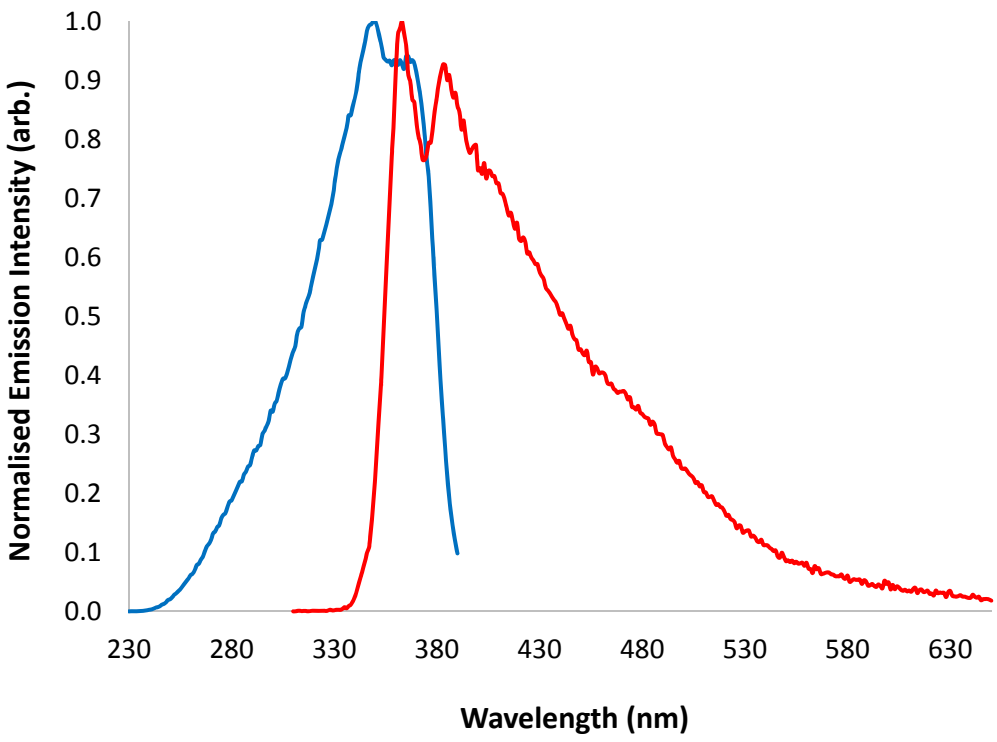


***Figure A3.22a***: Excitation and Emission profile of **22** in the solid state.

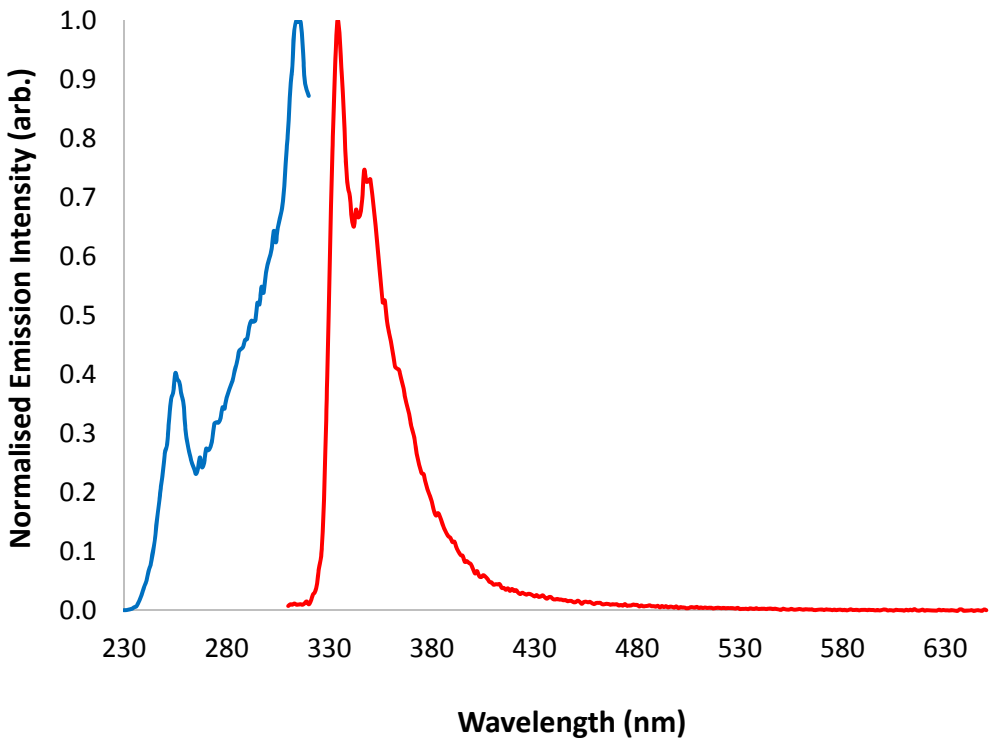


***Figure A3.22b***: Excitation and Emission profile of **22** in $H_2O$ ($10^{-6}$ M).

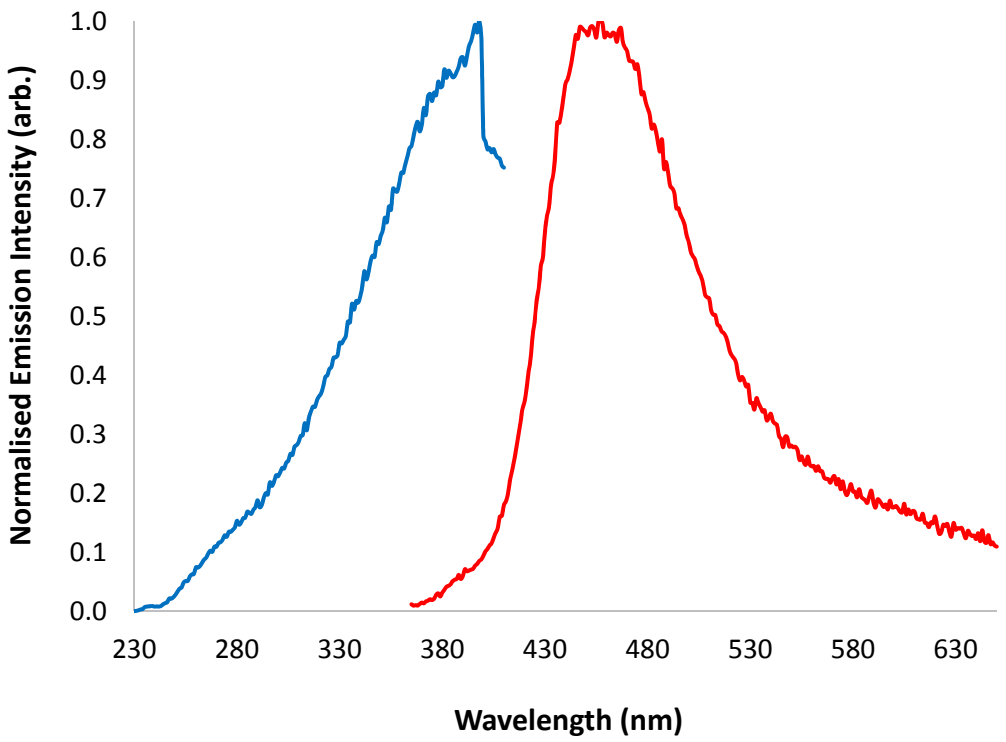


***Figure A3.23a***: Excitation and Emission profile of **23** in the solid state.

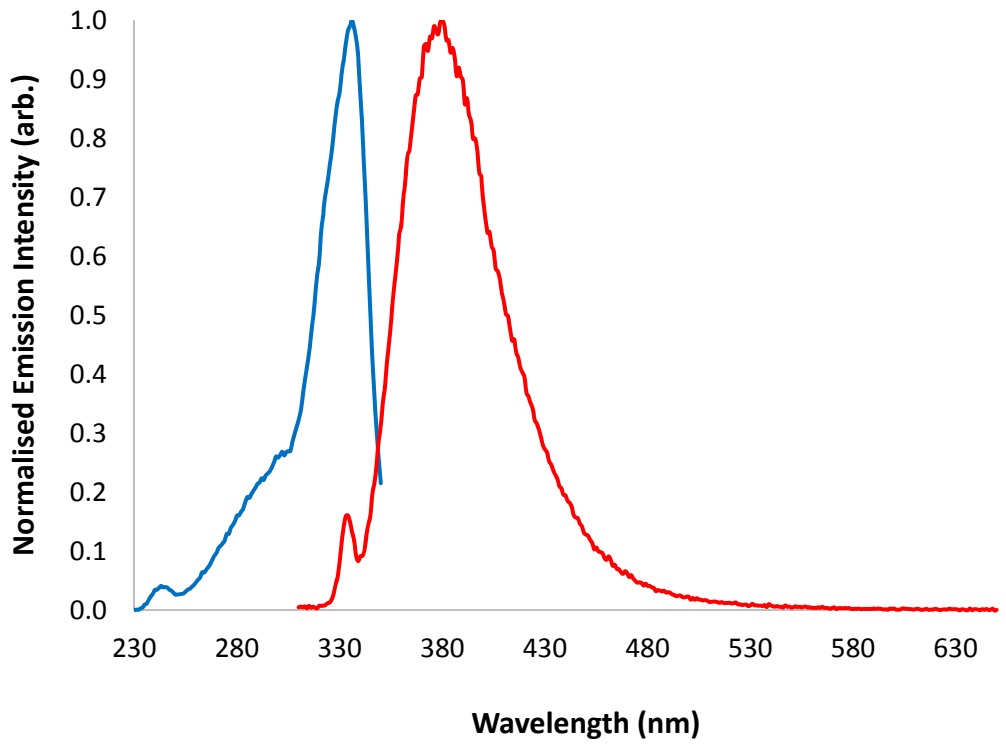


***Figure A3.23b***: Excitation and Emission profile of **23** in $H_2O$ ($10^{-6}$ M).

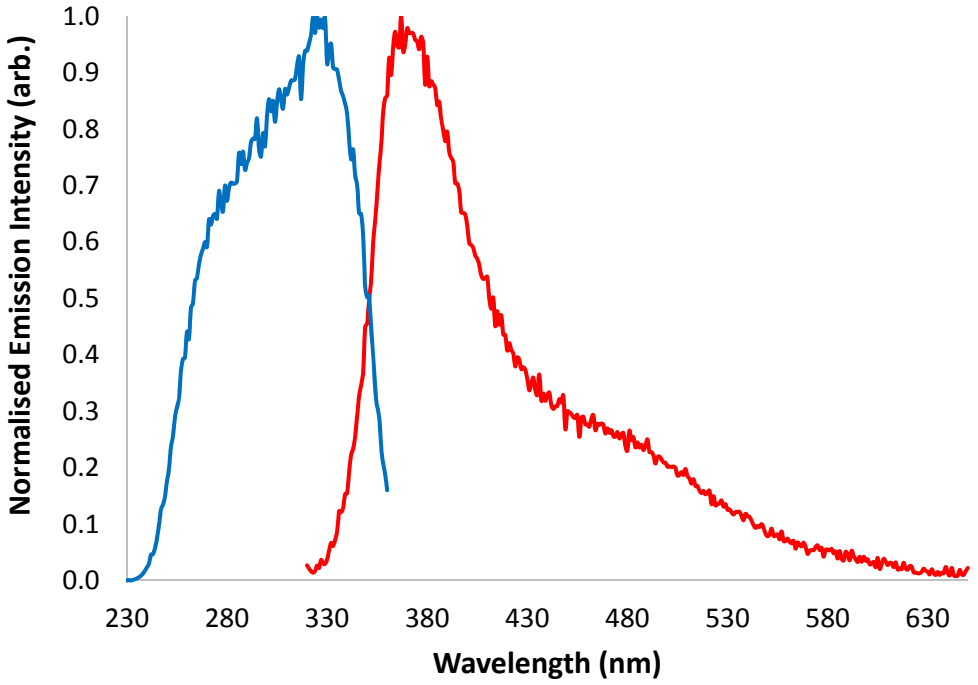


***Figure A3.24a***: Excitation and Emission profile of **24** in the solid state.

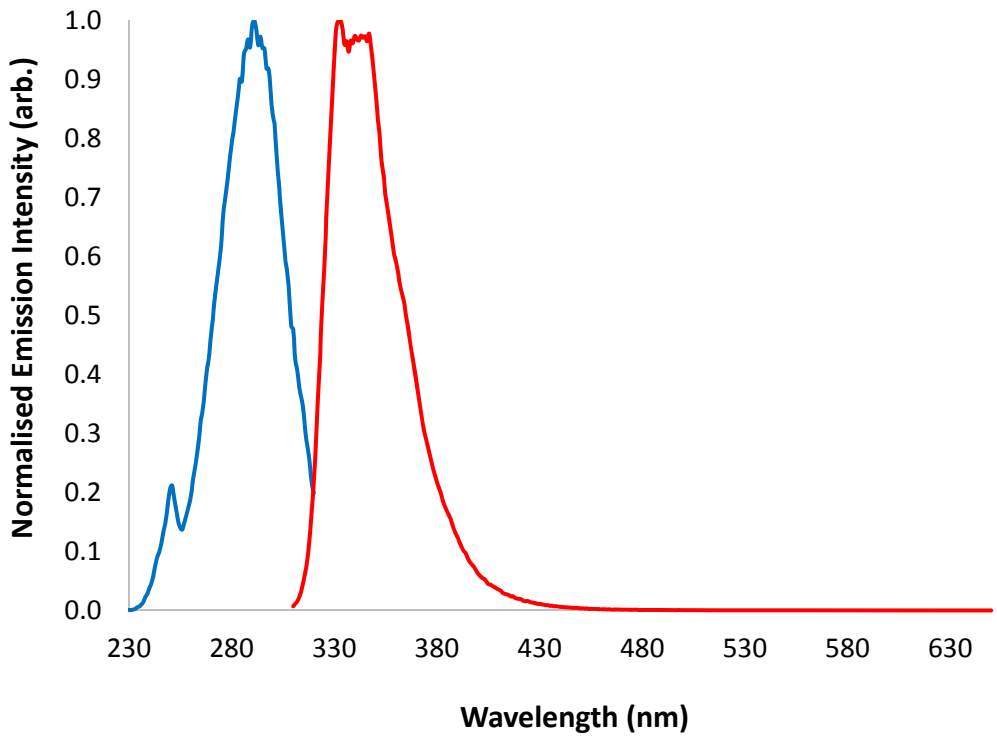


***Figure A3.24b***: Excitation and Emission profile of **24** in $H_2O$ ($10^{-6}$ M).

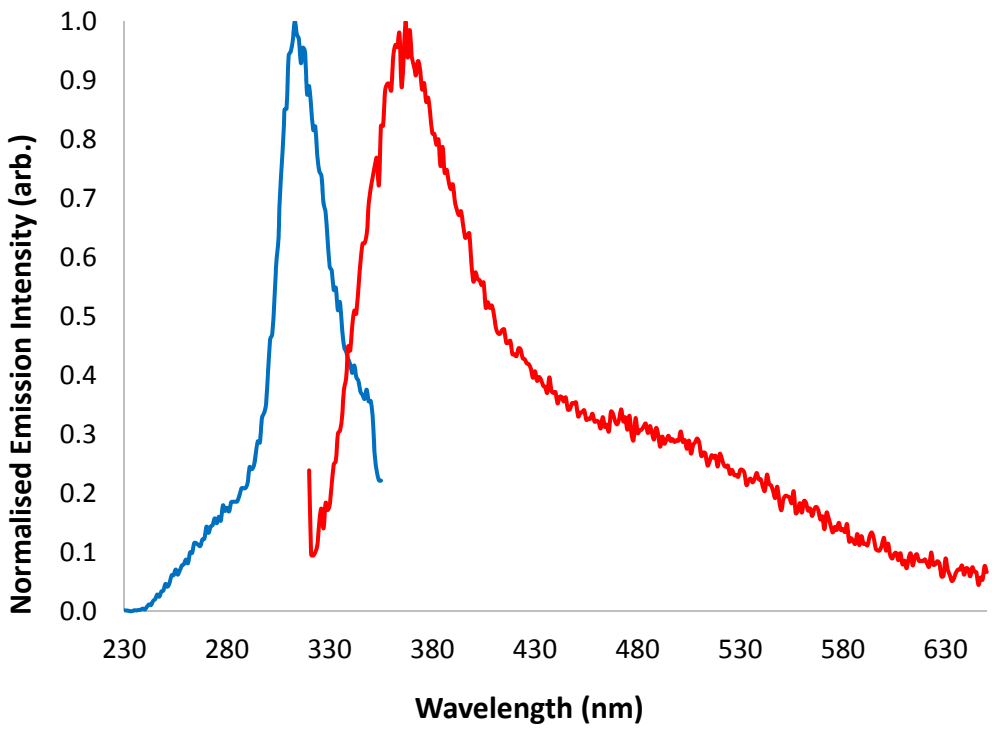


***Figure A3.25a***: Excitation and Emission profile of **25** in the solid state.

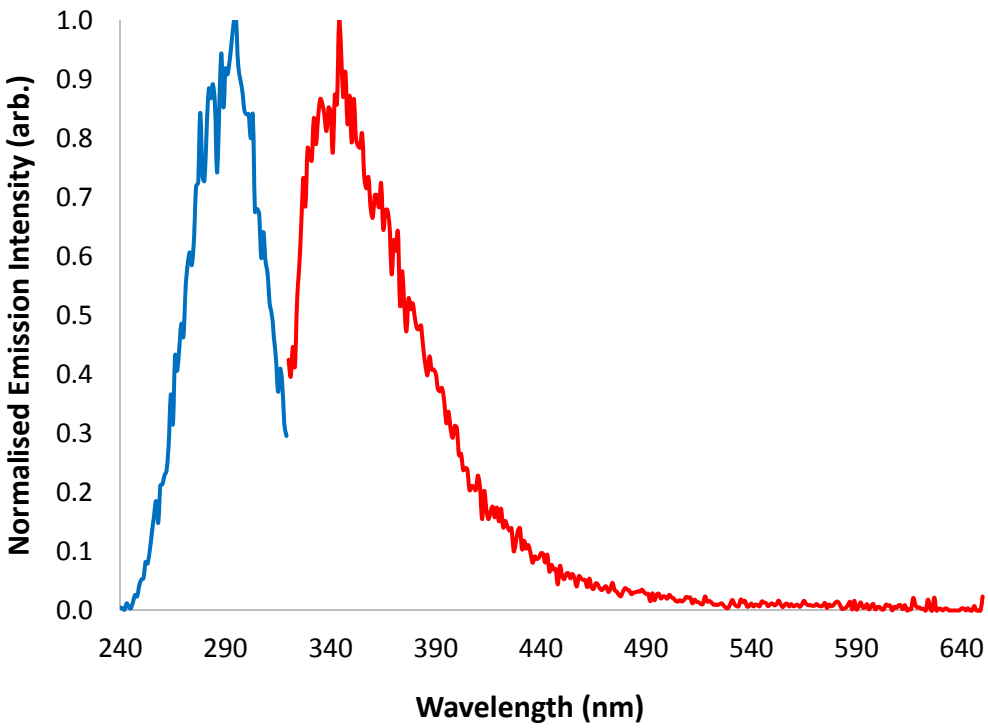


***Figure A3.25b***: Excitation and Emission profile of **25** in $H_2O$ ($10^{-6}$ M).

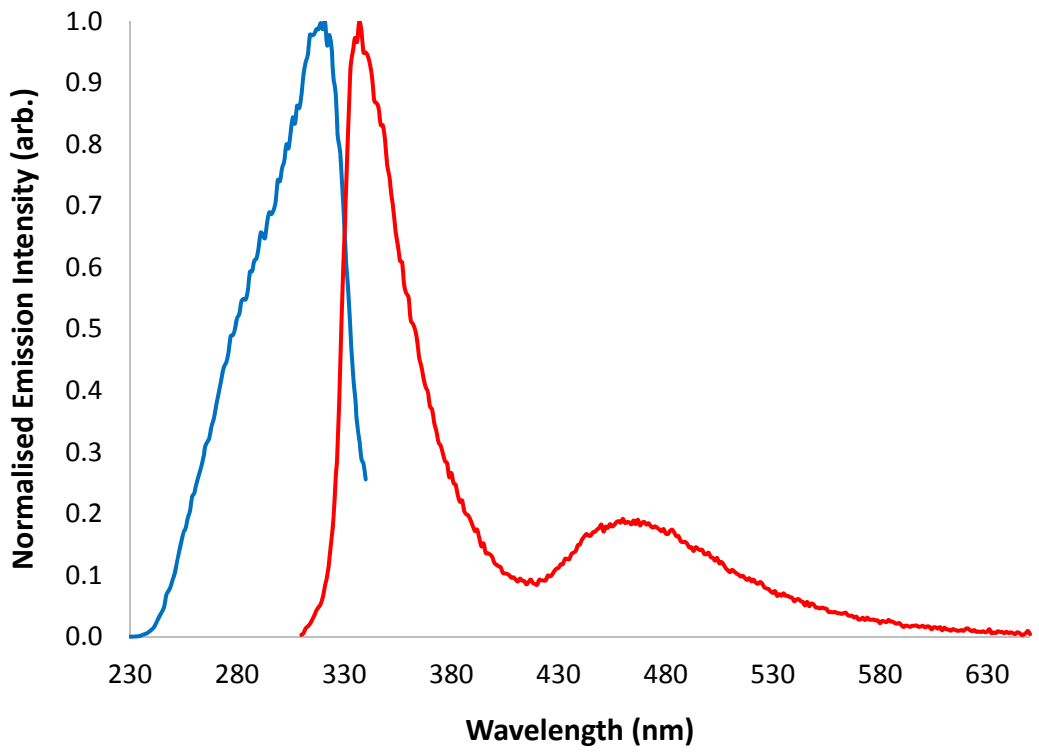


***Figure A3.26a***: Excitation and Emission profile of **26** in the solid state.

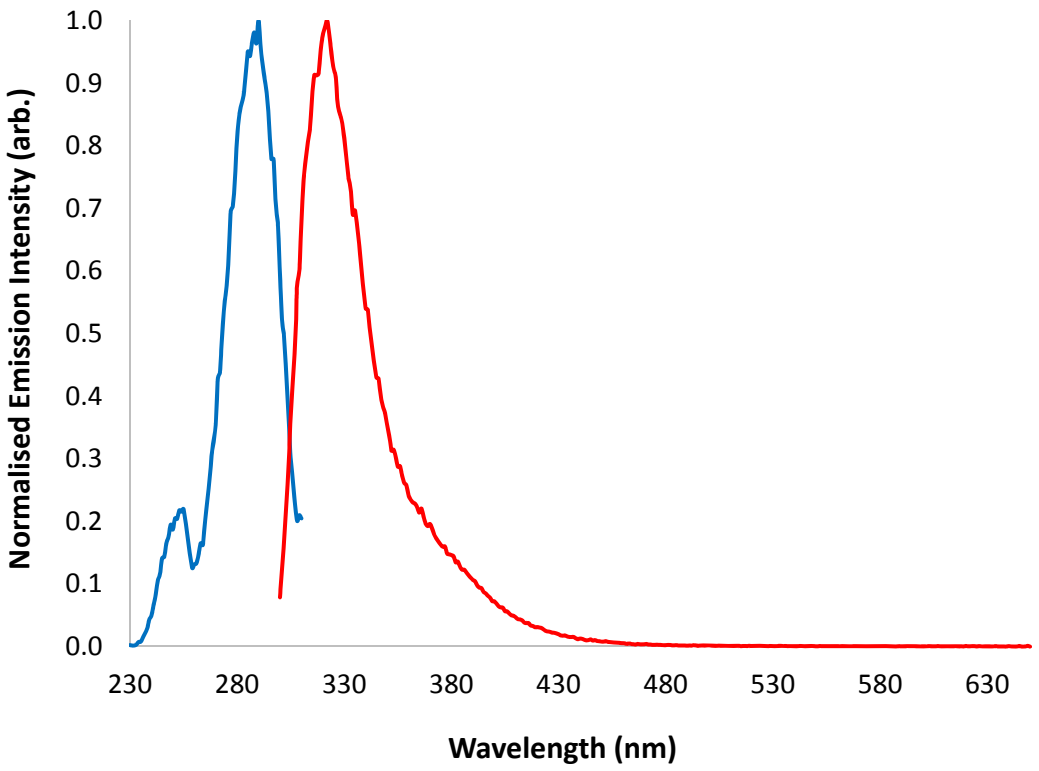


***Figure A3.26b***: Excitation and Emission profile of **26** in $H_2O$ ($10^{-6}$ M).

## A4 SEM Micrographs for Quantitative Analysis

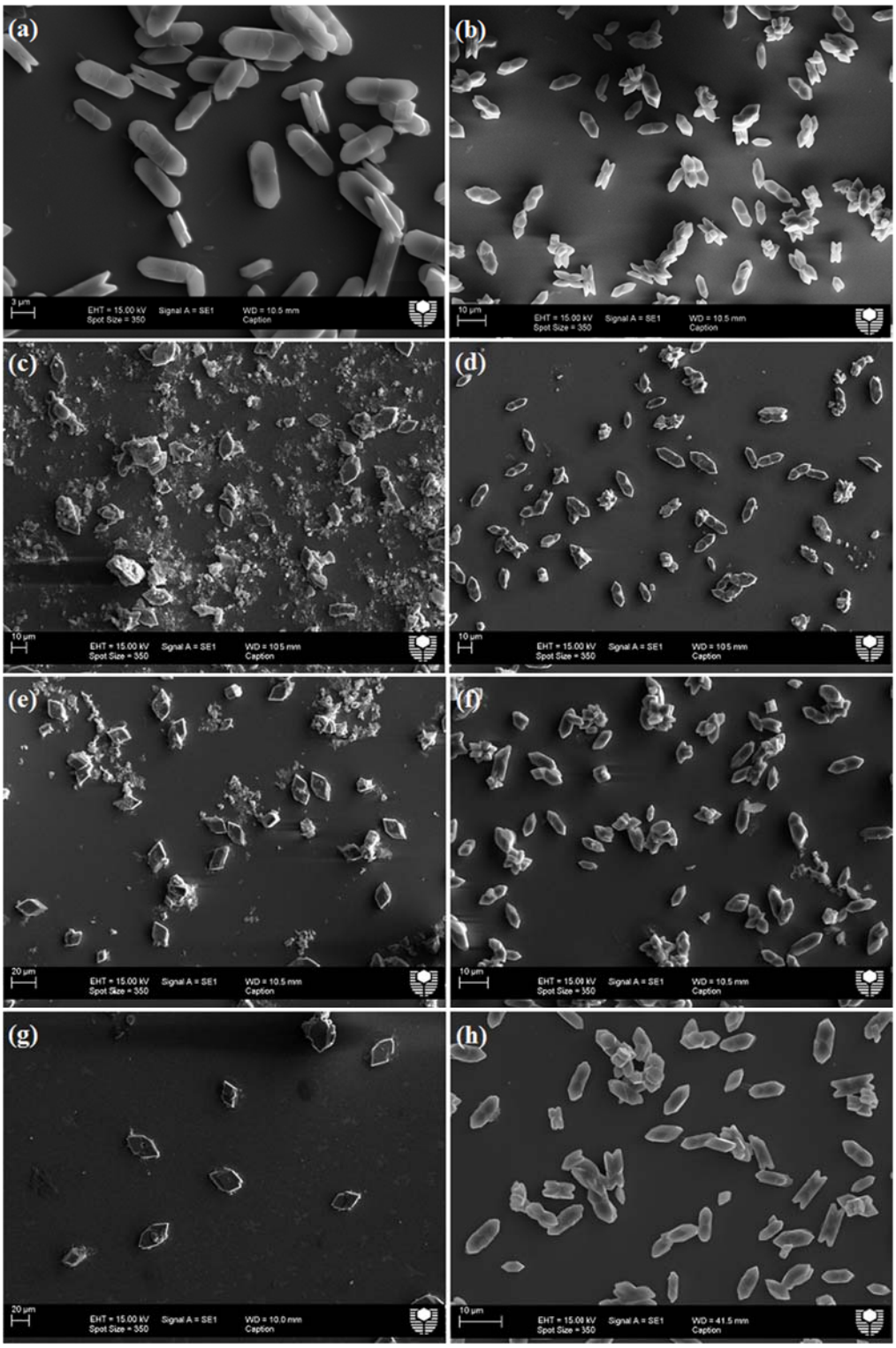


***Figure A4.1***: SEM micrographs of calcium oxalate crystal morphology in the presence of additives: (a) **1** at 4.90 mM, (b) **1** at 0.49 mM, (c) **2** at 5.31 mM, (d) **2** at 0.53 mM, (e) **4** at 5.74 mM, (f) **4** at 0.57 mM, (g) **5** at 5.84 mM, (h) **5** at 0.58 mM.

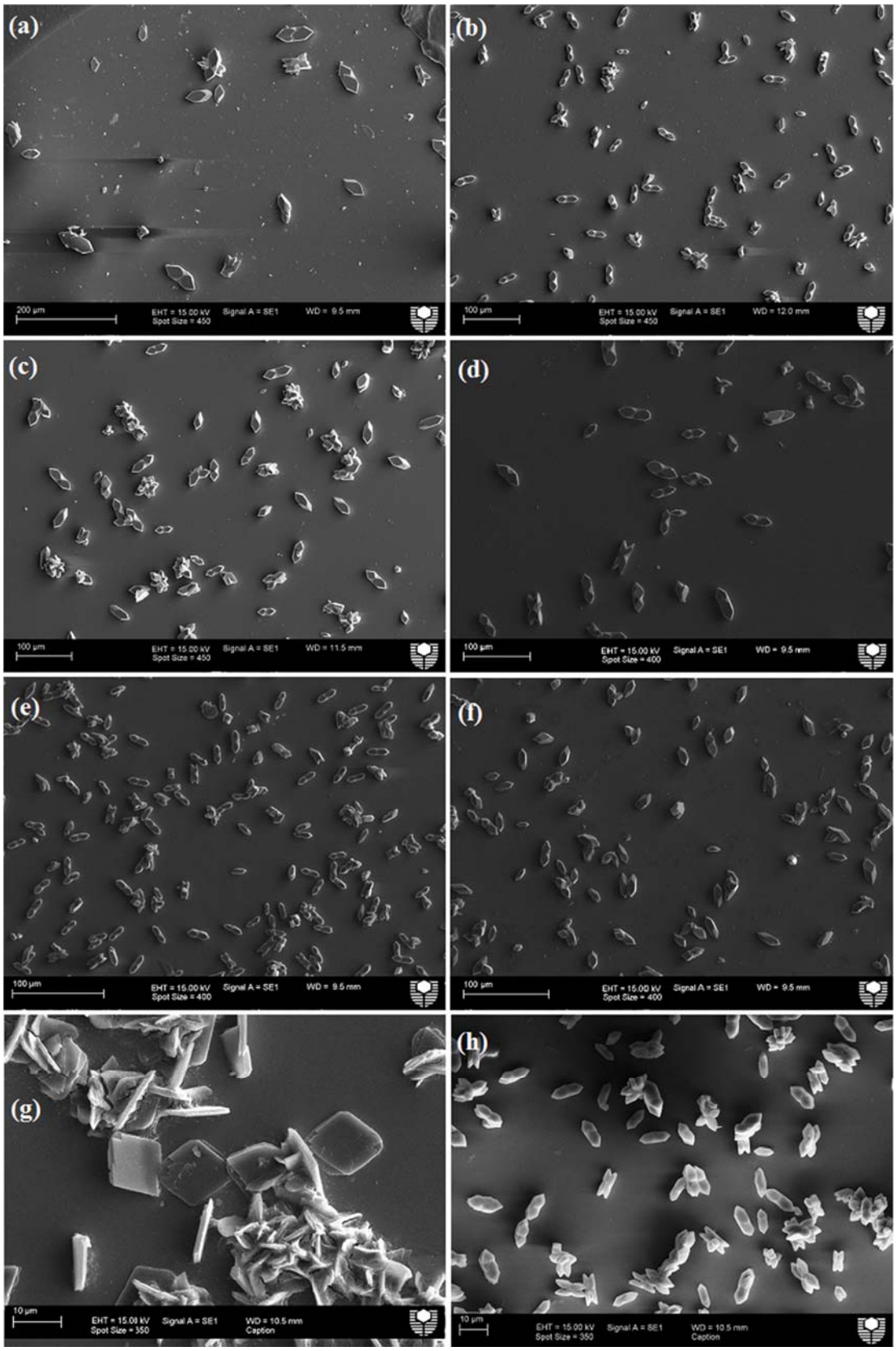


***Figure A4.2***: SEM micrographs of calcium oxalate crystal morphology in the presence of additives: (a) **6** at 5.26 mM, (b) **6** at 0.52 mM, (c) **8** at 4.67 mM, (d) **8** at 0.46 mM, (e) **9** at 4.67 mM, (f) **9** at 0.46 mM, (g) **10** at 4.67 mM, (h) **10** at 0.46 mM.

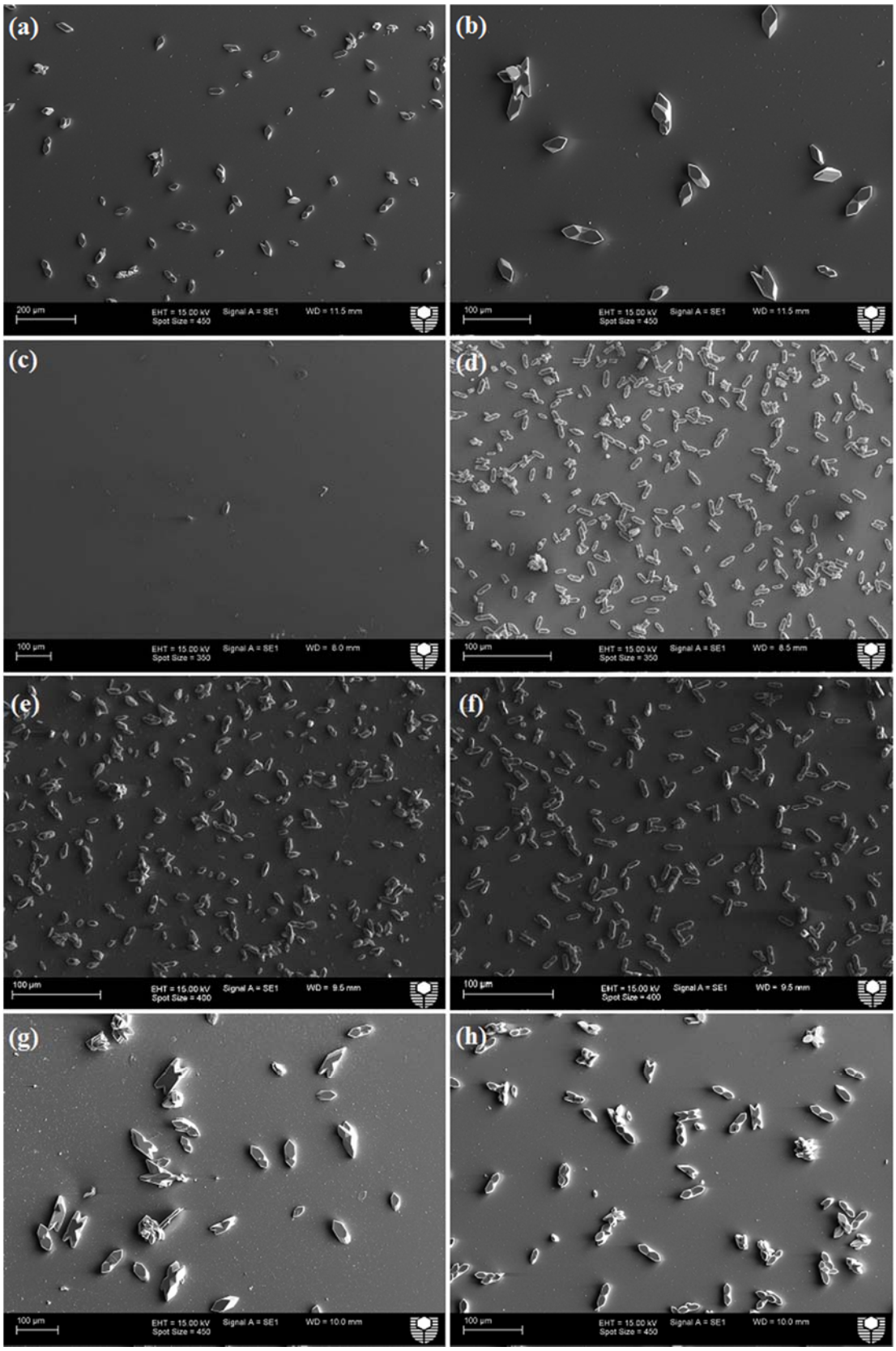


***Figure A4.3***: SEM micrographs of calcium oxalate crystal morphology in the presence of additives: (a) **11** at 4.65 mM, (b) **11** at 4.65 mM, (c) **16** at 4.44 mM, (d) **16** at 0.44 mM, (e) **8** at 5.29 mM, (f) **18** at 0.52 mM, (g) **20** at 4.42 mM, (h) **20** at 0.44 mM.

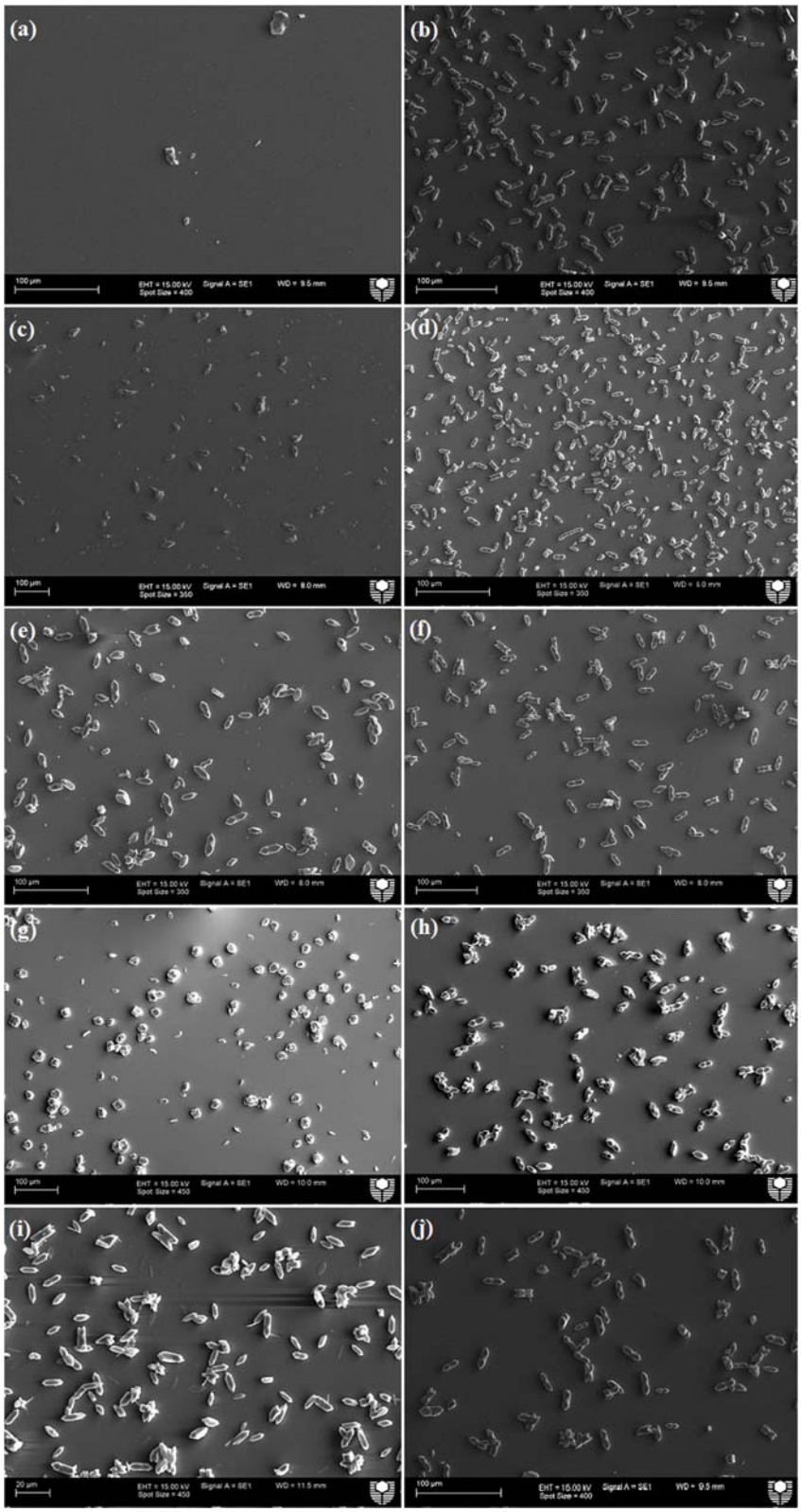


***Figure A4.4***: SEM micrographs of calcium oxalate crystal morphology in the presence of additives: (a) **7** at 4.90 mM, (b) **7** at 0.49 mM, (c) **17** at 5.68 mM, (d) **17** at 0.56 mM, (e) **19** at 6.17 mM, (f) **19** at 0.61 mM, (g) **21** at 5.31 mM, (h) **21** at 0.53 mM, (i) **26** at 6.17 mM, (j) **26** at 0.61 mM.

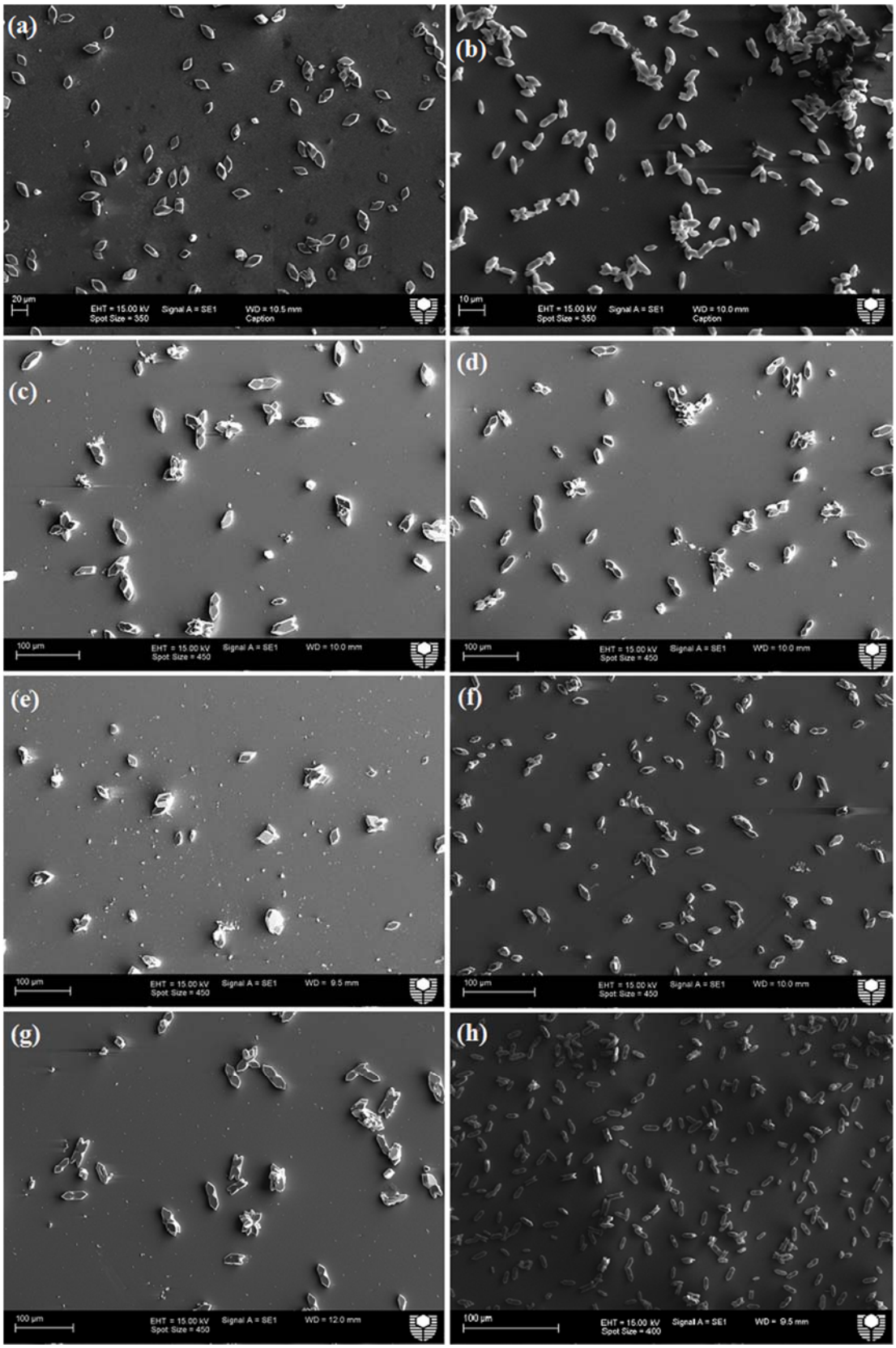


***Figure A4.5***: SEM micrographs of calcium oxalate crystal morphology in the presence of additives: (a) **3** at 6.84 mM, (b) **3** at 0.68 mM, (c) **22** at 5.07 mM, (d) **22** at 0.50 mM, (e) **23** at 5.10 mM, (f) **23** at 0.51 mM, (g) **24** at 5.10 mM, (h) **24** at 0.51 mM.

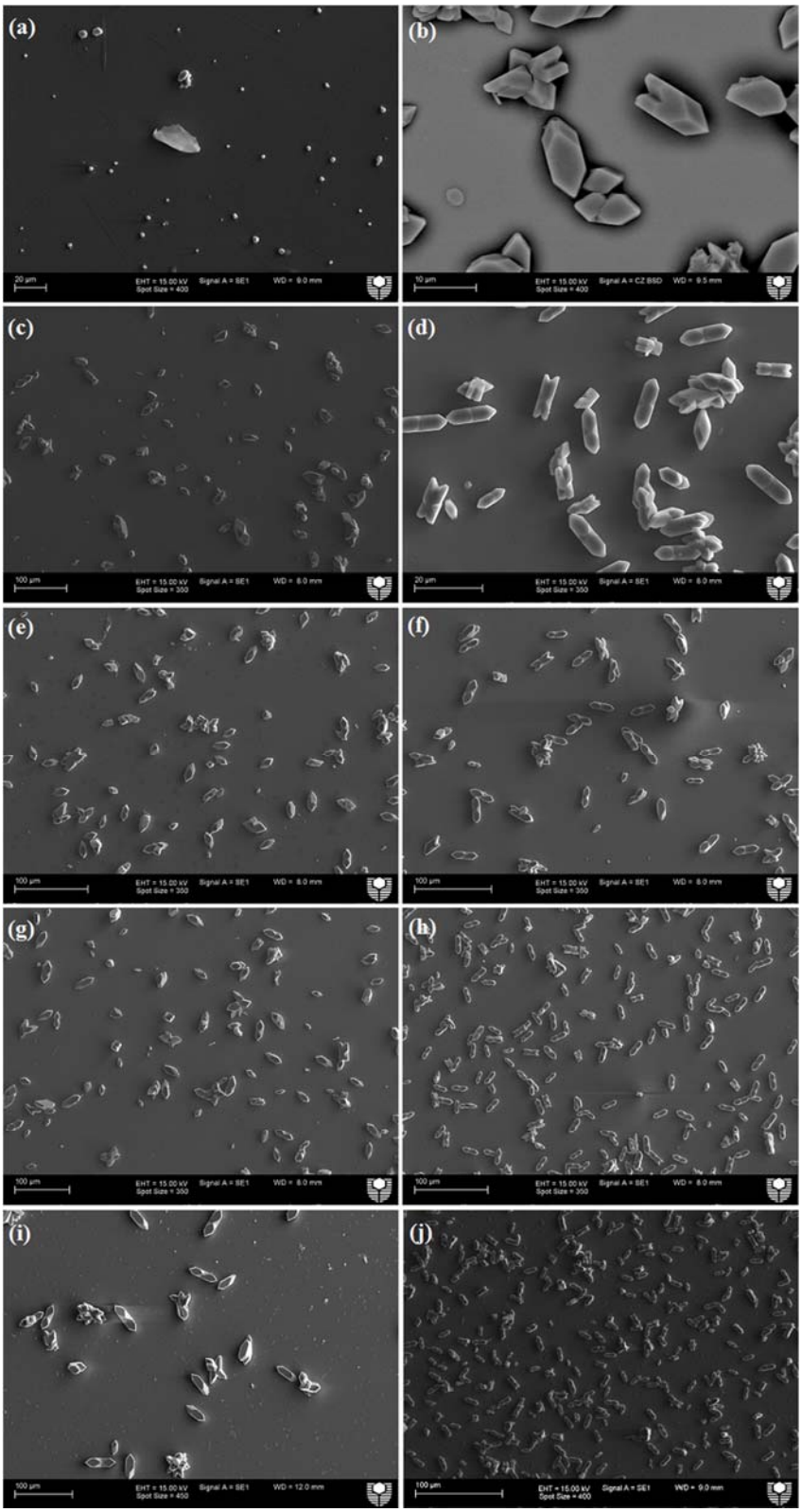


***Figure A4.6***: SEM micrographs of calcium oxalate crystal morphology in the presence of additives: (a) **12** at 6.80 mM, (b) **12** at 0.68 mM, (c) **13** at 6.80 mM, (d) **13** at 0.68 mM, (e) **14** at 6.80 mM, (f) **14** at 0.68 mM, (g) **15** at 6.75 mM, (h) **15** at 0.67 mM, (i) **25** at 6.75 mM, (j) **25** at 0.67 mM.

***Table A4a***: Quantitative data obtained from SEM micrographs ***Figures A4.1-6*** at a concentration of 1.0 g/L of the tetrazole series.

| Additive | Additive Concentration (g/ L) | Mean Particle Size (µm) | Standard Deviation | Aspect Ratio | Particles Counted |
|---|---|---|---|---|---|
| **Avg. Control** | - | 9.40 | 1.15 | 2.72 | 150 |
| **1a** | 1.0 | 7.46 | 1.83 | 2.84 | 50 |
| **2a** | 1.0 | 9.08 | 1.57 | 1.80 | 50 |
| **3a** | 1.0 | 21.35 | 2.92 | 2.11 | 50 |
| **4a** | 1.0 | 20.52 | 4.96 | 1.73 | 40 |
| **5a** | 1.0 | 31.73 | 7.94 | 1.70 | 12 |
| **6a** | 1.0 | 49.06 | 15.63 | 2.32 | 21 |
| **7a** | 1.0 | 18.29 | 3.72 | 2.04 | 4 |
| **8a** | 1.0 | 38.53 | 7.78 | 2.66 | 50 |
| **9a** | 1.0 | 21.62 | 1.85 | 3.11 | 50 |
| **10a** | 1.0 | 12.85 | 2.93 | 2.93 | 34 |
| **11a** | 0.1 | n/a | n/a | n/a | n/a |
| **12a** | 1.0 | 19.03 | 9.63 | 1.74 | 7 |
| **13a** | 1.0 | 27.87 | 9.40 | 2.20 | 37 |
| **14a** | 1.0 | 22.67 | 4.76 | 2.33 | 50 |
| **15a** | 1.0 | 30.9 | 7.29 | 2.41 | 50 |
| **16a** | 1.0 | 20.8 | 9.94 | 1.89 | 5 |
| **17a** | 1.0 | 25.96 | 6.52 | 2.77 | 36 |
| **18a** | 1.0 | 18.49 | 3.15 | 3.08 | 50 |
| **19a** | 1.0 | 22.42 | 4.56 | 2.65 | 50 |
| **20a** | 1.0 | 66.96 | 16.22 | 2.53 | 23 |
| **21a** | 1.0 | 25.38 | 3.44 | 1.35 | 50 |
| **22a** | 1.0 | 38.06 | 7.40 | 2.51 | 36 |
| **23a** | 1.0 | 21.47 | 6.49 | 2.01 | 20 |
| **24a** | 1.0 | 43.14 | 9.78 | 2.88 | 29 |
| **25a** | 1.0 | 50.8 | 8.25 | 3.05 | 22 |
| **26a** | 1.0 | 12.59 | 2.00 | 2.91 | 50 |

***Table A4b***: Quantitative data obtained from SEM micrographs ***Figures A4.1-6*** at a concentration of 0.1 g/L of the tetrazole series.

| Additive | Additive Concentration (g/ L) | Mean Particle Size (µm) | Standard Deviation | Aspect Ratio | Particles Counted |
|---|---|---|---|---|---|
| **Avg. Control** | - | 9.40 | 1.15 | 2.72 | 150 |
| **1b** | 0.10 | 10.52 | 1.66 | 2.74 | 50 |
| **2b** | 0.10 | 19.04 | 2.94 | 2.67 | 50 |
| **3b** | 0.10 | 6.95 | 0.89 | 2.50 | 50 |
| **4b** | 0.10 | 10.45 | 2.00 | 2.62 | 50 |
| **5b** | 0.10 | 7.99 | 1.58 | 2.60 | 38 |
| **6b** | 0.10 | 33.04 | 2.62 | 3.02 | 50 |
| **7b** | 0.10 | 17.68 | 1.74 | 3.14 | 50 |
| **8b** | 0.10 | 39.71 | 9.11 | 2.81 | 26 |
| **9b** | 0.10 | 22.96 | 3.22 | 2.60 | 50 |
| **10b** | 0.10 | 4.51 | 1.09 | 1.71 | 50 |
| **11b** | 0.10 | 48.63 | 8.57 | 2.51 | 50 |
| **12b** | 0.10 | 10.54 | 2.06 | 2.07 | 50 |
| **13b** | 0.10 | 12.85 | 2.87 | 2.90 | 50 |
| **14b** | 0.10 | 28.40 | 5.83 | 3.18 | 50 |
| **15b** | 0.10 | 22.10 | 2.47 | 3.03 | 50 |
| **16b** | 0.10 | 25.96 | 6.52 | 2.77 | 36 |
| **17b** | 0.10 | 14.39 | 2.81 | 2.97 | 50 |
| **18b** | 0.10 | 17.11 | 1.66 | 3.24 | 50 |
| **19b** | 0.10 | 25.09 | 1.75 | 3.24 | 50 |
| **20b** | 0.10 | 38.13 | 4.15 | 3.04 | 50 |
| **21b** | 0.10 | 31.89 | 3.92 | 2.74 | 50 |
| **22b** | 0.10 | 25.57 | 3.65 | 3.03 | 50 |
| **23b** | 0.10 | 18.42 | 2.89 | 2.61 | 50 |
| **24b** | 0.10 | 14.70 | 1.88 | 3.04 | 50 |
| **25b** | 0.10 | 15.59 | 1.25 | 3.07 | 50 |
| **26b** | 0.10 | 23.00 | 2.94 | 3.09 | 50 |

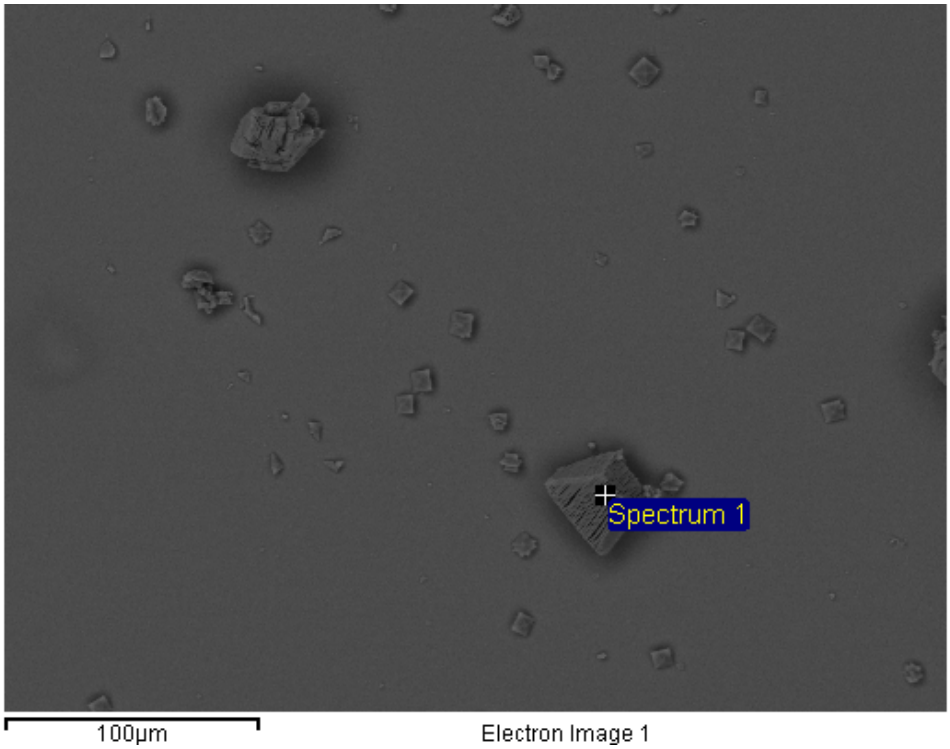


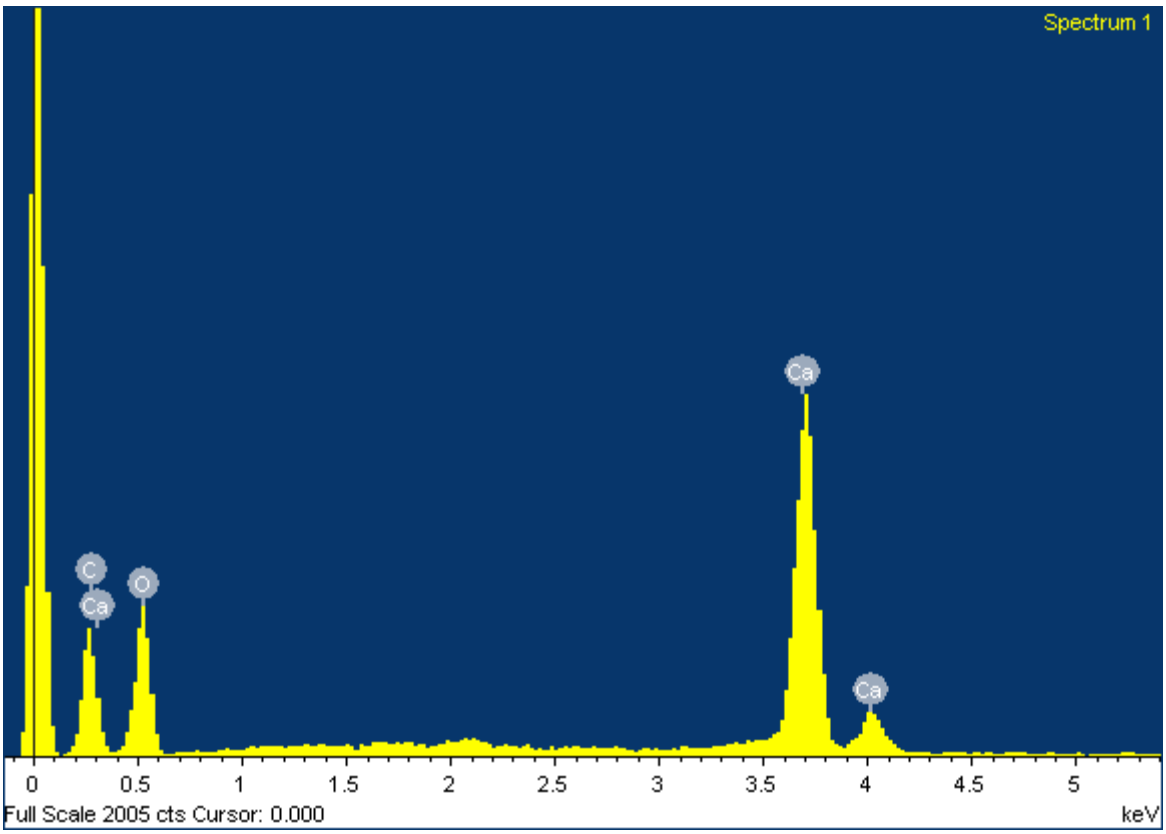


***Figure A4.7a***: EDS analysis of large particles as COM from AU control experiments

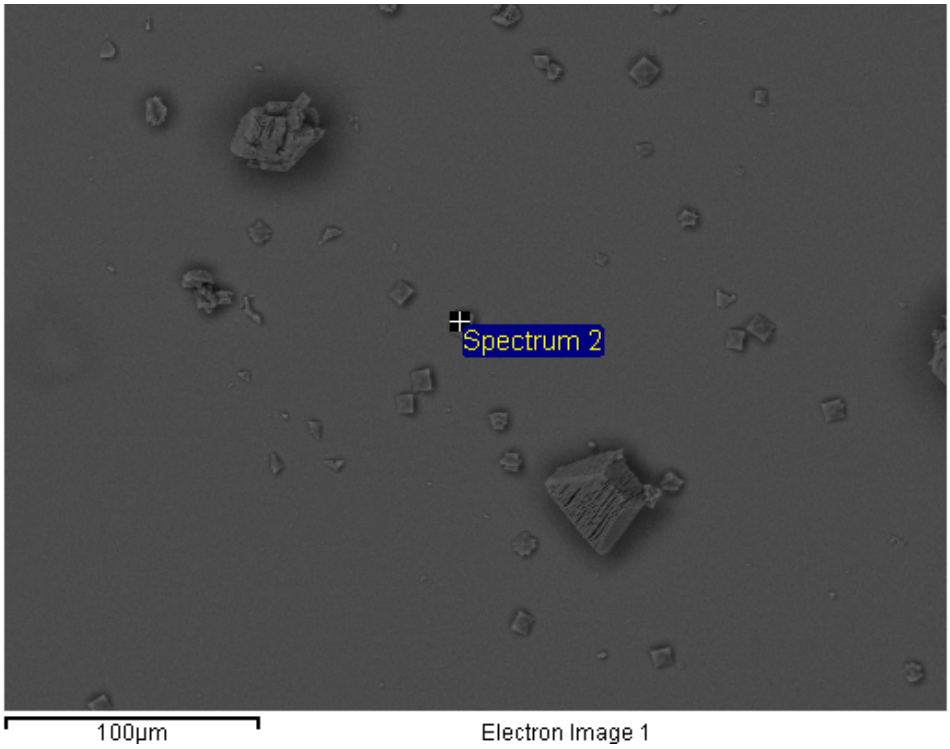


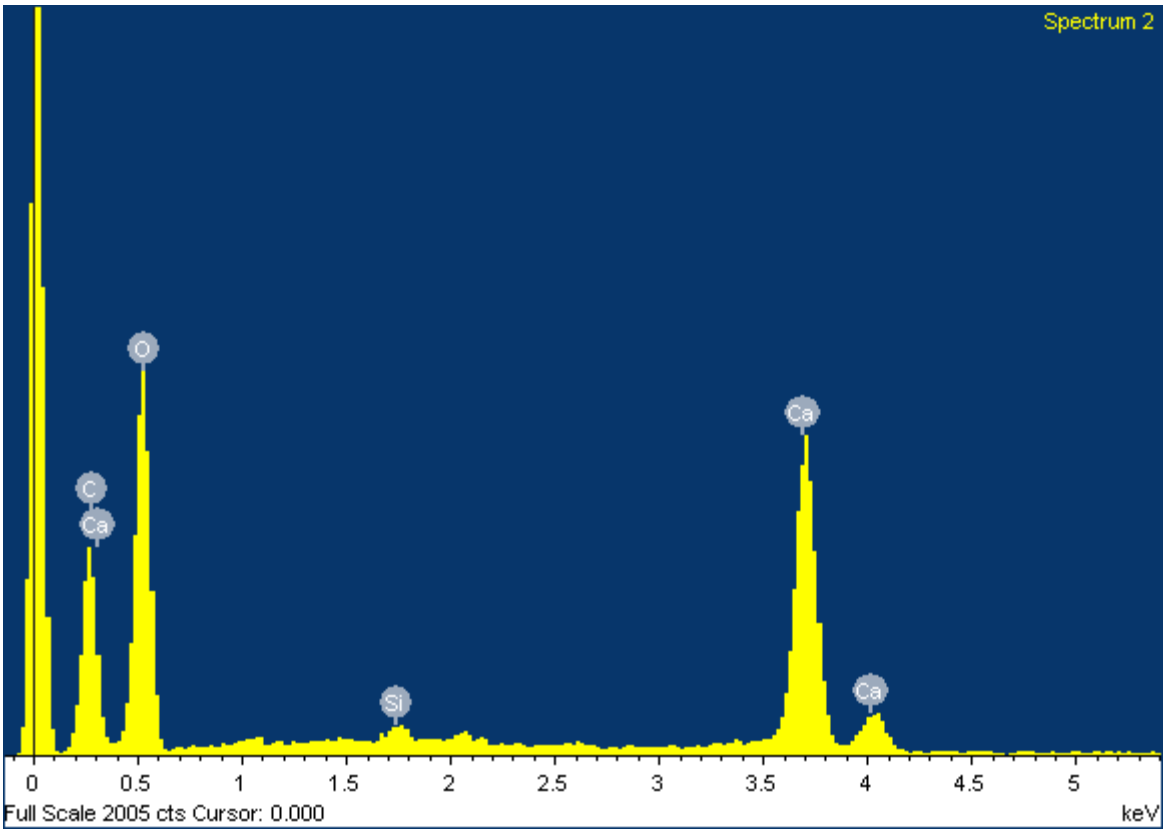


***Figure A4.7b***:EDS analysis of small particles as COD from AU control experiments.

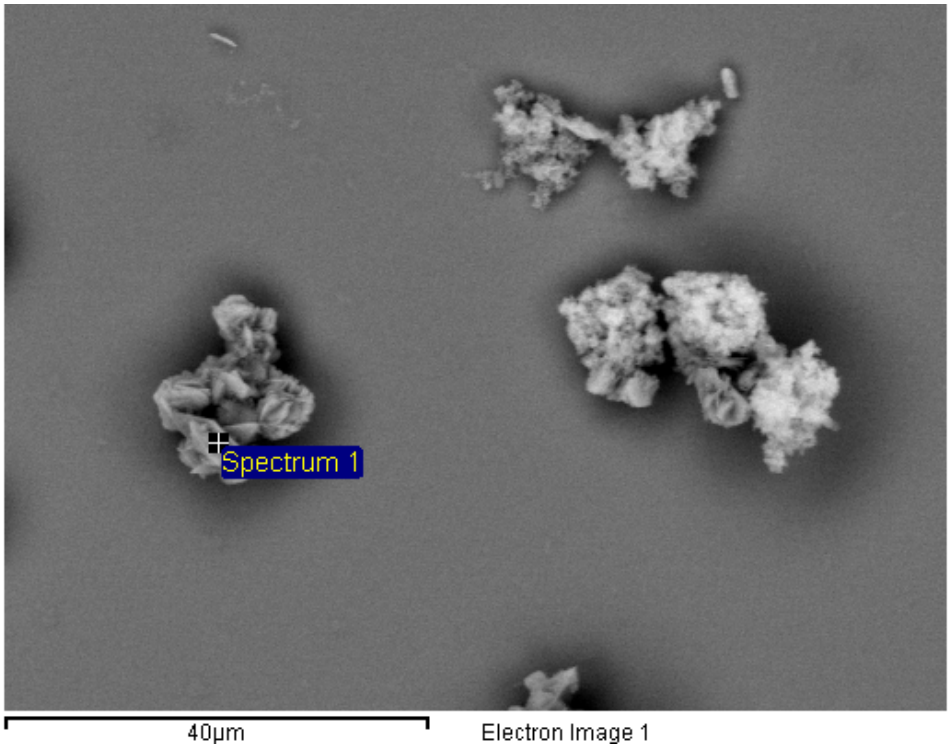


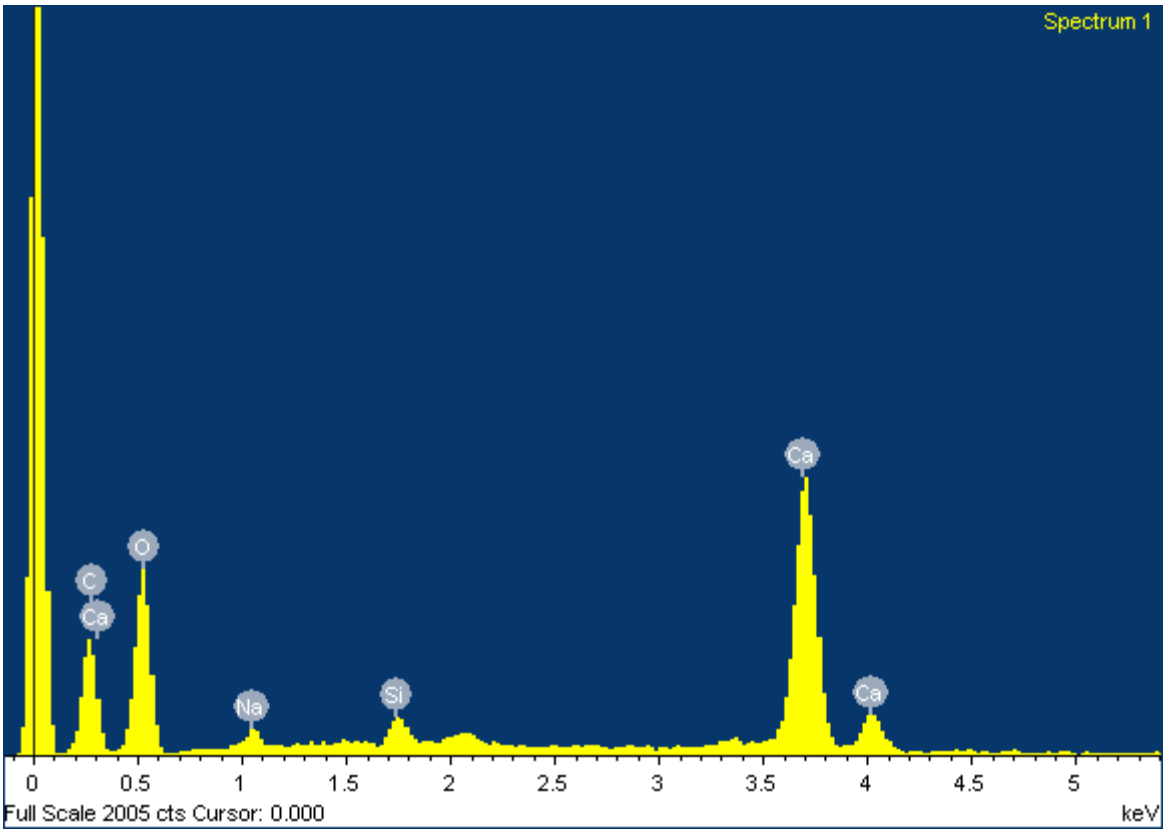


***Figure A4.8a***: EDS analysis of particles grown in AU and additive **4** (5.74 mM).

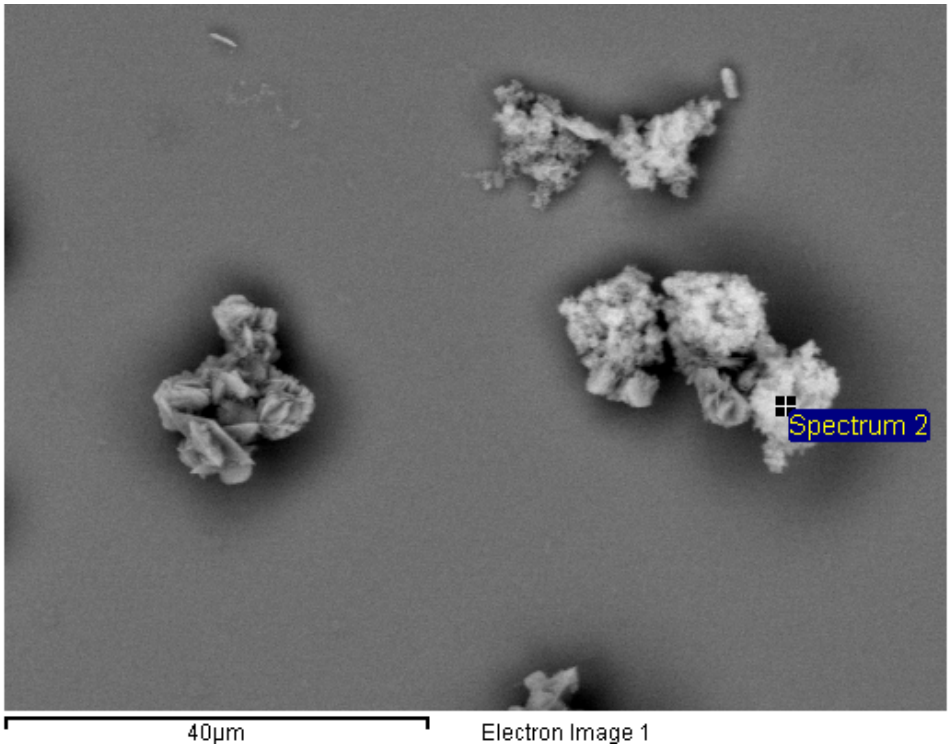


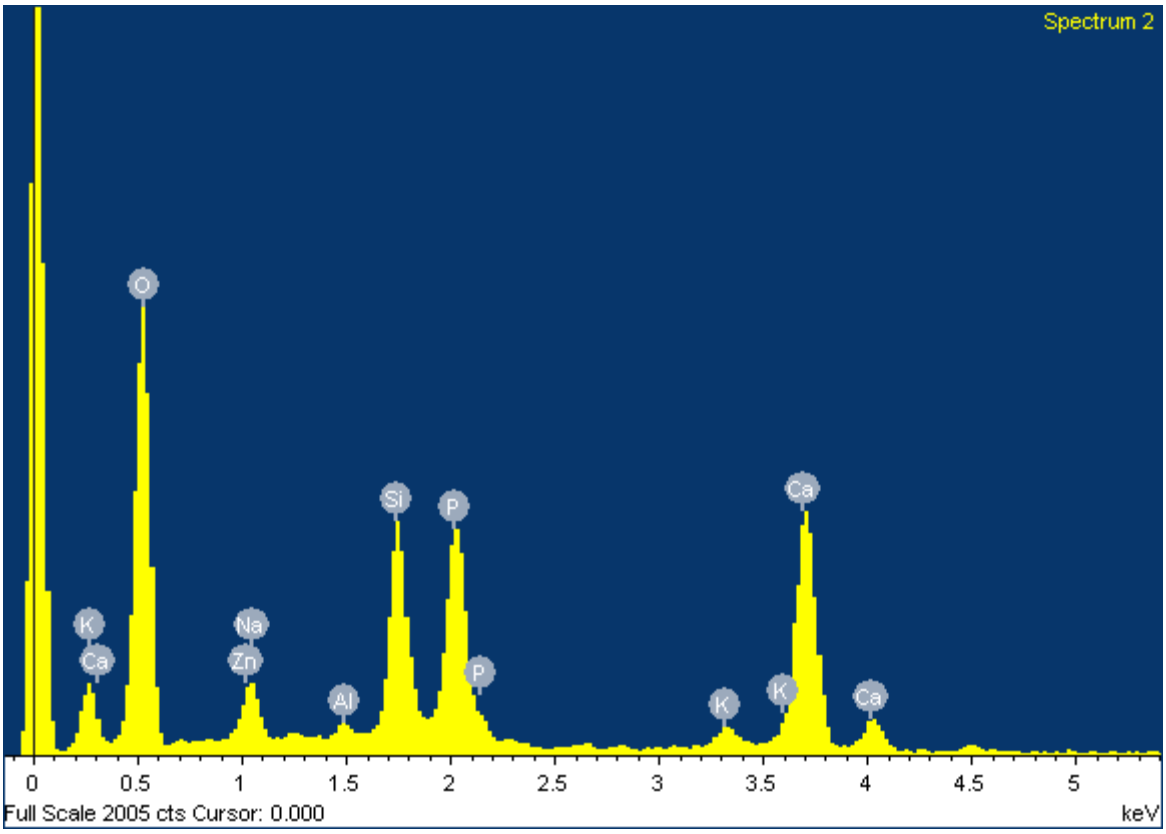


***Figure A4.8b***: EDS analysis of particles grown in AU and additive **4** (5.74 mM).

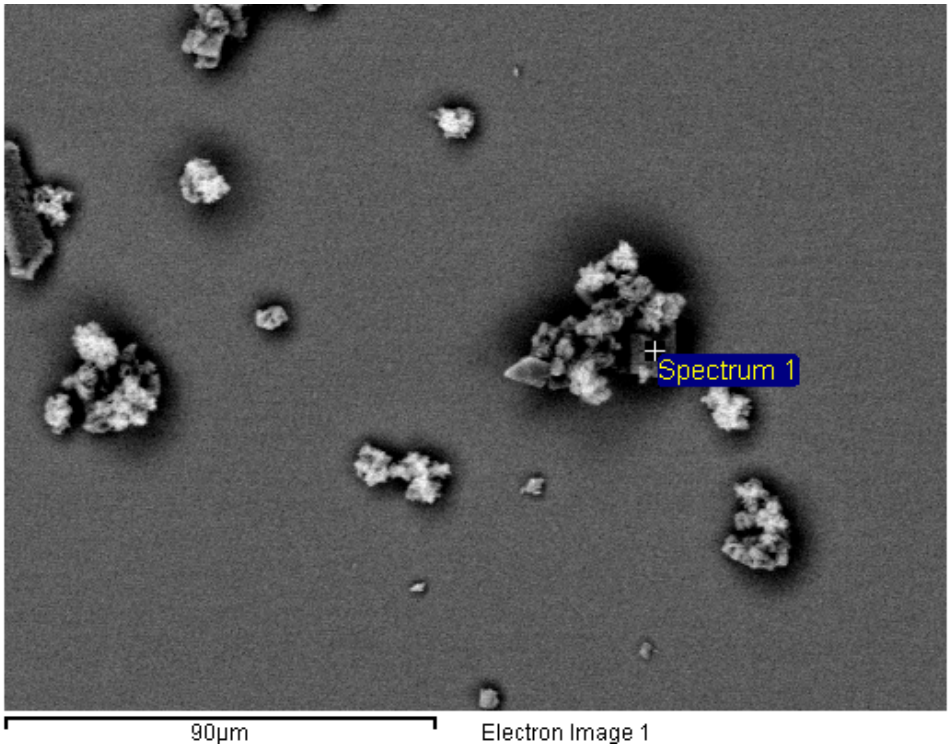


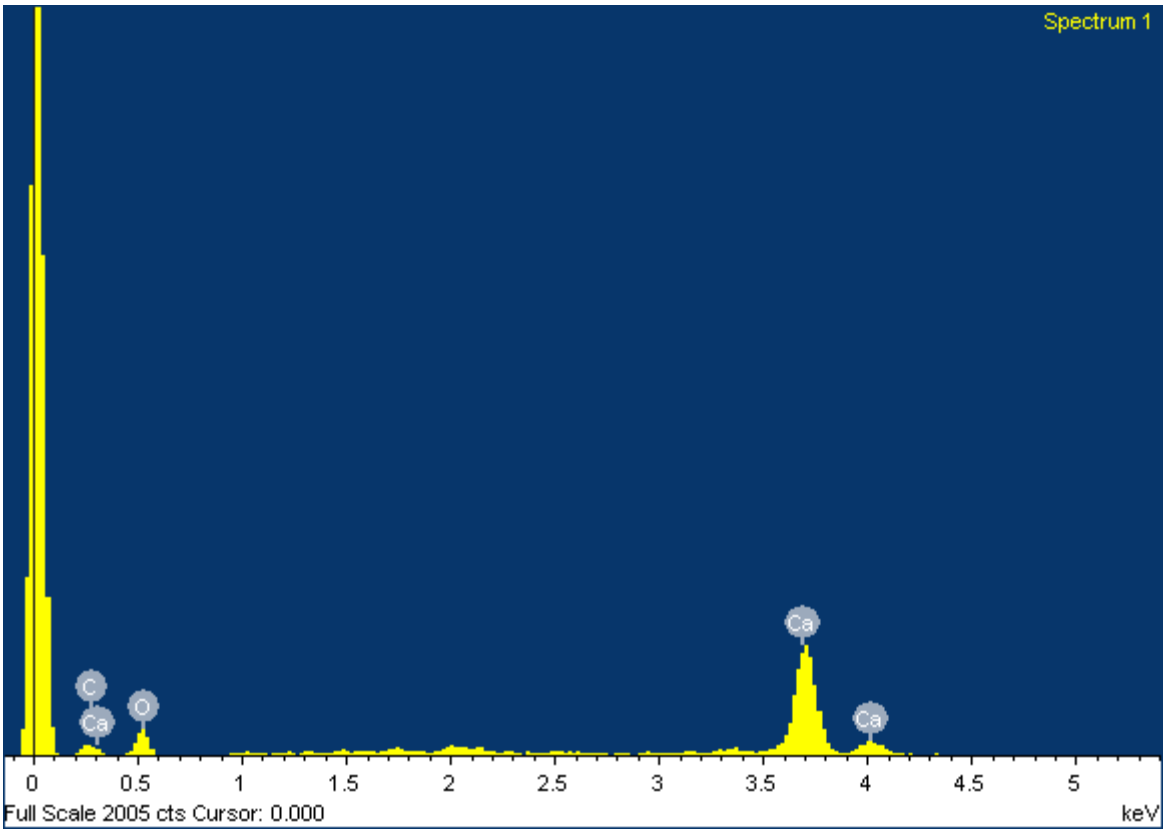


***Figure A4.9a***: EDS analysis of particles grown in AU and additive **5** (5.84 mM).

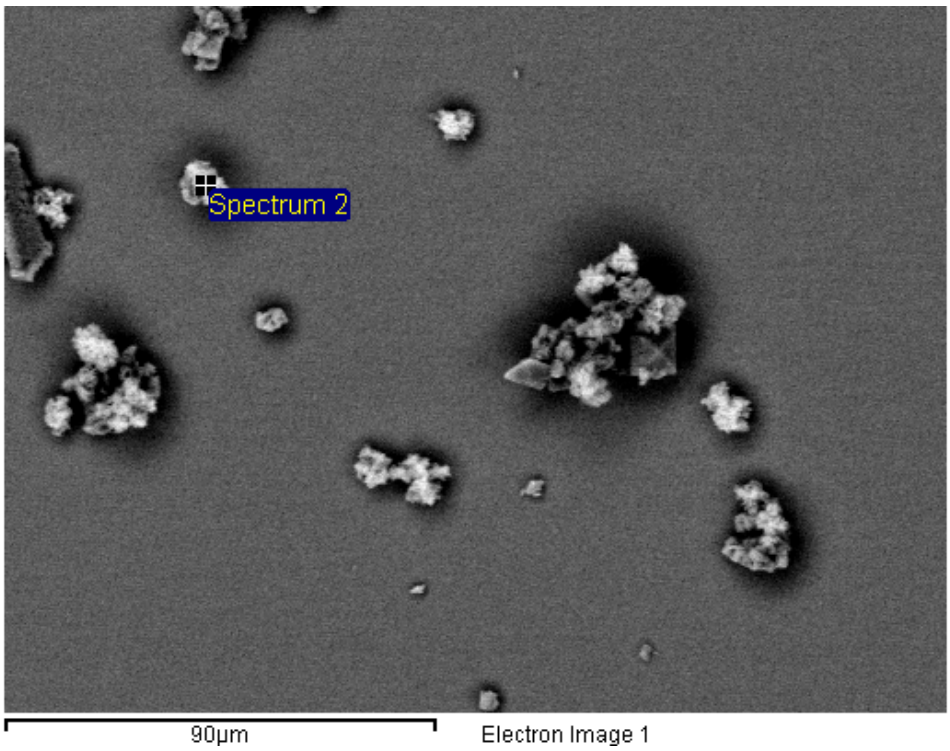


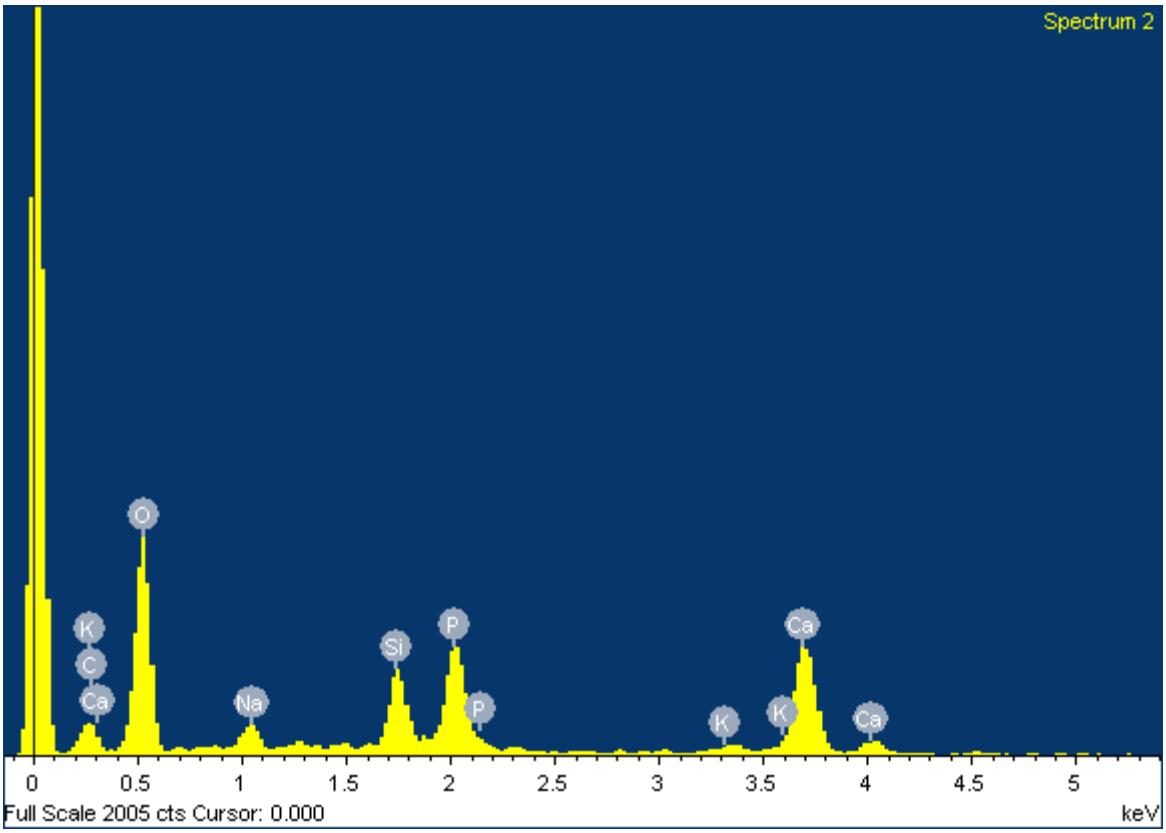


***Figure A4.9b***: EDS analysis of particles grown in AU and additive **5** (5.84 mM).

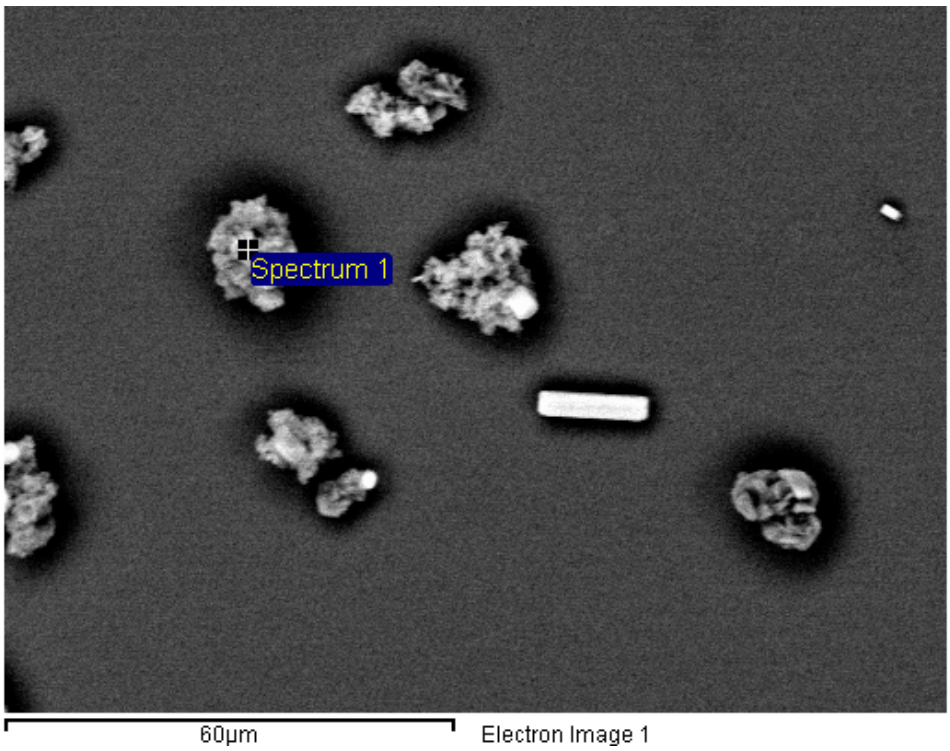


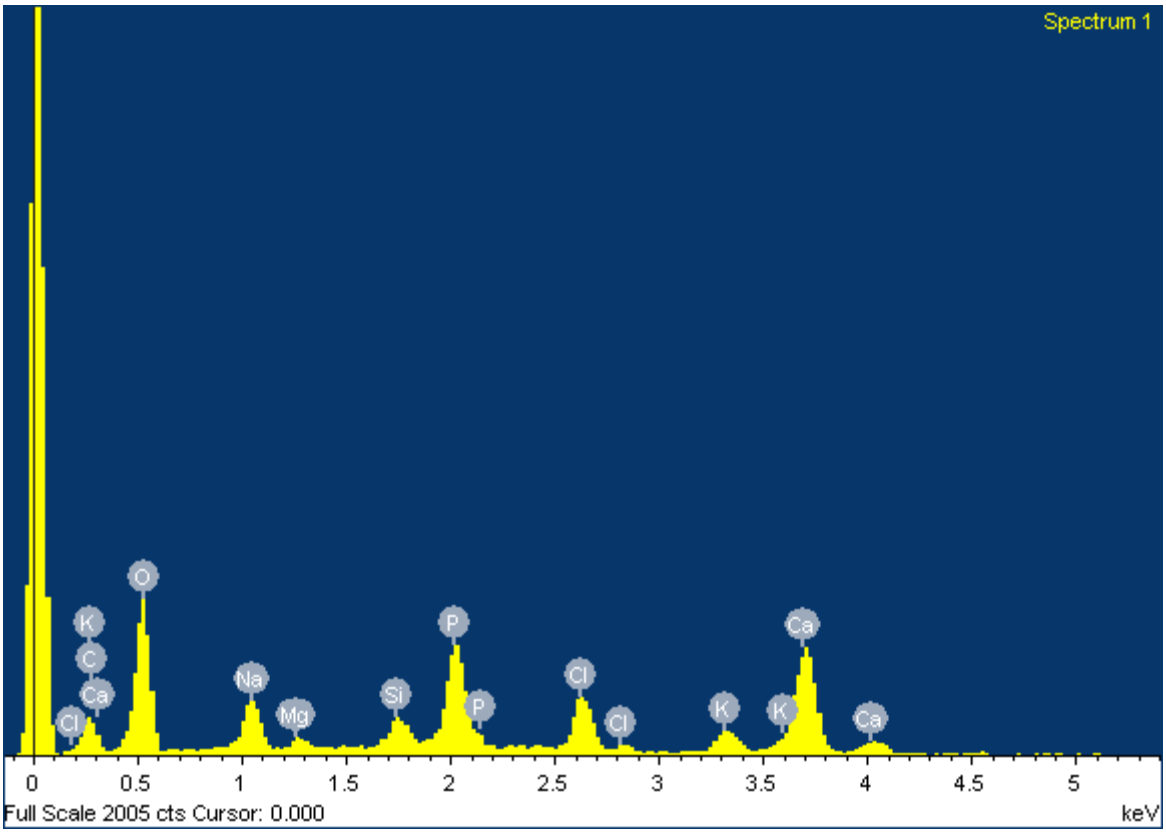


***Figure A4.10a***: EDS analysis of particles grown in AU and additive **14** (6.80 mM).

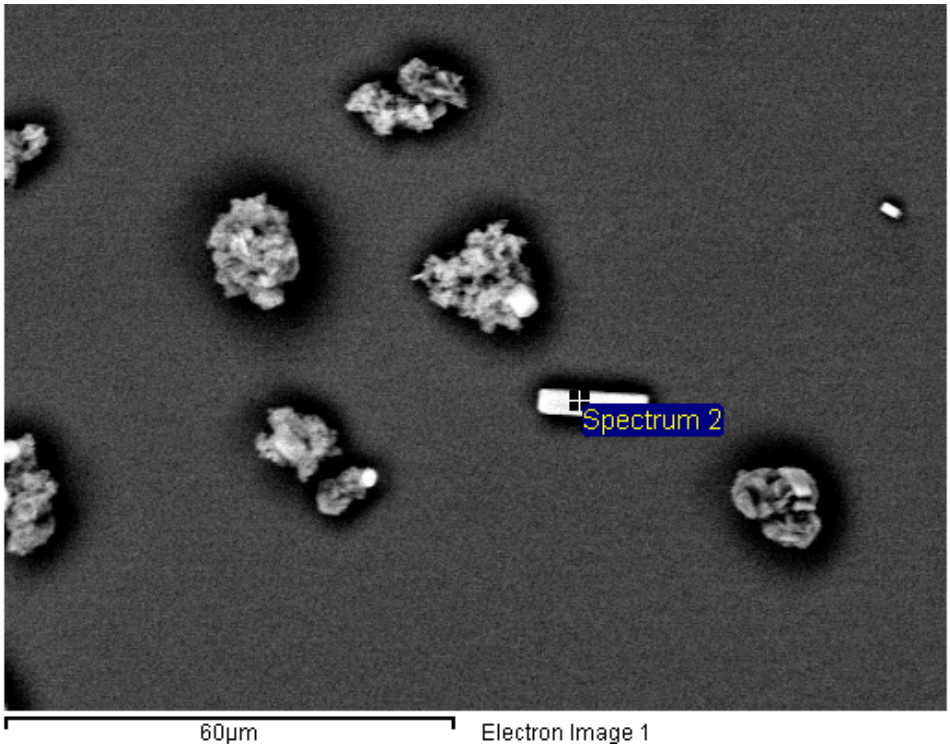


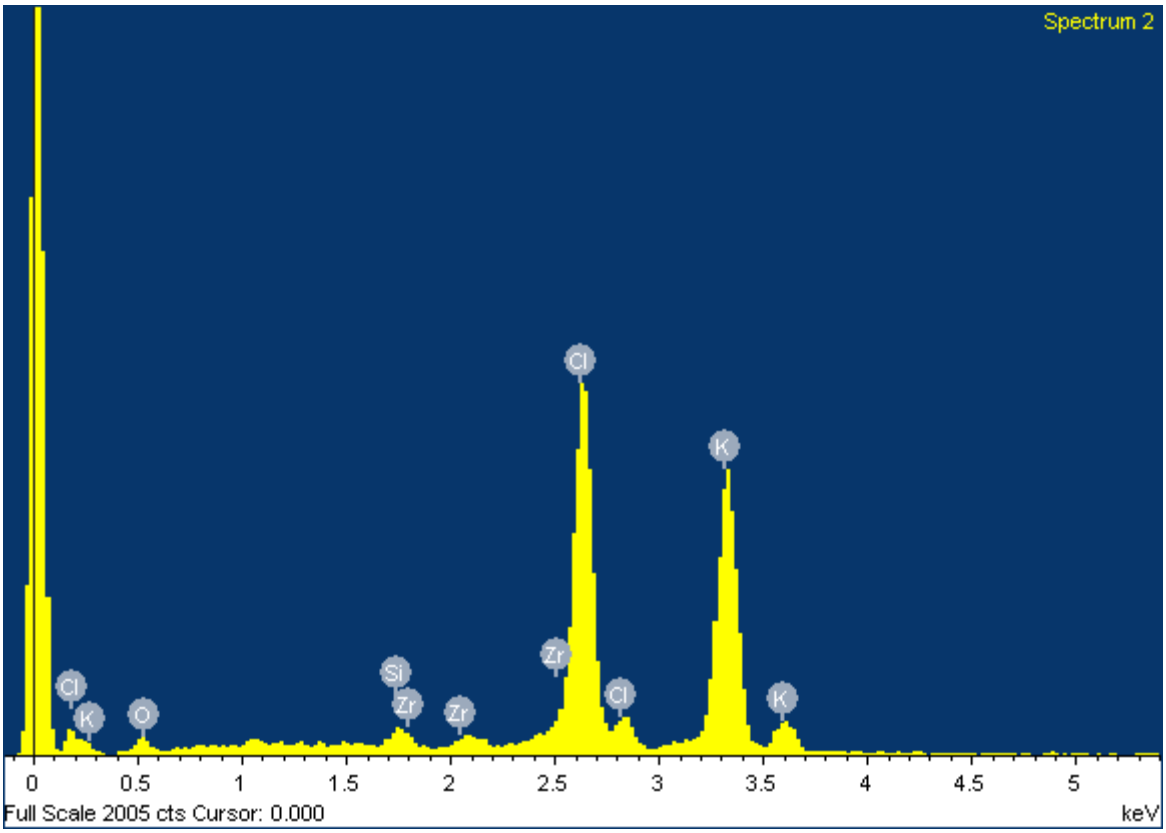


***Figure A4.10b***: EDS analysis of particles grown in AU and additive **14** (6.80 mM).

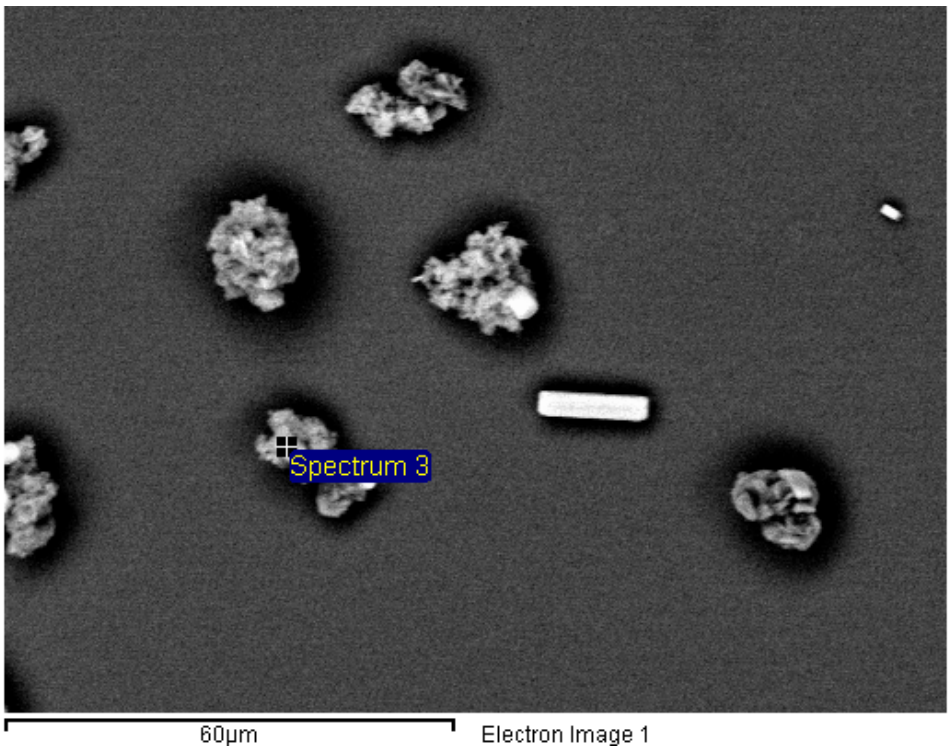


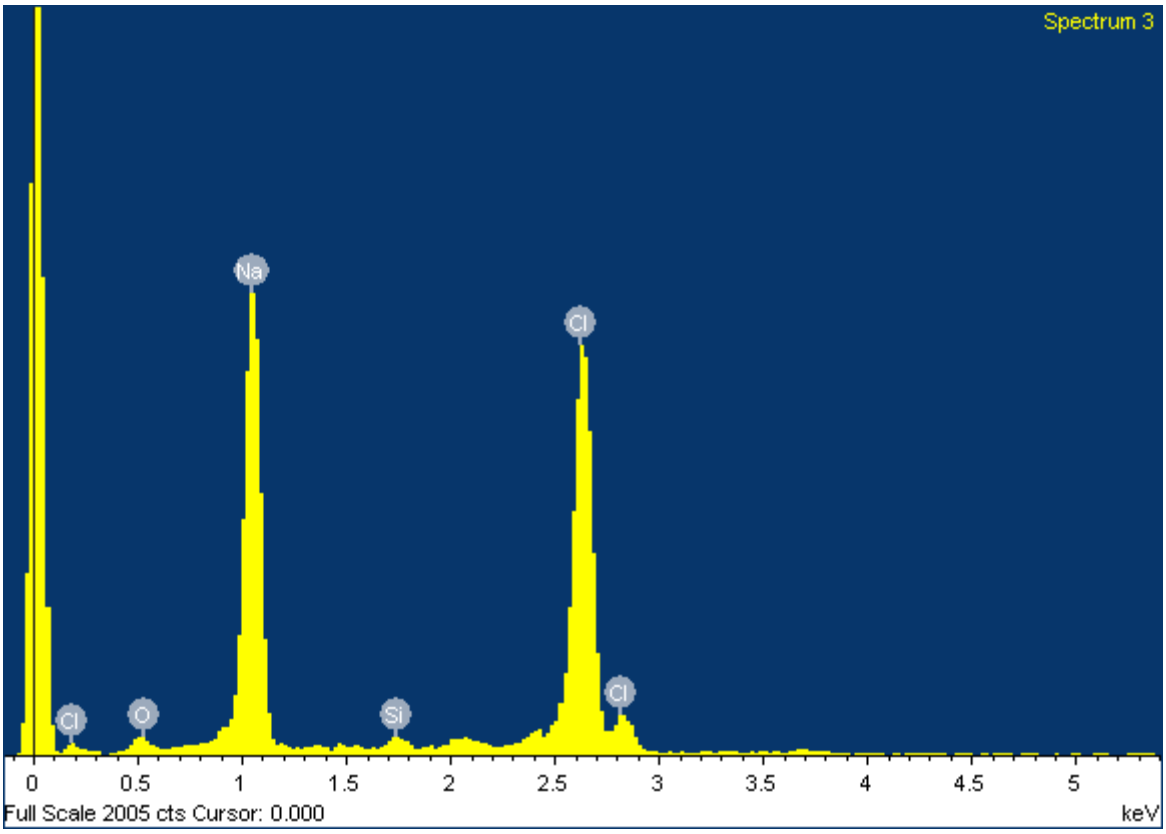


***Figure A4.10c***: EDS analysis of particles grown in AU and additive **14** (6.80 mM).

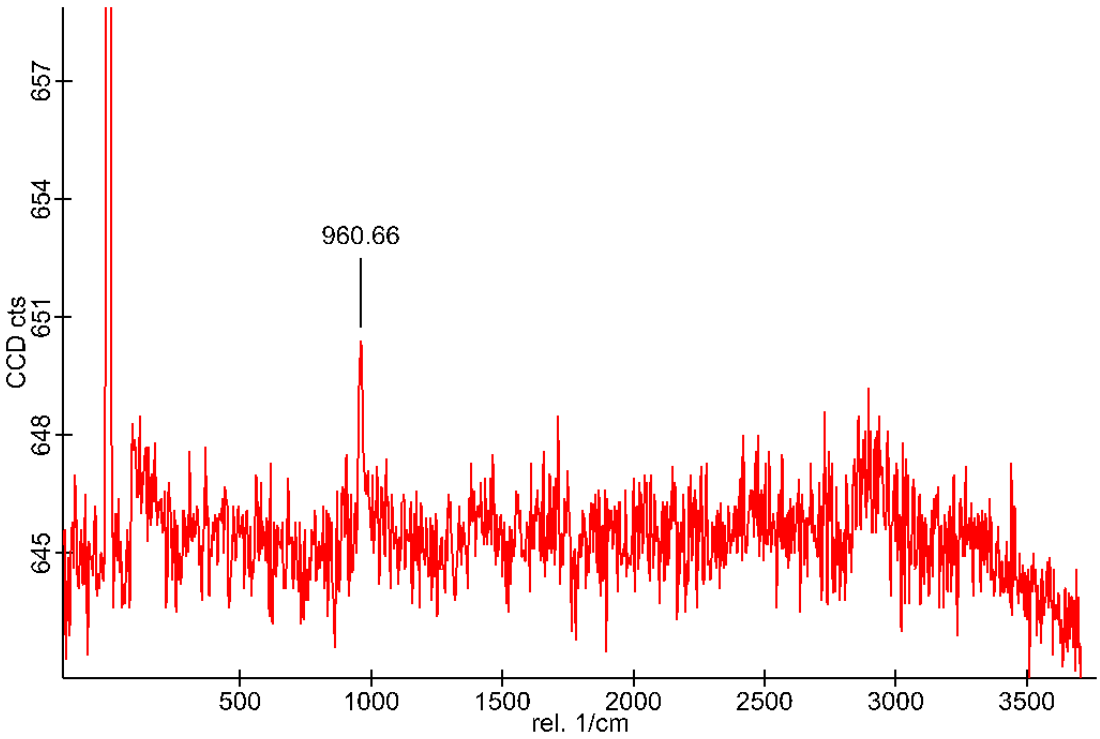


***Figure A4.11***: Raman spectrum of aggregate particles grown in the presence of additive **5**.

## A5 Aggregation Mechanism Investigation

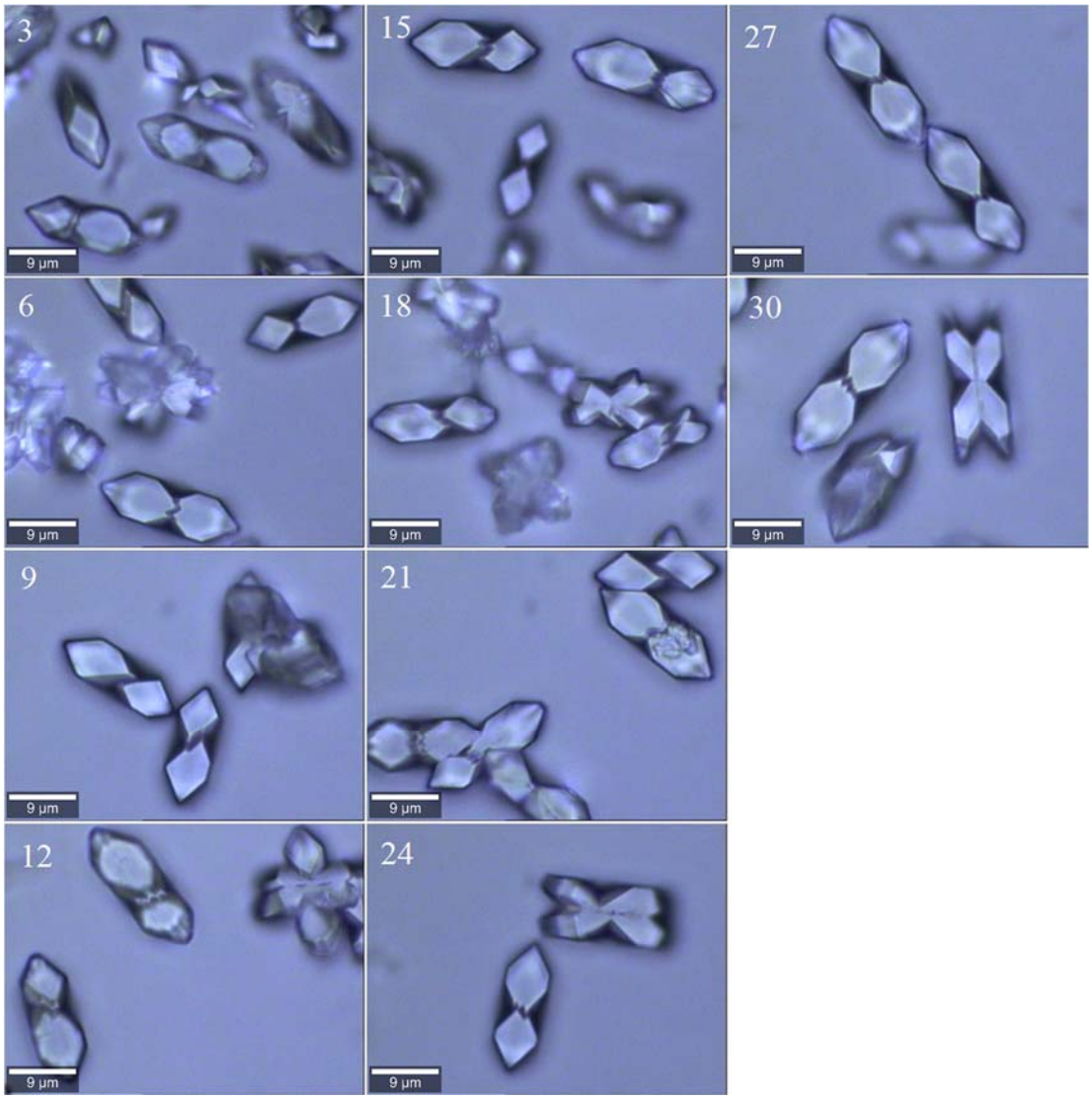


***Figure A5.1***: Optical images of COM grown without additives across 30 day time period with sodium azide (1%).

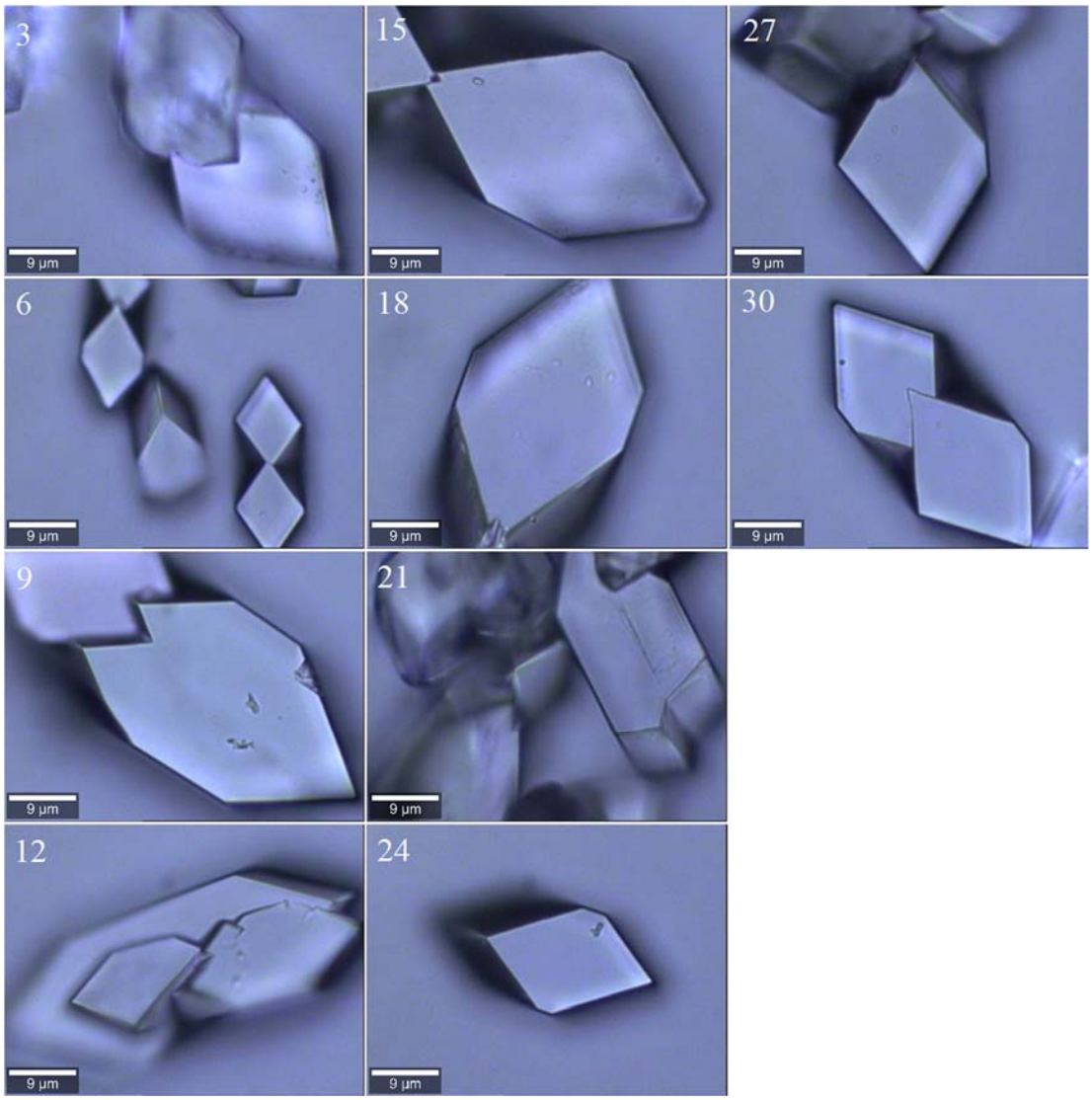


***Figure A5.2***: Optical images of COM grown in the presence of **3** (6.84 mM) over 30 days with sodium azide (1%).

## A6 AFM snapshots and Video Link

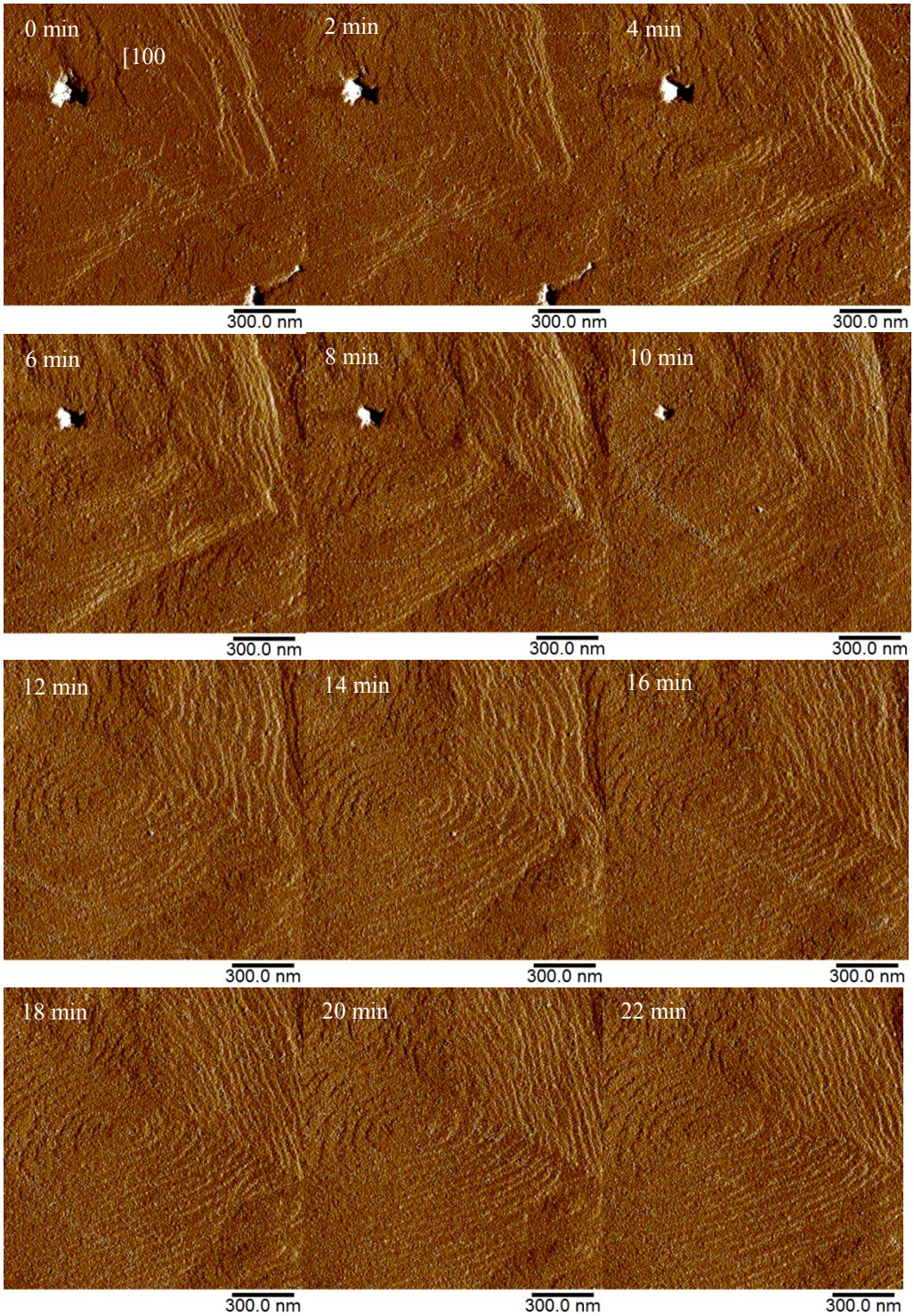


***Figure A6.1***: Snapshots of *in situ* AFM COM (010) surface grown in supersaturated CaOx solution without additives present.

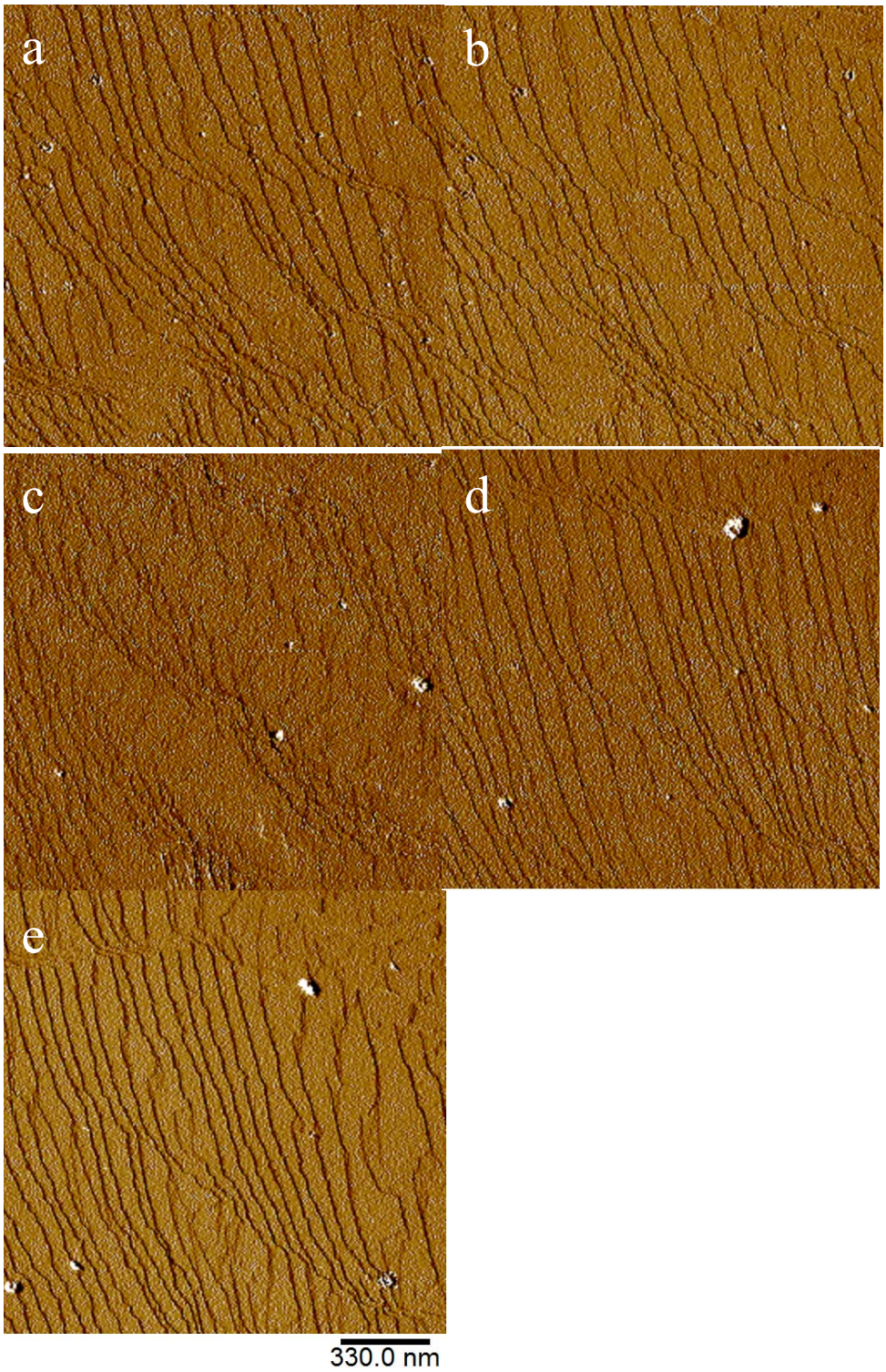


***Figure A6.2***: Snapshots from time resolved *in situ* AFM imaging of COM steps at constant supersaturation (a) without additives at 0 minutes, (b) in the presence of **5** (0.42 mg/mL) after 30 minutes, (c) in the presence of **5** (2.72 mg/mL) after 60 minutes, (d) regrowth without additives- 40 minutes after pumping with tetrazole **5** finished, and (e) in the presence of **10** (2.85 mg/mL) after 40 minutes.

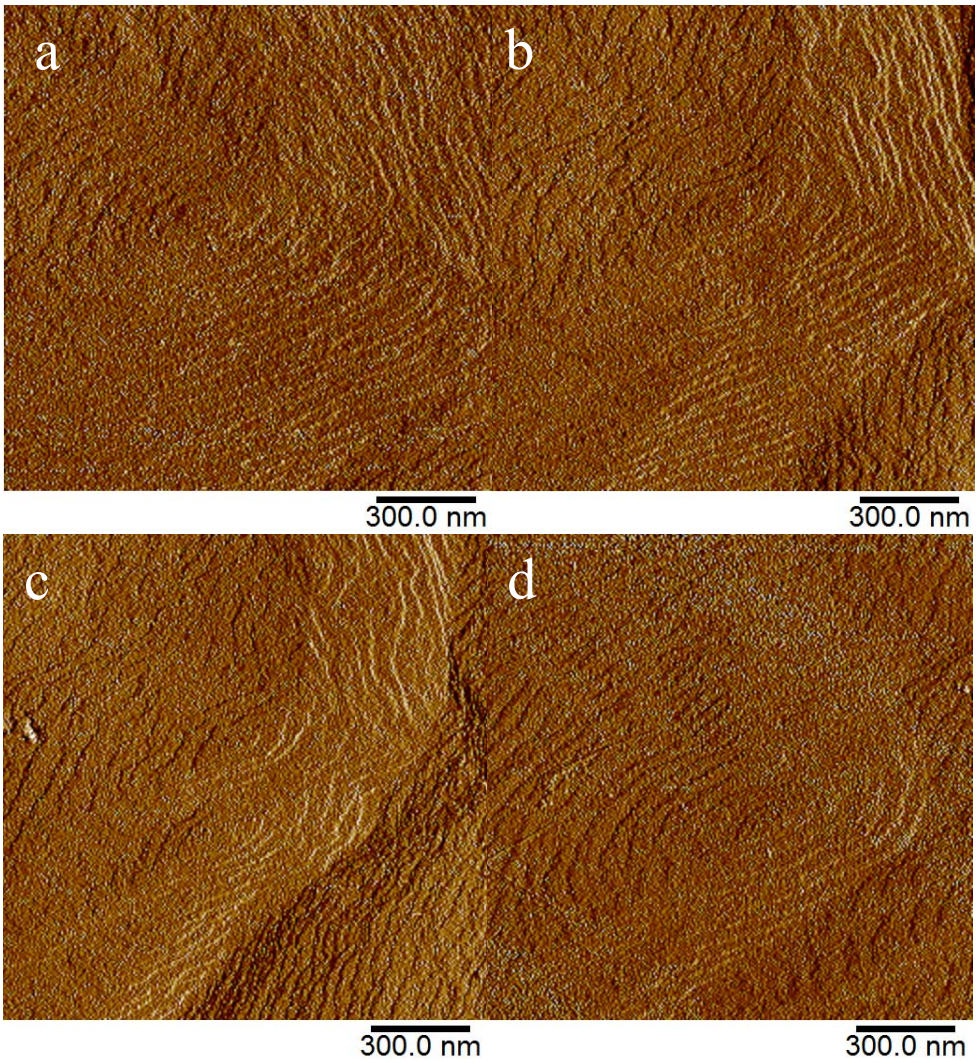


***Figure A6.3***: Snapshots from time resolved *in situ* AFM imaging of hillock growth on the COM (010) face in supersaturated CaOx solutions (a) without additives after 35 minutes, (b) in the presence of **12** (3.03 mg/mL) after 25 minutes (c) in the presence of **12** (3.03 mg/mL) after 45 minutes, and (d) regrowth without additives after 25 minutes.

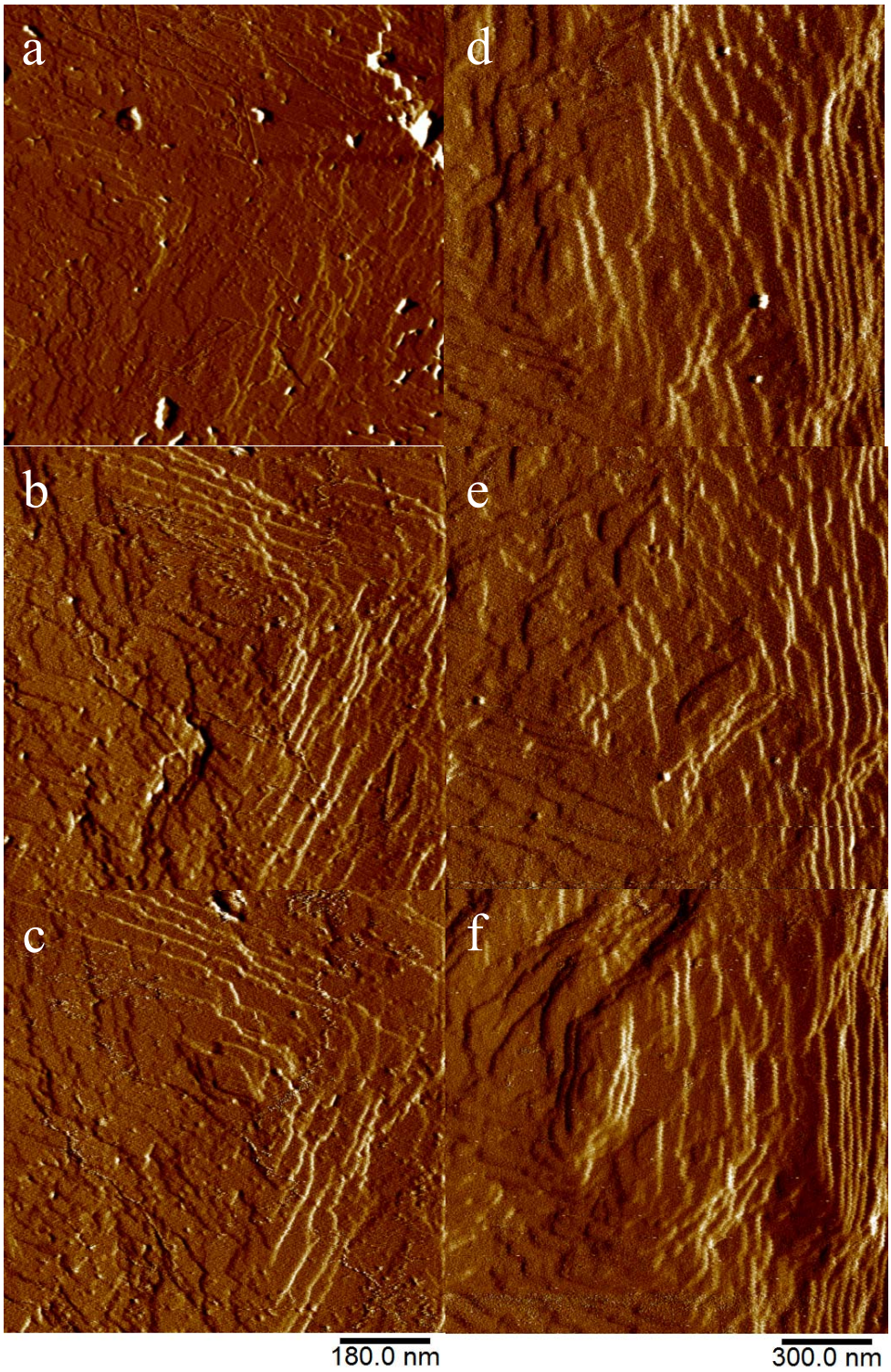


***Figure A6.4***: Snapshots from time resolved *in situ* AFM imaging of hillock growth on the COM (010) face in supersaturated CaOx solutions. (a) Growth: 20 minutes no additives, (b) Inhibition: 40 minutes with tetrazole **13** (3.33 mg/mL) present, and (c) Regrowth: 30 minutes without additives. (d) Growth: 30 minutes without additives, (e) Inhibition: 23 minutes with tetrazole **14** (3.12 mg/mL) present, and (f) Regrowth: 50 minutes without additives.

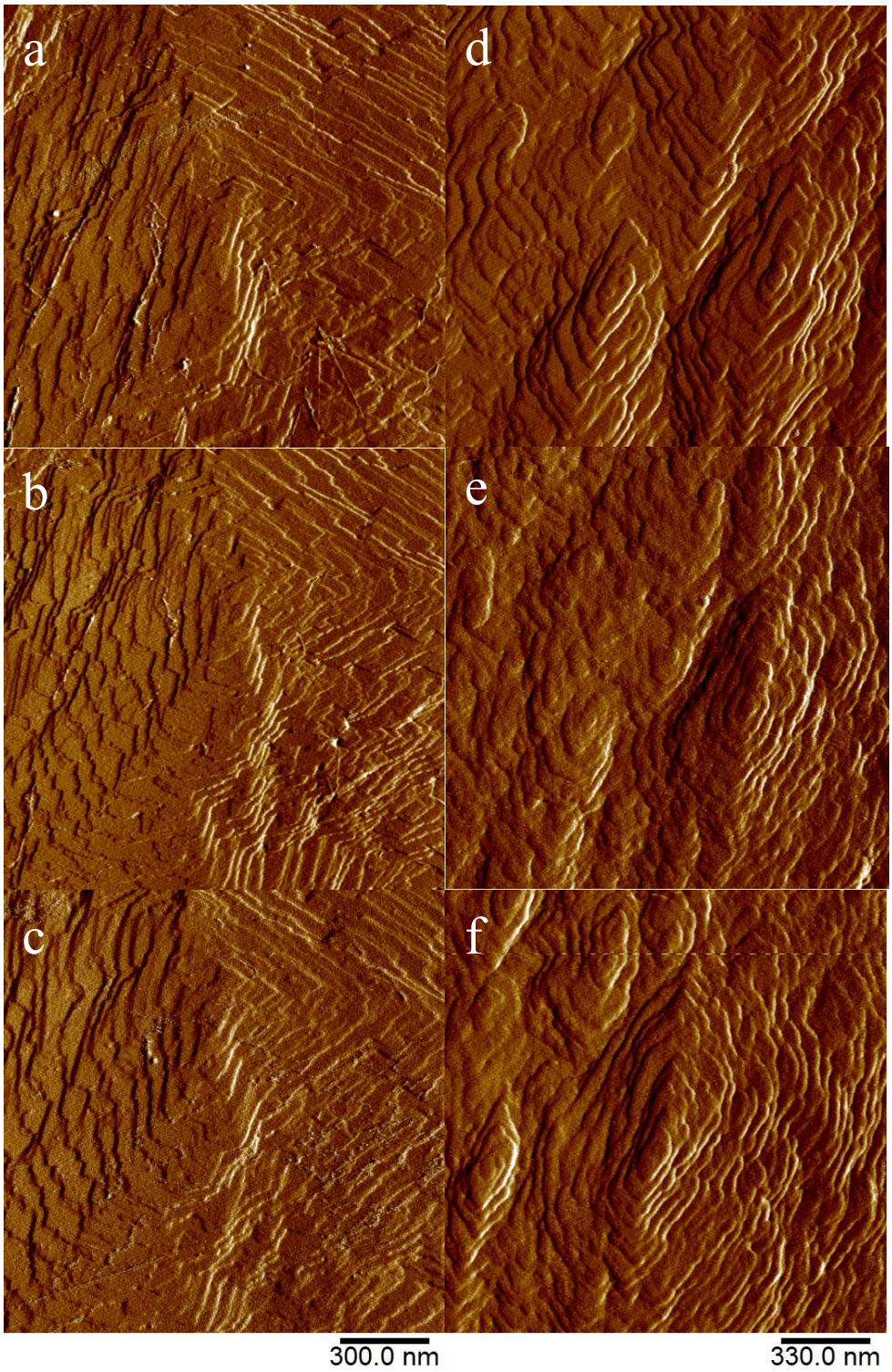


***Figure A6.5***: Snapshots from time resolved *in situ* AFM imaging of hillock growth on the COM (010) face in supersaturated CaOx solutions. (a) Growth: 20 minutes no additives, (b) Inhibition: 40 minutes with tetrazole **6** (3.12 mg/mL) present, and (c) Regrowth: 33 minutes without additives. (d) Growth: 60 minutes without additives, (e) Inhibition: 20 minutes with tetrazole **17** (5.00 mg/mL) present, and (f) Regrowth: 24 minutes without additives.

Snapshots of the complete AFM runs have been converted into video files for the figures from ***Chapter 7*** and ***Appendix 6***:

***Figure 7.2/ Figure A6.1***

***Figure 7.4/ Figure A6.2***

***Figure 7.5/ Figure A6.3***

***Figure 7.7/ Figure A6.4***

***Figure 7.9/ Figure A6.5***

The link to these video files can be found below, with each video in both PeakForce Error and Height modes:

https://cloudstor.aarnet.edu.au/plus/index.php/s/FN93NZW2h2gYmD1.

## A7 Copyright Permissions

I warrant that this thesis contains no material which infringes the copyright of any other person(s). I warrant that I have obtained, where necessary, permission from the copyright owners to use any third-party copyright material reproduced in the thesis. Permission details are presenteed as follows:

***Copyright Permission for Figure 1.2 in Chapter 1***

MINERALOGICAL SOCIETY OF AMERICA
3635 Concorde Pkwy Ste 500 · Chantilly VA 20151-1110 · USA
Tel: 1 (703) 652-9950 · Fax: 1 (703) 652-9951 · Internet: www.minsocam.org

September 21, 2017

Mr. Calum John McMulkin
Curtin University
GPO BOX U1987
Perth WA
Australia

Email: callum.mcmulkin@postgrad.curtin.edu.au

Dear Mr. McMulkin:

I received your e-mail message of 2017-09-21 requesting permission to reproduce the following figure in your thesis, "Crystallisation of calcium oxalate solids in the presence of tetrazoles", for the Curtin University open archive:

- Figure Number(s): 3 from Jeffrey A. Wesson, Michael D. Ward (2007), Pathological Biomineralization of Kidney Stones, *Elements*, v. 3, i. 6, p. 415-421.

It is with pleasure that we grant you permission to reproduce this figure without cost in this and all subsequent editions of the work, its ancillaries, advertisements and promotional materials, and other derivative works, in any form or medium, whether now known or hereafter developed, in all languages, for distribution throughout the world on the conditions that reference is given to the original publication of the Mineralogical Society of America.

Sincerely,

J. Alex Speer

J. Alexander Speer
Executive Director, MSA

***Copyright Permission for Figure 1.7 (B, C) in Chapter 1***

MINERALOGICAL SOCIETY OF AMERICA
3635 Concorde Pkwy Ste 500 · Chantilly VA 20151-1110 · USA
Tel: 1 (703) 652-9950 · Fax: 1 (703) 652-9951 · Internet: www.minsocam.org

September 25, 2017

Mr. Calum John McMulkin
Curtin University
GPO BOX U1987
Perth WA
Australia

Email: callum.mcmulkin@postgrad.curtin.edu.au

Dear Mr. McMulkin:

I received your e-mail message of 2017-09-21 requesting permission to reproduce the following figure in your thesis, "Crystallisation of calcium oxalate solids in the presence of tetrazoles", for the Curtin University open archive:

- Figure Number(s): 6(a) and 6 (c) from James J. De Yoreo, Peter G. Vekilov (21003) Principles of Crystal Nucleation and Growth, *Reviews in Mineralogy and Geochemistry*, v. 54, i. 1, p. 57-93.

It is with pleasure that we grant you permission to reproduce these figures without cost in this and all subsequent editions of the work, its ancillaries, advertisements and promotional materials, and other derivative works, in any form or medium, whether now known or hereafter developed, in all languages, for distribution throughout the world on the conditions that reference is given to the original publication of the Mineralogical Society of America.

Sincerely,

J. Alex Speer

J. Alexander Speer
Executive Director, MSA

***Copyright Permission for Figure 1.11 in Chapter 1***

This Agreement between Mr. Calum McMulkin ("You") and John Wiley and Sons ("John Wiley and Sons") consists of your license details and the terms and conditions provided by John Wiley and Sons and Copyright Clearance Center.

| | |
|---|---|
| License Number | 4197140403057 |
| License date | Sep 27, 2017 |
| Licensed Content Publisher | John Wiley and Sons |
| Licensed Content Publication | Angewandte Chemie International Edition |
| Licensed Content Title | Higher-Order Organization by Mesoscale Self-Assembly and Transformation of Hybrid Nanostructures |
| Licensed Content Author | Helmut Cölfen,Stephen Mann |
| Licensed Content Date | May 28, 2003 |
| Licensed Content Pages | 16 |
| Type of use | Dissertation/Thesis |
| Requestor type | University/Academic |
| Format | Print and electronic |
| Portion | Figure/table |
| Number of figures/tables | 1 |
| Original Wiley figure/table number(s) | Figure 1 |
| Will you be translating? | No |
| Title of your thesis / dissertation | Crystallisation of Calcium Oxalate solids in the presence of Tetrazoles |
| Expected completion date | Oct 2017 |
| Expected size (number of pages) | 250 |
| Requestor Location | Mr. Calum McMulkin<br>Kent Street, Bentley<br><br>Perth, WA 6102<br>Australia<br>Attn: Mr. Calum McMulkin |
| Publisher Tax ID | EU826007151 |
| Billing Type | Invoice |
| Billing Address | Mr. Calum McMulkin<br>Kent Street, Bentley<br><br>Perth, Australia 6102<br>Attn: Mr. Calum McMulkin |
| Total | 0.00 AUD |

***Copyright Permission for Figure 1.13 in Chapter 1***

This Agreement between Mr. Calum McMulkin ("You") and Royal Society of Chemistry ("Royal Society of Chemistry") consists of your license details and the terms and conditions provided by Royal Society of Chemistry and Copyright Clearance Center.

| | |
|---|---|
| License Number | 4198320695947 |
| License date | Sep 29, 2017 |
| Licensed Content Publisher | Royal Society of Chemistry |
| Licensed Content Publication | Chemical Communications (Cambridge) |
| Licensed Content Title | Identifying alkali metal inhibitors of crystal growth: a selection criterion based on ion pair hydration energy |
| Licensed Content Author | Sahar Farmanesh,Bryan G. Alamani,Jeffrey D. Rimer |
| Licensed Content Date | Jul 29, 2015 |
| Licensed Content Volume | 51 |
| Licensed Content Issue | 73 |
| Type of Use | Thesis/Dissertation |
| Requestor type | academic/educational |
| Portion | figures/tables/images |
| Number of figures/tables/images | 1 |
| Format | print and electronic |
| Distribution quantity | 5 |
| Will you be translating? | no |
| Order reference number | |
| Title of the thesis/dissertation | Crystallisation of Calcium Oxalate solids in the presence of Tetrazoles |
| Expected completion date | Oct 2017 |
| Estimated size | 250 |
| Requestor Location | Mr. Calum McMulkin<br>Kent Street, Bentley<br><br>Perth, WA 6102<br>Australia<br>Attn: Mr. Calum McMulkin |
| Billing Type | Invoice |
| Billing Address | Mr. Calum McMulkin<br>Kent Street, Bentley<br><br>Perth, Australia 6102<br>Attn: Mr. Calum McMulkin |
| Total | 0.00 AUD |

***Copyright Permission for Figure 1.14 in Chapter 1***

This Agreement between Mr. Calum McMulkin ("You") and Nature Publishing Group ("Nature Publishing Group") consists of your license details and the terms and conditions provided by Nature Publishing Group and Copyright Clearance Center.

| | |
|---|---|
| License Number | 4198221143936 |
| License date | Sep 29, 2017 |
| Licensed Content Publisher | Nature Publishing Group |
| Licensed Content Publication | Nature |
| Licensed Content Title | Molecular modifiers reveal a mechanism of pathological crystal growth inhibition |
| Licensed Content Author | Jihae Chung, Ignacio Granja, Michael G. Taylor, Giannis Mpourmpakis, John R. Asplin, Jeffrey D. Rimer |
| Licensed Content Date | Aug 8, 2016 |
| Licensed Content Volume | 536 |
| Licensed Content Issue | 7617 |
| Type of Use | reuse in a dissertation / thesis |
| Requestor type | academic/educational |
| Format | print and electronic |
| Portion | figures/tables/illustrations |
| Number of figures/tables/illustrations | 1 |
| High-res required | no |
| Figures | Figure 1: Effect of inhibitors on COM crystallisation |
| Author of this NPG article | no |
| Your reference number | |
| Title of your thesis / dissertation | Crystallisation of Calcium Oxalate solids in the presence of Tetrazoles |
| Expected completion date | Oct 2017 |
| Estimated size (number of pages) | 250 |
| Requestor Location | Mr. Calum McMulkin<br>Kent Street, Bentley<br><br>Perth, WA 6102<br>Australia<br>Attn: Mr. Calum McMulkin |
| Billing Type | Invoice |
| Billing Address | Mr. Calum McMulkin<br>Kent Street, Bentley<br><br>Perth, Australia 6102<br>Attn: Mr. Calum McMulkin |
| Total | 0.00 AUD |

***Copyright Permission for Figure 1.15 in Chapter 1***

This Agreement between Mr. Calum McMulkin ("You") and John Wiley and Sons ("John Wiley and Sons") consists of your license details and the terms and conditions provided by John Wiley and Sons and Copyright Clearance Center.

| | |
|---|---|
| License Number | 4200221134321 |
| License date | Oct 01, 2017 |
| Licensed Content Publisher | John Wiley and Sons |
| Licensed Content Publication | Chemistry - A European Journal |
| Licensed Content Title | Mimicking the Growth of a Pathologic Biomineral: Shape Development and Structures of Calcium Oxalate Dihydrate in the Presence of Polyacrylic Acid |
| Licensed Content Author | Annu Thomas,Elena Rosseeva,Oliver Hochrein,Wilder Carrillo-Cabrera,Paul Simon,Patrick Duchstein,Dirk Zahn,Rüdiger Kniep |
| Licensed Content Date | Feb 22, 2012 |
| Licensed Content Pages | 10 |
| Type of use | Dissertation/Thesis |
| Requestor type | University/Academic |
| Format | Print and electronic |
| Portion | Figure/table |
| Number of figures/tables | 1 |
| Original Wiley figure/table number(s) | Figure 2 |
| Will you be translating? | No |
| Title of your thesis / dissertation | Crystallisation of Calcium Oxalate solids in the presence of Tetrazoles |
| Expected completion date | Oct 2017 |
| Expected size (number of pages) | 250 |
| Requestor Location | Mr. Calum McMulkin<br>Kent Street, Bentley<br><br>Perth, WA 6102<br>Australia<br>Attn: Mr. Calum McMulkin |
| Publisher Tax ID | EU826007151 |
| Billing Type | Invoice |
| Billing Address | Mr. Calum McMulkin<br>Kent Street, Bentley<br><br>Perth, Australia 6102<br>Attn: Mr. Calum McMulkin |
| Total | 0.00 AUD |

***Copyright Permission for Figure 1.16 in Chapter 1***

This Agreement between Mr. Calum McMulkin ("You") and Royal Society of Chemistry ("Royal Society of Chemistry") consists of your license details and the terms and conditions provided by Royal Society of Chemistry and Copyright Clearance Center.

| | |
|---|---|
| License Number | 4198431205922 |
| License date | Sep 29, 2017 |
| Licensed Content Publisher | Royal Society of Chemistry |
| Licensed Content Publication | CrystEngComm |
| Licensed Content Title | Tetrazoles: a new class of compound for crystallization modification |
| Licensed Content Author | Massimiliano Massi,Mark I. Ogden,Tomoko Radomirovic,Franca Jones |
| Licensed Content Date | Aug 2, 2010 |
| Licensed Content Volume | 12 |
| Licensed Content Issue | 12 |
| Type of Use | Thesis/Dissertation |
| Requestor type | academic/educational |
| Portion | figures/tables/images |
| Number of figures/tables/images | 1 |
| Format | print and electronic |
| Distribution quantity | 5 |
| Will you be translating? | no |
| Order reference number | |
| Title of the thesis/dissertation | Crystallisation of Calcium Oxalate solids in the presence of Tetrazoles |
| Expected completion date | Oct 2017 |
| Estimated size | 250 |
| Requestor Location | Mr. Calum McMulkin<br>Kent Street, Bentley<br><br>Perth, WA 6102<br>Australia<br>Attn: Mr. Calum McMulkin |
| Billing Type | Invoice |
| Billing Address | Mr. Calum McMulkin<br>Kent Street, Bentley<br><br>Perth, Australia 6102<br>Attn: Mr. Calum McMulkin |
| Total | 0.00 AUD |